

PROBING SMALL-SCALE STRUCTURE IN
GALAXIES WITH STRONG GRAVITATIONAL
LENSING

BY ARTHUR BENJAMIN CONGDON

A dissertation submitted to the
Graduate School—New Brunswick
Rutgers, The State University of New Jersey
in partial fulfillment of the requirements
for the degree of
Doctor of Philosophy
Graduate Program in Physics and Astronomy

Written under the direction of

Charles R. Keeton

and approved by

New Brunswick, New Jersey

May, 2008

ABSTRACT OF THE DISSERTATION

Probing Small-Scale Structure in Galaxies with Strong Gravitational Lensing

by ARTHUR BENJAMIN CONGDON

Dissertation Director: Charles R. Keeton

We use gravitational lensing to study the small-scale distribution of matter in galaxies. First, we examine galaxies and their dark matter halos. Roughly half of all observed four-image quasar lenses have image flux ratios that differ from the values predicted by simple lens potentials. We show that smooth departures from elliptical symmetry fail to explain anomalous radio fluxes, strengthening the case for dark matter substructure. Our results have important implications for the “missing satellites” problem. We then consider how time delays between lensed images can be used to identify lens galaxies containing small-scale structure. We derive an analytic relation for the time delay between the close pair of images in a “fold” lens, and perform Monte Carlo simulations to investigate the utility of time delays for probing small-scale structure in realistic lens populations. We compare our numerical predictions with systems that have measured time delays and discover two anomalous lenses. Next, we consider microlensing, where stars in the lens galaxy perturb image magnifications. This is relevant at optical wavelengths, where the size of the lensed source is comparable to the Einstein radius of a typical star. Our simulations of negative-parity images show that raising the fraction of dark matter relative to stars increases image flux variability for small sources, and decreases it for large sources. This suggests that quasar accretion disks and

broad-emission-line regions may respond differently to microlensing. We also consider extended sources with a range of ellipticities, which has relevance to a population of inclined accretion disks. Depending on their orientation, more elongated sources lead to more rapid variability, which may complicate the interpretation of microlensing light curves. Finally, we consider prospects for observing strong lensing by the supermassive black hole at the center of the Milky Way, Sgr A*. Assuming a black hole on the million-solar-mass scale, we predict that the probability of observing strong lensing of a background star is roughly 56%. We also consider how lensing by Sgr A* could be used to test general relativity against alternative theories, concluding that microarcsecond resolution would make this possible.

Preface

This thesis consists of six chapters. Chapter 1 provides a thorough introduction to the theory and astrophysical applications of strong gravitational lensing. In the remaining chapters, we use gravitational lensing to study small-scale structure in galaxies in a wide variety of contexts. Chapter 2 presents multipole models of four-image lens systems to determine whether dark matter substructure provides the only viable explanation of anomalous flux ratios that have been observed in several radio lenses. This chapter is based on Congdon & Keeton (2005), which was published in *Monthly Notices of the Royal Astronomical Society* (MNRAS, 364, 1459-1466). Chapters 3 and 4 show how time delays between lensed images can be used to identify galaxies with small-scale structure. These chapters are based on Congdon, Keeton & Nordgren (2008), and are in preparation for submission to *Journal of Mathematical Physics* and *The Astrophysical Journal*, respectively. Chapter 5 considers microlensing of an extended source by a distribution of stars and dark matter, which can be used to probe the structure of lensed quasars and lensing galaxies. This is based on Congdon, Keeton & Osmer (2007), which appeared in *Monthly Notices of the Royal Astronomical Society* (MNRAS, 376, 263-272). Chapter 6 considers prospects for observing strong lensing by the supermassive black hole at the center of the Milky Way, and describes how such measurements could be used to test general relativity. This is based on Congdon, Keeton & Nordgren (2007) which has been submitted to *Physical Review D*.

Acknowledgements

I would like to thank all of those who have provided both professional and personal support from the earliest stages of my academic career to the ultimate completion of this thesis. I first wish to offer my sincere gratitude to Arthur Kosowsky, who encouraged me to pursue my graduate work at Rutgers, and who has contributed greatly to my intellectual development. I am also indebted to Arthur for introducing me to gravitational lensing and to my research advisor, Chuck Keeton. Arthur acquainted me with the astrophysical literature, and Chuck taught me the skills necessary to contribute to it. I could not have known ahead of time what would make for a good advisor, but the opportunity to work with Chuck has shown me what a great advisor is. Chuck has been there for me every step of the way, and it is in large part due to his guidance and support that I have made it to this point. Thank you. There are many others in the Rutgers physics department to whom I would like to offer appreciation. Whenever I needed to rekindle my enthusiasm for research, I knew that a half hour discussion with Jack Hughes would do the trick. I am also grateful to Tad Pryor and Jerry Sellwood, from whom I have learned much, both in the classroom and through informal discussions. I would like to thank both former and current graduate students whom I have had the chance to know: Ross Fadeley, Matthew Francis, Naseem Rangwala, Neelima Sehgal and Juntai Shen. There are several others at Rutgers whom I wish to acknowledge, especially Alex Bachmann for all of her hard work and assistance. The following people outside of Rutgers also deserve thanks: Michael Broscius, Ted Burkhardt, Greg Dobler, Tim Jones, Shannon Knight, Allan Moser, Erik Nordgren, Samantha Osmer, Saul Rappaport and Steve Wolbach. Finally I wish to thank my parents and brother, who have always encouraged me to follow my dreams. Their love and support have been invaluable.

Dedication

I dedicate this thesis to Allan Moser, who has been a constant friend and mentor for over a decade. His excitement about physics inspired me to pursue this subject as an undergraduate, which led naturally to my decision to continue in this field through graduate school. Our weekly discussions over pizza have contributed much to my growth as a physicist. The assistance he has provided me has made a real difference. I have always been able to count on him, especially during the completion of this thesis. It is rare to find someone with the kind of dedication Allan has displayed, and it is my honor to recognize him here. Thank you for everything.

Table of Contents

Abstract	ii
Preface	iv
Acknowledgements	v
Dedication	vi
List of Tables	xi
List of Figures	xii
1. Introduction	1
1.1. From Newton to Einstein	2
1.2. Strong Lensing	6
1.2.1. The Thin Lens Approximation	7
1.2.2. Positions, Magnifications and Time Delays of Lensed Images	9
1.2.3. Conditions for Multiple Imaging	14
1.2.4. Lensing by Non-Spherical Mass Distributions	16
1.3. Astrophysical Applications	28
1.3.1. Anomalous Flux Ratios and Gravitational Millilensing	30
1.3.2. Differential Time Delays and Dark Matter Substructure	34
1.3.3. Galaxy Structure and Quasar Microlensing	35
1.3.4. Supermassive Black Holes and Strong Lensing	37
2. Multipole Models of Four-Image Gravitational Lenses with Anomalous Flux Ratios	43
2.1. Introduction	44
2.2. Methods	46

2.2.1.	Multipole Lens Models	47
2.2.2.	The Minimum Wiggle Model	49
2.3.	Results	51
2.3.1.	External Shear	51
2.3.2.	Higher Order Multipoles	56
2.3.3.	Measurement Uncertainties	57
2.3.4.	A Multi-Source Lens Model	58
2.4.	Conclusions	62
 3. Analytic Relations for Fold and Cusp Lenses: Application to Galactic		
	Structure	65
3.1.	Introduction	65
3.2.	Mathematical Preliminaries	67
3.3.	The Fold Case	70
3.3.1.	Image Positions	70
3.3.2.	Time Delays	72
3.4.	The Cusp Case	74
3.4.1.	Image Positions	75
3.4.2.	Magnifications	77
3.4.3.	Time Delays	78
3.5.	Summary	78
 4. Using Differential Time Delays to Identify Gravitational Lenses with		
	Small-Scale Structure	81
4.1.	Introduction	82
4.2.	Dependence of Time Delay on Lens Potential and Position along Caustic	83
4.3.	Time Delay Distributions for a Realistic Lens Population	87
4.4.	Application to Observed Lenses	89
4.4.1.	Time-Delay Histograms	91
4.4.2.	Identifying Time Delay Anomalies in Observed Lenses	94

4.4.3. Predictions for the Remaining Lenses	97
4.5. Discussion and Conclusions	98
5. Microlensing of an Extended Source by a Power-Law Mass Distribu-	
tion	121
5.1. Introduction	121
5.2. Methods	124
5.3. Results	127
5.3.1. Source Size and Lens Mass	127
5.3.2. Dark Matter Content	132
5.3.3. Source Profile	136
5.3.4. Ellipticity and Position Angle	136
5.3.5. Accretion Disk Geometry	141
5.3.6. Light Curves	142
5.4. Conclusions	145
6. Prospects for Testing General Relativity with Lensing by Massive	
Black Holes	149
6.1. Introduction	150
6.2. Strong Lensing by the Galactic Supermassive Black Hole	153
6.2.1. Stellar Density Profiles and Luminosity Function	154
6.2.2. Strong Lensing of a Background Source Population by a Point Mass	156
6.2.3. Fiducial Model	159
6.2.4. Limiting Magnitude	160
6.2.5. Extinction by Dust	161
6.2.6. Slope of the Luminosity Function	163
6.2.7. Truncation Radius of the Cusp	163
6.2.8. Angular Distribution of Lensed Images	165
6.3. Lensing by Massive Black Holes in Other Systems	167
6.4. Constraining Gravity with SMBH Lensing	170

6.5. Conclusions	173
Vita	180

List of Tables

2.1. Parameters for minimum-wiggle models	55
4.1. Data for four-image lenses.	90
4.2. P-values for scaled time delays	110
4.3. P-values for time-delay ratios	111
4.4. Median values and confidence intervals for scaled time delays	112
4.4. Median values and confidence intervals for scaled time delays	113
4.4. Median values and confidence intervals for scaled time delays	114
4.4. Median values and confidence intervals for scaled time delays	115
4.5. Median values and confidence intervals for time-delay ratios	116
4.5. Median values and confidence intervals for time-delay ratios	117
4.5. Median values and confidence intervals for time-delay ratios	118
4.5. Median values and confidence intervals for time-delay ratios	119
6.1. Number of strong lenses for various limiting magnitudes	161

List of Figures

1.1. Schematic lensing diagram	11
1.2. Caustics for a singular isothermal sphere with shear	22
1.3. Four-image lens configurations	25
1.4. Caustics for a singular isothermal ellipsoid with shear	27
2.1. Isodensity contours for Q2237+0305	52
2.2. Isodensity contours and critical curve for B1422+231	52
2.3. Minimum-wiggle model for B1422+231	53
2.4. Minimum-wiggle model for B2045+265	54
2.5. Normalized RMS wiggle vs. Fourier truncation order	57
2.6. Minimum-wiggle model for B0712+472	59
2.7. Minimum-wiggle model for B1933+503	61
3.1. Local orthogonal coordinates	71
3.2. Dependence of time delay on image separation	74
4.1. Dependence of time delay on position of source along caustic for a sin- gular isothermal ellipsoid with $e = 0.1$	84
4.2. Same as Figure 4.1, but for $e = 0.3$	85
4.3. Same as Figure 4.1, but for $e = 0.5$	86
4.4. Time-delay histograms for fold lenses	100
4.5. Time-delay histograms for fold lenses, continued	101
4.6. Time-delay histograms for fold lenses, continued	102
4.7. Time-delay histograms for cusp lenses	103
4.8. Time-delay histograms for cross lenses	104
4.9. Histograms of time-delay ratios for fold lenses	105
4.10. Histograms of time-delay ratios for fold lenses, continued	106

4.11. Histograms of time-delay ratios for fold lenses, continued	107
4.12. Histograms of time-delay ratios for cusp lenses	108
4.13. Histograms of time-delay ratios for cross lenses	109
5.1. Magnification maps for a positive-parity image	126
5.2. Power-law mass functions	128
5.3. Magnification histograms for a positive-parity image	129
5.4. Magnification histograms for a negative-parity image	130
5.5. Magnification dispersion vs. source size for a positive-parity image . . .	131
5.6. Magnification histograms for different dark matter fractions	133
5.7. Magnification dispersion vs. source size for images of both parities for different dark matter fractions	134
5.8. Magnification dispersion vs. source size for a positive-parity image with different source profiles	137
5.9. Magnification dispersion vs. source size for a positive-parity image with different ellipticities and position angles	138
5.10. Illustration of why microlensing magnifications depend on the orientation of an elliptical source	139
5.11. Magnification dispersion vs. source size for a positive-parity image with various lens and source parameters	140
5.12. Magnification dispersion vs. source size for a positive-parity image with different disk geometries	141
5.13. Illustration for constructing light curves	143
5.14. Light curves and structure functions for a positive-parity image with different ellipticities and position angles	144
6.1. Stellar number density profiles of the Galactic cusp, bulge and disk . . .	155
6.2. Diagram for lensing by a black hole	158
6.3. Cumulative number of strongly-lensed stars behind Sgr A* vs. galacto- centric radius	162

6.4. Number of strongly-lensed stars behind Sgr A* vs. the power-law slope of the luminosity function	164
6.5. Angular distribution of lensed images	165
6.6. Cumulative number of strongly-lensed stars vs. the PPN expansion pa- rameter	172

Chapter 1

Introduction

Gravitational lensing describes the bending of light rays that pass near massive objects between a light source and an observer (see Schneider et al. 1992, for a comprehensive discussion of lens theory). Three roughly distinct subfields of lensing have emerged over the past couple of decades: microlensing in the Local Group, weak lensing, and strong lensing (see Kochanek et al. 2006, for a thorough review). Each of these has contributed greatly to our understanding of the universe.

Microlensing within the Local Group has become a powerful tool in the search for dark matter. As a massive compact halo object (MACHO) passes in front of a more distant star, the latter will appear to brighten and dim over the duration of the event, which is typically on the order of months (Paczynski 1986b). This effect allows for the otherwise invisible foreground object to be detected. Microlensing can also be used to search for extrasolar planets. A lens that consists of a star and planet will produce brightness variations in a lensed background star that differ from what would be observed if the lens were composed of a single massive object.

On a larger scale, the apparent shape of a distant galaxy can be distorted as its light is bent by mass concentrations along the line of sight. While such *weak lensing* is subtle, the combined signal of many lensed galaxies can constrain the amount of matter along the line of sight. This technique has been used to address a number of astrophysical problems, including the determination of galaxy cluster masses, from which the cluster mass function can be derived. This information makes it possible to constrain the value of w , which parameterizes the equation of state for dark energy.

Perhaps the most dramatic effect of light bending is *strong lensing*, where multiple images of a background source are produced. In typical situations, the lensing object is

a galaxy, while the lensed source is a quasar or galaxy. To date, roughly eighty quasar lenses ¹ and seventy galaxy lenses ² (Bolton et al. 2008) have been discovered. The positions and fluxes of lensed images provide important constraints on the structure of the lensed source and lensing object. Strong lensing can be used to study a wide range of astrophysical objects, from galaxies to clusters of galaxies. Such investigations have provided deep insight into the process of hierarchical structure formation, which is the foundation of modern cosmological theory. In this thesis, we use strong lensing to probe the small-scale structure of galaxies.

1.1 From Newton to Einstein

The law of universal gravitation presented by Isaac Newton in his *Philosophiæ Naturalis Principia Mathematica* constituted the first theory in the modern sense, in that it provided a framework for describing the motion of massive objects, whether observed on Earth or in the night sky. With the advent of classical mechanics, it became possible to explain the orbits of celestial bodies in terms of simple physical ideas expressed in a compact mathematical language. One of the first great successes of Newtonian gravity was to derive Kepler’s laws of planetary motion. Since a light ray was thought to consist of a beam of particles, it seemed natural to consider the behavior of light in the presence of gravity. Michell (1784) and Laplace (1795) showed that a light ray leaving the surface of a body with mass M cannot escape the gravitational attraction if the object has a radius less than

$$R_s = \frac{2GM}{c^2}, \quad (1.1)$$

where c is the speed of light and G is the gravitational constant. This work anticipated the concept of a black hole, which emerged from the work of Schwarzschild (1916a,b), who solved the Einstein field equation for a non-rotating, spherically-symmetric mass distribution. For this reason, R_s is now termed the Schwarzschild radius.

Another consequence of gravitational theory is that a light ray passing near a massive

¹See the CASTLES website: <http://www.cfa.harvard.edu/castles/>

²See the SLACS Survey website: <http://slacs.org/>

body will undergo a deflection, such that its apparent position to a foreground observer will differ from its true position. Assuming that a light ray travels at a constant speed c , Soldner (1804) calculated the bending angle due to a point mass:

$$\tan \frac{\tilde{\alpha}}{2} = \frac{GM}{c^2 r} \quad \Rightarrow \quad \tilde{\alpha} \approx \frac{2GM}{c^2 r}, \quad (1.2)$$

where we assume $0 < \tilde{\alpha} \ll 1$. This is reasonable since typical deflection angles are $\sim 1''$. To see this, consider the vector

$$\tilde{\boldsymbol{\alpha}} = \hat{\mathbf{v}}_i - \hat{\mathbf{v}}_f = \int_{\gamma} \frac{d\hat{\mathbf{v}}}{dl} dl, \quad (1.3)$$

where $\hat{\mathbf{v}}_i$ and $\hat{\mathbf{v}}_f$ are unit vectors that specify the initial and final directions of a light ray moving with velocity \mathbf{v} . In the absence of lensing, $\hat{\mathbf{v}}_i = \hat{\mathbf{v}}_f$. If $\tilde{\boldsymbol{\alpha}}$ is small, we can identify its magnitude with the bending angle. Since the direction of the light ray will change continuously as it travels from the source to the observer, we must integrate $d\hat{\mathbf{v}}/dl$ along the path γ from the observer to the source. Following C. R. Keeton (personal communication), we write the integrand as

$$\begin{aligned} \frac{d\hat{\mathbf{v}}}{dl} &= \frac{dt}{dl} \frac{d}{dt} \left[\frac{\mathbf{v}}{|\mathbf{v}|} \right] \\ &= \frac{1}{|\mathbf{v}|} \left[\frac{\mathbf{a}}{|\mathbf{v}|} - \frac{\mathbf{a} \cdot \mathbf{v}}{|\mathbf{v}|^3} \mathbf{v} \right] \\ &= \frac{1}{|\mathbf{v}|^2} [\mathbf{a} - (\mathbf{a} \cdot \hat{\mathbf{v}}) \hat{\mathbf{v}}] \\ &\equiv \frac{\mathbf{a}_{\perp}}{|\mathbf{v}|^2} \\ &= -\frac{\nabla_{\perp} \Phi}{c^2}, \end{aligned} \quad (1.4)$$

where \mathbf{a} is the acceleration vector and Φ is the gravitational potential. The subscript \perp denotes the component perpendicular to the direction of motion. The bending angle can now be written as

$$\tilde{\boldsymbol{\alpha}} = -\frac{1}{c^2} \int_{\gamma} \nabla_{\perp} \Phi dl. \quad (1.5)$$

It is not straightforward to perform this integral, since the path γ of the light ray depends on the deflection angle for which we are solving. If the deflection angle is small, we can approximate the trajectory of the light ray by a straight line, which we take to be along the z -axis. We have

$$\tilde{\boldsymbol{\alpha}} = -\frac{1}{c^2} \int_{-\infty}^{\infty} \nabla_{\perp} \Phi(x, y, z) dz = \frac{1}{c^2} \int_{-\infty}^{\infty} \nabla_{\perp} \Phi(x, y, z) dz. \quad (1.6)$$

Since the size of a typical lensing object is small compared with the total path length of a light ray, we assume that the light source and observer are infinitely far from the lens. It is conventional for the source to be located at $z \rightarrow -\infty$ and the observer at $z \rightarrow +\infty$. Thus we integrate over the range $-\infty < z < \infty$ (cf. Eq. 1.3).

For a point-mass lens, the potential is given by

$$\Phi = -\frac{GM}{r} \equiv -\frac{GM}{\sqrt{R^2 + z^2}}, \quad (1.7)$$

where r and R are the spherical and cylindrical radii of the light ray, respectively. The magnitude of the deflection angle takes the form

$$\begin{aligned} \tilde{\alpha} &= \frac{1}{c^2} \int_{-\infty}^{\infty} \frac{\partial \Phi(R, z)}{\partial R} dz \\ &= \frac{GMR}{c^2} \int_{-\infty}^{\infty} \frac{dz}{(R^2 + z^2)^{3/2}} \\ &= \frac{2GM}{c^2 R}, \end{aligned} \quad (1.8)$$

where R represents the impact parameter of the incoming light ray. This expression is identical to the small-angle formula derived by Soldner (1804). This result received little attention, and the problem of light deflection was not seriously considered again for more than a century. Einstein (1915) used his general theory of relativity to predict that the deflection angle is twice that obtained by Soldner (1804). This expression can be derived by making use of the spacetime metric in the weak-field limit:

$$ds^2 = \left(1 + \frac{2\Phi}{c^2}\right) d(ct)^2 - \left(1 - \frac{2\Phi}{c^2}\right) (dx^2 + dy^2 + dz^2), \quad (1.9)$$

where Φ is the Newtonian potential used above. Light rays follow null geodesics, along which $ds^2 = 0$. We can therefore write

$$c dt = \sqrt{\frac{1 - 2\Phi/c^2}{1 + 2\Phi/c^2}} dl \approx \left(1 - \frac{2\Phi}{c^2}\right) dl, \quad (1.10)$$

where $dl^2 \equiv dx^2 + dy^2 + dz^2$. We keep only the first-order term in $2\Phi/c^2$, since this quantity is small in the weak-field limit.

Consider a light ray emitted by a distant source at time t_i , which follows the path γ , and is received by an observer at t_f . The travel time is given by

$$c(t_f - t_i) = \int_{\gamma} F(x, y, z) dl = \int_{t_i}^{t_f} F(x, y, z) |\mathbf{v}| dt, \quad (1.11)$$

where $F \equiv 1 - 2\Phi/c^2$. Fermat's principle says that a light ray will follow the path of extremal time. This means that the functional $F|\mathbf{v}|$ obeys the Euler-Lagrange equations (C. R. Keeton, personal communication):

$$\frac{d}{dt} \frac{\partial F|\mathbf{v}|}{\partial \dot{x}_i} - \frac{\partial F|\mathbf{v}|}{\partial x_i} = 0, \quad (1.12)$$

which becomes

$$|\mathbf{v}| \frac{\partial F}{\partial x_i} - \sum_j \frac{\partial F}{\partial x_j} \frac{\dot{x}_i \dot{x}_j}{|\mathbf{v}|} - F \frac{\ddot{x}_i}{|\mathbf{v}|} + F \dot{x}_i \frac{\sum_j \dot{x}_j \ddot{x}_j}{|\mathbf{v}|^3} = 0, \quad (1.13)$$

where x_i labels the spatial coordinates. We can write Equation (1.13) in vector form as

$$|\mathbf{v}| \nabla F - (\nabla F \cdot \mathbf{v}) \hat{\mathbf{v}} - \frac{F}{|\mathbf{v}|} [\mathbf{a} - (\mathbf{a} \cdot \hat{\mathbf{v}}) \hat{\mathbf{v}}] = 0. \quad (1.14)$$

Dividing by $F|\mathbf{v}|$, and using Equation (1.4), we find

$$\begin{aligned} \frac{d\hat{\mathbf{v}}}{dl} &= \frac{\nabla_{\perp} F}{F} \\ &= -\frac{2}{c^2} \left(1 - \frac{2\Phi}{c^2}\right)^{-1} \nabla_{\perp} \Phi \\ &\approx -\frac{2}{c^2} \left(1 + \frac{2\Phi}{c^2}\right) \nabla_{\perp} \Phi \\ &\approx -\frac{2}{c^2} \nabla_{\perp} \Phi, \end{aligned} \quad (1.15)$$

which is accurate to first order in $2\Phi/c^2$. The relativistic deflection angle is then

$$\begin{aligned} \tilde{\alpha} &= -\frac{2}{c^2} \int_{\gamma} \nabla_{\perp} \Phi dl \\ &= \frac{2}{c^2} \int_{-\infty}^{\infty} \nabla_{\perp} \Phi dz \end{aligned} \quad (1.16)$$

(see discussion between Eqs. [1.5] and [1.6]).

This equation was confirmed for the case of a point mass deflector by Eddington during the solar eclipse of 1919. He found that the deflection angle of a light ray passing the solar limb agrees with Einstein's prediction of $\tilde{\alpha} = 1''.75$. The result was announced at a joint meeting of the Royal Society and Royal Astronomical Society, and was published the following year (Dyson et al. 1920). Although this is perhaps the most famous confirmation of general relativity, the deflection angle measured by Eddington was subject to errors of $\sim 30\%$. The errors have now been reduced to $\sim 0.01\%$ (Shapiro et al. 2004).

The term “lens” was first used in the context of gravity by Lodge (1919), who commented that the gravitational field is not a lens in the optical sense, since no focal length can be assigned. In any case, an analogy between gravitational light bending and optical lensing serves a useful pedagogical purpose and we will use the term “gravitational lensing” throughout this thesis.

In addition to altering the trajectory of a light ray, gravitational lensing can magnify light from a distant source and can lead to the production of multiple images. Eddington (1920) considered the case of a background star lensed by a foreground star. He found that if the stars are sufficiently aligned, two images of the background star will be produced. While he correctly determined that there is a bright primary image and a faint secondary image, the values he obtained for the magnification factors were in error. Einstein (1936) obtained the correct expression for the magnification of the background star, and Chwolson (1924) showed that the parity of the secondary image is negative, i.e., that the secondary is the inverted image of the primary. Chwolson (1924) also showed that if the foreground and background stars are perfectly aligned, a ring-shaped image of the background star will be formed. This result was later demonstrated by Einstein (1936) and such images are known as “Einstein rings.” Because it was not possible to resolve lensed images of a star, Einstein (1936) concluded that it would be unlikely for gravitational lensing to be observed.

1.2 Strong Lensing

While Zwicky (1937a,b) agreed with Einstein (1936) that the probability of observing lensing of a background star by a foreground star is small, he proposed that lensing of a background galaxy by a foreground galaxy is observationally feasible, due to the large masses of galaxies as compared with stars. As exciting a prospect as this was, it would be more than twenty-five years before further progress in lensing was made.

Several important results emerged during the 1960s and 1970s. A renewed interest in lensing (Klimov 1963; Liebes 1964; Refsdal 1964a) was inspired by the discovery of quasars by Schmidt (1963). Because quasars are so far away, there is a significant

probability that a foreground galaxy will act as a gravitational lens. In addition, quasars are bright enough to be seen at cosmological distances. Taken together, these two facts make quasars ideal targets for lensing observations and provide a powerful way to constrain cosmological parameters and models. Refsdal (1964a) showed that there is a time delay between lensed images, and discussed (1964b) how this effect could be used to constrain the Hubble constant. He also considered the possibility of testing cosmological theories with gravitational lensing (1966).

All of the papers mentioned above treat the lensing object as a point mass. Sanitt (1971) considered the case of lensing by spherical mass distributions. He noted that continuum-emission regions in quasars should be magnified to a greater extent than line-emission regions, since the former are smaller than the latter. We return to this idea in the context of microlensing in Chapter 5. Bourassa et al. (1973) and Bourassa & Kantowski (1975, 1976) generalized to the case of spheroidal lenses. Cooke & Kantowski (1975) derived an expression for the time delay between lensed images for a lens galaxy whose potential is described by a sum of point masses. They found that the time delay can be decomposed into a geometric term that accounts for the different paths corresponding to different lensed images, and a term due to the gravitational potential through which the light rays propagate. We derive this expression in the following subsection, and apply it to lensed quasars in Chapters 3 and 4. Finally, Chang & Refsdal (1979) showed that adding a point-mass perturber to a lens galaxy can alter the image magnifications. This effect is now referred to as quasar microlensing (Paczynski 1986a).

Most of this work seemed rather esoteric until the discovery of the first lensed quasar, 0957+561, by Walsh et al. (1979). The remainder of this section is devoted to the theory of strong lensing, where multiple images of a background source are produced. We discuss astrophysical applications in Section 1.3.

1.2.1 The Thin Lens Approximation

As we noted in Section 1.1, a typical strong gravitational lens is sufficiently localized so that we may assume that the observer and source are infinitely far from the lens. We

can therefore assume that the deflection of a light ray occurs at a single point (x, y) in the plane defined by $z = 0$ about which the lens is centered. It is then possible to write the deflection angle in terms of a projected potential $\phi(x, y)$ and surface mass density $\Sigma(x, y)$.

To see this, consider the gravitational potential in three dimensions:

$$\Phi(x, y, z) = -G \int \frac{\rho(x', y', z') dx' dy' dz'}{[(x - x')^2 + (y - y')^2 + (z - z')^2]^{1/2}}. \quad (1.17)$$

If the lens is confined to the plane $z = 0$, we can write the volume mass density as

$$\rho(x, y, z) = \Sigma(x, y) \delta(z), \quad (1.18)$$

where $\delta(z)$ is the Dirac delta function. The deflection angle (Eq. [1.16]) then takes the form

$$\begin{aligned} \tilde{\alpha}(x, y) &= -\frac{2G}{c^2} \int_{-\infty}^{\infty} dz \left(\mathbf{i} \frac{\partial}{\partial x} + \mathbf{j} \frac{\partial}{\partial y} \right) \int \frac{\Sigma(x', y') \delta(z') dx' dy' dz'}{[(x - x')^2 + (y - y')^2 + (z - z')^2]^{1/2}} \\ &= \frac{2G}{c^2} \int dx' dy' \int_{-\infty}^{\infty} dz \frac{(x - x') \mathbf{i} + (y - y') \mathbf{j}}{[(x - x')^2 + (y - y')^2 + z^2]^{3/2}} \Sigma(x', y') \\ &= \frac{4G}{c^2} \int d^2 x' \frac{(\mathbf{x} - \mathbf{x}') \Sigma(\mathbf{x}')}{|\mathbf{x} - \mathbf{x}'|^2} \\ &= \frac{4G}{c^2} \nabla \int \Sigma(\mathbf{x}') \ln |\mathbf{x} - \mathbf{x}'| d^2 x' \\ &\equiv \frac{4}{c^2} \nabla \phi(x, y), \end{aligned} \quad (1.19)$$

where \mathbf{x} and \mathbf{x}' are two-dimensional position vectors, \mathbf{i} and \mathbf{j} are unit vectors, and ∇ denotes the gradient with respect to \mathbf{x} . Comparing Equations (1.16) and (1.19), we find that ϕ and Φ are related by

$$\phi(x, y) = \frac{1}{2} \int_{-\infty}^{\infty} \Phi(x, y, z) dz + \text{const}. \quad (1.20)$$

We can ignore the constant term, since no lensing observables depend on it. We note for future reference that ϕ satisfies the two-dimensional Poisson equation,

$$\nabla^2 \phi = 2\pi G \Sigma. \quad (1.21)$$

The preceding analysis shows that we can transform the intrinsically three-dimensional situation of light deflection into a two-dimensional problem, provided that Equation (1.18) holds. This is called the *thin lens approximation*,³ and we will use it throughout this thesis. Within this framework, a light ray travels in a straight line from the source ($z \rightarrow -\infty$) to the lens plane ($z = 0$), where it is bent by the angle $\tilde{\alpha}$. It then continues in a straight line to the observer ($z \rightarrow \infty$).

1.2.2 Positions, Magnifications and Time Delays of Lensed Images

In this subsection, we consider lensing of a point source by a spherical mass distribution. We generalize to non-spherical lens potentials in Section 1.2.4. In realistic lensing situations, the observer and source are not infinitely far from the lens, but lie at finite distances. Since these distances are extremely large, we cannot apply the rules of Euclidean geometry, but must instead measure distances by means of the spacetime metric that describes the large-scale geometry of the universe (see Hogg 1999 for an overview of cosmological distances). The concordance cosmological model indicates that the universe is spatially flat (e.g., Spergel et al. 2007), and is therefore described by the Robertson-Walker (RW) metric:

$$\begin{aligned} ds^2 &= c^2 dt^2 - R^2(t) (d\xi_1^2 + d\xi_2^2 + d\xi_3^2) \\ &= R^2(\eta) (d\eta^2 - d\sigma^2) , \end{aligned} \quad (1.22)$$

where $R(t)$ sets the spatial scale of the universe, $d\sigma^2 \equiv \sum_i d\xi_i^2$, and the conformal time, η , is defined by

$$\eta = \int \frac{c dt}{R(t)} . \quad (1.23)$$

The comoving coordinates, ξ_i , are related to the physical coordinates, x_i , by $x_i = R(t)\xi_i$. The utility of conformal time and comoving coordinates will become clear.

Note that the RW metric applies to a homogeneous universe and therefore does not account for the lensing object. Since the lens is confined to a small region, we can use

³In the case that more than one lensing object is present along the line of sight to a background source, it is possible to construct multiple lens planes centered on the various lensing objects (see Schneider et al. 1992).

the RW metric to compute the path length of a lensed light ray. In order to calculate the deflection angle, however, we must use the perturbed Minkowski metric of equation (1.9).

We now determine the angular positions of lensed images for a given source position and gravitational potential. Consider a light source, S , with angular position β , whose comoving distance from the observer, O , is d_S . A light ray emitted at S travels a distance d_{LS} to the lens plane, L . The light ray is then bent through an angle $\tilde{\alpha}$, and then proceeds a distance d_L to O . From Figure 1.1, we see that images form at angular positions θ such that $\beta = \theta - \alpha$. We would like to write the angle α in terms of the physically meaningful angle $\tilde{\alpha}$. To do this, note from Figure 1.1 that

$$d_S \sin \beta + d_{LS} \sin (\tilde{\alpha} - \theta) + d_{LS} \cos (\tilde{\alpha} - \theta) \tan \theta = d_S \cos \beta \tan \theta. \quad (1.24)$$

Assuming that β, θ , and $\tilde{\alpha}$ are small, which is appropriate in the weak-field limit, this becomes

$$\beta = \theta - \frac{d_{LS}}{d_S} \tilde{\alpha} = \theta - \frac{D_{LS}}{D_S} \tilde{\alpha}, \quad (1.25)$$

where we have converted from comoving distance, d , to physical (angular diameter) distance, D . From this equation, we see that

$$\alpha = \frac{D_{LS}}{D_S} \tilde{\alpha}. \quad (1.26)$$

We refer to α as the *reduced deflection angle*. Note that α is a function of θ . In general, Equation 1.25 has multiple solutions for θ .

As noted earlier, lensed images will be magnified relative to an unlensed source. For a source of infinitesimal size, the magnification is defined to be the ratio of image area to source area, viz.,

$$\mu = \frac{\theta d\theta d\varphi}{\beta d\beta d\varphi}. \quad (1.27)$$

Note that the differential azimuth, $d\varphi$, is the same in the lens and source planes, since the deflection angle for a spherical lens has only a θ -component. Equation 1.25 gives the dependence of β on θ for a given lens potential, so it is more convenient to work with the inverse magnification,

$$\mu^{-1} = \frac{\beta d\beta}{\theta d\theta}. \quad (1.28)$$

In addition to the positions and magnifications of lensed images, a deflected light ray will experience a time delay relative to one that is not lensed. This time delay consists of two terms. If no lens were present, a light ray would travel in a straight line from S to O . A deflected light ray, however, follows a longer path. To compute the time difference, we make use of the conformal time. Since $ds^2 = 0$ for light rays, conformal time and comoving distance are identical. From Figure 1.1, the “geometric” time delay is given by $\Delta\eta_{\text{geom}} = d_L + d_{LS} - d_S$. We can write d_S in terms of d_L and d_{LS} by partitioning the triangle defined by d_L , d_{LS} and d_S into two right triangles. We then have

Applying the small-angle approximation $\cos x \approx 1$ ($0 < x \ll 1$), we find $\Delta\eta_{\text{geom}} = 0$. To obtain the first non-vanishing term, we must use the higher-order approximation

$\cos x \approx 1 - x^2/2$. We then have

$$\Delta\eta_{\text{geom}} = \left[\frac{(d_S - d_{LS})^2}{d_{LS}} - d_L \right] \frac{\alpha^2}{2}. \quad (1.30)$$

Since we are only interested in the leading-order non-vanishing term in $\Delta\eta_{\text{geom}}$, we may write $d_S \approx d_L + d_{LS}$ in this equation. We therefore obtain

$$\Delta\eta_{\text{geom}} = \frac{d_L d_S}{d_{LS}} \frac{\alpha^2}{2} = \frac{D_L D_S}{R(z_L) D_{LS}} \frac{\alpha^2}{2}, \quad (1.31)$$

where we write the scale factor, R , as a function of the lens redshift, z_L . To convert from conformal time to physical time, we combine Equation (1.23) with the fact that the relevant time scale is short compared to the Hubble time. We find

$$\begin{aligned} \Delta t_{\text{geom}} &= \frac{R_0}{c} \Delta\eta_{\text{geom}} \\ &= \frac{R_0 D_L D_S}{c R(z_L) D_{LS}} \\ &= \frac{1 + z_L}{c} \frac{D_L D_S}{D_{LS}}, \end{aligned} \quad (1.32)$$

where R_0 is the scale factor at the present epoch, and we have used the relation $R(z) = (1 + z)^{-1} R_0$.

In addition to the geometric time delay, the gravitational potential leads to an increase in travel time. To compute the “potential” time delay, we take the difference of the travel time when a gravitational field is present, and that for which the potential vanishes. Using Equation (1.10), we find

$$\frac{c\Delta t_{\text{pot}}}{1 + z_L} = \int \left(1 - \frac{2\Phi}{c^2} \right) dl - \int dl = -\frac{2}{c^2} \int_{-\infty}^{\infty} \Phi dz = -\frac{4}{c^2} \phi, \quad (1.33)$$

where the factor $1 + z_L$ accounts for the fact that the time measured by the observer differs from that measured at the lens plane.

We now combine the geometric and gravitational terms to obtain

$$\Delta t = \frac{1 + z_L}{c} \frac{D_L D_S}{D_{LS}} - \frac{4(1 + z_L)}{c^3} \phi = \frac{1 + z_L}{c} \frac{D_L D_S}{D_{LS}} \left[\frac{(\theta - \beta)^2}{2} - \psi \right], \quad (1.34)$$

where we introduce the *lens potential*,

$$\psi \equiv \frac{4}{c^2} \frac{D_{LS}}{D_L D_S} \phi. \quad (1.35)$$

In terms of this potential, the reduced deflection angle is given by $\alpha = \partial\psi/\partial\theta$, which implies that

$$\beta = \theta - \frac{\partial\psi}{\partial\theta}. \quad (1.36)$$

This is called the *lens equation*. Although we used a geometric argument to determine the image positions, an alternative approach that has become widely used is to derive the time delay, and then determine its stationary points in θ , which are the image positions (e.g., Blandford & Narayan 1986; Schneider et al. 1992).

To conclude this subsection, we compute the image positions and magnifications for a point-mass lens. We do not consider time delays for this lens model, as they will not be needed in this thesis. Using Equations (1.7) and (1.16), the reduced deflection angle of a point mass is given by

$$\alpha = \frac{D_{LS}}{D_S} \frac{4GM}{c^2 R} = \frac{D_{LS}}{D_L D_S} \frac{4GM}{c^2} \frac{1}{\theta}, \quad (1.37)$$

where we have written the radial coordinate R in terms of the angular coordinate θ , i.e., $R = D_L \theta$. Defining the *Einstein angle* as

$$\theta_E \equiv \sqrt{\frac{D_{LS}}{D_L D_S} \frac{4GM}{c^2}}, \quad (1.38)$$

the lens equation takes the simple form

$$\beta = \theta - \frac{\theta_E^2}{\theta}. \quad (1.39)$$

Multiplying by θ , and applying the quadratic formula, we find the image positions:

$$\theta_{\pm} = \frac{1}{2} \left(-\beta \pm \sqrt{\beta^2 + 4\theta_E^2} \right). \quad (1.40)$$

The corresponding magnifications are

$$\mu_{\pm} = \frac{\theta_{\pm}^4}{\theta_{\pm}^4 - \theta_E^4}. \quad (1.41)$$

The above expressions show that a point-mass lens always produces two images of a background source. The primary image at θ_+ has positive parity and is always magnified ($\mu_+ > 1$), while the secondary image at θ_- has negative parity and can be magnified or demagnified ($\mu_- < 0$). The magnifications of the two images satisfy the

relation $\mu_+ + \mu_- = 1$. In the special case that $\beta = 0$, the two images are infinitely magnified. One actually observes a ring-shaped image when $\beta = 0$, due to the circular symmetry of this case. The angular “radius” of the ring is θ_E . In the limit $\beta \gg \theta_E$, the position and magnification of the primary image approach the values for the true source position. Meanwhile, the secondary image approaches $\theta = 0$, and its magnification vanishes. In other words, if the projected separation between the source and lens is large, light bending can be neglected, and the apparent and true source positions and magnifications coincide. We return to point-mass lensing in Chapter 6, where we consider lensing by the supermassive black hole at the center of the Milky Way.

1.2.3 Conditions for Multiple Imaging

For the point-mass lens, we found that two images of a background source are always produced. In general, the number of images that are created depends both on the source position and on the lens model. Our interest in this subsection is to determine the conditions required for strong lensing. We begin by considering spherical mass distributions, for which the deflection angle takes the form

$$\alpha(\theta) = \frac{4G}{c^2} \frac{D_{LS}}{D_L D_S} \frac{M(\theta)}{\theta}, \quad (1.42)$$

where we have used Gauss’s Law (cf. Eq.[1.37]). If the source lies directly behind the lens, Equation (1.36) becomes

$$0 = \theta_E - \frac{4G}{c^2} \frac{D_{LS}}{D_L D_S} \frac{M(\theta_E)}{\theta_E}. \quad (1.43)$$

The mass enclosed by the Einstein angle is then

$$M(\theta_E) = \frac{c^2}{4G} \frac{D_L D_S}{D_{LS}} \theta_E^2. \quad (1.44)$$

The mean surface density within the Einstein ring is given by

$$\langle \Sigma \rangle = \frac{M(\theta_E)}{\pi D_L^2 \theta_E^2} = \frac{c^2}{4\pi G} \frac{D_S}{D_L D_{LS}} \equiv \Sigma_{\text{crit}}. \quad (1.45)$$

Physically, this equation means that if an Einstein ring is produced, the enclosed mean surface density of the lens is Σ_{crit} , which is independent of the lens model. Equivalently, if the surface density is always less than Σ_{crit} , an Einstein ring cannot form.

In all situations of practical importance, a lens can only produce multiple images of a background source if it can create an Einstein ring. For this reason, Σ_{crit} is called the *critical density* for lensing. Although this interpretation of Σ_{crit} is strictly valid only for spherical lenses, it provides a useful rule of thumb for determining whether a lens can produce multiple images.

It is convenient to write the surface density in units of the critical density, viz., $\kappa \equiv \Sigma/\Sigma_{\text{crit}}$. This quantity is known as the *convergence*. In terms of κ , the (two-dimensional) Poisson equation is

$$\nabla^2 \psi = 2\kappa \quad (1.46)$$

(cf. Eq. [1.21]), whose solution is

$$\psi(\mathbf{x}) = \frac{1}{\pi} \int \kappa(\mathbf{x}') \ln |\mathbf{x} - \mathbf{x}'| d^2 x', \quad (1.47)$$

where \mathbf{x} and \mathbf{x}' are two-dimensional *angular* position vectors (cf. Eq. [1.19]). Unless otherwise indicated, vectors appearing in the remainder of this thesis refer to angular coordinates rather than physical displacements.

Even for lenses that can produce multiple images, it is often the case that strong lensing results for some source positions but not for others. To illustrate this point, we consider the *singular isothermal sphere* (SIS), which is often used in galaxy lensing (e.g., Chapter 5). The SIS possesses a flat rotation curve, which is a feature of many observed galaxies. In addition, its lensing properties can be determined analytically. Its volume density (including both luminous and dark matter) is given by

$$\rho = \frac{\sigma^2}{4\pi G} \frac{1}{r^2} = \frac{\sigma^2}{4\pi G} \frac{1}{R^2 + z^2}, \quad (1.48)$$

where σ is the velocity dispersion of the SIS. The mass enclosed within an angle θ is given by

$$M(\theta) = \frac{\sigma^2}{4\pi G} \int_{-\infty}^{\infty} dz \int_0^{D_L \theta} dR \frac{2\pi R}{R^2 + z^2} = \frac{\pi \sigma^2 D_L}{2G} \theta, \quad (1.49)$$

which implies a deflection angle of

$$\alpha(\theta) = 2\pi \left(\frac{\sigma}{c} \right)^2 \frac{D_{LS}}{D_S} \equiv \theta_E. \quad (1.50)$$

In elliptical galaxies, which are most relevant to this thesis, luminous matter dominates at small radii while dark matter is dominant at large radii. Lensed images typically

form at intermediate radii, so lensing offers a way to probe the distribution of both stars and dark matter in galaxies.

It is customary to require that $\beta > 0$, but it is possible for θ to be positive or negative. This would have been apparent if we had included the direction of the deflection angle rather than considering only its magnitude. In particular, $\theta > 0 \Rightarrow \alpha > 0$, while $\theta < 0 \Rightarrow \alpha < 0$. If $\theta > 0$, the lens equation takes the form $\theta = \beta + \theta_E$. This equation is satisfied for all β . If $\theta < 0$, we have $\theta = \beta - \theta_E$, which is satisfied only if $\beta < \theta_E$. In other words, two images are produced if $\beta < \theta_E$, while there is only one image for $\beta > \theta_E$. If $\beta = 0$, an Einstein ring with radius θ_E is produced. It is quite common for different regions of the source plane to correspond to different numbers of lensed images, as described in the next subsection.

1.2.4 Lensing by Non-Spherical Mass Distributions

We now turn to the case of non-spherical lenses. The SIS provides a useful “toy” model, but it cannot by itself be used to describe realistic lens galaxies. It can, however, be modified to yield lens models that are both realistic and have properties that are straightforward to compute, albeit not analytically for most source positions. These models maintain an isothermal radial density profile ($\rho \propto r^{-2}$), but allow for departures from spherical symmetry. The latter property makes it possible to produce four-image lenses, which are the focus of Chapters 2 through 5. Asymmetry is typically modeled in one of two ways. First, the lens galaxy could remain spherical, but lie near mass concentrations that produce tidal forces. We model this effect by an external *shear* field. The other possibility is that the lensing object could be intrinsically non-spherical. To account for this effect, we introduce ellipticity into the lens galaxy. We will consider these two models in turn.

Before proceeding, we must write the lens equation in vector form. If the lens is spherical, the lens, source and images are collinear on the sky. This will no longer be the case if asymmetry is introduced to the lens potential. In this case, we replace the angles β and θ with two-dimensional vectors \mathbf{u} and \mathbf{x} . We must also work with the vector quantity $\boldsymbol{\alpha}(\mathbf{x})$, which generally includes a non-radial component (see Eq. [1.19]).

We can then write the lens equation as

$$\mathbf{u} = \mathbf{x} - \boldsymbol{\alpha}(\mathbf{x}) = \mathbf{x} - \nabla\psi(\mathbf{x}). \quad (1.51)$$

The magnification is again given by the ratio of image area to source area. The appropriate generalization of Equation (1.27) is given by the determinant of the *magnification tensor*. In terms of the source position \mathbf{u} , and image position \mathbf{x} , we have

$$\mu^{-1} = \det \left(\frac{\partial \mathbf{u}}{\partial \mathbf{x}} \right), \quad (1.52)$$

where

$$\frac{\partial \mathbf{u}}{\partial \mathbf{x}} \equiv \begin{pmatrix} \frac{\partial u}{\partial x} & \frac{\partial u}{\partial y} \\ \frac{\partial v}{\partial x} & \frac{\partial v}{\partial y} \end{pmatrix}, \quad (1.53)$$

and is known in mathematical terms as the Jacobian of \mathbf{u} . In component form, we have $\mathbf{u} = (u, v)$ and $\mathbf{x} = (x, y)$.

The Shear Approximation

Suppose that a perturbing galaxy lies far from the primary lens. We can then expand the potential of the perturber in a Taylor series:

$$\psi(x, y) = \psi_0 + \psi_x x + \psi_y y + \frac{1}{2} (\psi_{xx} x^2 + \psi_{yy} y^2) + \psi_{xy} xy + \dots \quad (1.54)$$

We choose coordinates (x, y) centered on the primary lens. The Taylor coefficients give the partial derivatives of the potential evaluated at the origin (e.g., $\psi_0 = \psi(\mathbf{0})$, $\psi_x = \partial\psi(\mathbf{0})/\partial x$, $\psi_{xy} = \partial^2\psi(\mathbf{0})/\partial x\partial y$). We can set $\psi_0 = 0$, since constant terms in the potential have no effect on lensing observables (cf. Eq. [1.20]). The linear terms in the potential correspond to constant terms in the reduced deflection angle, which represents a translation of the source position. Since the source position is unobservable, such terms can be neglected,⁴ i.e., $\psi_x = \psi_y = 0$. We have thus shown that the leading-order contribution to the potential is quadratic. For convenience we define

$$\kappa_0 \equiv \frac{1}{2} (\psi_{xx} + \psi_{yy}), \quad \gamma_1 \equiv \frac{1}{2} (\psi_{xx} - \psi_{yy}) \quad \text{and} \quad \gamma_2 \equiv \psi_{xy}. \quad (1.55)$$

⁴Linear terms in the potential do affect the general expression for the time delay, but do not affect the “differential” time delay between lensed images (Gorenstein et al. 1988). Since only the differential time delay is observable, we ignore linear terms in the potential.

This allows us to write the potential as

$$\begin{aligned}\psi(x, y) &= \frac{1}{2} \left[(\kappa_0 + \gamma_1) x^2 + (\kappa_0 - \gamma_1) y^2 \right] + \gamma_2 xy \\ &= \frac{r^2}{2} [\kappa_0 + \gamma \cos 2(\theta - \theta_\gamma)] ,\end{aligned}\tag{1.56}$$

where $(x, y) \equiv (r \cos \theta, r \sin \theta)$ and $(\gamma \cos 2\theta_\gamma, \gamma \sin 2\theta_\gamma) \equiv (\gamma_1, \gamma_2)$. The parameters γ and θ_γ specify the amplitude and direction of the shear, respectively. Note that shear describes the quadrupole term of the perturbing potential, and is therefore invariant under rotations by π . This accounts for the factor of two appearing in the argument of the cosine in Equation (1.56).

Physically, the external convergence, κ_0 , gives the surface density of the perturbing mass at the lens galaxy, and gives rise to isotropic magnification. While κ_0 is small, it cannot usually be ignored (Keeton & Zabludoff 2004). Unfortunately, the external convergence is not observable. To circumvent this difficulty, we rescale the distance factors in such a way that $\kappa_0 = 0$ (Gorenstein et al. 1988). This transformation does not affect image positions or magnifications, but does alter the time delays. This is known as the *mass-sheet degeneracy*, and we will return to it in Section 1.3.2.

Unlike convergence, shear produces anisotropic amplification. For example, it causes a circular source to appear elliptical. For reference, the typical shear amplitude is $\gamma \sim 0.1$ in galaxy strong lensing (Keeton et al. 1997; Holder & Schechter 2003; Momcheva et al. 2006).

Singular Isothermal Sphere with Shear

We can now consider lensing by an SIS embedded in a shear field. Without loss of generality, we choose coordinates aligned with the direction of shear ($\theta_\gamma = 0$). In rectangular coordinates, the potential of the SIS takes the form $\psi(x, y) = \theta_E \sqrt{x^2 + y^2}$, which comes from integrating Equation (1.50) over the radial coordinate. The lens equation then reads,

$$u = x - \frac{\theta_E x}{\sqrt{x^2 + y^2}} + \gamma x \tag{1.57}$$

$$v = y - \frac{\theta_E y}{\sqrt{x^2 + y^2}} - \gamma y . \tag{1.58}$$

We first consider the simplest case, where the source is at the origin ($\mathbf{u} = \mathbf{0}$). We find four images with positions

$$(x, y) = \left(0, \pm \frac{\theta_E}{1 - \gamma}\right) \quad \text{and} \quad (x, y) = \left(\pm \frac{\theta_E}{1 + \gamma}, 0\right). \quad (1.59)$$

We see that the breaking of spherical symmetry prevents the formation of Einstein rings. Images resembling Einstein rings can be formed if the source is spatially extended.

Let us now consider a source away from the origin. For the sake of analytic tractability, we assume that the source lies on a symmetry axis of the potential. We begin with the case $v = 0$. We find the following solutions:

$$(x, y) = \left(\frac{u + \theta_E}{1 + \gamma}, 0\right) \quad (\text{always}) \quad (1.60)$$

$$(x, y) = \left(\frac{u - \theta_E}{1 + \gamma}, 0\right) \quad (\text{if } u < \theta_E) \quad (1.61)$$

$$(x, y) = \left(\frac{u}{2\gamma}, \pm \sqrt{\frac{\theta_E^2}{(1 - \gamma)^2} - \frac{u^2}{4\gamma^2}}\right) \quad (\text{if } u < 2\gamma\theta_E/(1 - \gamma)). \quad (1.62)$$

We see from these solutions that for $\gamma < 1/3$, four images are produced if $u < 2\gamma\theta_E/(1 - \gamma)$, two images are produced if $2\gamma\theta_E/(1 - \gamma) < u < \theta_E$ and one image is produced if $u > \theta_E$. Although typical shear amplitudes are smaller than $1/3$, it is possible, although as yet unseen (Holder & Schechter 2003), to have $\gamma > 1/3$. In that case, four images are produced if $u < \theta_E$, three images are produced if $\theta_E < u < 2\gamma\theta_E/(1 - \gamma)$ and one image is produced if $u > 2\gamma\theta_E/(1 - \gamma)$. We now turn to the case of a source on the v -axis ($u = 0$). We find images at

$$(x, y) = \left(0, \frac{v + \theta_E}{1 - \gamma}\right) \quad (\text{always}) \quad (1.63)$$

$$(x, y) = \left(0, \frac{v - \theta_E}{1 - \gamma}\right) \quad (\text{if } v < \theta_E) \quad (1.64)$$

$$(x, y) = \left(\pm \sqrt{\frac{\theta_E^2}{(1 + \gamma)^2} - \frac{v^2}{4\gamma^2}}, -\frac{v}{2\gamma}\right) \quad (\text{if } v < 2\gamma\theta_E/(1 + \gamma)). \quad (1.65)$$

We see from these solutions that for $\gamma < 1$, four images are produced if $v < 2\gamma\theta_E/(1 + \gamma)$, two images are produced if $2\gamma\theta_E/(1 + \gamma) < v < \theta_E$ and one image is produced if $v > \theta_E$. Shear amplitudes exceeding unity are not observed and would indicate that terms in the perturbing potential beyond the quadrupole cannot be neglected (i.e., the shear

approximation breaks down). Note that a source on the v -axis must be closer to the origin than a source on the u -axis to produce four images.

For a source that is not on a symmetry axis, we must solve the lens equation numerically (e.g., Keeton 2001). While this precludes the type of analysis given in the preceding discussion, the results presented there are indicative of the general properties of lensing by non-spherical mass distributions. For a source on a symmetry axis, we found that different source positions correspond to different numbers of images. These transitions are marked by specific points on the u - and v -axes. It turns out that the source plane is divided into regions of differing image multiplicity by closed curves known as *caustics*. Examples of caustics for an SIS with shear are shown in Figure 1.2. For reference, the left-hand panel shows an SIS without shear. In that case, the source plane is separated by the Einstein angle into regions where one and two images are produced (cf. §1.2.3).

For a shear amplitude of 0.1 (middle panel), there are two caustics. The dotted curve shows the “radial” caustic, outside which one image is produced. Our analysis for on-axis sources would suggest that sources within the radial caustic produce two images. However, this is not actually the case. The reason is that realistic galaxies are presumably not singular at the origin, but instead have cores of finite density. The introduction of a central core causes sources within the radial caustic to produce three images, although one of them is typically too faint to be observed (see below). The solid curve shows the “tangential” caustic. In mathematical terms, the tangential caustic has the shape of an astroid. The four points are called “cusps” and the connecting curves are called “folds.” The term “cusp” is clear enough, while the term “fold” comes from geometric considerations that are beyond the scope of this introduction. Whereas singular models predict that a source within the astroid will appear as four separate images, “softened” models predict five images, with one of the images being highly demagnified. It turns out that an odd number of images is produced for a lens whose three-dimensional density profile is shallower than r^{-2} (Burke 1981), where r is the spherical radius. Since one of the images in a three-image or five-image configuration cannot readily be detected, we refer to these systems as two-image and four-image

lenses.

When $\gamma = 0.5$ (right-hand panel), the tangential caustic becomes quite large while the size of the radial caustic is unchanged. This is consistent with the result for on-axis sources that the boundary between the one-image and two-image regions is independent of the external shear. The structure of the tangential caustic also meets our expectations: its long axis is oriented in the u -direction, while its short axis is oriented in the v -direction. In other words, a source on the v -axis must be closer to the center of the caustic than a source on the u -axis to produce four images. Note also that the short-to-long axis ratio of the astroid increases with the shear amplitude. In particular, it is given by $(1 - \gamma)/(1 + \gamma)$, as indicated by our analytic results. Finally, we see that for $\gamma = 0.5$, the tangential caustic pokes through the radial caustic along the horizontal axis. Since the horizontal cusps are not “clothed” by the radial caustic in this case, they are referred to as “naked.” A source within the naked region of the astroid produces three observable lensed images, although such configurations are not often observed (see below).

Since the lens equation cannot be solved analytically for an arbitrary source position, finding the caustics might seem to be a daunting task. However, it turns out that caustics are curves along which the magnification is formally infinite (although we note that infinite magnification is not observed in practice, because no source is truly infinitesimal in size). The magnification is a function of image coordinates (x, y) , so it is most natural to work in the lens plane. We set $\mu^{-1} = 0$ in Equation (1.52), and solve for y in terms of x , which can often be done analytically. The resulting curve in the lens plane is known as the *critical curve* (see Fig. 1.3 and discussion thereof). We can then use the lens equation to determine the corresponding curve in the source plane, viz., the caustic. For a source just inside the radial caustic, one of the lensed images will be highly elongated in the radial direction, and *mutatis mutandis* for a source inside the tangential caustic, whence the terms “radial” and “tangential.”

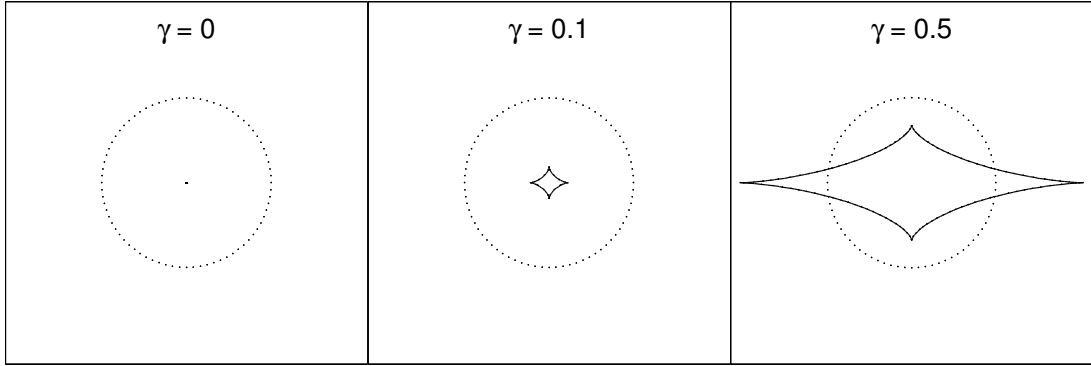


Figure 1.2 Caustics for a singular isothermal sphere with shear. The shear is aligned with the horizontal axis. From left to right, panels show cases with no shear ($\gamma = 0$), moderate shear ($\gamma = 0.1$) and large shear ($\gamma = 0.5$). Caustics are curves that separate regions of the source plane corresponding to different numbers of images. In each panel, the dotted curve shows the radial caustic while the solid curve shows the tangential caustic. A source outside the radial caustic produces one image; a source between the radial and tangential caustics produces three images; a source within both caustics produces five images. For a source inside a caustic, one of the images is typically too faint to be observed, so in practice, two-image and four-image configurations are observed. Three-image configurations can be observed for a source between the tangential and radial caustics if $\gamma > 1/3$ (see text). Such configurations are known as “naked cusps” (right-hand panel). If the shear vanishes, the tangential caustic collapses to a single point (left-hand panel).

Singular Isothermal Ellipsoid without Shear

We now consider the *singular isothermal ellipsoid* (SIE), which was described in detail by Kormann et al. (1994). Its density profile is the same as that of the SIS except that the angular “radius” is replaced by $\sqrt{q^2 x^2 + y^2}$, where q is the minor-to-major axis ratio of the lens. The corresponding potential is quite complicated, so for pedagogical purposes, we here consider the simpler *singular isothermal elliptical potential* (SIEP) defined by $\psi = \theta_E \sqrt{q^2 x^2 + y^2}$. While the corresponding density profile is somewhat unrealistic, especially for small values of q , the qualitative features are similar for the SIE and SIEP. In subsequent chapters, we use the SIE to model elliptical galaxies. The lens equation for the SIEP has the form

$$u = x - \frac{q^2 \theta_E x}{\sqrt{q^2 x^2 + y^2}} \quad (1.66)$$

$$v = y - \frac{\theta_E y}{\sqrt{q^2 x^2 + y^2}}. \quad (1.67)$$

We can solve these equations analytically if the source lies along one of the symmetry axes of the galaxy. Consider the case $v = 0$. We find the following solutions:

$$(x, y) = (u + q \theta_E, 0) \quad (\text{always}) \quad (1.68)$$

$$(x, y) = (u - q \theta_E, 0) \quad (\text{if } u < q \theta_E) \quad (1.69)$$

$$(x, y) = \left(\frac{u}{1 - q^2}, \pm \sqrt{\theta_E^2 - \frac{q^2 u^2}{(1 - q^2)^2}} \right) \quad (\text{if } u < (1 - q^2) \theta_E / q). \quad (1.70)$$

We see from these solutions that for $q > 1/\sqrt{2}$, four images are produced if $u < (1 - q^2) \theta_E / q$, two images are produced if $(1 - q^2) \theta_E / q < u < q \theta_E$, and one image is produced if $u > q \theta_E$. When $q < 1/\sqrt{2}$, $q \theta_E < (1 - q^2) \theta_E / q$, and naked cusps are produced. SIE lenses can also produce naked cusps, but the axis ratio must be somewhat smaller: $q < 0.394$ (Keeton et al. 2005b). Such axis ratios are relevant for lensing by spiral galaxies (Keeton & Kochanek 1998), although only one such lens is known to have a naked cusp (Lewis et al. 2002). Naked cusps can form for systems with larger axis ratios if the inner density profile is shallower than isothermal (Oguri & Keeton 2004). One example of a naked cusp produced by such a system is the lens SDSS J1029+2623 (Oguri et al. 2008).

As in the case of an SIS with shear, SIE lenses are modeled in practice with small finite-density cores. This means that caustics separate regions where one, three and five images are created. In the case of multiple imaging, we again find that one of the images is very dim. Because this image is expected to form near the center of the lens galaxy, the term “central image” has been introduced. Since the lens galaxy is often quite luminous at optical wavelengths, it is difficult to detect central images in optical lenses. To date, central images have only been detected in the quasar lenses PMN J1632-0033 (Winn et al. 2004) and SDSS J1004+4112 (Inada et al. 2005). At radio wavelengths, contamination from the lens galaxy should not be a problem, so it is surprising that central images are not found in radio lenses⁵ (e.g., Rusin & Ma 2001; Boyce 2006). This may not be so surprising in light of the work of Keeton (2003b). He found that massive galaxies with steep density profiles are most efficient at producing strong lenses, but that the central images they produce are much fainter than the other images. Moreover, Mao et al. (2001) found that the presence of a supermassive black hole at the center of the lens galaxy can also suppress central images. We return to lensing by black holes in the context of the Milky Way in Section 1.3.4 and Chapter 6.

We now describe the general properties of SIE lenses, ignoring the existence of central images. Caustics and critical curves for an SIE lens with projected ellipticity $e = 1 - q = 0.5$ are shown in Figure 1.3. The radial and tangential caustics have the same basic shape as for an SIS with moderate shear (middle panel of Fig. 1.2). The basic image configurations are also the same for the SIS with shear and the SIE. We only discuss four-image systems here, so the source is understood to be within the tangential caustic. For a source near a fold (filled circle in left-hand diagram in top panel), two of the four images (squares in right-hand diagram) are highly magnified and straddle the critical curve (ellipse in right-hand diagram). For a source near a cusp (filled circle in left-hand diagram in middle panel), three of the four images (squares in right-hand diagram) lie near the critical curve with two of the images outside and one inside. For a source that is not near the caustic (bottom panel), none of the images lie

⁵The central image in the lens B2319+051 reported by Boyce (2006) turned out to be a false detection upon deeper follow-up observations (E. R. Boyce, personal communication).

near the critical curve, and the image configuration is known as a “cross.”

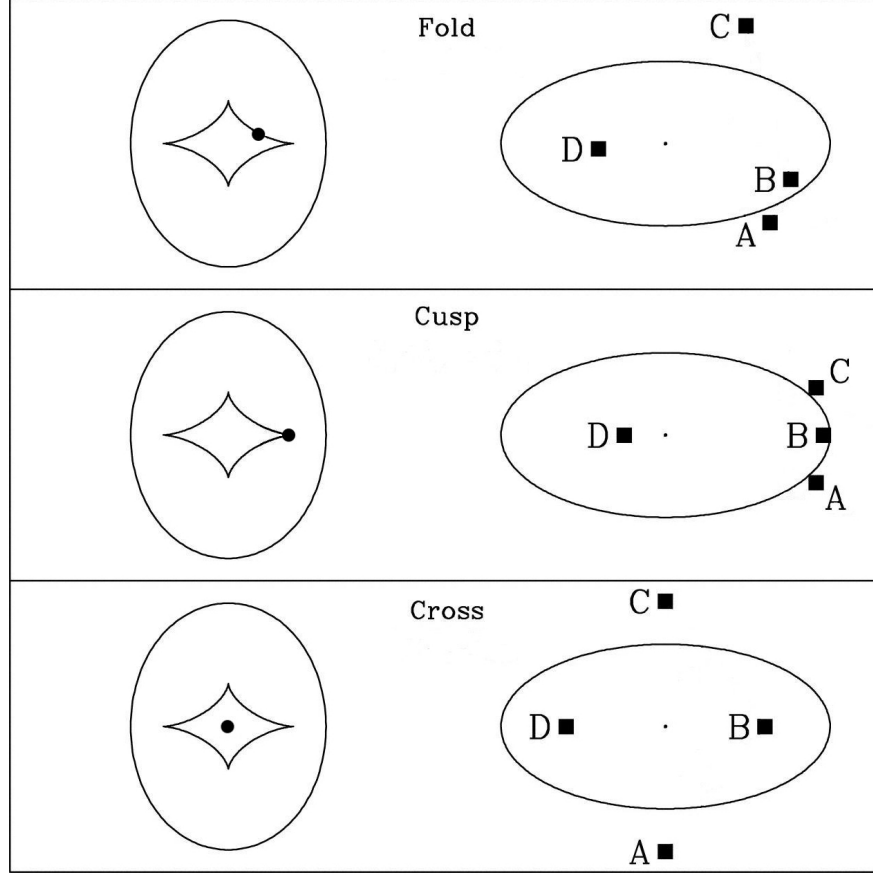


Figure 1.3 The three basic four-image lens configurations (based on Figure 1 of Keeton et al. 2005). Caustics (left) and critical curves (right) are shown for a singular isothermal ellipsoid (SIE) with axis ratio $q = 0.5$. The relationship between source position and image number is the same as that for an SIS with shear (see Fig. 1.2). Caustics are mapped via the lens equation (Eq. [1.51]) to critical curves (ellipse and dot in right-hand diagrams). In each panel, the lensed source (circle) produces four images (squares). A source lying near the tangential caustic (upper two panels) produces a pair (top) or triplet (middle) of bright images that straddle the tangential critical curve (ellipse).

Singular Isothermal Ellipsoid with Shear

In realistic lens systems, we must include the effects of both intrinsic ellipticity in the lens galaxy and tidal shear from perturbing bodies. Figure 1.4 shows caustics for an SIE with shear. We vary the ellipticity, e , from top to bottom, and the shear angle, θ_γ , from left to right. We fix the shear amplitude at $\gamma = 0.1$. For a fixed value of

θ_γ , increasing the ellipticity enlarges the tangential caustic, similar to what we found when increasing γ for an SIS with shear. For $e = 0.9$, which would be appropriate for a nearly edge-on disk (see Keeton & Kochanek 1998), naked cusps are produced for all three values of θ_γ . Meanwhile, the aspect ratio of the radial caustic decreases with increasing ellipticity, in agreement with our analysis of the SIEP, where this ratio is simply $q = 1 - e$. For an SIEP, the height of the radial caustic is constant, in contrast to its behavior seen in Figure 1.4. This is not surprising, since the SIEP and SIE make different predictions when the ellipticity is large.

We now consider the effects of shear angle on the structure of the caustics. When $\theta_\gamma = 0^\circ$, we find a small naked-cusp region when $e = 0.5$. If there were no external shear, we would need to have $e > 0.606$ in order to produce naked cusps. In other words, the shear conspires with the ellipticity to create a larger tangential caustic than would be possible with ellipticity alone. When $\theta_\gamma = 45^\circ$, the tangential caustic undergoes a counter-clockwise rotation, its size decreases and its shape is altered. Even with these changes, the tangential caustic maintains its identity as an astroid. We see that the reduction in size of the tangential caustic for $\theta_\gamma = 45^\circ$ removes the naked cusps for $\theta_\gamma = 0^\circ$, assuming an ellipticity of 0.5. When the shear and ellipticity are perpendicular ($\theta_\gamma = 90^\circ$), the shear and ellipticity partially cancel out, leading to a substantial decrease in the size of the tangential caustic.

Although the values of ellipticity and shear angle we have considered do not represent an exhaustive sampling of the $e - \gamma$ plane, the nine parameter combinations whose caustics are shown in Figure 1.4 provide a fair representation of caustic topologies expected for realistic lens populations. In particular, the tangential caustic almost always has an astroid shape, i.e., four cusps connected by four folds (Schneider et al. 1992; Petters et al. 2001). It is possible, given an appropriate combination of shear and ellipticity, to generate caustics for which six, or even eight, lensed images can be formed (Keeton et al. 2000). Such caustics are known as “swallowtails,” and are discussed by Schneider et al. (1992) and Petters et al. (2001). These exotic structures are expected to be rare and we do not discuss them further.

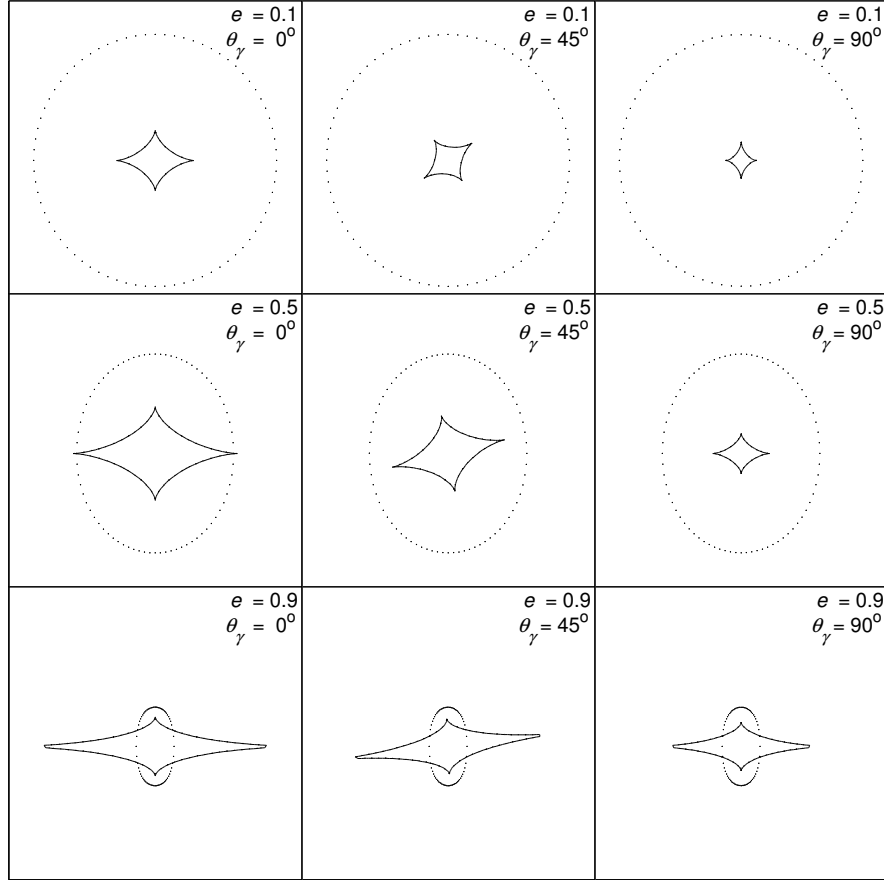


Figure 1.4 Caustics for an SIE with shear. The shear amplitude is fixed at $\gamma = 0.1$. From top to bottom, rows show caustics for an SIE with ellipticity $e \equiv 1 - q$ of 0.1, 0.5 and 0.9. From left to right, columns show caustics for an external shear with position angle θ_γ (measured from the horizontal axis) of 0° , 45° and 90° .

Beyond Ellipticity and Shear

Most lens systems can be quite accurately described by an SIE with shear. However, there are some cases where it is necessary to include more complicated structure. It is known that elliptical galaxies often have “boxy” or “disky” isophotes (Bender et al. 1989; Saglia et al. 1993), indicating the presence of higher-order multipole terms. It is usually sufficient to include Fourier modes up to fourth order. In Chapter 2, we consider models that allow for arbitrary truncation order and consider whether such models can explain the “flux-ratio anomalies” observed in many four-image quasar lenses. In addition to the “global” features of the lens potential (e.g., shear, ellipticity

and higher-order multipoles), it is possible for discrete objects, such as dark matter clumps, stars and black holes, to have a noticeable effect on lensing observables. These “local” features are considered in Chapters 3 through 6.

1.3 Astrophysical Applications

We now discuss the astrophysical applications of strong lensing, with particular emphasis on those aspects central to this thesis. After the discovery of the system 0957+561 (Walsh et al. 1979), and the subsequent identification of the lens galaxy (Young et al. 1980; Stockton 1980), it became clear that lensing could become an observational tool for probing cosmology. There remained one difficulty, however: two-image lenses such as 0957+561 (hereafter 0957) provide too few constraints to be useful for constraining the mass distribution of the lens (but see Grogin & Narayan 1996), which is one of the primary goals of lens modeling. Fortuitously, the lens PG 1115+080 (hereafter 1115) was discovered only a year after 0957. Although it was originally thought that 1115 had three images (Weymann et al. 1980), further observation managed to resolve one of the images into a closely-spaced doublet, showing that this lens actually contains four images (Hege et al. 1980, 1981). The unambiguous identification of this system as a gravitational lens would need to await the discovery of the lens galaxy several years later (Shaklan & Hege 1986).

In many ways, the lens 1115 is ideal for astrophysical investigation. For one thing, 1115 is a fold lens. As we will discuss in more detail in Chapters 2 through 4, fold lenses can be used to study small-scale structure in lens galaxies. In addition, the time delays between the lensed images of 1115 have been measured, which provides a way to constrain the Hubble constant (Keeton & Kochanek 1997) along the lines described by Refsdal (1964b).

The lens 1115 was the first of many four-image systems to be discovered. There are now more than twenty such systems known (for a compilation, see Chapter 4). In a pioneering work, Kochanek (1991) performed detailed lens modeling for twelve lens systems, including 1115 and four other quadruply-imaged quasars. Since galaxies contain

large amounts of dark matter, it is often not possible to determine their mass distributions using photometry. Gravitational lensing is sensitive to all mass, and therefore provides a unique probe of distant galaxies. In his study, Kochanek (1991) modeled the lens galaxies in his sample with five simple but reasonable potentials. He found that the image positions tightly constrain the mass they enclose, but they are not as useful for determining higher-order effects such as ellipticity. He used only the image positions as constraints. In principle, he could have used flux ratios as well, but simple lens models generally find it difficult to reproduce these data. This discrepancy between theory and observation inspired the term “flux-ratio anomaly.” This problem has turned out to be one of the most important challenges in lensing over the past decade or so. Flux-ratio anomalies are specifically addressed in Chapter 2, and are also relevant to Chapter 5.

Since there is a time-delay between lensed images, one might suspect that a perceived anomaly is simply due to this effect. In order for this to be the correct explanation, intrinsic variability of the lensed source would be required. However, there are several lens systems in which the combination of intrinsic variability and time delay is insufficient to explain the observed anomalies (e.g., Fassnacht et al. 1999). In addition, as we will see in Chapters 3 and 4, time delays between images in a fold pair or cusp triplet tend to be short, meaning that very rapid, large-amplitude variability would be needed for brightness variations in the source to be responsible for the anomalies in these systems. Since fold and cusp lenses comprise the relevant lens sample, and do not exhibit flux variation on the required timescale, we conclude that anomalous flux ratios are not a consequence of time delays, and thus constitute a genuine astrophysical problem.

As lens models and observational capabilities have improved, gravitational lensing has become an increasingly important technique for studying cosmology in general, and galaxies in particular. It is now possible to constrain not only the global properties of galaxy mass distributions, but also the small-scale structure of galaxies, which has profound implications for the *cold dark matter* (CDM) paradigm. We consider a number of lensing-based channels for studying small-scale structure in galaxies. The remainder of this introduction provides an overview of the specific problems studied in this thesis.

1.3.1 Anomalous Flux Ratios and Gravitational Millilensing

If the theory of hierarchical structure formation is correct, all CDM halos should contain substructure in the form of clumps with a wide range of masses. In particular, galaxies are expected to contain satellites with typical masses of $\sim 10^6 - 10^8 M_\odot$. Although the number of observed Galactic satellites has been steadily increasing (e.g., Martin et al. 2007), this number remains nearly an order of magnitude smaller than the number of dwarf galaxies predicted to orbit the Milky Way (Moore et al. 1999; Klypin et al. 1999). The discrepancy is even greater for the Local Group as a whole.

There may be a link between CDM substructure and lensed quasars. Roughly half of all observed four-image quasar lenses have image flux ratios that differ from the values predicted by a smooth mass distribution for the lens galaxy, regardless of the specific model assumed (Keeton et al. 2003, 2005). At optical wavelengths, microlensing by stars in the lens galaxy (see Chapter 5) may at least partly explain some of the flux-ratio anomalies. In contrast, radio-emitting regions in quasars are large enough to smooth over the effects of individual stars, so some other explanation is required. Dalal & Kochanek (2002) found that CDM substructure can explain the six known radio anomalies, if a few percent of the total mass of the lens galaxy is in the form of $\sim 10^6 M_\odot$ clumps, which is in broad agreement with the predictions of N-body simulations (Moore et al. 1999; Klypin et al. 1999).

To understand the effect of a clump on lensing observables, we consider a lens described by a smooth mass model, plus a clump in front of one of the lensed images. We assume a point source for simplicity (for the case of a finite source, see Dobler & Keeton 2006). As described in Section 1.2.4, we can expand the lens potential in a Taylor series about an appropriate origin. In the present situation we expand the potential of the primary lens about one of the lensed images. As in our earlier discussion, we choose coordinates aligned with the direction of shear ($\theta_\gamma = 0$), which in this case comes from the lens galaxy itself. The shear amplitude is again denoted by γ . The parameter κ_0 represents the surface density at the image position.

A lensed image described by κ_0 and γ can be categorized according to its parity. In

the absence of the perturbing clump, the magnification tensor is diagonal with elements $\lambda_{\pm} = 1 - \kappa_0 \pm \gamma$. If λ_+ and λ_- are both positive, the image occurs at a local minimum of the time-delay function; if λ_+ is positive and λ_- is negative, the image forms at a saddle point, and is inverted in the direction orthogonal to the shear; if λ_+ and λ_- are both negative, the image forms at a local maximum, and is inverted along both coordinate axes. Because of their relation to image orientation, minima and saddle points are referred to as positive-parity and negative-parity images, respectively. Maximum images are rarely observed in galaxy lensing since they usually correspond to the faint central images discussed in Section 1.2.4. As we will see, the effect of a clump depends on the parity of the “macro”-image described by κ_0 and γ .

We model the perturbing clump by an SIS. Since the clump is located at the origin, it cannot be modeled by an external convergence and shear. Using angular coordinates (r, θ) , the potential of an SIS clump is given by

$$\psi(r, \theta) = R_E r \quad (1.71)$$

where R_E is the Einstein angle of the clump. The lens equation for a source at the origin then takes the form

$$(\lambda_- r - R_E) \cos \theta = 0 \quad (1.72)$$

$$(\lambda_+ r - R_E) \sin \theta = 0. \quad (1.73)$$

We would like to solve these equations to find the image positions. To do this, we consider three cases:

i) $x \neq 0; y \neq 0 \Rightarrow \cos \theta \neq 0; \sin \theta \neq 0$. The lens equation takes the form

$$\lambda_- r - R_E = 0 \quad (1.74)$$

$$\lambda_+ r - R_E = 0, \quad (1.75)$$

which implies that $R_E/r = \lambda_+ = \lambda_-$. Given that $\gamma > 0$, this cannot be satisfied, so either x or y must vanish.

ii) $x \neq 0$; $y = 0 \Rightarrow \cos \theta \neq 0$; $\sin \theta = 0$. The lens equation takes the form $\lambda_- r - R_E = 0$. For a saddle or maximum ($\lambda_- < 0$), there are no solutions, since r cannot be negative. For a minimum ($\lambda_- > 0$), we find the solutions $x = \pm R_E / \lambda_-$.

iii) $x = 0$; $y \neq 0 \Rightarrow \cos \theta = 0$; $\sin \theta \neq 0$. The lens equation takes the form $\lambda_+ r - R_E = 0$. “Micro”-images are produced for minima and saddles where $\lambda_+ > 0$. Their positions are $y = \pm R_E / \lambda_+$.

To summarize, a clump at the origin produces micro-images at

$$(x, y) = \left(0, \pm \frac{R_E}{\lambda_+}\right) \quad (\text{minima and saddles}) \quad (1.76)$$

$$(x, y) = \left(\pm \frac{R_E}{\lambda_-}, 0\right) \quad (\text{minima only}). \quad (1.77)$$

For a maximum, no micro-images are created.

These results show that the separation between the lensed images is $\sim R_E$. For typical values of the distance factors D_L , D_S and D_{LS} , the Einstein angle is given by

$$R_E \sim \left(\frac{M}{10^{12} M_\odot}\right)^{1/2} \times 1''. \quad (1.78)$$

Formally, the mass of an SIS is infinite, and this formula does not apply to such a clump. The Einstein angle is given instead in terms of the velocity dispersion (see Eq. [1.50]). Note, however, that the infinite mass of an SIS is related to its infinite spatial extent, which is clearly unphysical. In practice, a truncation radius is introduced so that the mass of the clump becomes finite. For the type of clump predicted by CDM cosmology, a mass of $\sim 10^6 M_\odot$ is typical (see above). This means that the Einstein angle, and hence also the image separation, is $0''.001$, in agreement with detailed lensing studies of clumps (Dalal & Kochanek 2002; Dobler & Keeton 2006; Chen et al. 2007). It is for this reason that lensing by clumps is called “millilensing.” Astrometric perturbations on this scale are difficult to detect, but millilensing can still be observed thanks to the deviations in image magnification induced by clumps.

Let us now find the magnifications of the images. The magnification tensor is given by

$$\frac{\partial \mathbf{u}}{\partial \mathbf{x}} = \begin{pmatrix} \lambda_- - \frac{R_E}{r} \sin^2 \theta & \frac{R_E}{r} \sin \theta \cos \theta \\ \frac{R_E}{r} \sin \theta \cos \theta & \lambda_+ - \frac{R_E}{r} \cos^2 \theta \end{pmatrix}, \quad (1.79)$$

whose determinant is

$$\mu^{-1} = \mu_0^{-1} - \frac{R_E}{r}(1 - \kappa_0 - \gamma \cos 2\theta), \quad (1.80)$$

where $\mu_o = [(1 - \kappa_0)^2 - \gamma^2]^{-1}$ is the magnification produced by the background convergence and shear. For the images on the y -axis, the inverse magnification is $\mu^{-1} = -2\gamma\lambda_+ = (-2\gamma/\lambda_-)\mu_0^{-1}$; for the images on the x -axis, the inverse magnification is $\mu^{-1} = 2\gamma\lambda_- = (2\gamma/\lambda_+)\mu_0^{-1}$.

The total magnification (in absolute value) due to the macro-image and clump is given by the sum of the unsigned magnifications produced by each of the micro-images, viz., $A \equiv \sum_i |\mu_i|$. For a negative-parity macro-image, the total magnification is $A_- = |(\lambda_-/\gamma)\mu_0|$. This quantity can be larger or smaller than $|\mu_0|$, depending on the specific combination of κ_0 and γ . It will be larger if $\lambda_- < -\gamma$ or $\kappa_0 > 1$, and will be smaller otherwise. This means that a clump can magnify or demagnify a saddle-point image. Previous investigations have shown that perturbing bodies such as CDM clumps (Keeton 2003a; Kochanek & Dalal 2004) and stars (Schechter & Wambsganss 2002) tend to cause demagnification of saddles. To understand this result consider a macro-image with $\kappa_0 = \gamma = 0.55$, which corresponds to $|\mu_0| = 10$. Such values are typical for quadruply-imaged quasars. If an SIS clump is placed in front of the image, the magnification is reduced by a factor of ~ 5 , which is easily observable. For a positive-parity macro-image, the total magnification is $A_+ = |[2(1 - \kappa_0)/\gamma]\mu_0|$, which always exceeds μ_0 since $\lambda_- > 0$. For typical macro-parameters of $\kappa_0 = \gamma = 0.45$, a clump increases the magnification by more than a factor of two.

The preceding discussion provides an accurate qualitative description of clump lensing, but there are a few caveats. In realistic situations, a population of clumps will act in concert to produce magnification shifts that cannot be quantitatively described by the analysis given here for a single clump. Another complication is that the positions of clumps are not known, due to their presumed lack of light emission. It is possible to derive analytic expressions for the magnification due to a clump as a function of source position (Keeton 2003a), but we must resort to numerical simulations if we wish to consider a distribution of clumps with random positions.

Dalal & Kochanek (2002) accounted for the effects that were not included here, and they found that magnification perturbations induced by substructure are indeed great enough to resolve radio flux anomalies. This remarkable success does not, however, preclude other mechanisms from playing a role in understanding anomalous flux ratios. Globular clusters and luminous dwarf satellites have the appropriate masses, but are not abundant enough to account for the observed anomalies (Mao & Schneider 1998; Chiba 2002). Another alternative to CDM substructure is “smooth” perturbations to the lens potential, which might represent astrophysical features such as shells or tails. We show in Chapter 2 that multipole models provide poor fits to the flux-ratio data in four of the most highly anomalous radio lenses. Together with the constraints provided by Einstein rings (Yoo et al. 2005), our results provide strong evidence that CDM clumps offer the most attractive solution to the flux-ratio problem. In order for flux ratios to reach their potential in probing CDM substructure, we must identify a robust method for determining whether a given system is anomalous. Keeton et al. (2005) used perturbation theory to obtain an analytic expression for the fluxes of the two bright images in a fold lens. In Chapter 3, we apply their formalism to the three bright images in a cusp configuration and derive a scaling law whose validity currently rests on numerical simulations. Our results show that perturbation theory has an important role to play in gravitational lensing.

1.3.2 Differential Time Delays and Dark Matter Substructure

After establishing in Chapter 2 that CDM clumps are very likely present in lens galaxies, we work to identify new ways of detecting their presence with lensing. To complement flux-ratio studies (Keeton et al. 2003, 2005), Keeton & Moustakas (2008) have discussed the possibility of constraining substructure properties with lens time delays. In order to apply their method, it is first necessary to identify systems whose time delays reveal the presence of small-scale structure. This is the subject of Chapters 3 and 4. In Chapter 3, we derive an analytic expression for the time delay between the bright images in a fold configuration. Motivated by this result, we employ Monte Carlo simulations in Chapter 4 to identify small-scale structure in lens systems for which time delays have

been measured, and we make predictions for systems without observed time delays.

One difficulty we must overcome in using time delays is our ignorance of cosmological parameters. To see this, consider the time delay of an image at \mathbf{x} for a source at \mathbf{u} :

$$\tau(\mathbf{x}) = \tau_0 \left[\frac{1}{2} |\mathbf{x} - \mathbf{u}|^2 - \psi(\mathbf{x}) \right]. \quad (1.81)$$

The scale factor is given by

$$\tau_0 = \frac{1 + z_L}{c} \frac{D_L D_S}{D_{LS}}. \quad (1.82)$$

The lens redshift, z_L , is not always known, and the distance factors D_L , D_S and D_{LS} depend on the Hubble constant, whose value is not certain. In addition, we must contend with the mass-sheet degeneracy, which says that adding a constant convergence to the lens alters the time delay between images. Since this convergence is not observable, we cannot determine the time delay unambiguously. Fortunately, we can largely avoid these issues by constructing time-delay ratios. Such quantities do not involve τ_0 , and are thus independent of cosmological parameters. Since the convergence due to a mass sheet is the same for all of the images in a lens system, the degeneracy between constant convergence and time delay is also removed by using time-delay ratios.

There is one remaining difficulty that we cannot entirely overcome, known as the “radial profile” degeneracy: changing the slope of the density profile alters the time delays, but leaves all other observables unaffected (Keeton & Kochanek 1997; Saha 2000; Kochanek 2002). Fortunately, the systematic errors introduced by this degeneracy are not expected to be large for time-delay ratios (Keeton & Moustakas 2008). We can understand this qualitatively by noting that lensed images are typically confined to an annulus whose thickness is smaller than the Einstein radius of the lens galaxy (Kochanek 2002). This means that all images are affected in nearly the same way, and thus the radial profile degeneracy is mitigated by constructing time-delay ratios.

1.3.3 Galaxy Structure and Quasar Microlensing

Clumps of dark matter are not the only objects that can noticeably alter lensing observables. Nearly three decades ago, Chang & Refsdal (1979) considered the problem of a star embedded in an external convergence and shear. They concluded that even a single

star can affect the brightness of a lensed image. This problem is analogous to lensing by a galaxy plus a dark matter clump, except that we model the perturbing body (i.e., a star) as a point mass rather than an SIS (cf. §1.3.1). The deflection angle due to a star is given by $\boldsymbol{\alpha}(r) = (R_E^2/r) (\cos \theta, \sin \theta)$. We can then write the lens equation as

$$(\lambda_- r^2 - R_E^2) \cos \theta = 0 \quad (1.83)$$

$$(\lambda_+ r^2 - R_E^2) \sin \theta = 0, \quad (1.84)$$

for a star at the origin. The solutions are

$$(x, y) = \left(0, \pm \frac{R_E}{\sqrt{\lambda_+}}\right) \quad (\text{minima and saddles}) \quad (1.85)$$

$$(x, y) = \left(\pm \frac{R_E}{\sqrt{\lambda_-}}, 0\right) \quad (\text{minima only}). \quad (1.86)$$

For a star with mass $\sim M_\odot$, the image separation is $\sim R_E \sim 1 \mu\text{as}$ (microarcsecond). Lensing perturbations due to stars are therefore known as “microlensing.” Note that microlensing in the present context differs from its usage in the beginning of this chapter.

Let us now find the magnifications. The magnification tensor is given by

$$\frac{\partial \mathbf{u}}{\partial \mathbf{x}} = \begin{pmatrix} \lambda_- - \frac{R_E^2}{r^2} \cos 2\theta & \frac{R_E^2}{r^2} \sin \theta \cos \theta \\ \frac{R_E^2}{r^2} \sin \theta \cos \theta & \lambda_+ - \frac{R_E^2}{r^2} \cos 2\theta \end{pmatrix}. \quad (1.87)$$

We therefore find the inverse magnification to be

$$\mu^{-1} = \mu_0^{-1} - \frac{R_E^2}{r^2} \left(\frac{R_E^2}{r^2} - 2\gamma \cos 2\theta \right). \quad (1.88)$$

For the images on the y -axis, we have $\mu^{-1} = -4\gamma \lambda_+ = -(4\gamma/\lambda_-) \mu_0^{-1}$. For the images on the x -axis, we have $\mu^{-1} = 4\gamma \lambda_- = (4\gamma/\lambda_+) \mu_0^{-1}$. For a negative-parity macro-image, we have $A_- = (\lambda_-/2\gamma) \mu_0$, where we have summed over the unsigned magnifications of the two micro-images. The image will be demagnified relative to μ_0 if $\kappa_0 < 1$, which is satisfied for typical values of κ_0 . For instance, $\kappa_0 = \gamma = 0.55 \rightarrow \mu \approx 0.1 \mu_0$, where μ is the signed magnification. For a positive-parity macro-image, the total magnification is $A_+ = [(1 - \kappa_0)/\gamma] \mu_0$, which is always larger than μ_0 . Using parameters $\kappa_0 = \gamma = 0.45$, the magnification exceeds μ_0 by roughly 20%. As in the case of CDM clumps, we find that minima are magnified while saddles are suppressed.

The complications we discussed in Section 1.3.1 in the context of CDM clumps are relevant for stars as well. For microlensing, we must face an additional challenge. Because the number of stars near a lensed image is much greater than the number of clumps, the determination of magnification perturbations becomes a nonlinear problem. Wambsganss (1999) has developed a powerful numerical method that can handle the complicated “caustic networks” characteristic of quasar microlensing. In Chapter 5 we perform simulations using the software he has created to study microlensing of extended sources. This is relevant for determining the relative amount of stars and dark matter near lensed macro-images.

1.3.4 Supermassive Black Holes and Strong Lensing

As we mentioned in Section 1.2.4, black holes, particularly those of the supermassive variety, can have dramatic effects on lensing. In the case of a lensed quasar, a black hole at the center of the lens galaxy can cause the central image to be pushed below the detection limit. This is because there is a complicated interplay between the potentials describing the central black hole and the lensing galaxy in which it resides. There are other astrophysical situations in which a black hole is the only deflecting body. One example of this is lensing of stars in the Milky Way by the presumed supermassive black hole (SMBH) at the Galactic center (GC). It has already been established that a very massive, extremely compact object known as Sgr A* lies at the GC. While an SMBH is the likely explanation for the orbital dynamics of stars near the GC, lensing of a background star by the central object would virtually prove the existence of an SMBH in our galaxy. This is the subject of Chapter 6, where we consider prospects for observing strong lensing by Sgr A*, and use our results to discuss the possibility of testing general relativity.

Bibliography

- Bender R., Surma P., Döbereiner S., Möllenhoff C., Madejsky R., 1989, *A&A*, 217, 35
- Blandford R., Narayan R., 1986, *ApJ*, 310, 568

- Bolton A. S., Burles S., Koopmans L. V. E., Treu T., Gavazzi R., Moustakas L. A.,
Wayth R., Schlegel D. J., 2008, ApJ, submitted
- Bourassa R. R., Kantowski R., 1975, ApJ, 195, 13
- , 1976, ApJ, 205, 674
- Bourassa R. R., Kantowski R., Norton T. D., 1973, ApJ, 185, 747
- Boyce E. R., 2006, Ph.D. thesis, MIT
- Burke W. L., 1981, ApJ, 244, L1
- Chang K., Refsdal S., 1979, Nature, 282, 561
- Chen J., Rozo E., Dalal N., Taylor J. E., 2007, ApJ, 659, 52
- Chiba M., 2002, ApJ, 565, 17
- Chwolson O., 1924, Astronomische Nachrichten, 221, 329
- Cooke J. H., Kantowski R., 1975, ApJ, 195, L11
- Dalal N., Kochanek C. S., 2002, ApJ, 572, 25
- Dobler G., Keeton C. R., 2006, MNRAS, 365, 1243
- Dyson F. W., Eddington A. S., Davidson C., 1920, Philos. Trans. R. Soc. London,
220A, 291
- Eddington A. S., 1920, *Space, Time and Gravitation: an Outline of the General Relativity Theory*. Cambridge Science Classics, Cambridge: Univ. Press, 1920
- Einstein A., 1915, Sitzungsberichte der Königlich Preußischen Akademie der Wissenschaften (Berlin), Seite 831-839., 831
- , 1936, Science, 84, 506
- Fassnacht C. D., Blandford R. D., Cohen J. G., Matthews K., Pearson T. J., Readhead
A. C. S., Womble D. S., Myers S. T., Browne I. W. A., Jackson N. J., Marlow D. R.,

- Wilkinson P. N., Koopmans L. V. E., de Bruyn A. G., Schilizzi R. T., Bremer M., Miley G., 1999, *AJ*, 117, 658
- Gorenstein M. V., Shapiro I. I., Falco E. E., 1988, *ApJ*, 327, 693
- Grogin N. A., Narayan R., 1996, *ApJ*, 464, 92
- Hege E. K., Angel J. R. P., Weymann R. J., Hubbard E. N., 1980, *Nature*, 287, 416
- Hege E. K., Hubbard E. N., Strittmatter P. A., Worden S. P., 1981, *ApJ*, 248, L1
- Hogg D. W., 1999, *astro-ph/9905116*
- Holder G. P., Schechter P. L., 2003, *ApJ*, 589, 688
- Inada N., Oguri M., Keeton C. R., Eisenstein D. J., Castander F. J., Chiu K., Hall P. B., Hennawi J. F., Johnston D. E., Pindor B., Richards G. T., Rix H.-W. R., Schneider D. P., Zheng W., 2005, *PASJ*, 57, L7
- Keeton C. R., 2001, *astro-ph/0102340*
- , 2003a, *ApJ*, 584, 664
- , 2003b, *ApJ*, 582, 17
- Keeton C. R., Gaudi B. S., Petters A. O., 2003, *ApJ*, 598, 138
- , 2005a, *ApJ*, 635, 35
- Keeton C. R., Kochanek C. S., 1997, *ApJ*, 487, 42
- , 1998, *ApJ*, 495, 157
- Keeton C. R., Kochanek C. S., Seljak U., 1997, *ApJ*, 482, 604
- Keeton C. R., Kuhlen M., Haiman Z., 2005b, *ApJ*, 621, 559
- Keeton C. R., Mao S., Witt H. J., 2000, *ApJ*, 537, 697
- Keeton C. R., Moustakas L. A., 2008, *ApJ*, submitted
- Keeton C. R., Zabludoff A. I., 2004, *ApJ*, 612, 660

- Klimov Y. G., 1963, Soviet Physics Doklady, 8, 119
- Klypin A., Kravtsov A. V., Valenzuela O., Prada F., 1999, ApJ, 522, 82
- Kochanek C. S., 1991, ApJ, 373, 354
- , 2002, ApJ, 578, 25
- Kochanek C. S., Dalal N., 2004, ApJ, 610, 69
- Kochanek C. S., Schneider P., Wambsganss J., 2006, *Saas-Fee Advanced Course 33: Gravitational Lensing: Strong, Weak and Micro*, Meylan G., Jetzer P., North P., eds. Heidelberg: Springer-Verlag
- Kormann R., Schneider P., Bartelmann M., 1994, A&A, 284, 285
- Laplace P. S., 1795, *Exposition du système du monde*
- Lewis G. F., Carilli C., Papadopoulos P., Ivison R. J., 2002, MNRAS, 330, L15
- Liebes S., 1964, Physical Review, 133, 835
- Lodge O. J., 1919, Nature, 354
- Mao S., Schneider P., 1998, MNRAS, 295, 587
- Mao S., Witt H. J., Koopmans L. V. E., 2001, MNRAS, 323, 301
- Martin N. F., Ibata R. A., Chapman S. C., Irwin M., Lewis G. F., 2007, MNRAS, 380, 281
- Michell J., 1784, Trans. R. Soc. London, 74, 35
- Momcheva I., Williams K., Keeton C., Zabludoff A., 2006, ApJ, 641, 169
- Moore B., Ghigna S., Governato F., Lake G., Quinn T., Stadel J., Tozzi P., 1999, ApJ, 524, L19
- Oguri M., Keeton C. R., 2004, ApJ, 610, 663

- Oguri M., Ofek E. O., Inada N., Morokuma T., Falco E. E., Kochanek C. S., Kayo I., Broadhurst T., Richards G. T., 2008, *ApJ*, 676, L1
- Paczyński B., 1986a, *ApJ*, 301, 503
- , 1986b, *ApJ*, 304, 1
- Petters A. O., Levine H., Wambsganss J., 2001, *Singularity Theory and Gravitational Lensing*. Boston: Birkhäuser
- Refsdal S., 1964a, *MNRAS*, 128, 295
- , 1964b, *MNRAS*, 128, 307
- , 1966, *MNRAS*, 132, 101
- Rusin D., Ma C.-P., 2001, *ApJ*, 549, L33
- Saglia R. P., Bender R., Dressler A., 1993, *A&A*, 279, 75
- Saha P., 2000, *AJ*, 120, 1654
- Sanitt N., 1971, *Nature*, 234, 199
- Schechter P. L., Wambsganss J., 2002, *ApJ*, 580, 685
- Schmidt M., 1963, *Nature*, 197, 1040
- Schneider P., Ehlers J., Falco E. E., 1992, *Gravitational Lenses*. Berlin: Springer-Verlag
- Schwarzschild K., 1916a, *Sitzungsberichte der Königlich Preußischen Akademie der Wissenschaften, Phys.-Math. Kl.*, 1916, 424
- , 1916b, *Sitzungsberichte der Königlich Preußischen Akademie der Wissenschaften, Phys.-Math. Kl.*, 1916, 189
- Shaklan S. B., Hege E. K., 1986, *ApJ*, 303, 605
- Shapiro S. S., Davis J. L., Lebach D. E., Gregory J. S., 2004, *Physical Review Letters*, 92, 121101

- Soldner J., 1804, *Berliner Astronomisches Jahrbuch*, 1804, 161
- Spergel D. N., Bean R., Doré O., Nolte M. R., Bennett C. L., Dunkley J., Hinshaw G., Jarosik N., Komatsu E., Page L., Peiris H. V., Verde L., Halpern M., Hill R. S., Kogut A., Limon M., Meyer S. S., Odegard N., Tucker G. S., Weiland J. L., Wollack E., Wright E. L., 2007, *ApJS*, 170, 377
- Stockton A., 1980, *ApJ*, 242, L141
- Walsh D., Carswell R. F., Weymann R. J., 1979, *Nature*, 279, 381
- Wambsganss J., 1999, *J. Comp. Appl. Math.*, 109, 353
- Weymann R. J., Latham D., Roger J., Angel P., Green R. F., Liebert J. W., Turnshek D. A., Turnshek D. E., Tyson J. A., 1980, *Nature*, 285, 641
- Winn J. N., Rusin D., Kochanek C. S., 2004, *Nature*, 427, 613
- Yoo J., Kochanek C. S., Falco E. E., McLeod B. A., 2005, *ApJ*, 626, 51
- Young P., Gunn J. E., Oke J. B., Westphal J. A., Kristian J., 1980, *ApJ*, 241, 507
- Zwicky F., 1937a, *Physical Review*, 51, 290
- , 1937b, *Physical Review*, 51, 679

Chapter 2

Multipole Models of Four-Image Gravitational Lenses with Anomalous Flux Ratios

Abstract

It has been known for over a decade that many four-image gravitational lenses exhibit anomalous radio flux ratios. These anomalies can be explained by adding a clumpy cold dark matter (CDM) component to the background galactic potential of the lens. As an alternative, Evans & Witt (2003) have suggested that smooth multipole perturbations provide a reasonable alternative to CDM substructure in some but not all cases. We generalize their method in two ways so as to determine whether multipole models can explain highly anomalous systems. We carry the multipole expansion to higher order, and also include external tidal shear as a free parameter. Fitting for the shear proves crucial to finding a physical (positive-definite density) model. For B1422+231, working to order $k_{\max} = 5$ (and including shear) yields a model that is physical but implausible. Going to higher order ($k_{\max} = 9$) reduces global departures from ellipticity, but at the cost of introducing small-scale wiggles in proximity to the bright images. These localized undulations are more pronounced in B2045+265, where $k_{\max} = 17$ multipoles are required to smooth out large-scale deviations from elliptical symmetry. Such modes surely cannot be taken at face value; they must indicate that the models are trying to reproduce some other sort of structure. Our formalism naturally finds models that fit the data exactly, but we use B0712+472 to show that measurement uncertainties have little effect on our results. Finally, we consider the system B1933+503, where two sources are lensed by the same foreground galaxy. The additional constraints provided by the images of the second source render the multipole model unphysical. We conclude that external shear must be taken into account to obtain plausible models, and that a

purely smooth angular structure for the lens galaxy does not provide a viable alternative to the prevailing CDM clump hypothesis.

2.1 Introduction

It has been suspected since the time of Newton that a light ray would be deflected when it passes near a massive object. This phenomenon, now known as gravitational lensing, provided one of the earliest tests of the validity of general relativity. Since that time, lens theory has matured into an active field of astronomy (see Kochanek et al. 2006, for a recent review). Probing the structure of galaxies is one of the many areas to which lensing has been applied over the past fifteen years (e.g., Kochanek 1991; Keeton et al. 1998). Because lensing is sensitive to all mass, it is possible to study both dark and luminous components within galaxies.

In the case of strong lensing, where the light source is multiply imaged, we can use the positions and fluxes of the images to study small-scale structure within the lens galaxy. This technique can be most readily applied to four-image systems in a cusp or fold configuration. For a cusp lens we expect the three brightest images to satisfy the magnification sum rule (e.g., Schneider & Weiss 1992; Mao & Schneider 1998; Keeton et al. 2003),

$$\mu_1 + \mu_2 + \mu_3 \approx 0. \quad (2.1)$$

In the fold case an analogous relation holds for the two brightest images (Gaudi & Petters 2002a; Keeton et al. 2005):

$$\mu_1 + \mu_2 \approx 0. \quad (2.2)$$

Although these relations should hold for all smooth lens potentials, there are a number of observed systems for which they are violated (Mao & Schneider 1998; Keeton et al. 2003, 2005). Since the magnifications are not directly observable, systems that violate the sum rule are said to have “flux-ratio anomalies,” with the observed fluxes being related to the magnifications by the flux of the source (see also §3.1).

One might argue that violations of the magnification sum rule originate in electromagnetic effects of the interstellar medium on light emitted by the lensed source.

However, dust extinction is negligible at radio wavelengths, which are much larger than the typical size of a dust grain. The lack of wavelength dependence in radio flux ratios rules out electromagnetic effects as an explanation for radio anomalies (see e.g., Kochanek & Dalal 2004; Keeton et al. 2003, 2005, and references therein).

Explaining the observed anomalies therefore requires the addition of small-scale structure to the gravitational potential of the galaxy (Mao & Schneider 1998). A possible candidate for this substructure emerged through the work of Moore et al. (1999) and Klypin et al. (1999), whose numerical simulations predicted a quantity of cold dark matter (CDM) halos with masses $\sim 10^6 - 10^8 M_\odot$, greatly exceeding the observed numbers of such objects. This result motivated Metcalf & Madau (2001) to consider how the abundance of predicted CDM substructure might affect lensing. They pointed out that even if the small halos are completely dark — invisible to standard luminosity-based studies — they could still affect lens flux ratios and perhaps explain the observed anomalies. Indeed, Dalal & Kochanek (2002) found that putting $\sim 2\%$ of the mass in $\sim 10^6 M_\odot$ halos could reproduce the observed flux ratios for six anomalous lens systems, while broadly matching the predictions of the numerical simulations. But does this mean that the flux ratio problem is really solved, and that the “missing” CDM satellites have been found? Are there other plausible models that can solve the flux ratio problem?

Possibilities may include stellar microlensing, and complex structure such as isophote twists or triaxiality in the lens galaxy. Since the radio-emitting regions of the quasar sources we will consider have a much larger angular scale than the Einstein radius of a typical star in the lens galaxy, microlensing can be eliminated as a potential cause of flux-ratio anomalies. That leaves the question of whether models that alter the global structure of the lens potential offer a viable explanation of flux ratio anomalies. Our goal is to see whether we can fit four anomalous radio lenses using models with general but reasonable angular structure.

We begin with the self-similar multipole model of Evans & Witt (2003). In this framework, the potential of the lens galaxy is described by a generalized isothermal

model whose angular dependence is expressed as a Fourier series. The multipole coefficients are determined by fitting the observed image positions and flux ratios. The truncation order of the series is chosen so that the matrix of constraints is square. Evans & Witt (2003) found that such a model could explain some but not all observed lenses. In particular, for B1422+231 (the only radio anomaly they studied), they could find a physically acceptable model only by inflating the errorbars on the data, and even that model was highly non-elliptical and implausible.

In this chapter we extend the multipole formalism to include external shear — tidal distortions from objects near the lens galaxy (e.g., Keeton et al. 1997) — and higher order multipole modes. Shear in particular will prove essential for obtaining sensible solutions. While this is not the most general method, it is mathematically simple and may be a reasonable alternative to substructure in some lenses.

As a test case, we first apply our model to Q2237+0305, which is not anomalous at radio wavelengths. Then, we apply the model to B1422+231, B2045+265, B0712+472, and B1933+503, which are all highly anomalous. An exhaustive study of the known radio anomalies would also include B1555+375, but the position of the lens galaxy (a key ingredient in our formalism) is unknown.

2.2 Methods

We begin by writing the convergence (dimensionless surface mass density), κ , and lens potential, ψ , for a galaxy with a flat rotation curve and arbitrary angular structure. This model is often referred to as a generalized isothermal model (Witt et al. 2000; Zhao & Pronk 2001; Evans & Witt 2001, 2003):

$$\kappa(r, \theta) = \frac{1}{2r} G(\theta); \quad \psi(r, \theta) = rF(\theta). \quad (2.3)$$

Noting that $\nabla^2 \psi = 2\kappa$, we find that F and G are related by

$$G(\theta) = F(\theta) + F''(\theta). \quad (2.4)$$

For a given source position, $\mathbf{u} \equiv (u, v)$, we can find the image positions, $\mathbf{x} \equiv (r \cos \theta, r \sin \theta)$, via the lens equation,

$$\mathbf{u} = \mathbf{x} - \nabla \psi(\mathbf{x}). \quad (2.5)$$

The inverse magnification of an image at \mathbf{x} is given by

$$\mu^{-1} = \det \left(\frac{\partial \mathbf{u}}{\partial \mathbf{x}} \right) = 1 - \frac{G(\theta)}{r}. \quad (2.6)$$

An important property of the lens potential is the critical curve, along which the magnification is formally infinite. The critical curve in the image plane maps to the caustic in the source plane, which marks the transition between 2-image and 4-image systems. We see from Equation (2.6) that the critical curve is given by $r_{\text{crit}}(\theta) = G(\theta)$, which is equivalent to the isodensity contour with $\kappa = 1/2$.

2.2.1 Multipole Lens Models

Let us write the angular part of the potential, F , as a multipole (Fourier) expansion in θ , i.e.

$$F(\theta) \equiv \frac{a_0}{2} + \sum_{k=1}^{k_{\text{max}}} (a_k \cos k\theta + b_k \sin k\theta), \quad (2.7)$$

for some appropriate k_{max} . In the case of a circular lens, the Einstein radius is given by $R_{\text{Ein}} \equiv a_0/2$. While our models are non-circular, it is sometimes convenient to work in units of R_{Ein} . We can find the unknown source position, \mathbf{u} , and the Fourier coefficients, a_k and b_k , by introducing observational constraints, viz. the image positions and flux ratios.

From Equations (2.3) and (2.7), the lens equation (2.5) becomes

$$u = r_l \cos \theta_l - \frac{a_0}{2} \alpha_0(\theta_l) - \sum_{k=1}^{k_{\text{max}}} [a_k \alpha_k(\theta_l) + b_k \beta_k(\theta_l)], \quad (2.8)$$

$$v = r_l \sin \theta_l - \frac{a_0}{2} \hat{\alpha}_0(\theta_l) - \sum_{k=1}^{k_{\text{max}}} [a_k \hat{\alpha}_k(\theta_l) + b_k \hat{\beta}_k(\theta_l)], \quad (2.9)$$

where $l = 1, 2, \dots, n$ is the image number. The functions α_k , $\hat{\alpha}_k$, β_k , and $\hat{\beta}_k$ are defined in Evans & Witt (2003), equations (13) and (14):

$$\alpha_k(\theta) = \cos \theta \cos k\theta + k \sin \theta \sin k\theta, \quad (2.10)$$

$$\hat{\alpha}_k(\theta) = \sin \theta \cos k\theta - k \cos \theta \sin k\theta, \quad (2.11)$$

$$\beta_k(\theta) = \cos \theta \sin k\theta - k \sin \theta \cos k\theta, \quad (2.12)$$

$$\hat{\beta}_k(\theta) = \sin \theta \sin k\theta + k \cos \theta \cos k\theta. \quad (2.13)$$

Another set of constraints comes from the flux ratios. Relative to image n , we have

$$f_{nl} = \frac{\mu_n}{\mu_l}. \quad (2.14)$$

We then use (2.4), (2.6) and (2.7) to obtain

$$(f_{nl} - 1)r_n r_l = \frac{a_0}{2}\gamma_0(\theta_l) + \sum_{k=1}^{k_{\max}} [a_k \gamma_k(\theta_l) + b_k \delta_k(\theta_l)], \quad (2.15)$$

where $l = 1, 2, \dots, n-1$. The functions γ_k and δ_k are defined by Evans & Witt (2003), equation (18):

$$\gamma_k(\theta_l) = (1 - k^2)[f_{nl}r_l \cos k\theta_n - r_n \cos k\theta_l] \quad (2.16)$$

$$\delta_k(\theta_l) = (1 - k^2)[f_{nl}r_l \sin k\theta_n - r_n \sin k\theta_l]. \quad (2.17)$$

We can combine Equations (2.8), (2.9) and (2.15) into a single matrix equation:

$$\mathbf{A} \cdot \boldsymbol{\chi} = \mathbf{b}, \quad (2.18)$$

where $\boldsymbol{\chi}$ is the $(2k_{\max} + 3)$ -dimensional vector of parameters for which we are solving; $\boldsymbol{\chi} = (u, v, a_0, a_2, b_2, \dots, a_{k_{\max}}, b_{k_{\max}})$. We drop a_1 and b_1 , which represent an unobservable translation of coordinates in the source plane. The $(3n - 1)$ -dimensional vector \mathbf{b} contains the observed image positions and flux ratios;

$$\begin{aligned} \mathbf{b} = & (x_1, \dots, x_n, y_1, \dots, y_n, \\ & (f_{n1} - 1)r_n r_1, \dots, (f_{n,n-1} - 1)r_n r_{n-1}), \end{aligned} \quad (2.19)$$

where $x_l = r_l \cos \theta_l$ and $y_l = r_l \sin \theta_l$. The $(3n - 1) \times (2k_{\max} + 3)$ matrix, \mathbf{A} , is defined in equation (22) of Evans & Witt (2003):

$$\mathbf{A} = \begin{bmatrix} 1 & 0 & \alpha_{01} & \alpha_{21} & \beta_{21} & \dots \\ \vdots & \vdots & \vdots & \vdots & \vdots & \vdots \\ 1 & 0 & \alpha_{0n} & \alpha_{2n} & \beta_{2n} & \dots \\ 0 & 1 & \hat{\alpha}_{01} & \hat{\alpha}_{21} & \hat{\beta}_{21} & \dots \\ \vdots & \vdots & \vdots & \vdots & \vdots & \vdots \\ 0 & 1 & \hat{\alpha}_{0n} & \hat{\alpha}_{2n} & \hat{\beta}_{2n} & \dots \\ 0 & 0 & \gamma_{01} & \gamma_{21} & \delta_{21} & \dots \\ \vdots & \vdots & \vdots & \vdots & \vdots & \vdots \\ 0 & 0 & \gamma_{0,n-1} & \gamma_{2,n-1} & \delta_{2,n-1} & \dots \end{bmatrix}, \quad (2.20)$$

where $\alpha_{kl} \equiv \alpha_k(\theta_l)$ etc. Evans & Witt (2003) choose k_{\max} such that \mathbf{A} is square. We then have $k_{\max} = 5$ for a 4-image system ($n = 4$). With this choice of k_{\max} we can simply multiply equation (2.18) by \mathbf{A}^{-1} to solve for χ , provided that \mathbf{A} is non-singular. To ensure numerical stability, however, Evans & Witt (2003) solve for χ using *singular value decomposition* (SVD).

2.2.2 The Minimum Wiggle Model

There are two main limitations of the method of Evans & Witt (2003). On a technical point, their requirement that \mathbf{A} be square prevents one from probing the contributions of higher-order multipoles. More significantly, the effects of external shear have not been included for several of the systems they analyze. We now set out to address these two concerns.

In the case of arbitrary k_{\max} , SVD produces a particular solution $\chi^{(0)}$ as well as a basis for the null space of \mathbf{A} : $\{\nu^{(i)}\}$. We then have a family of solutions,

$$\chi = \chi^{(0)} + \sum_{i=1}^{N_p - N_c} c_i \nu^{(i)}, \quad (2.21)$$

where $N_p = (2k_{\max} + 3) > N_c = (3n - 1)$ are the numbers of parameters and constraints, respectively. We must now select appropriate coefficients c_i in order to construct the most plausible solution. Since the lens galaxies we are considering are elliptical, it seems reasonable to find the model with the smallest deviation from elliptical symmetry. In other words, we want to minimize the wiggles in the isodensity contours.

For a curve of constant κ , the deviation $\delta r(\theta)$ from perfect elliptical symmetry is given by:

$$\begin{aligned} \delta r(\theta) &\equiv r(\theta) - r_0(\theta), \\ &= \frac{1}{2\kappa} \sum_{k=3}^{k_{\max}} (1 - k^2) (a_k \cos k\theta + b_k \sin k\theta), \end{aligned} \quad (2.22)$$

where

$$r_0(\theta) = \frac{1}{2\kappa} \left[\frac{a_0}{2} - 3(a_2 \cos 2\theta + b_2 \sin 2\theta) \right]$$

is an isodensity curve for a perfectly elliptical galaxy.¹ To quantify the wiggles, we average δr^2 over θ :

$$\delta r_{\text{rms}}^2 \equiv \langle \delta r^2 \rangle_\theta = \frac{1}{8\kappa^2} \sum_{k=3}^{k_{\text{max}}} (1 - k^2)^2 (a_k^2 + b_k^2). \quad (2.23)$$

We are interested in the solution for which the root mean square wiggle is minimized.

If we consider higher order multipoles but ignore shear, we simply need to minimize the RMS wiggle with respect to the coefficients c_i . Since $\langle \delta r^2 \rangle$ is quadratic in a_k and b_k , and hence also in c_i , this minimization is straightforward.

When shear is included, the task of minimizing $\langle \delta r^2 \rangle$ becomes somewhat more involved. In particular, the lens potential of Equation (2.3) must be modified:

$$\psi(r, \theta) = rF(\theta) - \frac{\gamma_1}{2} r^2 \cos 2\theta - \frac{\gamma_2}{2} r^2 \sin 2\theta, \quad (2.24)$$

for constants γ_1, γ_2 . This modification requires that the functions γ_k and δ_k of Equation (2.15), and the vector \mathbf{b} of Equation (2.18) be redefined by the expressions of Appendix D of Evans & Witt (2003). Namely,

$$\begin{aligned} \gamma_k(\theta_l) = (1 - k^2) & \left[f_{nl} r_l \cos k\theta_n W(\theta_n) \right. \\ & \left. - r_n \cos k\theta_l W(\theta_l) \right] \end{aligned} \quad (2.25)$$

$$\begin{aligned} \delta_k(\theta_l) = (1 - k^2) & \left[f_{nl} r_l \sin k\theta_n W(\theta_n) \right. \\ & \left. - r_n \sin k\theta_l W(\theta_l) \right] \end{aligned} \quad (2.26)$$

where

$$W(\theta_l) = 1 + \gamma_1 \cos 2\theta_l + \gamma_2 \sin 2\theta_l \quad (2.27)$$

and

$$\begin{aligned} \mathbf{b} = & [(1 + \gamma_1)x_1 + \gamma_2 y_1, \dots, (1 + \gamma_1)x_n + \gamma_2 y_n, \\ & (1 - \gamma_1)y_1 + \gamma_2 x_1, \dots, (1 - \gamma_1)y_n + \gamma_2 x_n, \\ & (f_{n1} - 1)r_n r_1 (1 - \gamma_1^2 - \gamma_2^2), \dots, \\ & (f_{n,n-1} - 1)r_n r_{n-1} (1 - \gamma_1^2 - \gamma_2^2)]. \end{aligned} \quad (2.28)$$

¹Strictly speaking, an ellipse contains contributions from all Fourier modes with even k , but ignoring terms with $k > 2$ should provide a reasonable approximation (see Evans & Witt 2003).

We see that including (γ_1, γ_2) as parameters to be determined leads to a set of non-linear equations. To deal with this problem, we use a non-linear optimization procedure. For specific values of (γ_1, γ_2) , we can use SVD along with the minimum wiggle criterion to solve for the source position and Fourier coefficients. A minimization function can be employed to find the optimal values for (γ_1, γ_2) . We refer to the resulting solution as the *minimum wiggle model*.

2.3 Results

Let us now apply our methods to five quadruply-imaged quasars. We begin with the Einstein cross, Q2237+0305 (Huchra et al. 1985), which does not exhibit anomalous flux ratios at radio wavelengths, thus providing a simple test case for the multipole expansion approach. Figure 2.1 shows a model with $k_{\max} = 5$ and no external shear (cf. Evans & Witt 2003, Figure 2). The model exactly fits the observational data presented by Falco et al. (1996) and the CASTLES website². The elliptical appearance of the isodensity contour confirms that the multipole method can find reasonable solutions in lens systems that do not require small-scale structure. Now let us turn to four anomalous systems: B1422+231, B2045+265, B0712+472, and B1933+503.

2.3.1 External Shear

To motivate the need for external shear, we first study B1422+231 using a model that does not include shear. To facilitate comparison with the results of Evans & Witt (2003), we consider a fifth-order multipole model, which exactly fits the data of Impey et al. (1996) and Patnaik et al. (1999). It is clear from Figure 2.2(a) that this model is unphysical. In addition to having a completely non-elliptical appearance, the model isodensity contour crosses the origin, indicating that r becomes negative. Evans & Witt (2003) found a slightly better solution by inflating the measurement uncertainties (see their Figure 6). Even so, the model is incompatible with the observed structure of elliptical galaxies, a point noted by the authors.

²<http://www.cfa.harvard.edu/castles/>

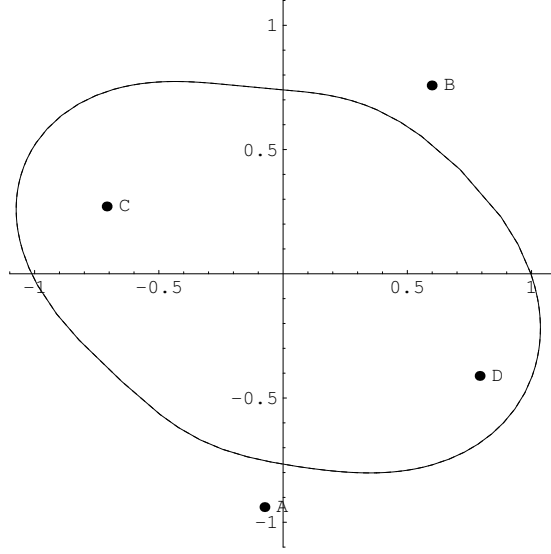


Figure 2.1 Isodensity contour with $\kappa = 1/2$ (coincident with critical curve) for Q2237+0305 with $k_{\max} = 5$ and no shear. The axes are labeled in arcseconds.

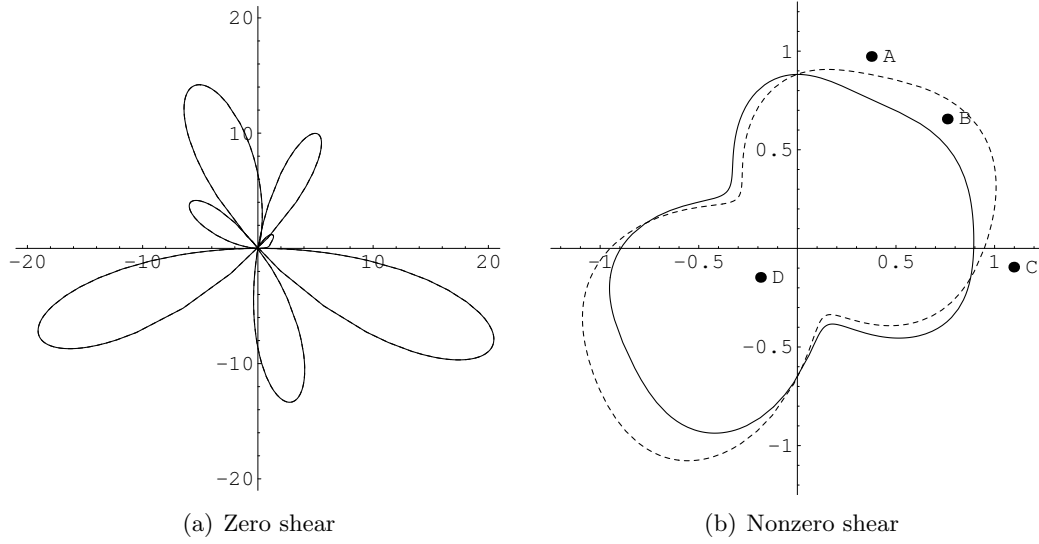


Figure 2.2 Isodensity contours with $\kappa = 1/2$ (solid) and critical curves (dashed) for B1422+231. Panel (a) shows a model with $k_{\max} = 5$ and no shear. Panel (b) shows the solution for the same value of k_{\max} , but nonzero shear parameters $(\gamma_1, \gamma_2) = (0.029, 0.170)$. The dots show the image positions (suppressed in panel (a) for clarity). Note that with nonzero shear, isodensity contours and critical curves are not identical.

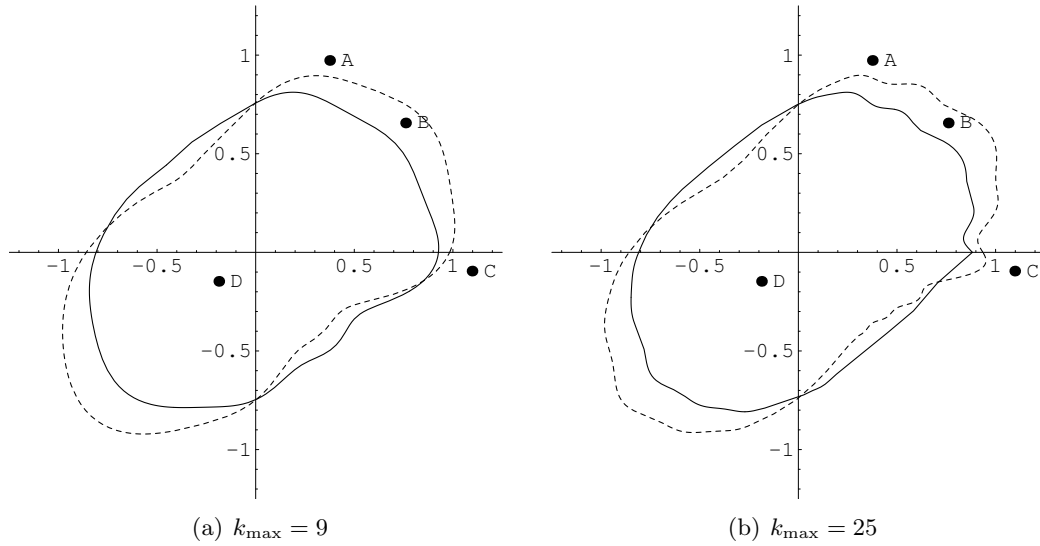


Figure 2.3 Isodensity contours (solid) and critical curves (dashed) for minimum wiggle models of B1422+231. Panel (a) shows a model for $k_{\max} = 9$ and shear parameters $(\gamma_1, \gamma_2) = (0.028, 0.175)$. Panel (b) shows a model for $k_{\max} = 25$ and shear parameters $(\gamma_1, \gamma_2) = (0.030, 0.167)$.

When we extend the model by including shear, it becomes possible to find a physical — albeit not necessarily plausible — angular structure for the lens galaxy, as can be seen in Figure 2.2(b). Before we can draw any conclusions from this result, however, we must determine whether the shear parameters and Fourier coefficients we obtain are compatible with other observations. The shear parameters we find for B1422+231 are reasonable, because the lens lies in a group of galaxies that create a strong tidal field (see Kundić et al. 1997; Momcheva et al. 2006). In particular, our shear amplitude of $\gamma \equiv \sqrt{\gamma_1^2 + \gamma_2^2} = 0.172$, and orientation $\theta_\gamma \equiv (1/2) \tan^{-1}(\gamma_2/\gamma_1) = 40^\circ$ are similar to those quoted by Kundić et al. (1997).

The Fourier coefficients through order 4, plus some other model properties, are given in Table 2.1. To interpret them, we can determine the dimensionless octopole amplitude, A_4 , which describes the “boxiness” or “diskiness” of the isodensity contours, and compare it with the octopole amplitudes measured for the isophotes of elliptical galaxies. The comparison is not perfect because lens models involve the mass while observations involve the light, but we can at least get a sense of whether the lens

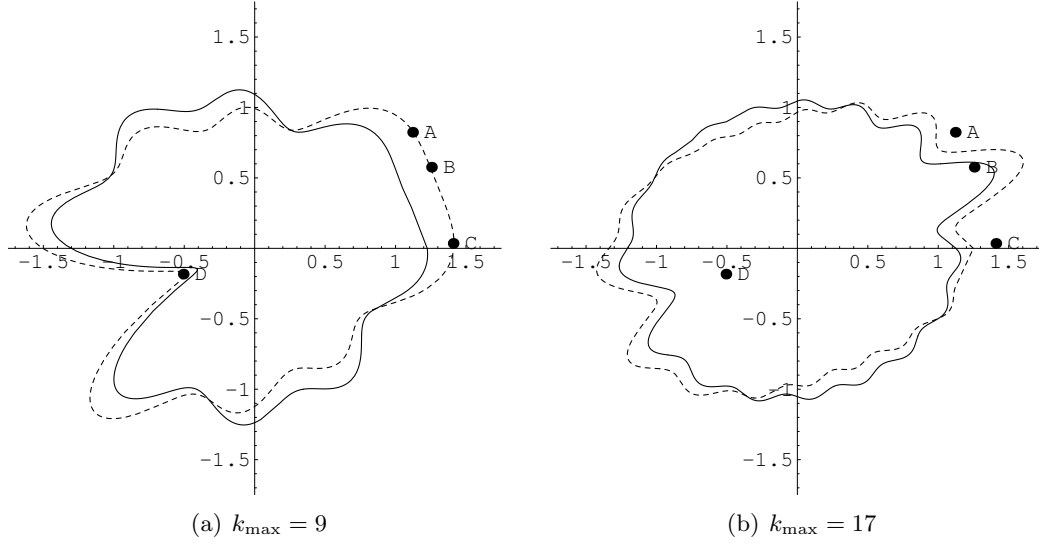


Figure 2.4 Isodensity contours (solid) and critical curves (dashed) for minimum wiggle models of B2045+265. Panel (a) shows the solution with $k_{\max} = 9$ and $(\gamma_1, \gamma_2) = (0.119, 0.125)$. Panel (b) shows the solution with $k_{\max} = 17$ and $(\gamma_1, \gamma_2) = (0.092, 0.090)$.

models are reasonable. The octopole amplitude A_4 is just the Fourier coefficient for the density, expressed in a coordinate frame aligned with the major axis of the galaxy, and normalized by the semi-major axis length. In terms of the coefficients in Table 2.1, the major axis lies along the angle $\theta_2 = (1/2) \tan^{-1}(b_2/a_2)$. Rotating into this coordinate frame then yields

$$A_4 = -\frac{15}{R_{\text{ein}}} (a_4 \cos 4\theta_2 + b_4 \sin 4\theta_2). \quad (2.29)$$

(The factor of -15 comes from $1 - k^2$, which appears when we convert from Fourier coefficients in the potential to those in the density.) If A_4 is negative (positive), the isodensity contours are boxy (disky). For B1422+231, our model with $k_{\max} = 5$ has $A_4 = -0.056$. For comparison, the octopole amplitudes for the isophotes of real elliptical galaxies are in the range $-0.015 \lesssim A_4 \lesssim 0.045$ (Bender et al. 1989; Saglia et al. 1993). In other words, the $k_{\max} = 5$ model is much more boxy than real galaxies, which is not surprising in light of Figure 2.2(b). If we increase k_{\max} to 9 (see below), we find $A_4 = -0.021$ which is still rather boxy. Going to $k_{\max} = 25$ yields $A_4 = -0.010$, which is no more boxy than many observed elliptical galaxies.

Table 2.1 Fourier coefficients, normalized RMS wiggle, and shear parameters for the various multipole lens models discussed in this chapter. We quote models that fit the data exactly.

System	B1422+231				B2045+265			B0712+472			B1933+503
k_{\max}	5	9	25		9	17		5	6	7	8
R_{Ein}	0.797	0.781	0.779		1.11	1.11		0.715	0.710	0.706	0.515
a_2	-0.0213	-0.0159	-0.0136		0.00158	-0.0211		-0.0306	-0.0424	-0.0361	-0.0112
b_2	-0.0689	-0.0492	-0.0517		0.0139	-0.0135		0.0394	0.0246	0.0239	-0.0586
a_3	-0.00817	-0.00359	-0.00223		-0.00928	-0.000950		-0.00333	0.000379	-0.000154	0.00144
b_3	0.0132	0.000983	0.0000806		-0.0159	-0.00401		-0.00595	-0.000511	0.0000860	-0.00143
a_4	-0.00226	-0.00119	-0.000685		0.000673	0.000580		-0.00466	-0.000709	-0.000234	0.000869
b_4	0.00198	0.000195	-0.000196		0.00367	-0.000128		-0.000546	0.000113	0.000287	-0.000358
$\delta r_{\text{rms}}/R_{\text{Ein}}$	0.166	0.0528	0.0376		0.235	0.0943		0.215	0.0993	0.0546	0.126
γ_1	0.029	0.028	0.030		0.119	0.092		-0.044	-0.072	-0.066	-0.033
γ_2	0.170	0.175	0.167		0.125	0.090		-0.078	-0.092	-0.085	0.024

2.3.2 Higher Order Multipoles

Our next step is to include higher order multipole terms. In the case of B1422+231, the lowest-order series for which a somewhat elliptical isodensity contour can be obtained is for $k_{\text{max}} = 9$ (see Fig. 2.3). As we increase k_{max} , the long-wavelength components of galactic structure disappear in favor of wiggles that are localized near the positions of the bright images A, B, and C. In other words, away from the images the model is smooth thanks to the minimum wiggle criterion. But there must be small-scale structure in the vicinity of the images in order to explain the observed flux ratios. Since the wiggles in the isodensity contour are not dramatic, it is not clear whether they should be interpreted as real features or just as approximations of other sorts of structure (such as CDM clumps).

Let us now turn our attention to B2045+265. We find models that exactly fit the data of Fassnacht et al. (1999). Unlike the case of B1422+231, the isodensity contour we obtain for $k_{\text{max}} = 9$ is completely unreasonable, and we must include multipoles of order 17 to obtain a remotely plausible model (see Fig. 2.4). Similar to B1422+231, we find that including higher order multipoles reduces the RMS wiggle, but pronounced deviations from ellipticity remain, primarily near the bright images. This suggests that the structure required to fit the anomaly in B2045+265 truly is local to the images.

While the most obvious anomaly in B2045+265 is in the A/B/C triplet, it is worth noting that our models also have small-scale structure in the vicinity of the faint image D. Dobler & Keeton (2005) also concluded that the flux of image D is puzzling, and suggested that it has more to do with complex structure in the lens galaxy (such as an isophote twist) than with substructure per se. We cannot examine that hypothesis here because our models are intrinsically self-similar, but it will be interesting to keep this image in mind as we develop more general models in the future.

When examining isodensity contours, it may not be completely obvious that high-order models with small-scale undulations really have a smaller total wiggle than low-order models. To understand that, recall that our minimum wiggle criterion is designed to select the model whose isodensity contours deviate least from elliptical symmetry.

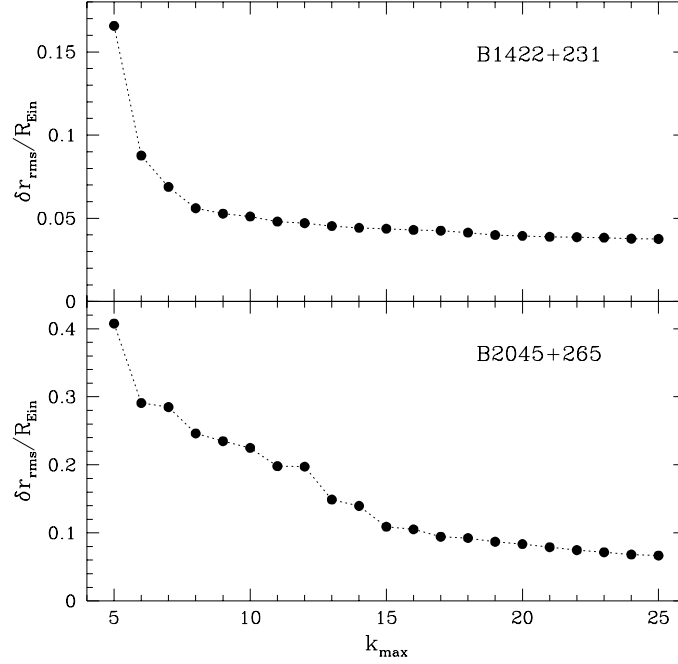


Figure 2.5 Normalized RMS wiggle ($\delta r_{\text{rms}}/R_{\text{Ein}}$) as a function of k_{\max} .

As k_{\max} increases, large-scale departures from ellipticity can be traded for smaller-scale features localized near the images in a way that does in fact decrease the total wiggle. Indeed, Figure 2.5 shows that $\delta r_{\text{rms}}/R_{\text{Ein}}$ does decrease monotonically as the order of the multipole expansion increases. The decrease is rapid at small k_{\max} but slows down as k_{\max} increases, and that gives us a sense of the order at which the multipoles have basically converged to have the minimum amount of small-scale structure.

2.3.3 Measurement Uncertainties

So far we have considered models that fit the data exactly, since that is the natural outcome of an SVD analysis of the underconstrained matrix equation (Eq. [2.18]). However, it is important to consider whether measurement uncertainties affect our conclusions. While we could do this analysis for B2045+265, we believe that the puzzling flux of image D would complicate the interpretation. We turn instead to B0712+472.

We assume the image positions to be precise to within ± 3 mas, which is slightly

conservative compared to the 1 mas uncertainties claimed by Jackson et al. (2000). For the flux ratios, we use the data of Koopmans et al. (2003), who found the uncertainties in the flux ratios of images B, C, and D relative to A to be 7.2%, 8.9%, and 43%, respectively. To be conservative, we construct models for which we take the B/A and C/A uncertainties to be 10% and 20%, while we always use the observed flux uncertainty of 43% for image D.

Since our formalism always produces models that fit the data exactly, the way we include measurement uncertainties is to add noise to the data and repeat our analysis. For every run, we perturb each datum by a random number drawn from a normal distribution with the appropriate dispersion, and then fit our model. We repeat this process 100 times, and select the case that has the smallest mean square wiggle. In this way we find the minimum wiggle model that fits the data within the measurement uncertainties.

Figure 2.6 shows the results for B0712+472. As we would expect, including measurement uncertainties produces models with slightly smaller wiggles. However, the changes are not significant enough to transform an implausible model into an acceptable solution.

2.3.4 A Multi-Source Lens Model

To conclude this section, we study B1933+503, where two sources are lensed by a single galaxy into two four-image configurations (Cohn et al. 2001, and references accompanying their Table 1). Both the image positions and flux ratios corresponding to one source are known, while only the image positions of the second source have been determined to reasonable precision. We therefore have $N_c = 2(n_1 + n_2) + n_1 - 1 = 19$ constraints, compared with $N_c = 3n - 1 = 11$ for the other systems we have analyzed, where $n_1 = n_2 = 4$. Since we must now fit a second source position, our list of parameters increases by two: $N_p = 2k_{\max} + 3$. The matrix \mathbf{A} then has the dimensions $[2(n_1 + n_2) + n_1 - 1] \times (2k_{\max} + 3)$, and is given by adding more rows that represent the additional position constraints, as follows:

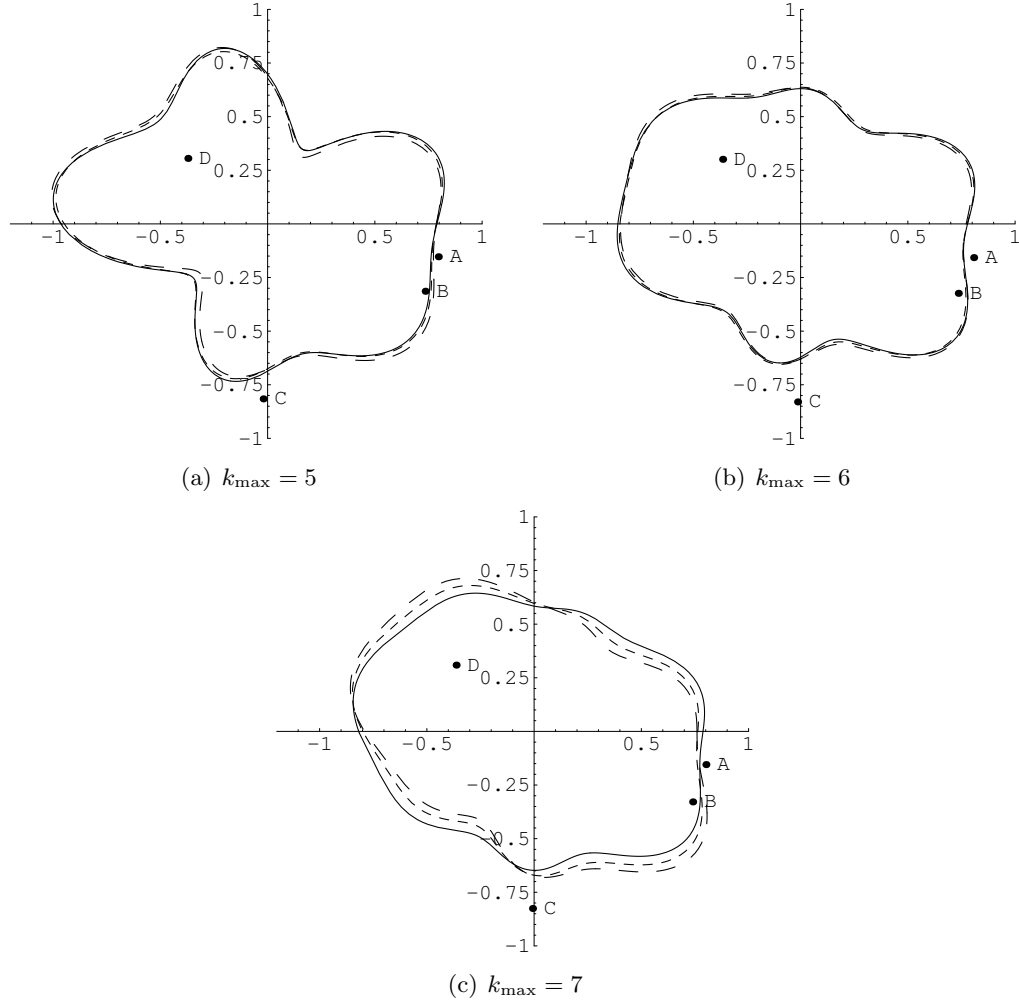


Figure 2.6 Model isodensity contours for B0712+472 with increasing multipole order. The solid curve in each panel fits the data exactly. The short and long-dashed curves fit the data to within 10% and 20% flux uncertainties, respectively (except for faint image D, whose flux uncertainty is fixed at the observed value of 43%; see Koopmans et al. 2003).

$$\mathbf{A} = \begin{bmatrix} 1 & 0 & 0 & 0 & \alpha_{01}^{(1)} & \alpha_{21}^{(1)} & \beta_{21}^{(1)} & \dots \\ \vdots & \vdots & \vdots & \vdots & \vdots & \vdots & \vdots & \vdots \\ 1 & 0 & 0 & 0 & \alpha_{0n_1}^{(1)} & \alpha_{2n_1}^{(1)} & \beta_{2n_1}^{(1)} & \dots \\ \\ 0 & 1 & 0 & 0 & \hat{\alpha}_{01}^{(1)} & \hat{\alpha}_{21}^{(1)} & \hat{\beta}_{21}^{(1)} & \dots \\ \vdots & \vdots & \vdots & \vdots & \vdots & \vdots & \vdots & \vdots \\ 0 & 0 & 1 & 0 & \alpha_{01}^{(2)} & \alpha_{21}^{(2)} & \beta_{21}^{(2)} & \dots \\ \vdots & \vdots & \vdots & \vdots & \vdots & \vdots & \vdots & \vdots \\ 0 & 0 & 1 & 0 & \alpha_{0n_2}^{(2)} & \alpha_{2n_2}^{(2)} & \beta_{2n_2}^{(2)} & \dots \\ \\ 0 & 0 & 0 & 1 & \hat{\alpha}_{01}^{(2)} & \hat{\alpha}_{21}^{(2)} & \hat{\beta}_{21}^{(2)} & \dots \\ \vdots & \vdots & \vdots & \vdots & \vdots & \vdots & \vdots & \vdots \\ 0 & 0 & 0 & 0 & \gamma_{01}^{(1)} & \gamma_{21}^{(1)} & \delta_{21}^{(1)} & \dots \\ \vdots & \vdots & \vdots & \vdots & \vdots & \vdots & \vdots & \vdots \\ 0 & 0 & 0 & 0 & \gamma_{0,n_1-1}^{(1)} & \gamma_{2,n_1-1}^{(1)} & \delta_{2,n_1-1}^{(1)} & \dots \end{bmatrix} \quad (2.30)$$

We first consider just the primary set of four images, which are labeled 1, 3, 4, and 6. (There is a flux ratio anomaly such that image 4 is brighter than expected.) The minimum wiggle model with $k_{\max} = 8$ that fits these images is not very plausible — it has a large protrusion near image 4, and a smaller one near image 1 — but at least the density is positive definite. When we add the additional constraints from the positions of images 2a, 2b, 5, and 7, they dramatically reduce the solution space ($k_{\max} = 8$ is the lowest order case that is not over-constrained). The only models that remain are unphysical. Modestly increasing k_{\max} does not help. In other words, multipole models cannot simultaneously fit the anomalous fluxes of images 1, 3, 4 and 6, and the positions of images 2a, 2b, 5 and 7.

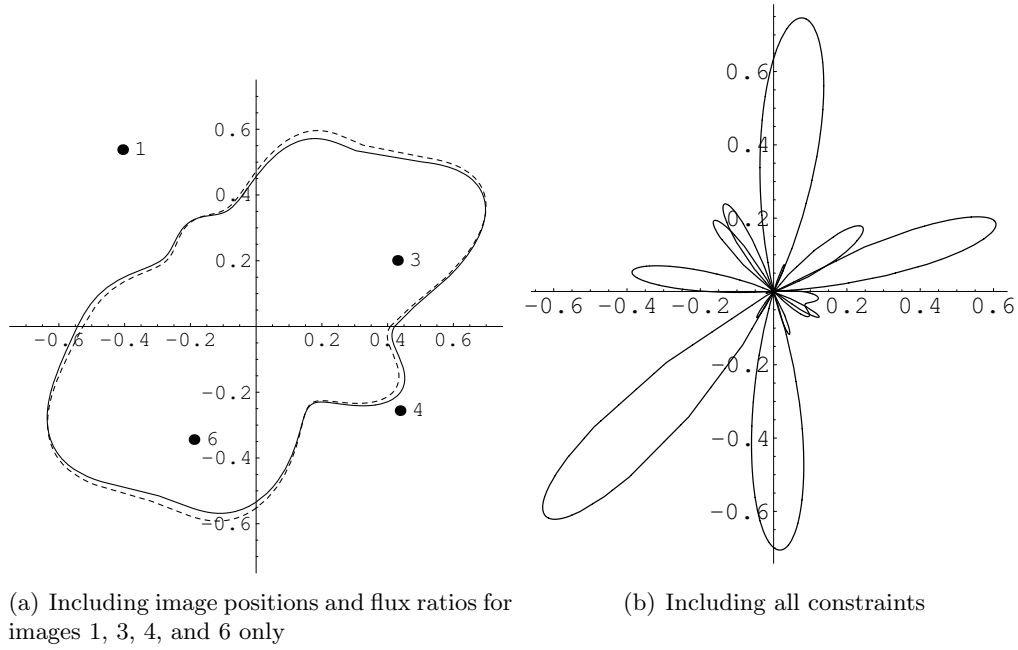


Figure 2.7 Isodensity contours (solid) and critical curves (dashed) for two models of B1933+503. Panel (a) includes the constraints for images 1, 3, 4 and 6. Panel (b) shows a model in which all of the observational constraints have been fit. Both models account for external shear and multipoles up to $k_{\text{max}} = 8$.

2.4 Conclusions

We have shown that extending the method of Evans & Witt (2003) by including external shear and higher-order Fourier terms is essential for understanding whether multipole models can fit observed lenses. The results for B1422+231 we have obtained are of a very different character from those of Evans & Witt (2003). Even so, we cannot conclude that the multipole approach provides an acceptable explanation of flux-ratio anomalies.

The system B2045+265 requires multipoles of order $\gtrsim 15$. Even this level of small-scale structure leads to a rather wiggly angular dependence of density near the three bright images. Next, our analysis of B1933+503 reveals that a fundamental difficulty exists in fitting a multi-source lens with a simple multipole model. Finally, our method naturally finds models that fit the data exactly, but we have shown that our conclusions are not very sensitive to measurement uncertainties.

Our results suggest that there is a more fundamental problem with the global approach taken by Evans & Witt (2003) and ourselves in the current chapter. It is possible that the problem simply comes from our choice of small-scale structure. Sines and cosines provide a useful but by no means unique basis for carrying out a series expansion of the angular part of the potential. In addition, we have assumed a self-similar, isothermal form for the radial dependence, which may need to be modified in order to find an acceptable galactic density function. While the present analysis rules out simple multipole models, the question of whether CDM clumps provide the only plausible solution has yet to be fully answered.

Acknowledgements

We thank Arthur Kosowsky, Tad Pryor, and Jerry Sellwood for helpful discussions. This work was supported by an NSF Graduate Research Fellowship.

Bibliography

Bender R., Surma P., Döbereiner S., Möllenhoff C., Madejsky R., 1989, A&A, 217, 35

- Cohn J. D., Kochanek C. S., McLeod B. A., Keeton C. R., 2001, *ApJ*, 554, 1216
- Dalal N., Kochanek C. S., 2002, *ApJ*, 572, 25
- Evans N. W., Witt H. J., 2001, *MNRAS*, 327, 1260
- , 2003, *MNRAS*, 345, 1351
- Falco E. E., Lehár J., Perley R. A., Wambsganss J., Gorenstein M. V., 1996, *AJ*, 112, 897
- Fassnacht C. D., Blandford R. D., Cohen J. G., Matthews K., Pearson T. J., Readhead A. C. S., Womble D. S., Myers S. T., Browne I. W. A., Jackson N. J., Marlow D. R., Wilkinson P. N., Koopmans L. V. E., de Bruyn A. G., Schilizzi R. T., Bremer M., Miley G., 1999, *AJ*, 117, 658
- Gaudi B. S., Petters A. O., 2002, *ApJ*, 574, 970
- Huchra J., Gorenstein M., Kent S., Shapiro I., Smith G., Horine E., Perley R., 1985, *AJ*, 90, 691
- Impey C. D., Foltz C. B., Petry C. E., Browne I. W. A., Patnaik A. R., 1996, *ApJ*, 462, L53
- Jackson N., Xanthopoulos E., Browne I. W. A., 2000, *MNRAS*, 311, 389
- Keeton C. R., Gaudi B. S., Petters A. O., 2003, *ApJ*, 598, 138
- , 2005, *ApJ*, 635, 35
- Keeton C. R., Kochanek C. S., Falco E. E., 1998, *ApJ*, 509, 561
- Keeton C. R., Kochanek C. S., Seljak U., 1997, *ApJ*, 482, 604
- Klypin A., Kravtsov A. V., Valenzuela O., Prada F., 1999, *ApJ*, 522, 82
- Kochanek C. S., 1991, *ApJ*, 373, 354
- Kochanek C. S., Dalal N., 2004, *ApJ*, 610, 69

- Kochanek C. S., Schneider P., Wambsganss J., 2006, *Saas-Fee Advanced Course 33: Gravitational Lensing: Strong, Weak and Micro*, Meylan G., Jetzer P., North P., eds. Heidelberg: Springer-Verlag
- Koopmans L. V. E., Biggs A., Blandford R. D., Browne I. W. A., Jackson N. J., Mao S., Wilkinson P. N., de Bruyn A. G., Wambsganss J., 2003, *ApJ*, 595, 712
- Kundić T., Hogg D. W., Blandford R. D., Cohen J. G., Lubin L. M., Larkin J. E., 1997, *AJ*, 114, 2276
- Mao S., Schneider P., 1998, *MNRAS*, 295, 587
- Metcalfe R. B., Madau P., 2001, *ApJ*, 563, 9
- Momcheva I., Williams K., Keeton C., Zabludoff A., 2006, *ApJ*, 641, 169
- Moore B., Ghigna S., Governato F., Lake G., Quinn T., Stadel J., Tozzi P., 1999, *ApJ*, 524, L19
- Patnaik A. R., Kembell A. J., Porcas R. W., Garrett M. A., 1999, *MNRAS*, 307, L1
- Saglia R. P., Bender R., Dressler A., 1993, *A&A*, 279, 75
- Schneider P., Weiss A., 1992, *A&A*, 260, 1
- Witt H. J., Mao S., Keeton C. R., 2000, *ApJ*, 544, 98
- Zhao H., Pronk D., 2001, *MNRAS*, 320, 401

Chapter 3

Analytic Relations for Fold and Cusp Lenses: Application to Galactic Structure

Abstract

Gravitational lensing provides a unique and powerful probe of distant galaxies. We consider lenses with fold or cusp configurations, where a bright pair or triplet of images is formed. Within the framework of singularity theory, we derive analytic relations that are satisfied for a light source that lies a small but finite distance from the astroid caustic of a four-image lens. Using a perturbative expansion of the image positions, we show that the time delay between the close pair of images in a fold lens scales with the cube of the image separation, with a constant of proportionality that depends only on one of the third derivatives of the lens potential. We also apply our formalism to cusp lenses, where we develop perturbative expressions for the image positions, magnifications and time delays for any pair of images in a cusp triplet. These results were derived previously for a source asymptotically close to a cusp point, but using a simplified form of the lens equation whose validity may be in doubt for sources that lie at astrophysically relevant distances from the caustic. Along with the work of Keeton et al. (2005), this paper demonstrates that perturbation theory promises to play an important role in theoretical lensing studies.

3.1 Introduction

Gravitational lensing, or the bending of light by gravity, offers an exciting synergy between mathematics and astrophysics. Singularity theory provides a powerful way to describe lensing near critical points (Petters et al. 2001), which turns out to have

important implications for astrophysics and the quest to understand dark matter. Four-image lensed quasars can be broadly classified, according to image geometry, as either folds, cusps or crosses. In fold and cusp lenses, a pair or triplet of bright images is formed. These configurations occur when the light source is close to the caustic curve, along which the lensing magnification is infinite. By expanding the gravitational potential of the lens galaxy in a Taylor series, one finds that the image magnifications satisfy simple analytic relations, viz.

$$|\mu_A| - |\mu_B| \approx 0 \quad \text{and} \quad |\mu_A| - |\mu_B| + |\mu_C| \approx 0 \quad (3.1)$$

for folds and cusps, respectively (Blandford & Narayan 1986; Mao 1992; Schneider & Weiss 1992; Schneider et al. 1992; Gaudi & Petters 2002a,b; Keeton et al. 2003, 2005). For a fold pair, the two images have opposite parity, hence the negative sign. For a cusp triplet, the middle image (B) has opposite parity from the outer images (A and C). Note that in practice, one works with the image fluxes, which are directly observable, rather than the magnifications, which are not. This leads to the equivalent relations:

$$R_{\text{fold}} \equiv \frac{F_A - F_B}{F_A + F_B} \approx 0 \quad \text{and} \quad R_{\text{cusp}} \equiv \frac{F_A - F_B + F_C}{F_A + F_B + F_C} \approx 0, \quad (3.2)$$

where the image flux F_i is related to the source flux F_0 by $F_i = |\mu_i| F_0$.

It was discovered (e.g., Hogg & Blandford 1994; Falco et al. 1997; Keeton et al. 1997) that several observed lenses violate these relations. Mao & Schneider (1998) showed that if the lens galaxy contains small-scale structure, it is possible to explain the strong “flux-ratio anomalies” observed in the quasar lens B1422+231. Subsequent work suggested that this small-scale structure is in the form of cold dark matter (CDM) clumps with masses of $\gtrsim 10^6 M_\odot$. Dalal & Kochanek (2002) showed that the amount of CDM substructure needed to explain anomalous flux ratios broadly agrees with theoretical predictions. This conclusion seemed to show that violations of the ideal fold and cusp relations indicate the presence of CDM substructure. However, Keeton et al. (2003, 2005) pointed out that the ideal relations only hold for a source asymptotically close to the caustic; thus, for a realistic lens population, one would expect R_{fold} and R_{cusp} to be non-zero. Keeton et al. (2003) used a Taylor-series approach to demonstrate

that $R_{\text{cusp}} = 0$ to leading order, and used Monte Carlo simulations to suggest that $R_{\text{cusp}} \propto d_1^2$, where d_1 is the separation between a pair of cusp images. In order to derive the leading-order scaling for R_{cusp} analytically, one must extend the Taylor series to a higher order of approximation. This has not been done before, since including higher-order terms substantially complicates the analysis. Instead, previous authors have made assumptions about which terms are important and which terms can be neglected, thus resulting in an analytically manageable problem.

As we shall see, perturbation theory provides a natural way to overcome the difficulties of the Taylor-series approach. Keeton et al. (2005) used perturbation theory to show that for fold lenses, R_{fold} is proportional to the image separation d_1 of the fold pair. We extend their analysis in several important ways. We derive the leading-order nonvanishing expression for R_{cusp} using perturbation theory. We also show how this approach can be used to study time delays between lensed images for both cusp and fold systems. In the following chapter, we will show how this analysis can be used in practice to identify lenses with small-scale structure.

3.2 Mathematical Preliminaries

To study lensing of a source near a caustic, it is convenient to work in coordinates centered at a point on the caustic. Nonspherical lenses typically have two caustics. The “radial” caustic separates regions in the source plane for which one (outside) and two (inside) images are produced. Within the radial caustic is the “tangential” caustic or astroid, which separates regions in the source plane for which two (between the two caustics) and four (inside the astroid) images are produced. We are interested in four-image lenses, where the source is within the astroid. We therefore make no further reference to the radial caustic. A typical astroid is shown in Figure 3.1(a) for a lens galaxy modeled by a singular isothermal ellipsoid (SIE), which is commonly used in the literature (e.g., Kormann et al. 1994). It is customary to define source-plane coordinates (y_1, y_2) centered on the caustic and aligned with its symmetry axes. However, for fold and cusp configurations, where the source is a small distance from the caustic, it is more natural to work in coordinates (u_1, u_2) centered on the fold or cusp

point. For convenience, we define the u_1 axis tangent to (and the u_2 axis orthogonal to) the caustic at that point. Transforming from the (y_1, y_2) plane to the (u_1, u_2) plane requires a translation plus a rotation. To derive this coordinate transformation, we follow the discussion in appendix A1 in Keeton et al. (2005), which summarizes the results of Petters et al. (2001).

We begin by considering the lens equation $\mathbf{y} = \mathbf{x} - \nabla\psi(\mathbf{x})$, which maps the image plane to the source plane. The solutions to this equation give the image positions $\mathbf{x} \equiv (x_1, x_2)$ corresponding to a given source position $\mathbf{y} \equiv (y_1, y_2)$. The function $\psi(\mathbf{x})$ is the dimensionless gravitational potential of the lens galaxy projected onto the source plane. A caustic is a curve along which the magnification is infinite, i.e., $\det(\partial\mathbf{y}/\partial\mathbf{x}) = \mu^{-1} = 0$, where $\partial\mathbf{y}/\partial\mathbf{x}$ is the Jacobian of \mathbf{y} , and is known as the magnification tensor. We choose coordinates such that the origin of the source plane $\mathbf{y} = \mathbf{0}$ is on the caustic. In addition, we require that the origin of the lens plane $\mathbf{x} = \mathbf{0}$ maps to the origin of the source plane. We consider sources sufficiently close to the caustic so that we may expand the magnification tensor in a Taylor series about the caustic point. For $\mathbf{x} = \mathbf{0}$ we have

$$\left. \frac{\partial\mathbf{y}}{\partial\mathbf{x}} \right|_{\mathbf{0}} = \begin{bmatrix} 1 - 2\hat{a} & -\hat{b} \\ -\hat{b} & 1 - 2\hat{c} \end{bmatrix}, \quad (3.3)$$

where

$$\hat{a} = \frac{1}{2}\psi_{11}(\mathbf{0}), \quad \hat{b} = \psi_{12}(\mathbf{0}), \quad \hat{c} = \frac{1}{2}\psi_{22}(\mathbf{0}). \quad (3.4)$$

The subscripts indicate partial derivatives of ψ with respect to \mathbf{x} . Note that ψ has no linear part (since $\mathbf{y} = \mathbf{0}$ when $\mathbf{x} = \mathbf{0}$). For $\mathbf{y} = \mathbf{0}$ to be a caustic point, we must have $(1 - 2\hat{a})(1 - 2\hat{c}) - \hat{b}^2 = 0$. In addition, at least one of $(1 - 2\hat{a})$, $(1 - 2\hat{c})$, and \hat{b}^2 must be non-zero (Petters et al. 2001, p. 349). Consequently, $(1 - 2\hat{a})$ and $(1 - 2\hat{c})$ cannot both vanish. Without loss of generality, we assume that $1 - 2\hat{a} \neq 0$.

We now introduce the orthogonal matrix (see Petters et al. 2001, p. 344)

$$\mathbf{M} = \frac{1}{\sqrt{(1 - 2\hat{a})^2 + \hat{b}^2}} \begin{bmatrix} 1 - 2\hat{a} & -\hat{b} \\ \hat{b} & 1 - 2\hat{a} \end{bmatrix}, \quad (3.5)$$

which diagonalizes $\partial\mathbf{y}/\partial\mathbf{x}|_{\mathbf{0}}$. We then define new orthogonal coordinates by

$$\boldsymbol{\theta} \equiv (\theta_1, \theta_2) \equiv \mathbf{M}\mathbf{x}, \quad \mathbf{u} \equiv (u_1, u_2) \equiv \mathbf{M}\mathbf{y}. \quad (3.6)$$

Note that the coordinate changes are the *same* in the lens and source planes. The advantage of using the same transformation in both the lens and source planes is that the lens equation takes the simple form

$$\mathbf{u} = \boldsymbol{\theta} - \nabla\psi(\boldsymbol{\theta}). \quad (3.7)$$

The old and new coordinate systems in the source and image planes are shown in Figure 3.1. In the source plane, the dotted and dashed axes are centered on fold and cusp points, respectively. Since the caustic in the source plane maps to the critical curve in the image plane, the origin of the (θ_1, θ_2) frame can be determined from that of the (u_1, u_2) frame. The orientation of the (θ_1, θ_2) axes is determined by the matrix \mathbf{M} , and is independent of the tangent to the critical curve.

Using the local orthogonal coordinates \mathbf{u} and $\boldsymbol{\theta}$, Petters et al. (2001, p. 346) showed that $\mathbf{x} = \mathbf{0}$ is a fold critical point if and only if the following conditions hold

$$(1 - 2\hat{a})(1 - 2\hat{c}) = \hat{b}^2, \quad 1 - 2\hat{a} \neq 0, \quad \psi_{222}(\mathbf{0}) \neq 0. \quad (3.8)$$

For a cusp, the third condition above is replaced by the requirements that

$$\psi_{222}(\mathbf{0}) = 0, \quad \psi_{122}(\mathbf{0}) \neq 0, \quad \psi_{2222}(\mathbf{0}) \neq 0. \quad (3.9)$$

Note in particular that $\psi_{222}(\mathbf{0}) = 0$ for a cusp while $\psi_{222}(\mathbf{0}) \neq 0$ for a fold; this indicates that these two cases must be treated separately.

We are interested in obtaining the time delays for a fold doublet and the image positions, magnifications and time delays for a cusp triplet. Since these quantities depend only on the behavior of the lens potential near the fold or cusp point, we can expand $\psi(\boldsymbol{\theta})$ in a Taylor series about the point $\boldsymbol{\theta} = \mathbf{0}$. To obtain all the quantities of interest to leading order, we must expand the lens potential to fourth order in $\boldsymbol{\theta}$ (Petters et al. 2001, pp. 346–347):

$$\begin{aligned} \psi(\theta_1, \theta_2) = & \frac{1}{2}(1 - K)\theta_1^2 + \frac{1}{2}\theta_2^2 + e\theta_1^3 + f\theta_1^2\theta_2 + g\theta_1\theta_2^2 + h\theta_2^3 \\ & + k\theta_1^4 + m\theta_1^3\theta_2 + n\theta_1^2\theta_2^2 + p\theta_1\theta_2^3 + r\theta_2^4, \end{aligned} \quad (3.10)$$

where the coefficients $\{K, e, f, g, \dots, r\}$ are partial derivatives of the potential evaluated at the origin. Lensing observables are independent of a constant term in the potential, so

we have not included one. Since $\boldsymbol{\theta} = \mathbf{0}$ maps to $\mathbf{u} = \mathbf{0}$, any linear terms in the potential must vanish. In the second order terms, the coefficients of the $\theta_1\theta_2$ and θ_2^2 terms are set to 0 and 1/2, respectively, following the arguments in Appendix A1 of Keeton et al. (2005).

3.3 The Fold Case

In this section, we use perturbation theory (e.g., Bellman 1966) to derive an analytic relation between the time delays in a fold pair. To derive this expression, we must first obtain the image positions at which the time delay is evaluated. These results were derived by Keeton et al. (2005). We offer a summary of their analysis in Section 3.3.1 and present our new results for the time delay in Section 3.3.2.

3.3.1 Image Positions

Since we are considering a source near a fold point, we write its position in terms of a scalar parameter ϵ which we take to be small but finite. In particular, let $\mathbf{u} \rightarrow \epsilon\mathbf{u}$. Combining Equations (3.7) and (3.10) we can write the lens equation as

$$\begin{aligned} \epsilon u_1 &= K\theta_1 - \left(3e\theta_1^2 + 2f\theta_1\theta_2 + g\theta_2^2\right) \\ &\quad - \left(4k\theta_1^3 + 3m\theta_1^2\theta_2 + 2n\theta_1\theta_2^2 + p\theta_2^3\right), \end{aligned} \quad (3.11)$$

$$\epsilon u_2 = -\left(f\theta_1^2 + 2g\theta_1\theta_2 + 3h\theta_2^2\right) - \left(m\theta_1^3 + 2n\theta_1^2\theta_2 + 3p\theta_1\theta_2^2 + 4r\theta_2^3\right) \quad (3.12)$$

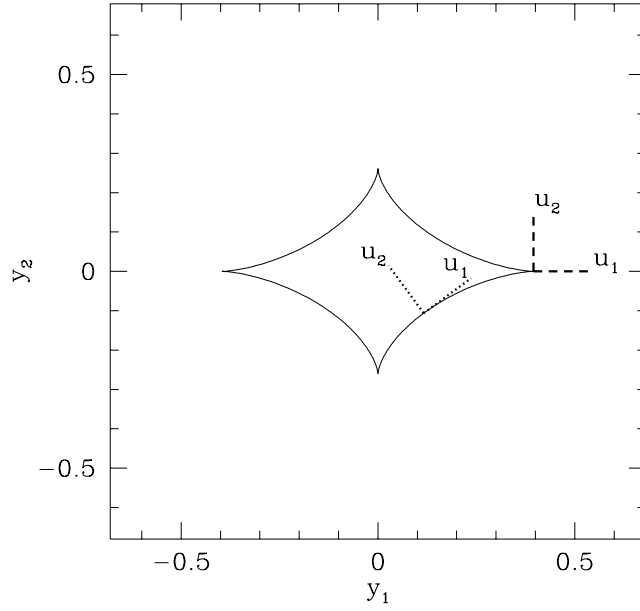
(see Petters et al. 2001, Theorem 9.1). To find the image positions, we expand θ_1 and θ_2 in a power series in ϵ . Since the left-hand sides of Equations (3.11) and (3.12) are accurate to $\mathcal{O}(\epsilon)$, the right-hand sides must be accurate to the same order. Noting that the lowest-order terms on the right-hand side are linear or quadratic in $\boldsymbol{\theta}$, we write

$$\theta_1 = \alpha_1\epsilon^{1/2} + \beta_1\epsilon + \mathcal{O}(\epsilon)^{3/2}, \quad (3.13)$$

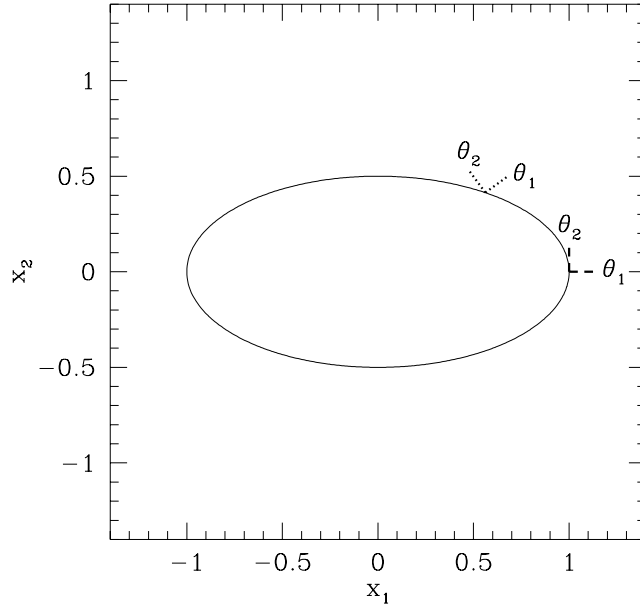
$$\theta_2 = \alpha_2\epsilon^{1/2} + \beta_2\epsilon + \mathcal{O}(\epsilon)^{3/2}. \quad (3.14)$$

Substituting into the lens equation, we obtain

$$0 = (\alpha_1 K)\epsilon^{1/2} - (3\alpha_1^2 e + 2\alpha_1\alpha_2 f + \alpha_2^2 g - \beta_1 K + u_1)\epsilon + \mathcal{O}(\epsilon)^{3/2}, \quad (3.15)$$



(a) Source plane



(b) Image plane

Figure 3.1 Local orthogonal coordinates defined by the rotation matrix \mathbf{M} , for a singular isothermal ellipsoid (SIE) lens with minor-to-major axis ratio $q = 0.5$. (a) A source with position (y_1, y_2) measured from the center of the caustic (astroid) has position (u_1, u_2) in the rotated coordinates centered on a fold point (dotted-axes) or a cusp (dashed-axes). (b) An image with position (x_1, x_2) measured from the center of the critical curve (ellipse) has position (θ_1, θ_2) in the rotated coordinates. The origin of the (θ_1, θ_2) frame is given in terms of that for the (u_1, u_2) frame by means of the lens equation.

$$\begin{aligned}
0 = & -(\alpha_1^2 f + 2\alpha_1 \alpha_2 g + 3\alpha_2^2 h + u_2)\epsilon - [2\alpha_1 \beta_1 f + 2(\alpha_1 \beta_2 + \alpha_2 \beta_1)g \\
& + 6\alpha_2 \beta_2 h + \alpha_1^3 m + 2\alpha_1^2 \alpha_2 n + 3\alpha_1 \alpha_2^2 p + 4\alpha_2^3 r] \epsilon^{3/2} + \mathcal{O}(\epsilon)^2.
\end{aligned} \tag{3.16}$$

Note that these equations are carried to different orders in ϵ , since the leading-order term in Equation (3.11) is linear in $\boldsymbol{\theta}$, while the leading-order term in Equation (3.12) is quadratic in $\boldsymbol{\theta}$.

Since ϵ is non-zero, Equations (3.15) and (3.16) must be satisfied at each order in ϵ . We can then write the image positions as

$$\theta_1^\pm = \frac{3hu_1 - gu_2}{3hK} \epsilon + \mathcal{O}(\epsilon)^{3/2}, \tag{3.17}$$

$$\theta_2^\pm = \pm \sqrt{\frac{-u_2}{3h}} \epsilon^{1/2} - \frac{3ghu_1 - g^2 u_2}{9h^2 K} \epsilon + \mathcal{O}(\epsilon)^{3/2}, \tag{3.18}$$

where the \pm labels indicate the parities of the images. From these equations, we see that two images form near the point $\boldsymbol{\theta} = \mathbf{0}$ on the critical curve, provided that $(-u_2/3h) > 0$. Since $h \leq 0$ for standard lens potentials (e.g., an isothermal ellipsoid or isothermal sphere with shear), we must have $u_2 > 0$. In other words, the source must lie inside the caustic in order to produce a pair of fold images. In practice, a more useful quantity is the image separation, defined by

$$d_1 = \sqrt{\frac{-4u_2}{3h}} \epsilon^{1/2} + \mathcal{O}(\epsilon)^{3/2}. \tag{3.19}$$

3.3.2 Time Delays

To find the time delay between the two fold images, we begin with the general expression for the scaled time delay

$$\hat{\tau}(\boldsymbol{\theta}) \equiv \tau(\boldsymbol{\theta})/\tau_0 = \frac{1}{2} |\boldsymbol{\theta} - \mathbf{u}|^2 - \psi(\boldsymbol{\theta}). \tag{3.20}$$

The scale factor is given by

$$\tau_0 = \frac{1 + z_L}{c} \frac{D_L D_S}{D_{LS}}, \tag{3.21}$$

where D_L, D_S and D_{LS} are the angular-diameter distances from the observer to lens, observer to source, and lens to source, respectively. The lens redshift is denoted by z_L . Making the substitution $\mathbf{u} \rightarrow (\epsilon u_1, \epsilon u_2)$, we have for the two fold images

$$\hat{\tau}_- \equiv \hat{\tau}(\boldsymbol{\theta}_-) = \sqrt{-\frac{4}{27h}} (\epsilon u_2)^{3/2} + \mathcal{O}(\epsilon)^2, \tag{3.22}$$

$$\hat{\tau}_+ \equiv \hat{\tau}(\boldsymbol{\theta}_+) = -\sqrt{-\frac{4}{27h}} (\epsilon u_2)^{3/2} + \mathcal{O}(\epsilon)^2. \quad (3.23)$$

The time delay between images is then

$$\Delta\hat{\tau}_{\text{fold}} \equiv \hat{\tau}_- - \hat{\tau}_+ = \sqrt{-\frac{16}{27h}} (\epsilon u_2)^{3/2} + \mathcal{O}(\epsilon)^2 = -\frac{h}{2} d_1^3 + \mathcal{O}(\epsilon)^2, \quad (3.24)$$

which is positive, in agreement with the general result that images with negative parity trail those with positive parity. We find that the only coefficient from the lens potential that enters the expression for the differential time delay is the parameter $h = \psi_{222}(\mathbf{0})/6$. We also see that to leading order in ϵ , the image separation and the differential time delay depend only on the u_2 component of the source position. Unlike the image positions, our expression for the time delay does not involve any of the fourth-order terms in the potential. This is because the time delay involves the potential directly, while the image positions depend on first derivatives of the potential. This means that all fourth-order terms in the potential enter the time delay at $\mathcal{O}(\epsilon)^2$, while these same terms enter at $\mathcal{O}(\epsilon)^{3/2}$ in quantities involving derivatives.

To summarize, $\Delta\hat{\tau}_{\text{fold}} \propto (\epsilon u_2)^{3/2} \propto d_1^3$. For comparison, $R_{\text{fold}} \propto d_1$. Since d_1 is small, a violation of the ideal relation $\Delta\hat{\tau}_{\text{fold}} = 0$ is more likely to indicate the presence of small-scale structure in the lens galaxy than would be indicated by a non-zero value of R_{fold} .

Our analytic expression for $\Delta\hat{\tau}_{\text{fold}}$ is only valid for sources close to the caustic. To quantify this statement (see Fig. 3.2), we compare our prediction with the differential time delay computed numerically from the exact form of the lens equation. This requires that we assume a specific lens model. For this purpose, we consider an SIE with axis ratio $q = 0.5$, which provides a representative example. We use the software of Keeton (2001) to obtain the time delay numerically. The first step is to compute the astroid caustic for the model. We then choose a point on the caustic, far from a cusp, to serve as the origin of the (u_1, u_2) frame. For a given value of u_2 , we solve the exact lens equation to obtain the image positions and time delay for the fold doublet. In the left-hand panel of Figure 3.2 we plot the time delay in units of squared Einstein angle, θ_E^2 , as a function of u_2 in units of θ_E . The analytic and numerical results are in excellent agreement for sources within $0.05\theta_E$ of the caustic, although the curves

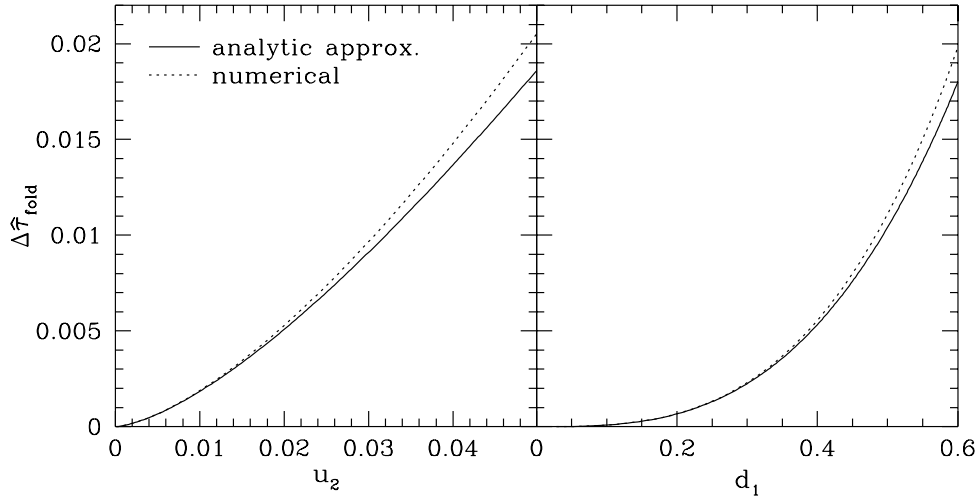


Figure 3.2 Dependence of the time delay of a fold pair on source position (left) and image separation (right), for an SIE lens with axis ratio $q = 0.5$. The solid line shows our analytic approximation while the dotted line shows the exact result obtained from solving the lens equation numerically. The quantities u_2 and d_1 are defined in the text, and are shown here in units of the Einstein angle, θ_E .

begin to diverge slightly at $u_2 \sim 0.02\theta_E$. Since u_2 is not observable, we show the time delay versus d_1 in the right-hand panel. The range of d_1 corresponds to that used for u_2 in the left-hand panel. For a canonical fold lens with $d_1 = 0.46\theta_E$ (Keeton et al. 2005), our scaling nearly matches the numerical result, indicating that our analysis can be applied to astrophysically-relevant situations. Although the difference between the curves is small, note that the numerical prediction is always larger than the analytic result. This suggests that the next non-vanishing term in the Taylor expansion of the time delay is positive.

3.4 The Cusp Case

We now apply our perturbative method to the case of a source near a cusp point. This approach has not been applied to cusp lenses before. Appendix A of Keeton et al. (2003) derives the image positions and magnifications for a cusp triplet assuming a simplified form of the lens equation. As we noted in Section 3.1, this simplified lens equation assumes that certain terms may be set to zero, using criteria that are less

than rigorous. We use the lens equation derived from the fourth-order lens potential, and using perturbation theory, verify the results of Keeton et al. (2003) and extend the analysis to a higher order of approximation. We also study time delays for a cusp lens for the first time. Our analysis does not involve simplifying assumptions, and indicates that perturbation theory could become a powerful method in the study of lensing.

3.4.1 Image Positions

We again expand the image positions, magnifications and time delays in the parameter ϵ , but with one notable difference. For a cusp oriented in the u_1 direction, a small “horizontal” displacement of ϵu_1 from the cusp point permits a “vertical” displacement of only $\epsilon^{3/2} u_2$ (see Fig. 3.1), since larger vertical displacements would imply a source position outside the caustic (Blandford & Narayan 1986). The lens equation is then

$$\begin{aligned} \epsilon u_1 = & K \theta_1 - \left(3e \theta_1^2 + 2f \theta_1 \theta_2 + g \theta_2^2 \right) \\ & - \left(4k \theta_1^3 + 3m \theta_1^2 \theta_2 + 2n \theta_1 \theta_2^2 + p \theta_2^3 \right), \end{aligned} \quad (3.25)$$

$$\epsilon^{3/2} u_2 = - \left(f \theta_1^2 + 2g \theta_1 \theta_2 \right) - \left(m \theta_1^3 + 2n \theta_1^2 \theta_2 + 3p \theta_1 \theta_2^2 + 4r \theta_2^3 \right) \quad (3.26)$$

(see Petters et al. 2001, Theorem 9.1), where the θ_2^2 term of Equation (3.12) does not appear, since $\psi_{222}(\mathbf{0}) = 0$ for a cusp, corresponding to $h = 0$ in Equation (3.10).

As before, we write the image positions as a series expansion in ϵ , but now keeping an additional term (i.e., $\gamma_i \epsilon^{3/2}$). This is necessary since the vertical component of the source position enters the lens equation as $\epsilon^{3/2} u_2$, rather than ϵu_2 as in the fold case. We have

$$\theta_1 = \alpha_1 \epsilon^{1/2} + \beta_1 \epsilon + \gamma_1 \epsilon^{3/2} + \mathcal{O}(\epsilon)^2, \quad (3.27)$$

$$\theta_2 = \alpha_2 \epsilon^{1/2} + \beta_2 \epsilon + \gamma_2 \epsilon^{3/2} + \mathcal{O}(\epsilon)^2. \quad (3.28)$$

The lens equation then becomes

$$\begin{aligned} 0 = & \alpha_1 K \epsilon^{1/2} - \left(3e \alpha_1^2 + 2f \alpha_1 \alpha_2 + g \alpha_2^2 - \beta_1 K + u_1 \right) \epsilon \\ & - \left[4k \alpha_1^3 + 3m \alpha_1^2 \alpha_2 + p \alpha_2^3 + 2\alpha_1 (n \alpha_2^2 + 3e \beta_1 + f \beta_2) \right. \\ & \left. + 2\alpha_2 (f \beta_1 + g \beta_2) - K \gamma_1 \right] \epsilon^{3/2} + \mathcal{O}(\epsilon)^2, \end{aligned} \quad (3.29)$$

$$\begin{aligned}
0 &= -(f\alpha_1^2 + 2g\alpha_1\alpha_2)\epsilon \\
&\quad - \left(u_2 + m\alpha_1^3 + 2n\alpha_1^2\alpha_2 + 3p\alpha_1\alpha_2^2 + 4r\alpha_2^3 + 2f\alpha_1\beta_1 + 2g\alpha_2\beta_1 + 2g\alpha_1\beta_2\right)\epsilon^{3/2} \\
&\quad - \left\{\beta_1(f\beta_1 + 2g\beta_2) + \alpha_1^2(3m\beta_1 + 2n\beta_2) + 3\alpha_2^2(p\beta_1 + 4r\beta_2) + 2g\alpha_2\gamma_1\right. \\
&\quad \left.+ 2\alpha_1[\alpha_2(2n\beta_1 + 3p\beta_2) + f\gamma_1 + g\gamma_2]\right\}\epsilon^2 + \mathcal{O}(\epsilon)^{5/2}.
\end{aligned} \tag{3.30}$$

As in the fold case (see Eq. [3.15]), we find $\alpha_1 = 0$. Note that γ_2 appears only in the ϵ^2 coefficient of Equation (3.30), but in a term multiplied by α_1 . Hence, it will not be possible to solve for γ_2 . Fortunately, it turns out that the expressions we would like to derive do not involve this parameter.

We can now write the lens equation as

$$\begin{aligned}
0 &= -\left(g\alpha_2^2 - \beta_1 K + u_1\right)\epsilon \\
&\quad - \left[p\alpha_2^3 + 2\alpha_2(f\beta_1 + g\beta_2) - K\gamma_1\right]\epsilon^{3/2} + \mathcal{O}(\epsilon)^2,
\end{aligned} \tag{3.31}$$

$$\begin{aligned}
0 &= -\left(u_2 + 4r\alpha_2^3 + 2g\alpha_2\beta_1\right)\epsilon^{3/2} - (\beta_1(f\beta_1 + 2g\beta_2) \\
&\quad + 3\alpha_2^2(p\beta_1 + 4r\beta_2) + 2g\alpha_2\gamma_1)\epsilon^2 + \mathcal{O}(\epsilon)^{5/2}.
\end{aligned} \tag{3.32}$$

Recalling that these equations must be satisfied at each order in ϵ , we then solve for the unknown coefficients:

$$\beta_1 = \frac{g\alpha_2^2 + u_1}{K}, \tag{3.33}$$

$$\beta_2 = -\frac{(5fg^2 + 5gKp)\alpha_2^4 + (6fgu_1 + 3Kpu_1)\alpha_2^2 + fu_1^2}{2K(3g^2\alpha_2^2 + 6Kr\alpha_2^2 + gu_1)}, \tag{3.34}$$

$$\begin{aligned}
\gamma_1 &= \left[K^2(3g^2\alpha_2^2 + 6Kr\alpha_2^2 + gu_1)\right]^{-1} \left[(fg^3 - 2g^2Kp + 12fgKr + 6K^2pr)\alpha_2^5\right. \\
&\quad \left.+ (2fg^2u_1 - 2gKpu_1 + 12fKru_1)\alpha_2^3 + fg u_1^2\alpha_2\right]
\end{aligned} \tag{3.35}$$

where α_2 satisfies the equation

$$\alpha_2^3 + \frac{gu_1}{2Kr + g^2}\alpha_2 + \frac{Ku_2}{4Kr + 2g^2} = 0. \tag{3.36}$$

This is equivalent to equation (A8) from Keeton et al. (2003), after making the replacements $\alpha_2 \rightarrow z$, $K \rightarrow c$, $g \rightarrow -b/2$, $r \rightarrow -a/4$. To leading order, the image positions can be written as

$$\theta_1 = \beta_1\epsilon = \frac{g\alpha_2^2 + u_1}{K}\epsilon, \tag{3.37}$$

$$\theta_2 = \alpha_2\epsilon^{1/2}, \tag{3.38}$$

which are equivalent to equation (A7) from Keeton et al. (2003). The distance between any two images i and j is then

$$d_{ij} = [\alpha_2^{(i)} - \alpha_2^{(j)}] \epsilon^{1/2} + \mathcal{O}(\epsilon) . \quad (3.39)$$

3.4.2 Magnifications

The inverse magnification of a cusp image is given by

$$\begin{aligned} \mu^{-1} = & -2[gu_1 + 3(g^2 + 2Kr)\alpha_2^2] \epsilon \\ & + [(24fr - 12gp)\alpha_2^3 + (6Kp - 4fg)\alpha_2\beta_1 - (8g^2 + 24Kr)\alpha_2\beta_2 - gK\gamma_1] \epsilon^{3/2} \\ & + \mathcal{O}(\epsilon)^2 . \end{aligned} \quad (3.40)$$

We then find from Equation (3.2) that

$$R_{\text{cusp}} = 0 + \mathcal{O}(\epsilon) \approx A_{\text{cusp}} d_1^2, \quad (3.41)$$

where $d_1 = \min_{ij} d_{ij}$. This expression implies that correction terms to the ideal cusp relation enter at second order in the image separation, which agrees with the numerical result of Keeton et al. (2003). To see this, we define $m_i \equiv |\mu_i^{-1}|$, which allows us to write

$$R_{\text{cusp}} = \frac{m_B m_C - m_A m_C + m_A m_B}{m_B m_C + m_A m_C + m_A m_B} . \quad (3.42)$$

If the leading-order term in the numerator vanishes, so does the leading-order term in R_{cusp} . The zeroth-order term in R_{cusp} corresponds to a term of $\mathcal{O}(\epsilon)^2$ in the numerator, since the leading-order term in the denominator is $\mathcal{O}(\epsilon)^2$. By substituting the solutions for α_2 into the numerator, we find that $R_{\text{cusp}} = 0$ to lowest order, in agreement with Keeton et al. (2003). We repeat this procedure for the next-leading term of $\mathcal{O}(\epsilon)^{5/2}$ in the numerator, and find that $R_{\text{cusp}} = 0$ at linear order in d_1 [i.e., $\mathcal{O}(\epsilon)^{1/2}$] as well; this result was unattainable using the formalism of Keeton et al. (2003). Moving to the next term, we find that R_{cusp} is nonvanishing at quadratic order in d_1 [i.e., $\mathcal{O}(\epsilon)$]. The coefficient of d_1^2 is denoted by A_{cusp} , which we do not here write out explicitly (since that would require several pages). We have thus placed the numerical result of Keeton et al. (2003) on solid mathematical ground.

3.4.3 Time Delays

For the cusp case, the scaled time delay takes the form

$$\hat{\tau} = \frac{1}{2} \left[(\theta_1 - \epsilon u_1)^2 + (\theta_2 - \epsilon^{3/2} u_2)^2 \right] - \psi(\theta_1, \theta_2). \quad (3.43)$$

We find

$$\hat{\tau} = \frac{1}{2K} \left[(3g^2 + 6Kr)\alpha_2^4 + 2gu_1\alpha_2^2 + (K-1)u_1^2 \right] \epsilon^2 + \mathcal{O}(\epsilon)^{5/2}, \quad (3.44)$$

corresponding to a differential time delay of

$$\Delta \hat{\tau}_{\text{cusp}}^{(ij)} = \frac{1}{4K} \left[2g \left(\alpha_2^{(i)} + \alpha_2^{(j)} \right) u_1 + 3Ku_2 \right] \left(\alpha_2^{(j)} - \alpha_2^{(i)} \right) \epsilon^2. \quad (3.45)$$

Unlike the fold case, the time delay for a pair of cusp images depends on both source coordinates (u_1, u_2) . This means that it is not possible to write our current expression strictly in terms of observables, such as the image separation. Instead, all we can say is that the time delay scales quadratically with ϵ , or alternatively, with the fourth power of the image separation.

In the fold case, we found that the time delay scales as $\epsilon^{3/2}$ and only depends on the lens potential through the parameter h . For a cusp, however, $h = 0$, so it is not surprising that the lowest-order term in the time delay is of $\mathcal{O}(\epsilon)^2$. Furthermore, if we had not included the $\gamma_i \epsilon^{3/2}$ terms in our expansions of the image positions for a cusp (Eqs. [3.27] and [3.28]), it would not have been possible to obtain a perturbative expression for the time delay; instead, we would simply have found $\hat{\tau} = 0 + \mathcal{O}(\epsilon)^2$.

3.5 Summary

We have developed a unified, rigorous framework for studying lensing near fold and cusp critical points, which can (in principle) be extended to arbitrary order. We have found that the differential time delay of a fold pair assumes a particularly simple form, depending only on the image separation and the Taylor coefficient $h = \psi_{222}(\mathbf{0})/6$. This result is astrophysically relevant, since it is quite accurate even for sources that are not asymptotically close to the caustic. We have also obtained perturbative expressions for the image positions, magnifications and time delays of a cusp triplet. These results rest

on the key insight that a source at a given distance ϵ from a cusp along the relevant symmetry axis of the caustic can only move a perpendicular distance of $\epsilon^{3/2}$ in order to remain inside the caustic (Blandford & Narayan 1986). We have shown rigorously that the distance dependence of the magnification ratio R_{cusp} conjectured by Keeton et al. (2003) is correct. We have also demonstrated that the leading-order expression for the image positions is given by the relations presented by Keeton et al. (2003), and have provided the necessary framework for deriving the image positions corresponding to a Taylor expansion of the lens potential at arbitrary truncation order. Finally, we have derived cusp time delays analytically for the first time.

Acknowledgement

We thank A. O. Petters for helpful discussions and suggestions.

Bibliography

Bellman R., 1966, *Perturbation Techniques in Mathematics, Engineering, and Physics*.

Perturbation Techniques in Mathematics, Engineering, and Physics / Bellman, R. Mineola : Dover, c1966.

Blandford R., Narayan R., 1986, ApJ, 310, 568

Dalal N., Kochanek C. S., 2002, ApJ, 572, 25

Falco E. E., Lehar J., Shapiro I. I., 1997, AJ, 113, 540

Gaudi B. S., Petters A. O., 2002a, ApJ, 574, 970

—, 2002b, ApJ, 580, 468

Hogg D. W., Blandford R. D., 1994, MNRAS, 268, 889

Keeton C. R., 2001, astro-ph/0102340

Keeton C. R., Gaudi B. S., Petters A. O., 2003, ApJ, 598, 138

—, 2005, ApJ, 635, 35

- Keeton C. R., Kochanek C. S., Seljak U., 1997, ApJ, 482, 604
- Kormann R., Schneider P., Bartelmann M., 1994, A&A, 284, 285
- Mao S., 1992, ApJ, 389, 63
- Mao S., Schneider P., 1998, MNRAS, 295, 587
- Petters A. O., Levine H., Wambsganss J., 2001, *Singularity Theory and Gravitational Lensing*. Boston: Birkhäuser
- Schneider P., Ehlers J., Falco E. E., 1992, *Gravitational Lenses*. Berlin: Springer-Verlag
- Schneider P., Weiss A., 1992, A&A, 260, 1

Chapter 4

Using Differential Time Delays to Identify Gravitational Lenses with Small-Scale Structure

Abstract

We examine the ability of gravitational lens time delays to identify galaxies that contain small-scale structure. Inspired by the simple analytic scaling relation for the time delay between the close pair of images in a “fold” lens, which we derived in the previous chapter, we study the dependence of the time delay on various lens properties. For a lensed source near a caustic, we find that the time delay is not very sensitive to the exact position of the source along the caustic, provided that the source is not in the immediate neighborhood of a cusp. For a lens modeled as an elliptical galaxy with octopole perturbations, we find that the time delay increases with the projected ellipticity, but is nearly independent of the octopole moment. In realistic lensing situations, it is often difficult to determine the mass distribution of the lens galaxy, so we must perform Monte Carlo simulations in order to compare predicted time delays with observed values. Motivated by our theoretical results for individual lenses, we construct mock lenses with parameters determined from observational samples of elliptical galaxies. Using a simple criterion for matching mock lenses and observed systems, we construct distributions for the time delay between lensed images, and use this information to look for “time-delay anomalies” in four-image lenses. We find evidence that the cusp lenses RX J1131–1231 and RX J0911+0551 are anomalous. Based on our work, we suggest that time delays provide an important complementary probe to flux ratios for identifying lens systems with small-scale structure.

4.1 Introduction

Gravitational lensing has become a powerful probe of dark matter in distant galaxies. A growing body of evidence suggests that anomalous flux ratios observed in many four-image lenses can be explained if a few percent of the lens galaxy’s mass is contained in cold dark matter (CDM) substructure (Dalal & Kochanek 2002). Keeton & Moustakas (2008) recently proposed that time delays between lensed images could provide a way to determine properties of the CDM “clumps,” which is not possible with flux ratio studies. In particular, they discuss the possibility of using time delays to constrain the substructure mass function, and show that it is possible for substructure to alter the arrival-time order of lensed images compared with smooth mass models. In order to apply their method in practice, it is necessary to determine whether a given four-image lens is likely to contain CDM substructure. Since the time delays predicted by a smooth model differ from those resulting from a model with substructure, we expect lenses with substructure to have “time-delay anomalies.” Developing an approach to identify such anomalies is the focus of this chapter.

We follow the approach of Keeton et al. (2003, 2005), who derived analytic flux-ratio relations for lenses with fold or cusp configurations, in order to identify lenses with small-scale structure. To be more specific, a fold lens contains a bright pair of images whose fluxes F_A and F_B satisfy the equation

$$R_{\text{fold}} = \frac{F_A - F_B}{F_A + F_B} \approx A_{\text{fold}} d_1, \quad (4.1)$$

where d_1 is the image separation and A_{fold} depends on properties of the lens potential. For a cusp lens, a triplet of images is produced, whose fluxes satisfy the relation

$$R_{\text{cusp}} = \frac{F_A - F_B + F_C}{F_A + F_B + F_C} \approx A_{\text{cusp}} d_1^2, \quad (4.2)$$

where d_1 is the distance between the closest pair of images and A_{cusp} depends on properties of the lens potential. These relations should be obeyed by all lenses with smooth potentials, so any systems that violate these relations are said to be anomalous. However, in practice, determining that a given lens is anomalous requires some care. Since similar image configurations can be produced by lens potentials with different

parameter values, Keeton et al. (2003, 2005) performed Monte Carlo simulations to determine distributions for R_{fold} and R_{cusp} . With this information, it is possible to determine the probability that an observed lens is anomalous and hence contains small-scale structure.

Oguri (2007) employs the method of Keeton et al. (2003, 2005) to study time delays, although his emphasis is different from ours. For a multiple-image lens system, he characterizes a given image pair by the image asymmetry and opening angle, as measured from the lens center. He then examines the dependence of the time delay on the assumed potential of the lens galaxy, for a given image configuration. Using this information, he determines which image morphologies are best suited for computing the Hubble constant. While we are also interested in the dependence of time delays on the lens potential, we focus on fold and cusp lenses, which are best suited for identifying the presence of small-scale structure within the lens galaxy. We note here that small-scale structure is not synonymous with substructure, since the former includes other effects such as microlensing by stars. However, Keeton & Moustakas (2008) find that time delays are insensitive to stars and other low-mass objects, so it is likely that CDM substructure is present in lenses with anomalous time delays.

4.2 Dependence of Time Delay on Lens Potential and Position along Caustic

In Chapter 3 we showed that the time delay between a close pair of images in a fold lens scales with the cube of the image separation and depends on the coefficient h that comes from the Taylor expansion for the lens potential about the fold point. In this section we examine the dependence of the time delay $\Delta\hat{\tau}_{\text{fold}}$ both on the lens potential and the distance between the fold point and the nearest cusp point. This is equivalent to studying the dependence of h on these properties. Since $h < 0$, we find it more convenient to work with its absolute value.

Almost all lens galaxies are elliptical, so we compute $|h|$ for a singular isothermal ellipsoid (SIE) lens. To determine an appropriate value for the ellipticity parameter

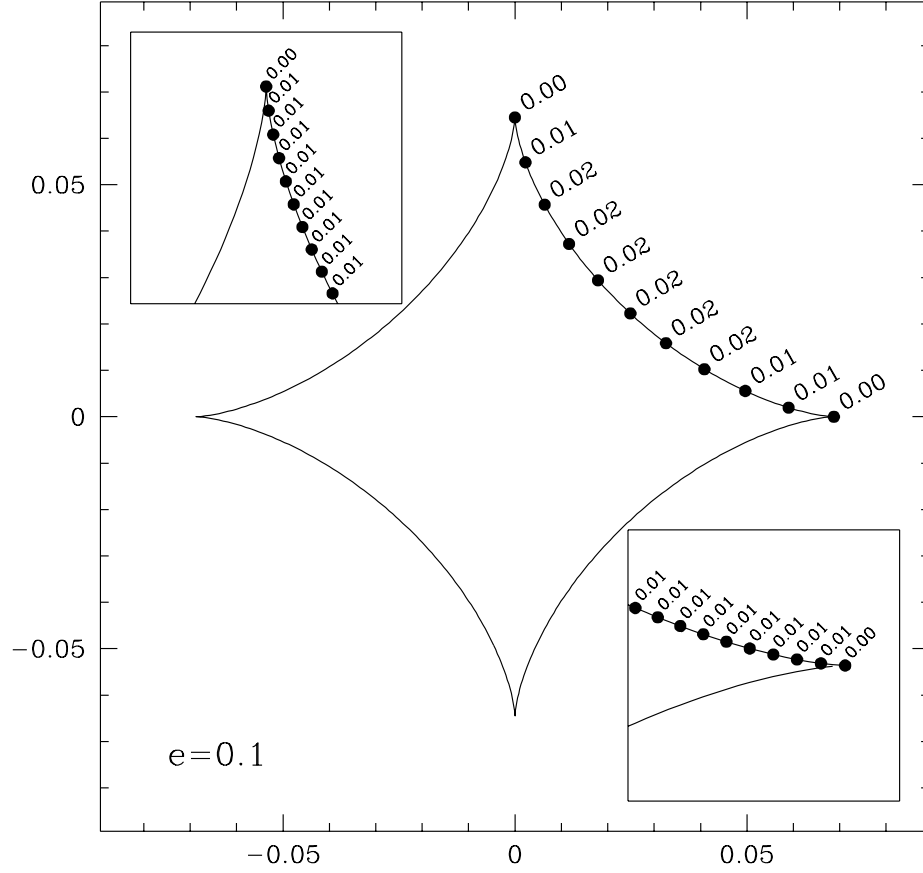


Figure 4.1 Values of $|h|$ at various points on the caustic for an SIE lens with $e = 0.1$. Insets show close-up views of the upper and right-hand cusp points.

e , we turn to the lens samples of Bender et al. (1989), Jørgensen et al. (1995) and Saglia et al. (1993). These collaborations find mean ellipticities and dispersions of $(\bar{e}, \sigma_e) = (0.28, 0.15), (0.31, 0.18)$ and $(0.30, 0.16)$ respectively. Note that these values measure the distribution of light rather than mass, so it is possible that the dark matter halo in which the galaxy presumably resides is rounder or flatter than the observed isophotes.

To account for this possibility, we compute $|h|$ at various points on the caustic, for ellipticities of 0.1, 0.3 and 0.5 as shown in Figures 4.1, 4.2 and 4.3, respectively. While this does not encompass the full range of possible values, the results presented here are

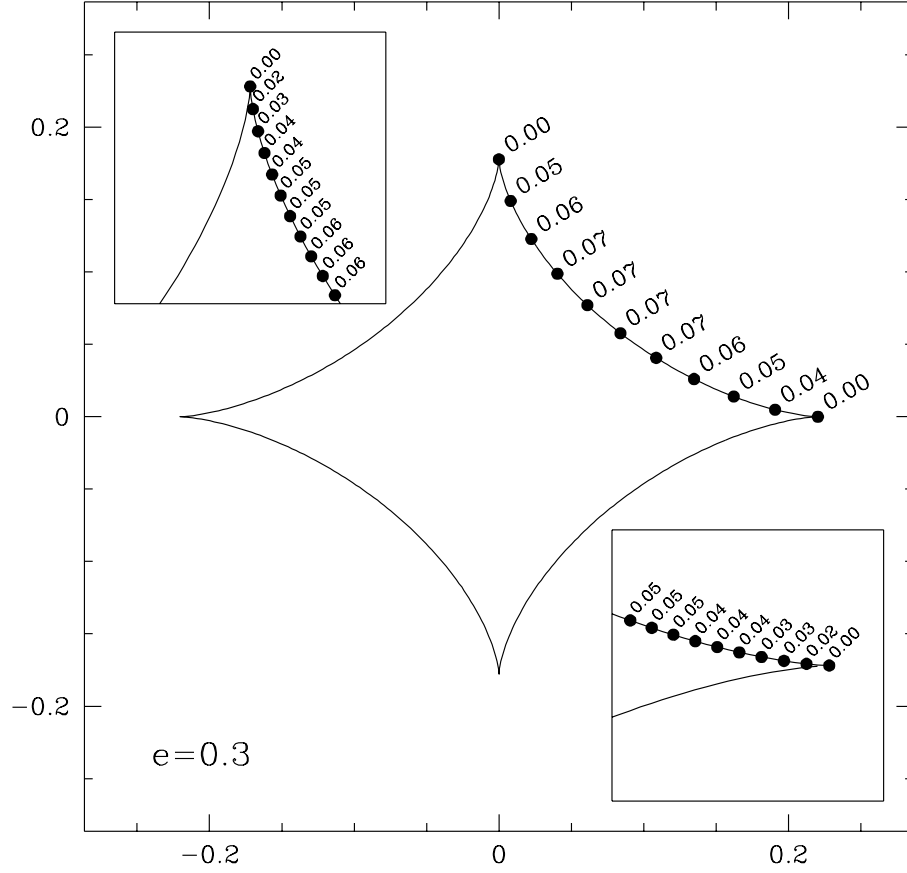


Figure 4.2 Same as Figure 4.1, but for $e = 0.3$.

not very sensitive to the specific ellipticity assumed. We see that $|h|$ remains roughly constant for points away from the cusps. This suggests that lenses whose fold pairs have comparable separations will have similar time delays as well, at least for galaxies with similar ellipticities. Testing this prediction will require large samples of fold lenses, for which both the differential time delay between the fold pair and the ellipticity of the lens galaxy are known. For points near a cusp, $|h|$ varies rapidly, as seen more clearly in the insets of the figures. For a source at the cusp, $|h| = 0$ as it must (see §3.2). Finally, we see that $|h|$ depends on the size of the caustic. It is not yet clear whether this merely reflects the correlation between $|h|$ and e or is indicative of a more subtle model-independent relationship between caustic size and the time delay for a fold pair.

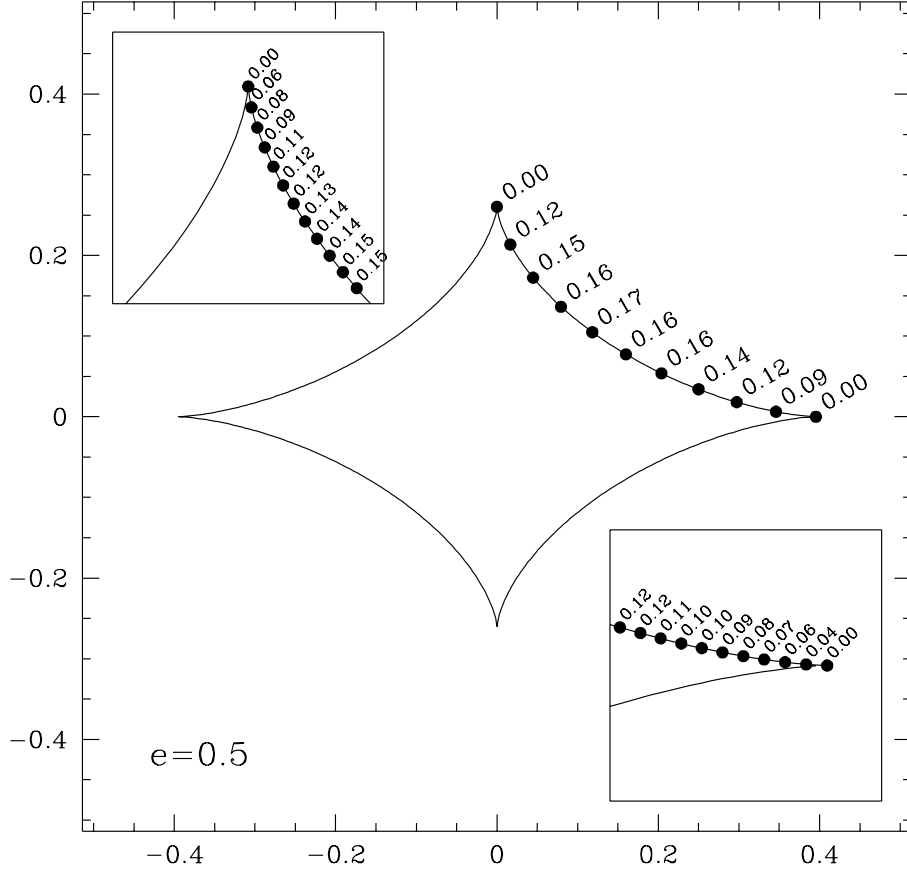


Figure 4.3 Same as Figure 4.1, but for $e = 0.5$.

In addition to ellipticity, Bender et al. (1989) and Saglia et al. (1993) find that many galaxies have “disky” or “boxy” isophotes, which require higher-order multipole terms. The octopole ($m = 4$) Fourier mode, with coefficient denoted by a_4 , is the relevant term to account for these departures from elliptical symmetry. For typical values of $a_4 = -0.01, 0.01, 0.02$ we find maximum $|h|$ -values of 0.07, 0.08 and 0.09, respectively. We therefore conclude that octopole terms have little effect on the time delay for a fold pair, regardless of whether the isophote is diskly ($a_4 > 0$) or boxy ($a_4 < 0$).

Since many lensed galaxies lie within groups or clusters, a nonzero tidal shear is expected. Using numerical simulations and semianalytic models, Holder & Schechter (2003) find that shear is described by a lognormal distribution with mean $\bar{\gamma} = 0.11$ and

dispersion $\sigma_\gamma = 0.15$. For such shear amplitudes, the caustic structure is similar to what is seen in Figures 4.1-4.3, so we do not show its effect on $|h|$. We return to shear when considering realistic lens populations in the following section.

4.3 Time Delay Distributions for a Realistic Lens Population

For a random lens galaxy, we cannot know its exact lens potential or parameters. For a large collection of galaxies, however, we can describe the population in terms of a statistical distribution of parameters. Having characterized the lens population, we can determine the distribution of time delays by using Monte Carlo simulations. We use the galaxy samples discussed above (Bender et al. 1989; Jørgensen et al. 1995; Saglia et al. 1993). Although the mean ellipticities and dispersions are roughly the same for all three samples, the underlying galaxy population is not uniform among the samples. Jørgensen et al. (1995) and Saglia et al. (1993) include galaxies within clusters, while Bender et al. (1989) use bright nearby galaxies to construct their sample. In addition, the Bender et al. (1989) and Saglia et al. (1993) samples contain a_4 distributions, while those of Jørgensen et al. (1995) do not. The numerical method described below is carried out separately for each of the three galaxy samples. To model the environment of a lens galaxy, we add tidal shear using 100 random values drawn from the distribution of Holder & Schechter (2003).

We follow the approach of Keeton et al. (2003, 2005). We create a lens galaxy with model parameters drawn from a distribution appropriate to one of the three galaxy samples. For the Jørgensen et al. (1995) catalog, we can simply construct a histogram of e , and choose lens ellipticities from this distribution. For the Bender et al. (1989) and Saglia et al. (1993) catalogs, we could construct separate distributions for e and a_4 ; however, these two parameters are correlated, so we instead construct lenses with the (e, a_4) pairs measured by these collaborations. This results in 87 independent model lens galaxies for the Bender et al. (1989) sample and 54 model galaxies for the Saglia et al. (1993) sample.

For each model lens, we use the software of Keeton (2001) to solve the lens equation

numerically to obtain the image positions and time delays. We perform this process for a large set of random source positions on the sky. While our assumed lens potential can produce configurations with one, two, or four images, we are only interested in four-image configurations, which can produce cusps and folds. We thus create a mock lens catalog consisting of all four-image lenses produced by the simulations. The catalogs generated from the data of Bender et al. (1989), Jørgensen et al. (1995) and Saglia et al. (1993) contain 1,267,555, 2,205,515 and 851,261 mock lens systems, respectively.

Motivated by our analytic relation for the time delay between the images in a fold pair (Eq. [3.24]), we wish to compare our simulated lenses with observed lenses, particularly those with folds and cusps.¹ To do this, we select in turn each of the four mixed-parity image pairs from a given observed lens, and characterize the pair by its separation, d_1 , as well as the distance to the next-nearest image, d_2 . To obtain d_2 , we consider the distance between each image of the original pair and its next-nearest image of opposite parity, and use the smaller of these two distances. We only consider pairs whose images have opposite parity, since this is the situation for a fold pair, for which our analytic expression for the time delay was derived. For a fold lens, $d_1 \ll d_2 \sim \theta_E$; for a cusp lens, $d_1 \sim d_2 \ll \theta_E$; for a cross lens, $d_1 \sim d_2 \sim \theta_E$. The Einstein angle, θ_E , sets the overall scale of the lens system.

For a given image pair in an observed lens system, we scan through our mock lens catalog and select all image pairs with values of d_1 and d_2 that agree with those for the observed pair to within a tolerance of $0.05\theta_E$. To fully characterize the image configuration of a four-image lens system, we would need to know the distance of the fourth image from the image pair in question. Without this information, our criteria for matching mock images and observed lenses may allow for the inclusion of mock lenses with image configurations that differ from that of a given observed lens. Since we seek a model-independent way of identifying small-scale structure in observed lenses, we only require that an image pair of a mock lens match a pair in an observed lens.

¹We do not use Equation (3.24) to make quantitative predictions in this chapter, so it is reasonable to consider non-fold pairs, as well as cusp and cross lenses, in our comparisons between observed lenses and Monte Carlo simulations.

For each mock image pair that satisfies our distance filter, we compute the differential time delay, and then combine these data to construct a time-delay histogram. We can then determine whether the corresponding observed lens is anomalous (see below); if so, this indicates the presence of small-scale structure.

4.4 Application to Observed Lenses

The number of observed four-image lenses has been steadily increasing in recent years; 22 such systems are currently known (see Table 4.1). The time delays computed from our simulations are in units of θ_E^2 . To compare these values with observed time delays, we must divide the observed data by $\tau_0 \theta_E^2$. We use model values for θ_E obtained from Keeton et al. (2005). The scale factor is given by

$$\tau_0 = \frac{1 + z_L}{c} \frac{D_L D_S}{D_{LS}}, \quad (4.3)$$

where D_L , D_S and D_{LS} are the angular-diameter distances from the observer to lens, observer to source, and lens to source, respectively. The distance factors in τ_0 depend on both the lens redshift z_L and the source redshift z_S . To compute τ_0 , we assume cosmological parameters $\Omega_M = 0.3$, $\Omega_\Lambda = 0.7$ and $H_0 = 70 \text{ km s}^{-1} \text{ Mpc}^{-1}$. Since z_L and z_S are not both known for every four-image lens, there are some systems with measured time delays that we cannot compare with our simulations. Table 4.1 includes fold, cusp and cross lenses, whose image morphologies are defined in Section 1.2.4.

We are interested in determining whether an observed time delay indicates an anomaly. We do this by comparing the observed value to the values predicted by our simulations. We compute the statistical P-value, which gives the fraction of predicted time delays that are smaller than the observed value. To remove the dependence of our results on cosmology, we compute P-values for ratios of time delays as well. It is convenient to construct a ratio that is always positive. To do this, we adopt the following sign convention. By definition, any image pair we consider will consist of a minimum (positive parity) image and a saddle (negative parity) image. If the next-nearest image is a minimum, we have a triplet consisting of a saddle surrounded by two minima. We

Table 4.1 Data for the known four-image lenses, as given by Oguri (2007) and the CASTLES website (<http://www.cfa.harvard.edu/castles/>). Question marks indicate parameters for which no measured value is available. The Einstein angle θ_E is computed from lens models (Keeton et al. 2003, 2005). The timescale τ_0 depends on z_L and z_S . We assume cosmological parameters $\Omega_M = 0.3$, $\Omega_\Lambda = 0.7$ and $H_0 = 70 \text{ km s}^{-1} \text{ Mpc}^{-1}$. The table is divided into three sections: fold lenses (top), cusp lenses (middle) and cross lenses (bottom).

Lens Name	z_S	z_L	θ_E (arcsec)	τ_0 (days/arcsec ²)
B0128+437	3.12	?	0.20	?
HE 0230–2130	2.16	0.52	0.82	85.7
MG 0414+0534	2.64	0.96	1.08	193.2
B0712+472	1.34	0.41	0.68	72.9
SDSS 0924+0219	1.52	0.39	0.87	64.8
SDSS 1004+4112	1.73	0.68	6.91	140.7
PG 1115+080	1.74	0.31	1.03	46.5
B1555+375	?	?	0.24	?
B1608+656	1.39	0.63	0.77	143.7
B1933+503	2.63	0.76	0.49	135.8
WFI 2026–4536	2.23	?	0.65	?
WFI 2033–4723	1.66	0.66	1.06	137.6
RX J0911+0551	2.80	0.77	0.95	134.8
RX J1131–1231	0.66	0.30	1.81	65.0
B1422+231	3.62	0.34	0.76	46.1
B2045+265	1.28	0.87	1.13	342.1
HE 0435–1223	1.69	0.46	1.18	75.0
HST 12531–2914	?	0.69	0.55	?
HST14113+5211	2.81	0.46	0.83	68.8
H1413+117	2.55	?	0.56	?
HST 14176+5226	3.40	0.81	1.33	135.7
Q2237+030	1.69	0.04	0.85	4.9

denote the minima by M_1 and M_2 and the saddle by S , and define

$$\Delta t_1 = t(M_1) - t(S) \quad \text{and} \quad \Delta t_2 = t(M_2) - t(S), \quad (4.4)$$

where the image pair of interest is M_1S and $t(x)$ denotes the scaled time delay of image x . The time-delay ratio is given by $\Delta t_1/\Delta t_2 > 0$, since saddles trail (i.e., have larger time delays than) minima. In the case that the next-nearest image is a saddle, we define

$$\Delta t_1 = t(S_1) - t(M) \quad \text{and} \quad \Delta t_2 = t(S_2) - t(M), \quad (4.5)$$

where the pair of interest is MS_1 . Again, the ratio $\Delta t_1/\Delta t_2 > 0$. When labeling images, we always list the minimum first, as we have done here.

To get a better picture of the meaning of a given P-value, we show histograms of the scaled time delay and time-delay ratio for all image pairs in the 22 known four-image lenses. There are many lenses for which observational data are not available, but the histograms for those cases are still pedagogically useful and provide a way to predict what the time delay should be if the lens in question is not anomalous. We begin by discussing the general features of our time-delay histograms. We next analyze the lenses with known time delays, and then make predictions for the remainder.

4.4.1 Time-Delay Histograms

For all four mixed-parity image pairs in each lens, we construct histograms of the scaled time delays (Figs. 4.4-4.8) and time-delay ratios (Figs. 4.9-4.13). For each lens, we define d_1^* to be the smallest value of the image separation d_1 . We divide the lenses into three groups: folds, cusps and crosses. The vertical arrangement of lenses in each group is such that d_1^* increases from top to bottom. For each given lens, the panels are arranged from left to right in order of increasing d_1 . As a check for systematic effects, we compute and plot separately the distributions corresponding to the Bender et al. (1989), Jørgensen et al. (1995) and Saglia et al. (1993) samples (solid, dashed and dotted curves, respectively). We find that our conclusions do not depend on the assumed galaxy sample, so we do not distinguish between the three datasets in the following discussion. In each panel, the horizontal axis runs from four standard

deviations below to four standard deviations above the mean time delay (or ratio). We expand this range if data would otherwise be excluded from the plot. Each panel is vertically scaled to the peak height of the three histograms.

We first consider Figures 4.4-4.8, which show histograms of the scaled time delay, measured in units of $\tau_0\theta_E^2$. We notice two general trends. First, for almost all image pairs, we find that the time delays are described by a bimodal distribution. This makes sense in light of our criterion for matching mock image pairs with observed pairs. We only require that the d_1 and d_2 values for a given mock pair agree with the values for an observed pair, without reference to image parity. According to the sign convention as defined above, if the triplet of images formed by a given pair and its nearest neighbor image comprise a minimum flanked by two saddles, then the differential time delay for the pair of interest will be positive; while a triplet consisting of a saddle between two minima will result in a negative time delay for the pair of interest. Each image morphology gives rise to separate peaks in the distribution, whose positions (relative to $\Delta t_1 = 0$) and widths display varying degrees of asymmetry. A moderate degree of asymmetry is not surprising, but there are several cases where the peaks centered at positive and negative values of the time delay are noticeably different from each other. This is straightforward to understand for cusp lenses. For the two pairs in the cusp triplet, the values of d_1 and d_2 do not contain any information about image parity. However, this is not the case for the two pairs that involve the image that is not part of the cusp triplet. The position of this image relative to the lens center indicates whether the lensed source lies on the long or short symmetry axis of the caustic. For a source on the long axis, it is a general result of lens theory that the middle image in the cusp triplet has negative parity, which implies a negative parity for the non-cusp image as well. For convenience, we refer to the two image pairs that involve the non-cusp image as “non-cusp pairs.” A non-cusp pair and its closest neighboring pair form a triplet, whose middle image is one of the positive-parity cusp images, and whose outer images are the central cusp image and the non-cusp image (both of which have negative parity); hence, the time delays for the non-cusp pairs will be positive. This can be seen in the third and fourth panels for the long-axis cusp lenses B2045+265,

RX J1131-1231, and B1422+231, where the peak centered at the positive scaled time delay contains more weight than that centered at the negative value. The system RX J0911+0551 is a short-axis cusp lens, where we would expect more of the weight to be contained in the left-hand peak, since the non-cusp image has positive parity in this case. This is indeed borne out by the figure. We also find asymmetric behavior for the third and fourth pairs in the fold lenses, although there is a great degree of variation from one lens to another. The reasoning we apply to short-axis and long-axis cusps has no obvious analog for folds, so this behavior is a bit puzzling and will require closer scrutiny. For the cross lenses, no significant asymmetry is expected or found.

The second general feature in our histograms of scaled time delays does not require detailed explanation. In particular, as d_1^* increases from one lens to the next, and d_1 increases from one image pair to the next, the peaks begin to separate and become broader. This is consistent with our analytic scaling of Chapter 3, which shows that the time delay increases with image separation, of which both d_1 and d_1^* provide a measure. The width of the distribution simply increases in proportion to the median value.

We now consider the histograms for time-delay ratios (Figs. 4.9-4.13). The bimodality we noted above for the scaled time delays now disappears. This is simply because our sign convention was chosen so that the time-delay ratios are always positive. We also find that the overall structure of the histograms shown in these figures does not vary much from one lens to another, or between image pairs of a given lens. This is a sign that conclusions drawn from time-delay ratios are not terribly sensitive to parity or to the image morphology (fold, cusp, or cross), which may prove quite useful. We do find one subtlety in these histograms: the distributions are slightly skewed to the right, toward larger time-delay ratios. The simplest explanation is that the time-delay ratios are bounded by zero on the left, but unbounded on the right. In the cases of HE 0230-2130 and B1608+656, the skewness is manifested as a “shoulder” on the right side of the main peak for the image pair with smallest separation. Each of these systems contains two lens galaxies, and it is likely that this unusual feature in the histograms is related to the complexity in the lens potential. Our simulations assume a single lens

galaxy, so the connection between our simulations and the observed lens systems is subtle. In any case, these shoulders do not dramatically alter the overall shape of the distributions.

4.4.2 Identifying Time Delay Anomalies in Observed Lenses

For image pairs with observed differential time delays, we can use our simulations to determine whether any of their host lenses contain small-scale structure. Seven of the 22 lenses in the observed sample of quadruply-imaged systems have at least one image pair with an observed time delay. We discuss each of these systems in turn (see also Tables 4.2 and 4.3). Since our choice of galaxy sample does not affect our conclusions, the P-values discussed in this subsection were computed using only the sample of Bender et al. (1989), which is the larger of the two samples that include octopole contributions.

SDSS J1004+4112

This lens (hereafter 1004) is produced by a cluster of galaxies and contains five lensed images (Inada et al. 2005). The temporal ordering of the images is C-B-A-D-E (Fohlmeister et al. 2007b). The images C and B are minima, A and D are saddles, and E is a maximum. Maximum images are rarely observed, so we do not consider them here. The time delays for pairs BA and CA are known (Fohlmeister et al. 2007a), but the time delays of the pairs DB and DC are not known. (Note that the temporal ordering given by Fohlmeister et al. 2007a for images A and B is incorrect.) The P-value for the fold pair BA is 0.365 for Δt_1 , which does not indicate an anomaly. This is somewhat surprising, since we would not expect an SIE with shear to be a very good model for a cluster lens, mainly because the density profile is expected to be shallower than isothermal and the shear should lie at the high- γ tail of the distribution. Since observed time delays have error bars, perhaps our conclusion that BA is not anomalous is in doubt. We thus compute the P-values for the lower and upper values of the error interval, and find values of 0.353 and 0.378; these values do not change our conclusion. We cannot construct the time-delay ratio $\Delta t_1/\Delta t_2$ for pair BA because we do not know the time delay for the closest neighboring pair (BD). We now turn to the pair CA, which involves

one of the fold images. Its P-value is 0.275, slightly lower than that for pair BA, but still not anomalous. Since the spatial scale probed by the pair CA is relatively large, we would expect to find structure on scales smaller than the image separation, so it is not surprising the the P-value for this pair is farther from 0.5 (the median) than BA. It is possible to construct the time-delay ratio for CA, since its nearest neighboring image pair is BA. The corresponding P-value is 0.0243, which indicates a marginal anomaly. Perhaps the discrepancy in P-values for the scaled time delay and time-delay ratio arises from the inclusion of the fold pair in the ratio.

PG 1115+080

This lens (hereafter 1115) was the first observed fold, and has a well-known flux-ratio anomaly at optical wavelengths. The time-delay data for 1115 provided in Tables 4.2 and 4.3 come from the optical band. If flux ratios and time delays both provide a measure of small-scale structure within the lens, we might expect a flux-ratio anomaly to have a corresponding time-delay anomaly. The flux anomaly in 1115 is due to microlensing, which has been shown by Keeton & Moustakas (2008) not to affect time delays. It is therefore no great surprise that none of the P-values for the scaled time delays nor time-delay ratios reveal anomalies. As we found for the lens 1004, the image pair in 1115 with the largest separation (CA2) has the P-value for scaled time delay that deviates most from the median, although not enough to be considered anomalous. Again, this is to be expected for an image pair with a large separation.

B1608+656

Like 1004, this system (hereafter 1608) has a lens that we would not expect to be described by our assumed lens potentials, which apply to single galaxies. In this case, the reason is that the lensed images of 1608 are caused by two lens galaxies. The P-values quoted in the tables do not reveal anomalous time delays. The dashes in the entries for image pair BD indicate that that P-values cannot be properly constructed for this pair. This is because only one simulated image pair matches BD. In other words, the distances d_1 and d_2 for the pair BD cannot be produced by a lens potential

that includes only a single galaxy.

RX J0911+0551

We now turn to the cusp lenses. Although the system RX J0911+0551 (hereafter 0911) has two close pairs of images, we cannot use them to probe small-scale structure because the relevant time delays have not been measured with sufficient precision. We nevertheless find clear evidence of a time-delay anomaly using the image pairs with the two largest separations. Since the lens galaxy in 0911 should be well described by the sample of Bender et al. (1989), P-values that exceed 0.99 are surprising, even though the image separations of the pairs DC and DA are relatively large. To be absolutely sure that we have found a time-delay anomaly, we need to construct time-delay ratios, which can be done once the time delays for the cusp triplet have been measured precisely enough. Given that initial values have been measured, albeit with large error bars, we are hopeful that the data we need will become available in the near future (see Chartas et al. 2001).

RX J1131–1231

Keeton & Moustakas (2008) provide strong evidence that dark-matter substructure is present in this lens (hereafter 1131). For the scaled time delays, the cusp pairs BA and CA have P-values of 0, even when the error bars on the time delay are taken into account. This provides nearly irrefutable evidence for small-scale structure. That the corresponding P-values for the time-delay ratios are on the border between anomalous and normal is a bit surprising. One explanation is that a clump of dark matter is affecting both image pairs in a way that partially cancels upon division of their time delays. Another interesting result is that the P-values for the time-delay ratios indicate anomalies for the pairs BD and CD, but the corresponding P-values for the scaled time delays do not. There is no obvious interpretation of this, but at the very least, this finding provides additional evidence that 1131 is an unusual lens that warrants further study.

B1422+231

The behavior of the time delays in this system (hereafter 1422) is similar to what we found for 1131. P-values for the scaled time delays of the image pairs in the cusp triplet (AB and CB) show a strong anomaly, while the P-values of the time-delay ratios are within the range expected for a lens galaxy described by the Bender et al. (1989) dataset.

HE 0435–1223

As a reference case, we consider the cross lens HE 0435–1223 (hereafter 0435). As we would expect, all of the P-values are consistent with a galaxy modeled as an SIE with octopole perturbations and external shear.

4.4.3 Predictions for the Remaining Lenses

To conclude this section, we offer a compilation of confidence intervals of the scaled time delays (Table 4.4) and time-delay ratios (Table 4.5) for all mixed-parity image pairs in all 22 known four-image lenses, which should be a valuable source for identifying anomalous lenses in the future, as more observational data on lensing time delays become available. For each lens, we use the histograms derived from the galaxy sample of Bender et al. (1989) to compute the median value of the scaled time delay and the time-delay ratio. This gives a sense of what the observed value will be for a lens that is described adequately by an elliptical galaxy subject to tidal shear, but we cannot use this information to determine whether a given system is anomalous. For this purpose, we compute confidence intervals, whose endpoints are chosen such that a specified fraction of the simulated data lie within this range. We would not consider a lens to be anomalous if it lies within the 95% confidence interval. A lens that lies outside the 95% interval but within the 99% interval might be regarded as marginally anomalous, while any lens falling outside the 99% interval would very likely be anomalous. The case for an anomaly is strongest if both the scaled time delay and the time-delay ratio separately appear anomalous. Since there is currently great interest in lens monitoring (see Oguri

2007), we are optimistic that the sample of time delays will increase significantly in the near future, making it possible to apply our results to the existing lens sample as well as to those that have not yet been discovered.

4.5 Discussion and Conclusions

In the decade since Mao & Schneider (1998) pointed out that simple lens models have great difficulty reproducing the observed flux ratios in four-image gravitational lenses, it has become generally accepted that lens galaxies contain clumps of dark matter, in agreement with predictions from numerical simulations (Moore et al. 1999; Klypin et al. 1999). Placing constraints on the amount of substructure with lensing depends on having a reliable way to identify lens galaxies that contain small-scale structure. Keeton et al. (2003, 2005) have developed such a method in the context of flux ratios. We have sought in this chapter to extend their formalism to differential time delays. To get a sense of how this could work, we determined the dependence of the time delay between the close pair of images in a fold lens on the position of the lensed source along the caustic, and the assumed form of the lens potential. For a source near a fold point, we found that the time delay remains approximately constant. There is a small region around a cusp point where the time delay quickly drops to zero. This is a reflection of the analytic scaling we used, which is strictly valid only for sources sufficiently far from a cusp point. While an analogous scaling relation for cusps has not been fully worked out, we can nevertheless understand the general behavior of the time delays for sources near these points. If the lens is modeled as an elliptical galaxy with octopole perturbations, the time delay increases with the ellipticity of the galaxy, but is not very sensitive to the octopole amplitude. For a galaxy that is subject to tidal shear, we expect that the time delay will increase with the shear amplitude, in analogy with ellipticity.

Using Monte Carlo simulations, we have constructed distributions of the time delays in four-image lenses. This approach can handle fold, cusp and cross lenses, which comprise the three basic four-image lens morphologies. By constructing a catalogue of mock lenses based on observed populations of elliptical galaxies, we have computed the

range of time delays that would be expected for a smooth lens potential. To compare our mock lenses with observed systems, we require that the distance between the images in a chosen pair, as well as the distance to the next-nearest image, agree for a simulated lens and an actual lens. Since it is not possible to measure these distances with infinite precision, we have allowed for a discrepancy of $\pm 0.05\theta_E$ between the simulated and measured image separations. For all mock lenses that meet this criterion, we calculated the time delays for the pair in question and the closest neighboring pair. From these data, we have looked for anomalous time delays, which would be a clear sign that small-scale structure is present in an observed lens. By computing P-values for all image pairs in all lenses with observed time delays, we have seen that the systems RX J1131–1231 and RX J0911+0551 are anomalous. In the case of 0911, almost all of the simulated time delays have larger absolute values than the observed time delays, at least for the two image pairs for which precise time delays have been obtained observationally. Our result for 1131 is consistent with conclusions based on anomalous flux ratios, and agrees with the recent work of Keeton & Moustakas (2008), who were the first to consider time delays in the context of dark-matter substructure.

To avoid cosmology dependence in our conclusions, we have constructed histograms for time-delay ratios. Since the time delay and Hubble constant are degenerate, it is desirable to work with time-delay ratios, where the Hubble constant is not involved. These ratios also serve to scale out any global effects, which would affect all image pairs in roughly the same way, but would be hard to distinguish from small-scale structure. The histograms we have obtained are more uniform than those we found for scaled time delays, indicating that we have successfully removed those features that depend on the specific image morphology. The only drawback of using time-delay ratios is that we must have more data, since two time delays are needed to construct a single ratio.

In the hope that the sample of observed time delays will increase, we have computed confidence intervals for all 22 known four-image lenses, and all image pairs in each lens. We have provided criteria for identifying whether a lens is normal, marginally anomalous or highly anomalous. If lens galaxies really contain dark-matter substructure, time delays should be able to find it. All that will be required is to compare an observed

time delay with the values we have tabulated. Flux ratios provide a powerful way to find small-scale structure, but they are not unique in this; time delays hold great promise for contributing to our understanding of the role played by dark matter in the universe.

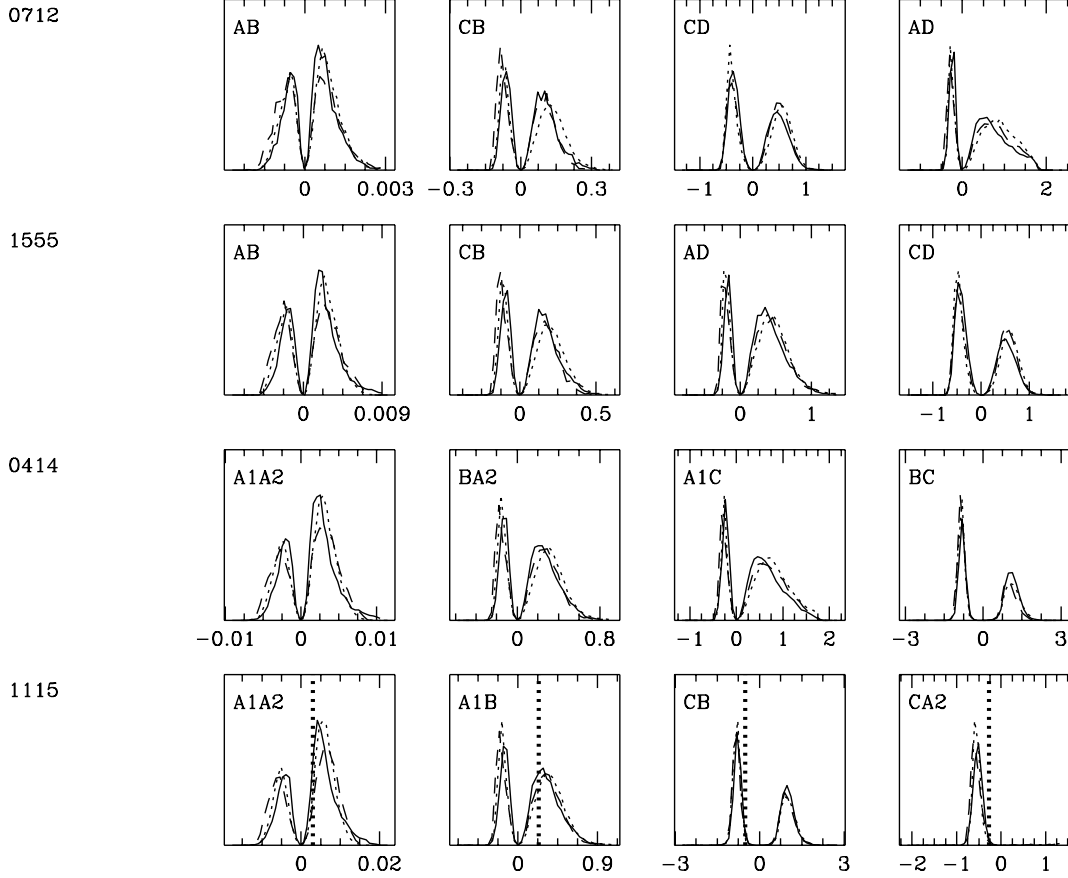


Figure 4.4 Time-delay histograms for 4 of the 12 known fold lenses. The horizontal axes show the scaled time delay in units of $\tau_0 \theta_E^2$. The vertical axes are in arbitrary units, with each panel scaled to the maximum value of its three histograms. From top to bottom, systems are arranged in order of increasing d_1^* ; the abbreviated lens name appears at far left. (See Table 4.1 for the full names.) From left to right, the panels correspond to image pairs with increasing values of d_1 . The solid, dotted and dashed curves show histograms corresponding to the data of Bender et al. (1989), Jørgensen et al. (1995) and Saglia et al. (1993), respectively. For image pairs with observed time delays, vertical dashed lines show the measured values.

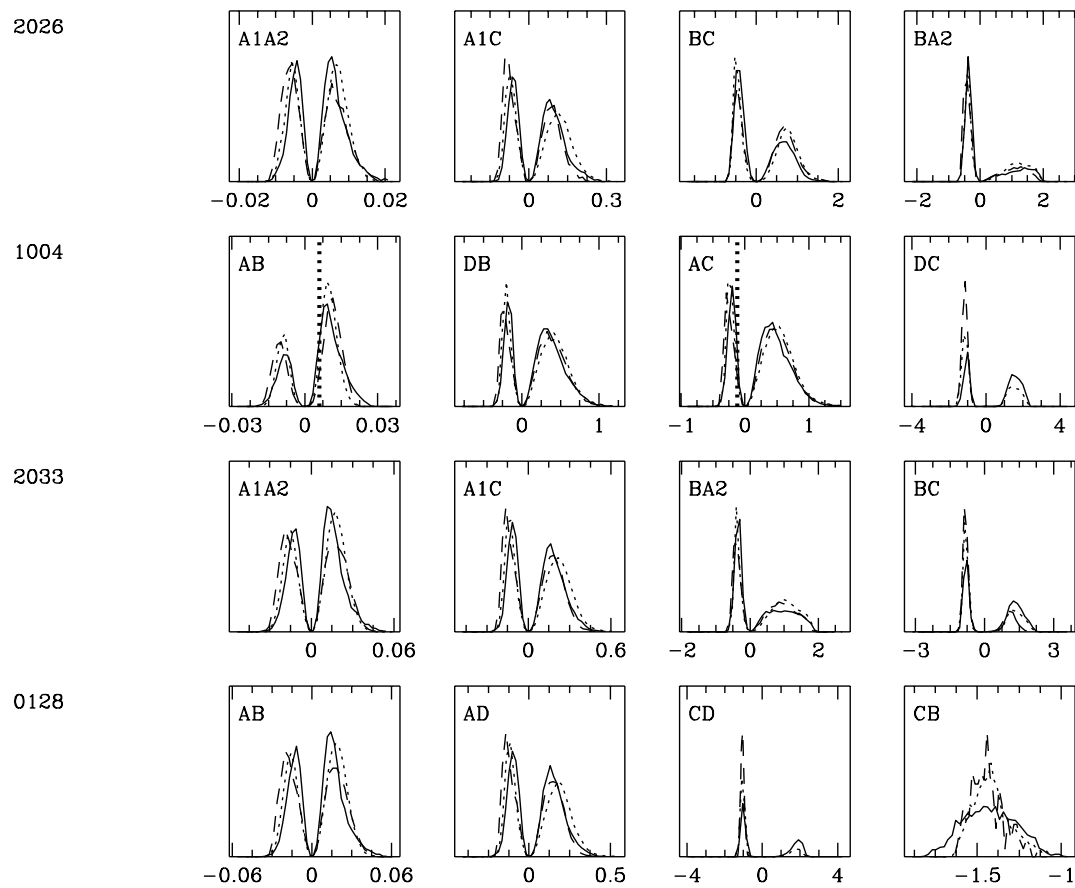


Figure 4.5 Continuation of Figure 4.4.

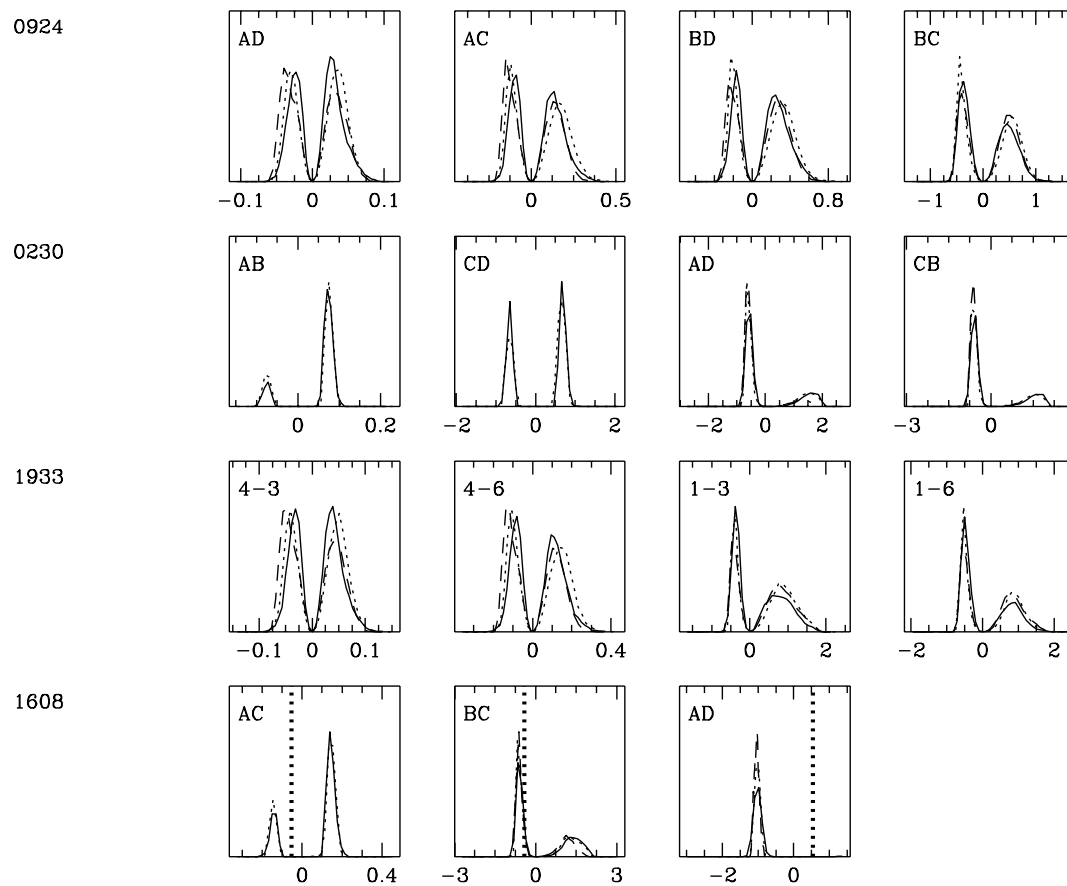


Figure 4.6 Continuation of Figure 4.5.

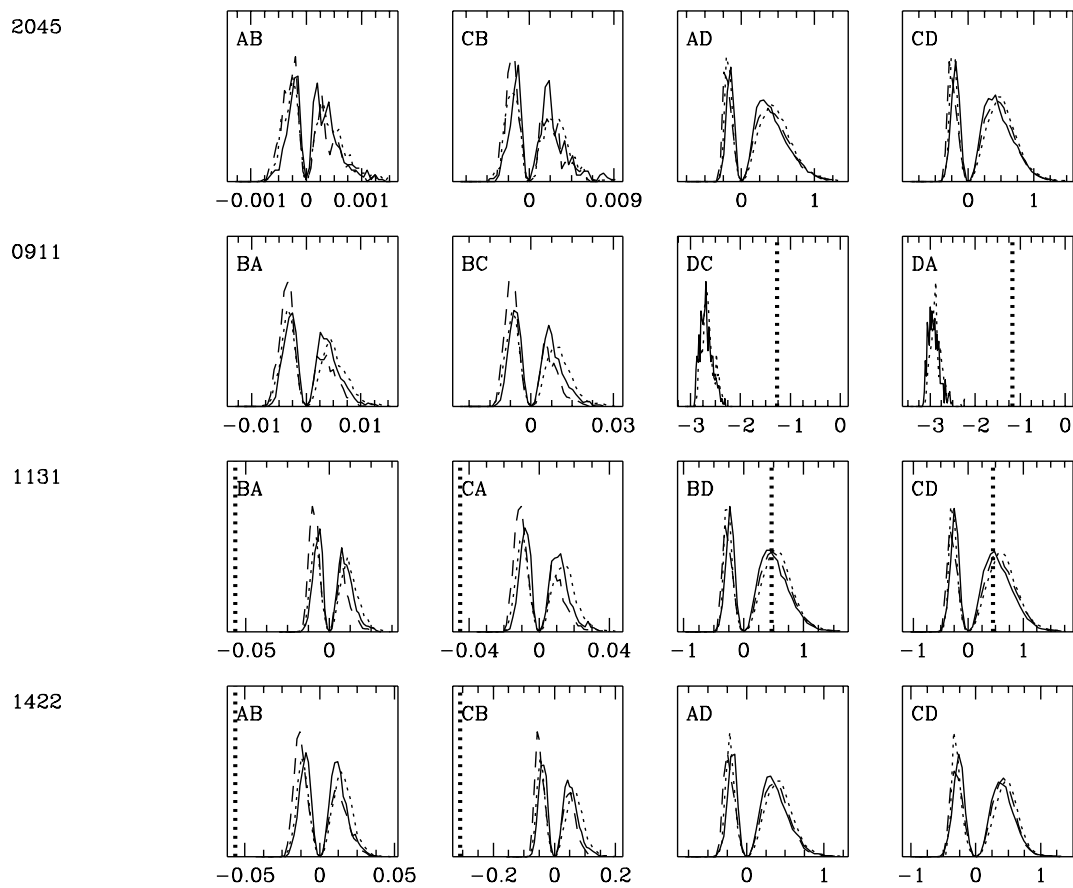


Figure 4.7 Same as Figure 4.4, but for the 4 known cusp lenses.

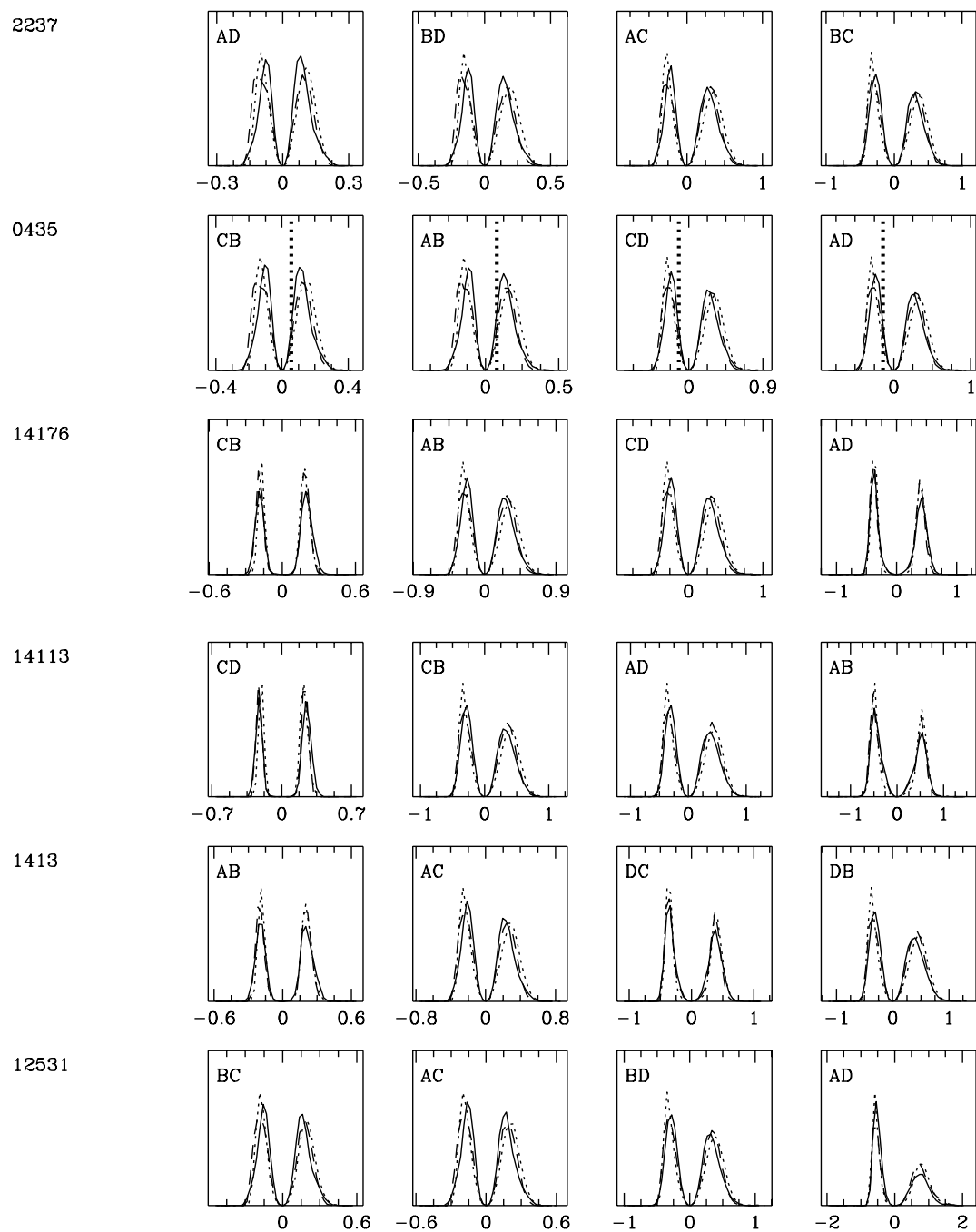


Figure 4.8 Same as Figure 4.4, but for the 6 known cross lenses.

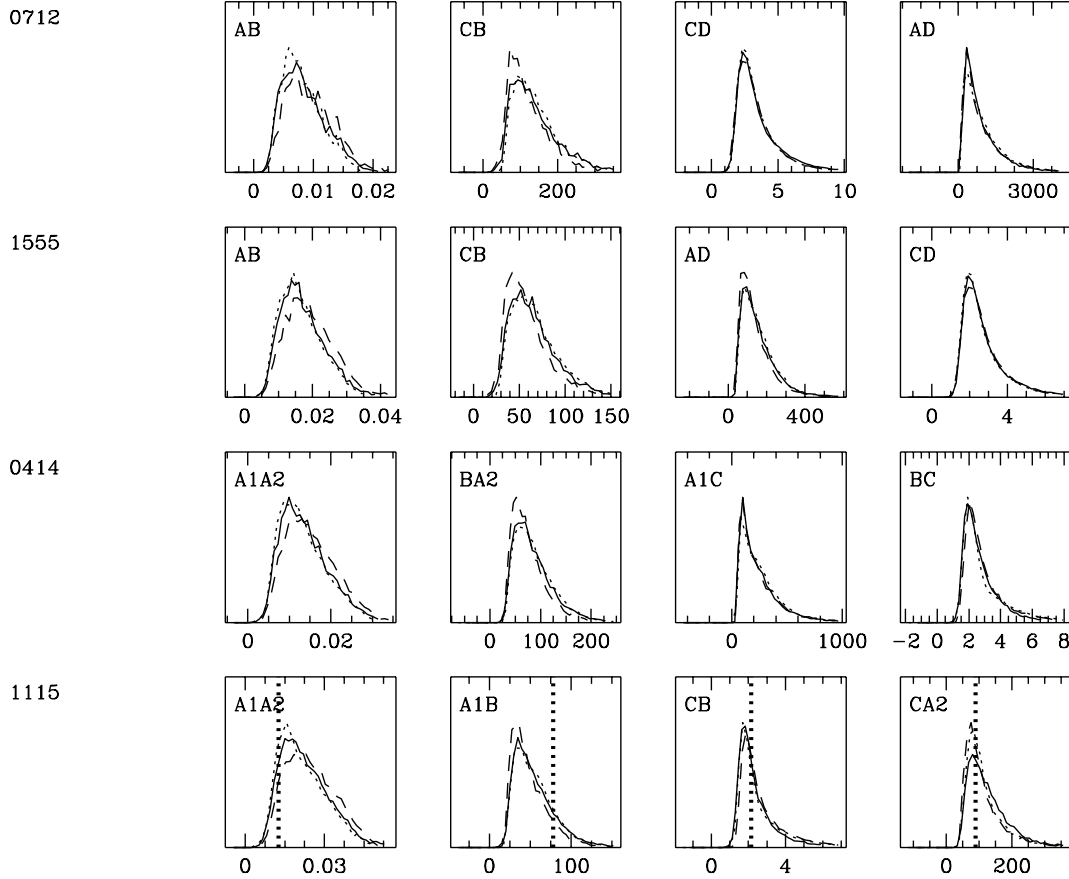


Figure 4.9 Histograms of time-delay ratios for 4 of the 12 known fold lenses. The horizontal axes show the (dimensionless) time-delay ratio. The vertical axes are in arbitrary units, with each panel scaled to the maximum value of its three histograms. From top to bottom, systems are arranged in order of increasing d_1^* ; the abbreviated lens name appears at far left. (See Table 4.1 for the full names.) From left to right, the panels correspond to image pairs with increasing values of d_1 . The solid, dotted and dashed curves show histograms corresponding to the data of Bender et al. (1989), Jørgensen et al. (1995) and Saglia et al. (1993), respectively. For image pairs where it is possible to construct time-delay ratios from observational data, vertical dashed lines show these values.

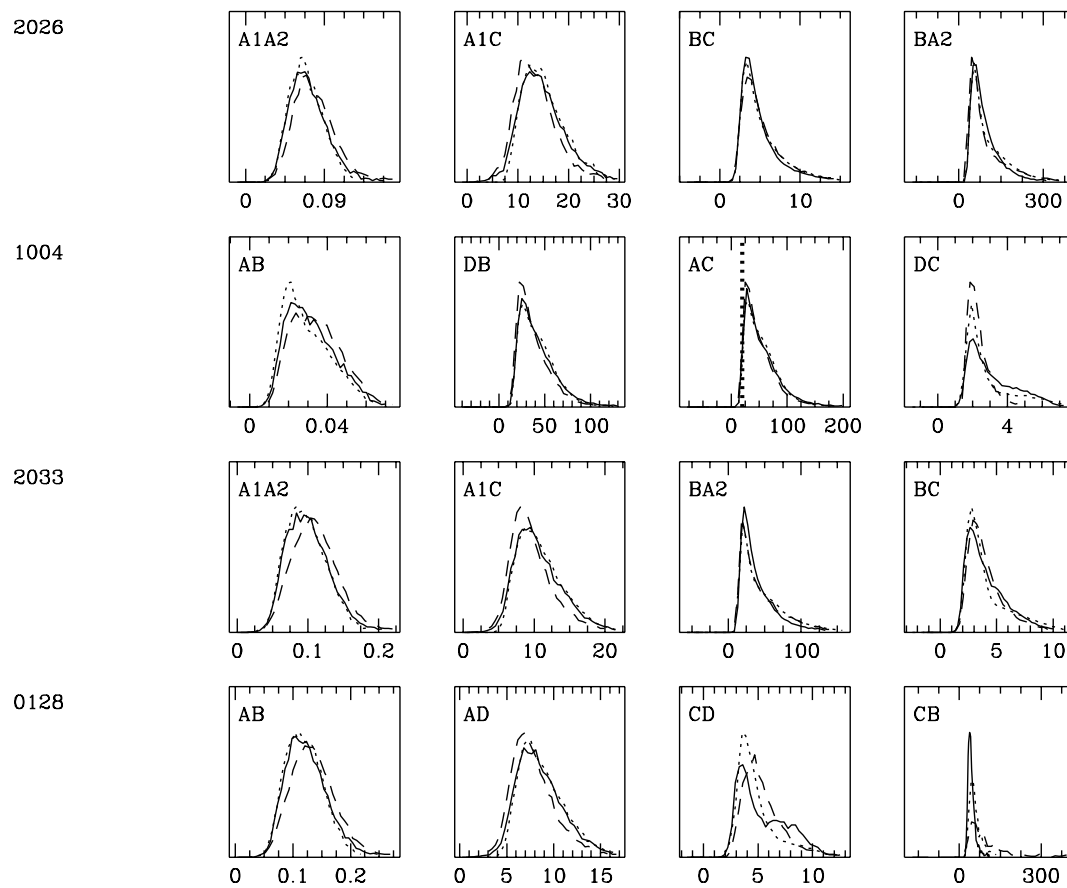


Figure 4.10 Continuation of Figure 4.9.

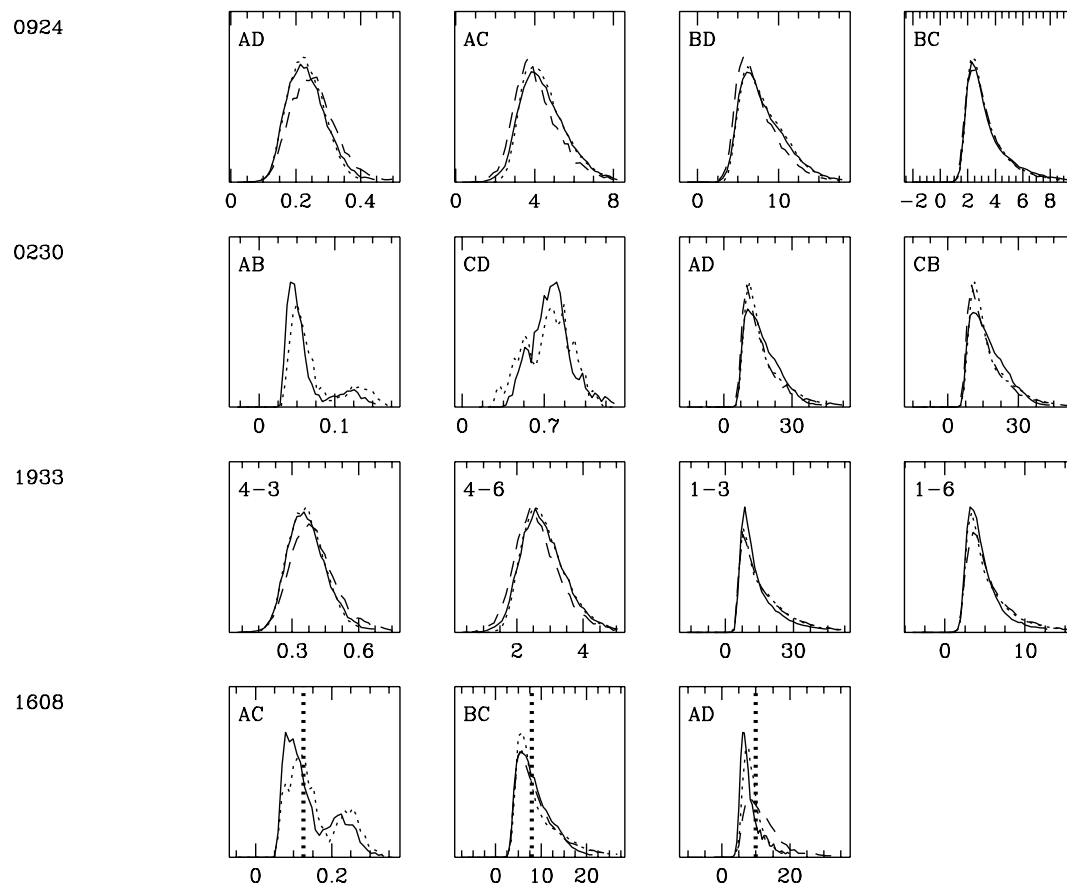


Figure 4.11 Continuation of Figure 4.10.

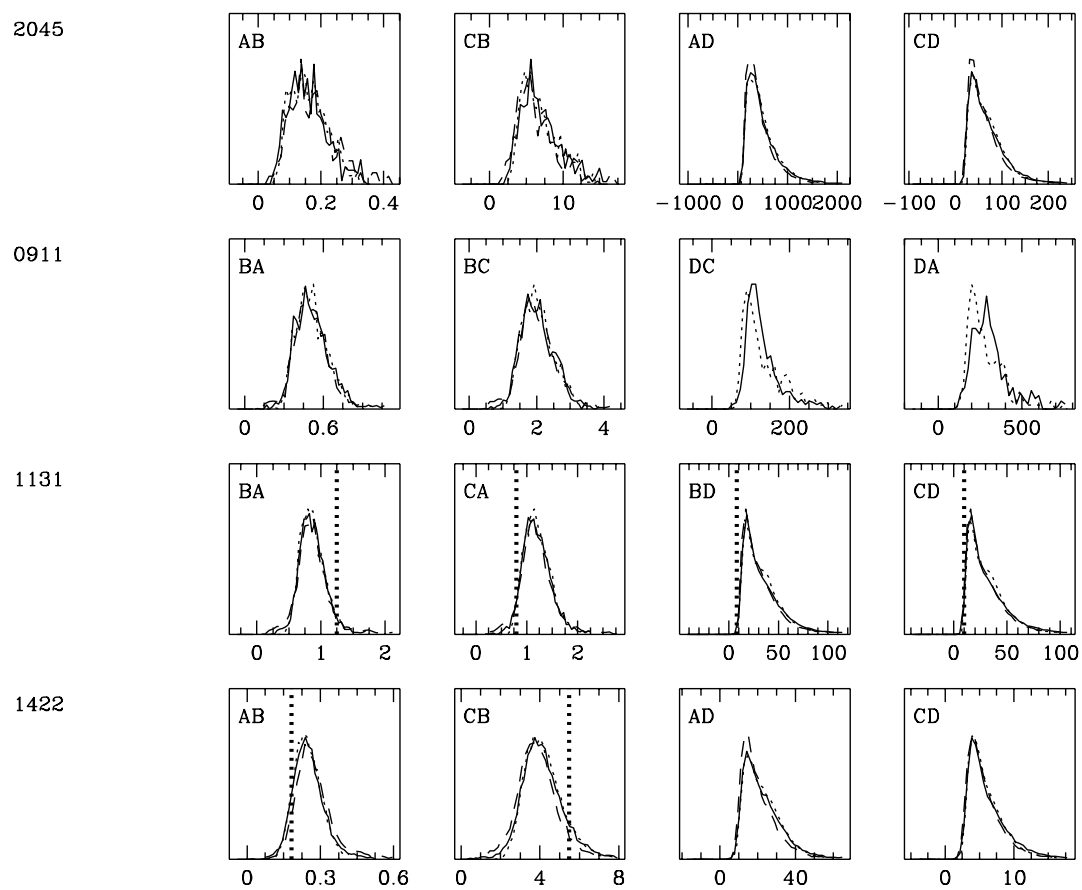


Figure 4.12 Same as Figure 4.9, but for the 4 known cusp lenses.

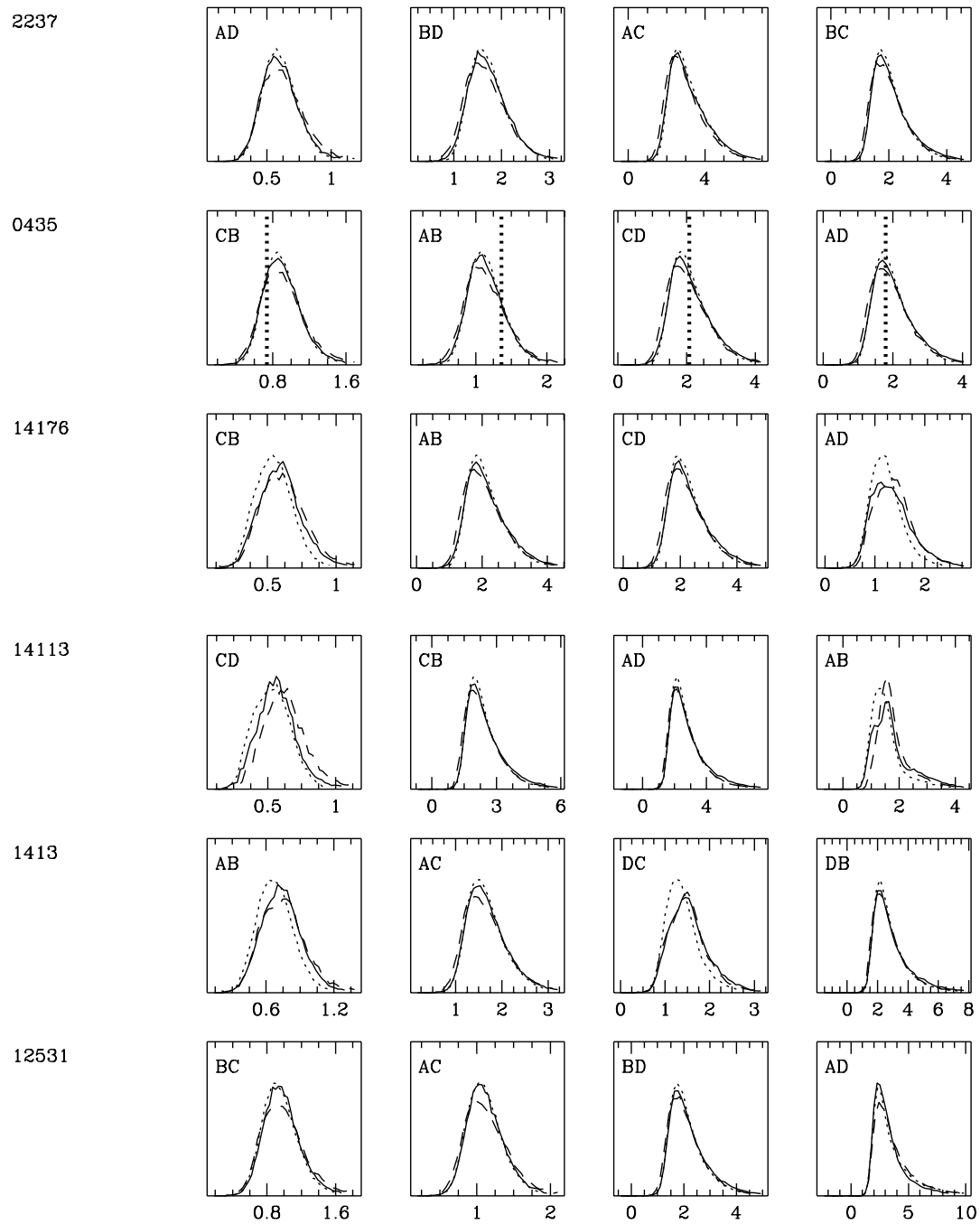


Figure 4.13 Same as Figure 4.9, but for the 6 known cross lenses.

Table 4.2. P-values for scaled time delays

Lens Name	Image Pair	Rank	obs. Δt_1 (days)	error interval	P-value for Δt_1	P-values for err. interval
1004	BA	1	40.6	(38.8, 42.4)	0.365	(0.353, 0.378)
1004	CA	3	-822.	(-824., -819.)	0.275	(0.275, 0.275)
1115	A1A2	1	0.149	(0.143, 0.155)	0.392	(0.382, 0.401)
1115	A1B	2	11.7	(10.5, 12.9)	0.520	(0.480, 0.564)
1115	CB	3	-25.0	(-26.6, -23.4)	0.509	(0.503, 0.513)
1115	CA2	4	-13.3	(-14.3, -12.3)	0.927	(0.924, 0.931)
1608	AC	1	-4.50	(-6.00, -3.00)	0.258	(0.258, 0.258)
1608	BC	2	-36.0	(-37.5, -34.5)	0.574	(0.560, 0.584)
1608	AD	3	45.5	(44.0, 47.0)	0.930	(0.930, 0.930)
1608	BD	4	77.0	(76.0, 79.0)	—	(—, —)
0911	DC	3	-154.	(-170., -138.)	0.998	(0.998, 0.998)
0911	DA	4	-143.	(-149., -137.)	0.997	(0.997, 0.997)
1131	BA	1	-12.0	(-13.3, -10.5)	0	(0, 0)
1131	CA	2	-9.60	(-11.2, -7.60)	0	(0, 0)
1131	BD	3	99.0	(91.0, 107.)	0.626	(0.583, 0.669)
1131	CD	4	96.6	(88.6, 105.)	0.575	(0.535, 0.618)
1422	AB	1	-1.50	(-2.90, -0.100)	0	(0, 0.425)
1422	CB	2	-8.20	(-10.2, -6.20)	0	(0, 0)
0435	CB	1	5.90	(5.10, 6.70)	0.483	(0.470, 0.499)
0435	AB	2	8.00	(7.30, 8.80)	0.505	(0.491, 0.525)
0435	CD	3	-12.3	(-13.1, -11.5)	0.435	(0.427, 0.442)
0435	AD	4	-14.4	(-15.2, -13.5)	0.432	(0.424, 0.441)

Note. — Column 1 gives abridged lens names (see Table 4.1 for the corresponding full names). Image pairs contain one minimum and one saddle. The labels in column 2 list the minimum image first. We rank image pairs according to their separation in column 3, with smaller numbers corresponding to smaller separations. Columns 4 and 5 list the observed time delays, as well as the minimum and maximum values allowed by the measurement uncertainties. The time-delay data given here can be found in Table 1 of Oguri (2007), except for the lens 1004, where we use the data of Fohlmeister et al. (2007a). (However, note the incorrect temporal ordering for images A and B given in Fohlmeister et al. 2007a.) Columns 6 and 7 give P-values for the time delays shown in columns 4 and 5, using the galaxy sample of Bender et al. (1989).

Table 4.3. P-values for time-delay ratios

Lens Name	Image Pair	Rank	observed $\Delta t_1/\Delta t_2$	error interval	P-value for $\Delta t_1/\Delta t_2$	P-values for err. interval
1004	AC	3	20.2	(19.3, 21.2)	0.0243	(0.0159, 0.0354)
1115	A1A2	1	0.0127	(0.0109, 0.0146)	0.122	(0.0640, 0.198)
1115	A1B	2	78.5	(67.3, 89.7)	0.830	(0.734, 0.892)
1115	CB	3	2.14	(1.78, 2.49)	0.527	(0.295, 0.674)
1115	CA2	4	89.3	(79.0, 99.6)	0.324	(0.233, 0.409)
1608	AC	1	0.125	(0.0781, 0.172)	0.537	(0.131, 0.701)
1608	BC	2	8.00	(5.00, 11.0)	0.518	(0.150, 0.755)
1608	AD	3	10.1	(6.41, 13.8)	0.766	(0.296, 0.907)
1608	BD	4	2.14	(2.02, 2.28)	—	(—, —)
1131	BA	1	1.25	(0.854, 1.61)	0.948	(0.502, 0.988)
1131	CA	2	0.800	(0.567, 1.05)	0.0515	(0.00652, 0.321)
1131	BD	3	8.25	(6.55, 9.81)	0.000673	(0.000158, 0.00336)
1131	CD	4	10.1	(7.13, 12.6)	0.00977	(0.000470, 0.0573)
1422	AB	1	0.183	(−0.0324, 0.398)	0.112	(0, 0.962)
1422	CB	2	5.47	(−0.969, 11.9)	0.888	(0, 0.999)
0435	CB	1	0.738	(0.564, 0.902)	0.214	(0.0317, 0.528)
0435	AB	2	1.36	(1.05, 1.68)	0.786	(0.383, 0.950)
0435	CD	3	2.08	(1.67, 2.50)	0.535	(0.226, 0.751)
0435	AD	4	1.80	(1.52, 2.07)	0.403	(0.183, 0.593)

Note. — Columns 1-3 have the same meaning as in Table 4.2. Columns 4 and 5 list time-delay ratios and corresponding error intervals constructed from observed time delays. Columns 6 and 7 give P-values for the time-delay ratios shown in columns 4 and 5, using the galaxy sample of Bender et al. (1989).

Table 4.4. Median values and confidence intervals for scaled time delays

Lens Name	Image Pair	d_1 (arcsec)	Median Δt_1	95% conf. interval	99% conf. interval
0128	AB	0.14	0.000415	(−0.000912, 0.00148)	(−0.00110, 0.00185)
0128	AD	0.27	0.00379	(−0.00609, 0.0123)	(−0.00734, 0.0150)
0128	CD	0.42	−0.0361	(−0.0478, 0.0871)	(−0.0498, 0.0905)
0128	CB	0.5	−0.0571	(−0.0686, −0.0455)	(−0.0711, −0.0412)
0230	AB	0.74	0.0482	(−0.0575, 0.0634)	(−0.0634, 0.0702)
0230	CD	1.46	0.401	(−0.522, 0.557)	(−0.556, 0.601)
0230	AD	1.64	−0.348	(−0.514, 1.28)	(−0.559, 1.35)
0230	CB	1.65	−0.360	(−0.523, 1.29)	(−0.569, 1.36)
0414	A1A2	0.41	0.00226	(−0.00469, 0.00890)	(−0.00584, 0.0110)
0414	BA2	1.71	0.215	(−0.222, 0.688)	(−0.256, 0.885)
0414	A1C	1.96	0.531	(−0.386, 1.68)	(−0.460, 1.92)
0414	BC	2.13	0.676	(−1.17, 1.84)	(−1.29, 2.15)
0712	AB	0.17	0.000206	(−0.000528, 0.000909)	(−0.000672, 0.00137)
0712	CB	0.91	0.0321	(−0.0428, 0.108)	(−0.0488, 0.138)
0712	CD	1.18	0.0856	(−0.240, 0.388)	(−0.266, 0.470)
0712	AD	1.25	0.218	(−0.154, 0.748)	(−0.181, 0.807)
0924	AD	0.69	0.0135	(−0.0323, 0.0482)	(−0.0385, 0.0587)
0924	AC	1.18	0.0645	(−0.118, 0.210)	(−0.141, 0.255)
0924	BD	1.46	0.136	(−0.201, 0.410)	(−0.239, 0.492)
0924	BC	1.53	0.124	(−0.397, 0.636)	(−0.438, 0.770)
1004	AB	3.73	0.396	(−0.635, 1.03)	(−0.780, 1.20)
1004	DB	11.44	12.7	(−12.4, 37.8)	(−14.7, 49.4)
1004	AC	11.84	16.2	(−14.2, 47.8)	(−16.9, 59.0)
1004	DC	14.38	58.7	(−62.7, 103.)	(−69.1, 107.)
1115	A1A2	0.48	0.00439	(−0.00826, 0.0145)	(−0.0101, 0.0177)
1115	A1B	1.67	0.239	(−0.239, 0.731)	(−0.282, 0.970)

Table 4.4 (cont'd)

Lens Name	Image Pair	d_1 (arcsec)	Median Δt_1	95% conf. interval	99% conf. interval
1115	CB	1.99	-0.581	(-1.05, 1.50)	(-1.21, 1.76)
1115	CA2	2.16	-0.547	(-0.756, 1.94)	(-0.841, 2.15)
1555	AB	0.09	0.0000952	(-0.000193, 0.000377)	(-0.000245, 0.000494)
1555	CB	0.35	0.00687	(-0.00807, 0.0216)	(-0.00928, 0.0268)
1555	AD	0.4	0.0177	(-0.0139, 0.0531)	(-0.0165, 0.0673)
1555	CD	0.42	-0.0145	(-0.0341, 0.0500)	(-0.0370, 0.0601)
1608	AC	0.87	0.0797	(-0.0977, 0.111)	(-0.110, 0.122)
1608	BC	1.51	-0.296	(-0.456, 1.11)	(-0.498, 1.18)
1608	AD	1.69	-0.596	(-0.714, 1.19)	(-0.745, 1.30)
1608	BD	2	0.593	—	—
1933	4.3	0.46	0.00558	(-0.0137, 0.0197)	(-0.0169, 0.0238)
1933	4.6	0.63	0.0164	(-0.0338, 0.0558)	(-0.0412, 0.0675)
1933	1.3	0.9	0.0566	(-0.127, 0.349)	(-0.142, 0.404)
1933	1.6	0.91	-0.0870	(-0.157, 0.319)	(-0.171, 0.393)
2026	A1A2	0.33	0.00151	(-0.00347, 0.00594)	(-0.00415, 0.00764)
2026	A1C	0.83	0.0235	(-0.0396, 0.0850)	(-0.0454, 0.102)
2026	BC	1.19	-0.111	(-0.248, 0.477)	(-0.272, 0.601)
2026	BA2	1.28	-0.131	(-0.231, 0.759)	(-0.258, 0.805)
2033	A1A2	0.72	0.0112	(-0.0249, 0.0399)	(-0.0303, 0.0503)
2033	A1C	1.54	0.131	(-0.197, 0.412)	(-0.235, 0.497)
2033	BA2	2.01	-0.176	(-0.572, 1.90)	(-0.640, 2.04)
2033	BC	2.13	0.955	(-1.09, 2.20)	(-1.17, 2.33)
0911	BA	0.48	0.00160	(-0.00461, 0.00799)	(-0.00533, 0.0112)
0911	BC	0.62	0.00322	(-0.00877, 0.0160)	(-0.0102, 0.0222)
0911	DC	2.96	-2.43	(-2.60, -2.14)	(-2.62, -2.02)
0911	DA	3.08	-2.65	(-2.81, -2.31)	(-2.82, -2.23)

Table 4.4 (cont'd)

Lens Name	Image Pair	d_1 (arcsec)	Median Δt_1	95% conf. interval	99% conf. interval
1131	BA	1.19	0.0152	(−0.0387, 0.0666)	(−0.0471, 0.0864)
1131	CA	1.26	0.0184	(−0.0445, 0.0826)	(−0.0512, 0.102)
1131	BD	3.14	1.16	(−1.09, 3.36)	(−1.29, 4.16)
1131	CD	3.18	1.26	(−1.17, 3.64)	(−1.39, 4.46)
1422	AB	0.5	0.00403	(−0.00948, 0.0151)	(−0.0111, 0.0184)
1422	CB	0.82	0.0168	(−0.0346, 0.0640)	(−0.0399, 0.0785)
1422	AD	1.25	0.148	(−0.160, 0.438)	(−0.194, 0.573)
1422	CD	1.29	0.150	(−0.233, 0.448)	(−0.266, 0.559)
2045	AB	0.28	0.000209	(−0.000669, 0.00156)	(−0.000875, 0.00252)
2045	CB	0.56	0.00172	(−0.00351, 0.0100)	(−0.00431, 0.0131)
2045	AD	1.91	0.385	(−0.282, 1.21)	(−0.334, 1.55)
2045	CD	1.93	0.417	(−0.358, 1.24)	(−0.427, 1.56)
0435	CB	1.53	0.0897	(−0.257, 0.330)	(−0.301, 0.390)
0435	AB	1.59	0.104	(−0.285, 0.373)	(−0.334, 0.443)
0435	CD	1.85	0.177	(−0.481, 0.666)	(−0.550, 0.791)
0435	AD	1.88	0.177	(−0.513, 0.702)	(−0.591, 0.829)
12531	BC	0.77	0.0249	(−0.0759, 0.0923)	(−0.0867, 0.108)
12531	AC	0.78	0.0243	(−0.0796, 0.0984)	(−0.0913, 0.116)
12531	BD	0.91	0.0454	(−0.128, 0.177)	(−0.144, 0.210)
12531	AD	1.02	−0.120	(−0.208, 0.350)	(−0.223, 0.441)
14113	CD	1.13	0.138	(−0.194, 0.227)	(−0.210, 0.250)
14113	CB	1.38	0.113	(−0.291, 0.421)	(−0.330, 0.500)
14113	AD	1.41	0.130	(−0.314, 0.476)	(−0.356, 0.568)
14113	AB	1.42	−0.171	(−0.423, 0.491)	(−0.474, 0.560)
1413	AB	0.76	0.0452	(−0.0829, 0.0992)	(−0.0913, 0.109)
1413	AC	0.87	0.0343	(−0.105, 0.138)	(−0.120, 0.165)

Table 4.4 (cont'd)

Lens Name	Image Pair	d_1 (arcsec)	Median Δt_1	95% conf. interval	99% conf. interval
1413	DC	0.91	0.0373	(−0.143, 0.176)	(−0.155, 0.198)
1413	DB	0.96	0.0606	(−0.146, 0.223)	(−0.166, 0.267)
14176	CB	1.73	0.260	(−0.427, 0.506)	(−0.470, 0.563)
14176	AB	2.09	0.233	(−0.631, 0.878)	(−0.721, 1.04)
14176	CD	2.13	0.256	(−0.663, 0.944)	(−0.757, 1.10)
14176	AD	2.13	0.277	(−0.824, 1.00)	(−0.891, 1.11)
2237	AD	1.01	0.0360	(−0.102, 0.129)	(−0.120, 0.154)
2237	BD	1.18	0.0625	(−0.158, 0.219)	(−0.184, 0.260)
2237	AC	1.37	0.120	(−0.255, 0.396)	(−0.293, 0.470)
2237	BC	1.4	0.102	(−0.297, 0.406)	(−0.335, 0.482)

Note. — The first column gives the abbreviated lens name (the full names appear in the first column of Table 4.1). The next two columns list the image pair label and the separation between the images in arcseconds. The last three columns present data computed from our numerical simulations, using the galaxy sample of Bender et al. (1989). The fourth column gives the median value of the differential time delay, and the fifth and sixth columns give the 95% and 99% confidence intervals of this same quantity.

Table 4.5. Median values and confidence intervals for time-delay ratios

Lens Name	Image Pair	d_1 (arcsec)	Median $\Delta t_1/\Delta t_2$	95% conf. interval	99% conf. interval
0128	AB	0.14	0.121	(0.0667, 0.215)	(0.0533, 0.290)
0128	AD	0.27	8.26	(4.65, 15.0)	(3.44, 18.6)
0128	CD	0.42	4.85	(2.60, 10.5)	(2.24, 12.0)
0128	CB	0.5	41.7	(27.1, 101.)	(25.2, 160.)
0230	AB	0.74	0.0508	(0.0332, 0.142)	(0.0312, 0.161)
0230	CD	1.46	0.760	(0.458, 1.21)	(0.404, 1.38)
0230	AD	1.64	15.8	(7.56, 37.6)	(6.51, 57.0)
0230	CB	1.65	15.9	(7.62, 37.5)	(6.59, 56.5)
0414	A1A2	0.41	0.0129	(0.00530, 0.0275)	(0.00375, 0.0337)
0414	BA2	1.71	77.4	(36.3, 191.)	(29.7, 291.)
0414	A1C	1.96	194.	(63.1, 890.)	(53.0, 1490)
0414	BC	2.13	2.41	(1.45, 6.41)	(1.24, 8.53)
0712	AB	0.17	0.00795	(0.00319, 0.0174)	(0.00242, 0.0254)
0712	CB	0.91	126.	(57.5, 313.)	(39.4, 407.)
0712	CD	1.18	3.07	(1.69, 9.18)	(1.43, 12.6)
0712	AD	1.25	702.	(196., 3620)	(159., 6260)
0924	AD	0.69	0.232	(0.135, 0.393)	(0.112, 0.512)
0924	AC	1.18	4.31	(2.54, 7.39)	(1.95, 8.89)
0924	BD	1.46	7.60	(4.23, 15.8)	(3.47, 20.8)
0924	BC	1.53	2.99	(1.65, 8.88)	(1.41, 12.3)
1004	AB	3.73	0.0301	(0.0130, 0.0598)	(0.00983, 0.0713)
1004	DB	11.44	38.1	(18.0, 107.)	(15.2, 181.)
1004	AC	11.84	48.2	(20.3, 172.)	(17.2, 315.)
1004	DC	14.38	2.74	(1.49, 6.33)	(1.27, 7.22)
1115	A1A2	0.48	0.0213	(0.00910, 0.0431)	(0.00697, 0.0513)
1115	A1B	1.67	49.7	(23.8, 129.)	(20.0, 206.)

Table 4.5 (cont'd)

Lens Name	Image Pair	d_1 (arcsec)	Median $\Delta t_1/\Delta t_2$	95% conf. interval	99% conf. interval
1115	CB	1.99	2.09	(1.30, 5.80)	(1.09, 8.17)
1115	CA2	2.16	112.	(51.3, 327.)	(44.4, 505.)
1555	AB	0.09	0.0163	(0.00745, 0.0336)	(0.00556, 0.0441)
1555	CB	0.35	61.4	(29.7, 134.)	(22.7, 178.)
1555	AD	0.4	136.	(54.2, 487.)	(45.9, 901.)
1555	CD	0.42	2.44	(1.44, 6.70)	(1.24, 9.05)
1608	AC	0.87	0.120	(0.0651, 0.282)	(0.0603, 0.332)
1608	BC	1.51	7.82	(3.85, 18.9)	(3.33, 27.9)
1608	AD	1.69	7.44	(4.78, 19.0)	(4.22, 25.0)
1608	BD	2	2.21	—	—
1933	4.3	0.46	0.364	(0.220, 0.595)	(0.178, 0.776)
1933	4.6	0.63	2.75	(1.68, 4.54)	(1.29, 5.60)
1933	1.3	0.9	11.9	(5.72, 43.8)	(4.90, 60.2)
1933	1.6	0.91	4.20	(2.28, 12.5)	(1.92, 17.6)
2026	A1A2	0.33	0.0698	(0.0376, 0.135)	(0.0298, 0.212)
2026	A1C	0.83	14.3	(7.40, 26.6)	(4.71, 33.2)
2026	BC	1.19	4.30	(2.30, 13.3)	(1.94, 17.9)
2026	BA2	1.28	78.4	(35.9, 292.)	(30.8, 486.)
2033	A1A2	0.72	0.0985	(0.0515, 0.177)	(0.0405, 0.230)
2033	A1C	1.54	10.2	(5.64, 19.4)	(4.34, 24.7)
2033	BA2	2.01	32.9	(14.9, 128.)	(12.8, 192.)
2033	BC	2.13	3.66	(1.95, 8.62)	(1.67, 10.4)
0911	BA	0.48	0.502	(0.302, 0.827)	(0.221, 1.12)
0911	BC	0.62	1.99	(1.20, 3.30)	(0.850, 4.37)
0911	DC	2.96	118.	(73.6, 292.)	(55.1, 551.)
0911	DA	3.08	292.	(156., 741.)	(126., 912.)

Table 4.5 (cont'd)

Lens Name	Image Pair	d_1 (arcsec)	Median $\Delta t_1/\Delta t_2$	95% conf. interval	99% conf. interval
1131	BA	1.19	0.852	(0.511, 1.40)	(0.357, 1.83)
1131	CA	1.26	1.17	(0.712, 1.96)	(0.546, 2.79)
1131	BD	3.14	29.0	(12.5, 105.)	(10.3, 172.)
1131	CD	3.18	26.6	(11.2, 98.8)	(9.43, 156.)
1422	AB	0.5	0.247	(0.148, 0.432)	(0.118, 0.669)
1422	CB	0.82	4.05	(2.31, 6.76)	(1.46, 8.40)
1422	AD	1.25	20.5	(10.1, 54.5)	(8.37, 94.5)
1422	CD	1.29	5.43	(2.85, 15.6)	(2.40, 25.4)
2045	AB	0.28	0.153	(0.0668, 0.324)	(0.0502, 0.391)
2045	CB	0.56	6.47	(3.04, 14.9)	(2.44, 19.7)
2045	AD	1.91	411.	(143., 1650)	(116., 3150)
2045	CD	1.93	60.4	(24.9, 207.)	(21.2, 371.)
0435	CB	1.53	0.888	(0.548, 1.43)	(0.450, 1.78)
0435	AB	1.59	1.13	(0.700, 1.83)	(0.563, 2.24)
0435	CD	1.85	2.03	(1.23, 3.77)	(1.02, 4.66)
0435	AD	1.88	1.93	(1.18, 3.65)	(0.999, 4.64)
12531	BC	0.77	0.962	(0.612, 1.52)	(0.509, 1.86)
12531	AC	0.78	1.10	(0.704, 1.78)	(0.586, 2.16)
12531	BD	0.91	2.04	(1.25, 4.49)	(1.06, 6.34)
12531	AD	1.02	2.95	(1.69, 8.21)	(1.44, 11.5)
14113	CD	1.13	0.563	(0.307, 0.950)	(0.236, 1.20)
14113	CB	1.38	2.30	(1.37, 5.29)	(1.16, 7.57)
14113	AD	1.41	2.59	(1.49, 6.87)	(1.26, 10.3)
14113	AB	1.42	1.61	(0.832, 4.00)	(0.690, 5.35)
1413	AB	0.76	0.730	(0.421, 1.14)	(0.338, 1.44)
1413	AC	0.87	1.63	(1.02, 2.87)	(0.870, 3.55)

Table 4.5 (cont'd)

Lens Name	Image Pair	d_1 (arcsec)	Median $\Delta t_1/\Delta t_2$	95% conf. interval	99% conf. interval
1413	DC	0.91	1.50	(0.851, 2.73)	(0.705, 3.61)
1413	DB	0.96	2.62	(1.50, 7.23)	(1.27, 10.8)
14176	CB	1.73	0.590	(0.325, 0.967)	(0.252, 1.18)
14176	AB	2.09	2.06	(1.24, 3.89)	(1.02, 4.86)
14176	CD	2.13	2.21	(1.32, 4.36)	(1.10, 5.66)
14176	AD	2.13	1.31	(0.740, 2.49)	(0.609, 3.28)
2237	AD	1.01	0.596	(0.361, 0.961)	(0.299, 1.16)
2237	BD	1.18	1.68	(1.04, 2.78)	(0.859, 3.38)
2237	AC	1.37	2.98	(1.75, 6.13)	(1.47, 8.03)
2237	BC	1.4	1.99	(1.23, 4.16)	(1.04, 5.73)

Note. — The first three columns are the same as those in Table 4.4. The last three columns present data computed from our numerical simulations, using the galaxy sample of Bender et al. (1989). The fourth column gives the median value of the time-delay ratio $\Delta t_1/\Delta t_2$. The subscripts on Δt refer to the time delay of the labeled image pair (Δt_1) and that for the closest neighboring pair (Δt_2). The fifth and sixth columns give the 95% and 99% confidence intervals of the time-delay ratio.

Bibliography

- Bender R., Surma P., Döbereiner S., Möllenhoff C., Madejsky R., 1989, *A&A*, 217, 35
- Chartas G., Dai X., Gallagher S. C., Garmire G. P., Bautz M. W., Schechter P. L., Morgan N. D., 2001, *ApJ*, 558, 119
- Dalal N., Kochanek C. S., 2002, *ApJ*, 572, 25
- Fohlmeister J., Kochanek C. S., Falco E. E., Morgan C. W., Wambsganss J., 2007a, *ArXiv e-prints*, 710
- Fohlmeister J., Kochanek C. S., Falco E. E., Wambsganss J., Morgan N., Morgan C. W., Ofek E. O., Maoz D., Keeton C. R., Barentine J. C., Dalton G., Dembicky J., Ketzeback W., McMillan R., Peters C. S., 2007b, *ApJ*, 662, 62
- Holder G. P., Schechter P. L., 2003, *ApJ*, 589, 688

- Inada N., Oguri M., Keeton C. R., Eisenstein D. J., Castander F. J., Chiu K., Hall P. B., Hennawi J. F., Johnston D. E., Pindor B., Richards G. T., Rix H.-W. R., Schneider D. P., Zheng W., 2005, PASJ, 57, L7
- Jørgensen I., Franx M., Kjaergaard P., 1995, MNRAS, 273, 1097
- Keeton C. R., 2001, astro-ph/0102340
- Keeton C. R., Gaudi B. S., Petters A. O., 2003, ApJ, 598, 138
- , 2005, ApJ, 635, 35
- Keeton C. R., Moustakas L. A., 2008, ApJ, submitted
- Klypin A., Kravtsov A. V., Valenzuela O., Prada F., 1999, ApJ, 522, 82
- Mao S., Schneider P., 1998, MNRAS, 295, 587
- Moore B., Ghigna S., Governato F., Lake G., Quinn T., Stadel J., Tozzi P., 1999, ApJ, 524, L19
- Oguri M., 2007, ApJ, 660, 1
- Saglia R. P., Bender R., Dressler A., 1993, A&A, 279, 75

Chapter 5

Microensing of an Extended Source by a Power-Law Mass Distribution

Abstract

Microensing promises to be a powerful tool for studying distant galaxies and quasars. As the data and models improve, there are systematic effects that need to be explored. Quasar continuum and broad-line regions may respond differently to microensing due to their different sizes. To understand this effect, we study microensing of finite sources by a mass function of stars. We find that microensing is insensitive to the slope of the mass function, but does depend on the mass range. For negative-parity images, diluting the stellar population with dark matter increases the magnification dispersion for small sources and decreases it for large sources. This implies that the quasar continuum and broad-line regions may experience very different microensing in negative-parity lensed images. We confirm earlier conclusions that the surface brightness profile and geometry of the source have little effect on microensing. Finally, we consider non-circular sources. We show that elliptical sources that are aligned with the direction of shear have larger magnification dispersions than sources with perpendicular alignment, an effect that becomes more prominent as the ellipticity increases. Elongated sources can lead to more rapid variability than circular sources, which raises the prospect of using microensing to probe source shape.

5.1 Introduction

Microensing is an increasingly important tool for studying small-scale structure in lens galaxies and source quasars. In recent years, microensing has been observed in a

number of multiply-imaged quasars (e.g., Woźniak et al. 2000; Schechter et al. 2003; Richards et al. 2004; Keeton et al. 2006; Paraficz et al. 2006). Microlensing modeling has also been improving. For example, Kochanek (2004) has introduced a sophisticated technique for analyzing light curves. Even so, there are aspects of the models for the lens and source that still need to be considered for microlensing to reach its full potential. This is especially important for quasar microlensing, where several length scales are involved.

Different regions of a quasar emit radiation in roughly distinct bands. For example, continuum (blackbody) radiation in the optical and x-ray bands is emitted from the accretion disk surrounding the supermassive black hole, while broad emission lines in the optical and UV are thought to originate from clouds in a region outside of and larger than the accretion disk. Radio emission comes from even larger structures. Roughly speaking, a source can only be affected by objects in the lens galaxy whose Einstein radii are comparable to or larger than the source size. Consequently, the continuum, broad-line and radio regions probe different structures in the lens galaxy. Radio jets can be used to probe dark matter substructure (Metcalf & Madau 2001; Dalal & Kochanek 2002) in lens galaxies, while the accretion disk (Jaroszyński et al. 1992; Mortonson et al. 2005; Pooley et al. 2007) and broad-line region (BLR) are used for studying the stellar component (Schneider & Wambsganss 1990; Richards et al. 2004; Keeton et al. 2006). In principle, both methods can also be used to examine the light source. This is of particular interest for the BLR, whose properties are not well understood (e.g., Peterson & Horne 2005). In this chapter, we investigate the potential of microlensing to deepen our knowledge of the BLR and accretion disk, and to determine both the abundance and mass function of stars in lens galaxies.

Until recently, sources relevant for microlensing could not be resolved. Therefore, many theoretical models have assumed a point source, and have focused on determining properties of the lensing galaxy. Such investigations have found that microlensing magnification distributions are not very sensitive to the shape of the microlens mass function if it spans an order of magnitude or so in mass (e.g., Wyithe & Turner 2001).

The magnification distributions do look different if there are two distinct mass components: not just stars, but also dark matter that could come in the form of a smooth mass component (e.g., Schechter & Wambsganss 2002) or a set of discrete objects that are much less massive than the stars (Schechter et al. 2004; Lewis & Gil-Merino 2006). We generalize the previous studies by considering microlensing of an extended source. The source size, R_S , introduces a new length scale, which heuristically divides the microlenses into two categories: microlenses with $R_E \gtrsim R_S$ are massive enough to be felt individually, while those with $R_E \lesssim R_S$ act collectively as a smooth component. We therefore conjecture that the finite source size makes the magnification distributions sensitive to the microlens mass function, even when it spans just 1–1.5 orders of magnitude. Lewis & Gil-Merino (2006) recently studied microlensing of an extended source by a bimodal mass function. We now consider a continuous mass function.

Studying microlensing of an extended source is especially relevant for the BLR, because recent observations suggest it has a size of $R_{BLR} \sim 10^{16}\text{--}10^{18}$ cm (Richards et al. 2004; Keeton et al. 2006), which is comparable to stellar Einstein radii. Understanding the effects of source size should help us probe BLR length scales more precisely. In principle, microlensing can also be used to probe the shape, geometry and surface brightness profile of the source, although we note that Mortonson et al. (2005) found that microlensing for a circular source is not very sensitive to the surface brightness profile.

The possibility of a non-circular source has not been considered in previous microlensing analyses. However, accretion disks viewed at random inclinations would generically appear elliptical rather than circular. A similar situation may apply to the BLR if it has a disk structure (e.g., Murray & Chiang 1998; Elvis 2000; Richards et al. 2004). We also consider annular accretion disks. Such models are important for two reasons. First, quasar accretion disks have inner radii defined by the innermost stable circular orbit of a particle in motion around the central black hole. Second, typical models (e.g., the Shakura-Sunyaev disk), emit over a wide range of wavelengths, with each band corresponding to a different annular region.

This chapter is organized as follows. Lens modeling and simulations are discussed

in Section 5.2. Our results are presented in Section 5.3. We first consider the general problem of how source size and lens mass impact microlensing (§5.3.1). In following subsections, we investigate the effects of dark matter (§5.3.2), source profile (§5.3.3), source ellipticity and position angle (§5.3.4) and accretion disk geometry (§5.3.5). We construct light curves in Section 5.3.6 to investigate variability timescales. Our conclusions are summarized in Section 5.4.

5.2 Methods

We consider microlensing of an extended source by a distribution of stars and dark matter. We zoom in on a region in the lens galaxy around a lensed image. The size of the region is chosen to satisfy two conditions. First, it must be large compared to a typical stellar Einstein radius, which is the relevant scale for microlensing. Second, it must be small compared to the scale of the lens galaxy, namely the image separation. The latter allows us to take the mean densities of stars and dark matter to be constant. These criteria are not very restrictive, since stellar Einstein radii are typically on scales of microarcseconds, while image separations are on scales of arcseconds.

We describe the stellar population of the lens by a mass function, dN/dm , which gives the number of stars per unit mass between m and $m + dm$. We use a power law of the form

$$\frac{dN}{dm} \propto m^{-\alpha} \quad (m_1 \leq m \leq m_2), \quad (5.1)$$

for some m_1 and m_2 . Rather than specifying the mass limits explicitly, we adopt the equivalent approach of giving the mass ratio m_1/m_2 along with the mean mass, \bar{m} . A typical choice for the power law index is $\alpha = 2.35$, the Salpeter initial mass function. The mass function is normalized so that the scaled mass density of stars is κ_* . In addition to stars, the galaxy may include a continuous component with density κ_c . The total scaled density is then $\kappa \equiv \kappa_* + \kappa_c$. The final ingredient is the shear, γ , which accounts for tidal forces from outside the patch of stars being considered. To obtain a relation between κ and γ , we must choose a mass model for the lens galaxy. We use a singular isothermal ellipsoid, for which $\kappa = \gamma$. This model is simple and provides a

reasonable fit to observed systems (e.g., Treu & Koopmans 2004; Rusin & Kochanek 2005; Treu et al. 2006).

In the absence of microlensing, the magnification of a lensed image is given by

$$\mu_0 = [(1 - \kappa)^2 - \gamma^2]^{-1}. \quad (5.2)$$

We consider a typical bright image with $\mu_0 = \pm 10$, corresponding to $\kappa = \gamma = 0.5 \mp 0.05$. In microlensing, the spatial distribution of stars is random, so the magnification at a given time will be drawn from a probability distribution. If the distribution is broad, chances are high that the magnification will differ from that predicted for a smooth model, viz., μ_0 . The effects of microlensing are therefore naturally described by the dispersion (standard deviation) of the probability distribution.

Computing the magnification distribution for given κ , γ and dN/dm can only be done numerically. We use the microlensing code of Wambsganss (1999), which gives the magnification of a point source¹ as a function of position over a square region of the source plane with side length $L = 15R_E(M_\odot)$. In units of the mean stellar mass, the side-length is given by $L = 15R_E(\bar{m})$ for $m_1/m_2 = 1$, $L = 31.71R_E(\bar{m})$ for $m_1/m_2 = 0.1$ and $L = 52.26R_E(\bar{m})$ for $m_1/m_2 = 0.03$. We create magnification maps with a resolution of $L/1024$ (see Fig. 5.1). To obtain a statistical sample, we perform 100 realizations for each set of parameters we consider.

We must convolve the magnification map with a surface brightness profile in order to compute the magnification of an extended source. We use Gaussian, uniform and linear profiles, respectively defined by

$$I_1(R) \equiv \frac{\ln 2}{\pi R_S^2} \exp\left(-\frac{R^2 \ln 2}{R_S^2}\right) \quad (0 \leq R < \infty), \quad (5.3)$$

$$I_2(R) \equiv \frac{1}{2\pi R_S^2} \quad (0 \leq R \leq \sqrt{2}R_S) \quad (5.4)$$

and

$$I_3(R) \equiv \frac{3}{4\pi R_S^2} \left(1 - \frac{R}{2R_S}\right) \quad (0 \leq R \leq 2R_S), \quad (5.5)$$

¹Strictly speaking, the map gives the magnification of a source with the shape of the pixel. In practice, the source sizes that interest us are much larger than the pixels.

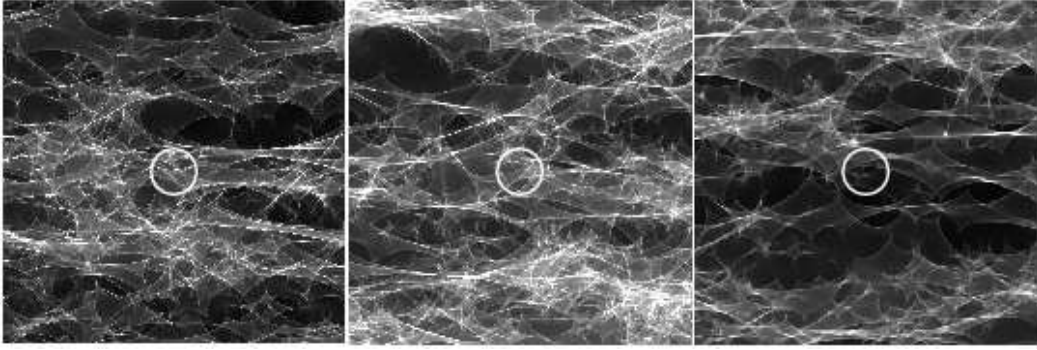


Figure 5.1 Magnification maps for a positive-parity image with $\kappa = \gamma = 0.45$, implying a macro-magnification of $\mu_0 = 10$. The gray scale indicates the magnification with values in the range $\mu = 1$ (black) and $\mu = 30$ (white). Panels show Salpeter mass functions with $m_1/m_2 = 1$ (left), 0.1 (middle) and 0.03 (right). Each map has a side-length of $L = 15R_E(\bar{m})$. Magnification histograms are generated by convolving the surface brightness profile of the source (indicated by circles) with the magnification map.

where R_S is the half-light radius of the source, and the sources are normalized to unit flux. In microlensing, the natural length scale is the Einstein radius of the mean stellar mass (e.g., Lewis & Irwin 1996). We henceforth quote the source size as $r_S \equiv R_S/R_E(\bar{m})$.

These models are simple but nevertheless useful. The Gaussian model is popular in microlensing studies (e.g., Wambsganss et al. 1990; Wyithe et al. 2002), the uniform disk is the simplest model conceivable and the linear disk has at least one physical connection (see Abajas et al. 2002). These same three models were used by Mortonson et al. (2005), so we can compare their results with ours. While Mortonson et al. (2005) (and many others) applied the models to accretion disks, they may also be useful for describing BLRs as well. In particular, the linear disk is similar to the biconical BLR of Abajas et al. (2002).

We consider an elliptical source by making the substitution

$$I(R) \rightarrow I(\rho)/q, \quad (5.6)$$

where q is the minor-to-major axis ratio and the elliptical “radius” is defined by $\rho^2 \equiv R^2 \cos^2 \theta + R^2 \sin^2 \theta / q^2$. We also consider a uniform annular disk with inner-to-outer

radius ratio Q by making the replacement

$$I_2(R) \rightarrow I_2(R) \frac{1+Q^2}{1-Q^2}, \quad (5.7)$$

for radii satisfying

$$\frac{\sqrt{2}QR_S}{1+Q^2} \leq R \leq \frac{\sqrt{2}R_S}{1+Q^2}. \quad (5.8)$$

In the following section our fiducial model assumes a Gaussian source and a lens described by a stellar population whose masses are given by a Salpeter mass function with $m_1/m_2 = 0.1$. We assume that $\kappa = \kappa_* = 0.5 \mp 0.05$ for images of positive and negative parity, respectively. We explicitly state when other models are used.

5.3 Results

We now study microlensing of an extended source by a power-law mass distribution. Wyithe & Turner (2001) conclude that point-source microlensing magnification distributions are not significantly affected by the choice of mass function. We consider whether this result can be extended to the case of a finite source (§5.3.1). Dark matter can affect microlensing in surprising ways, raising the possibility of using microlensing to measure the density of dark matter at the image positions (Schechter & Wambsganss 2002, 2004). We generalize earlier work by including a mass function of stars and an extended source (§5.3.2).

We also explore how varying properties of the source impacts microlensing magnification distributions. In Section 5.3.3, we describe a source by three surface brightness profiles. We broaden the discussion in Section 5.3.4 to include elliptical sources. Such models lead to particularly interesting implications, so we construct light curves in Section 5.3.6 to examine the dependence of microlensing on source shape in more detail. Finally, we consider annular sources in Section 5.3.5.

5.3.1 Source Size and Lens Mass

We begin by examining how microlensing of a finite source is affected when we vary the mass range and logarithmic slope of the mass function (cf. Wambsganss 1992).

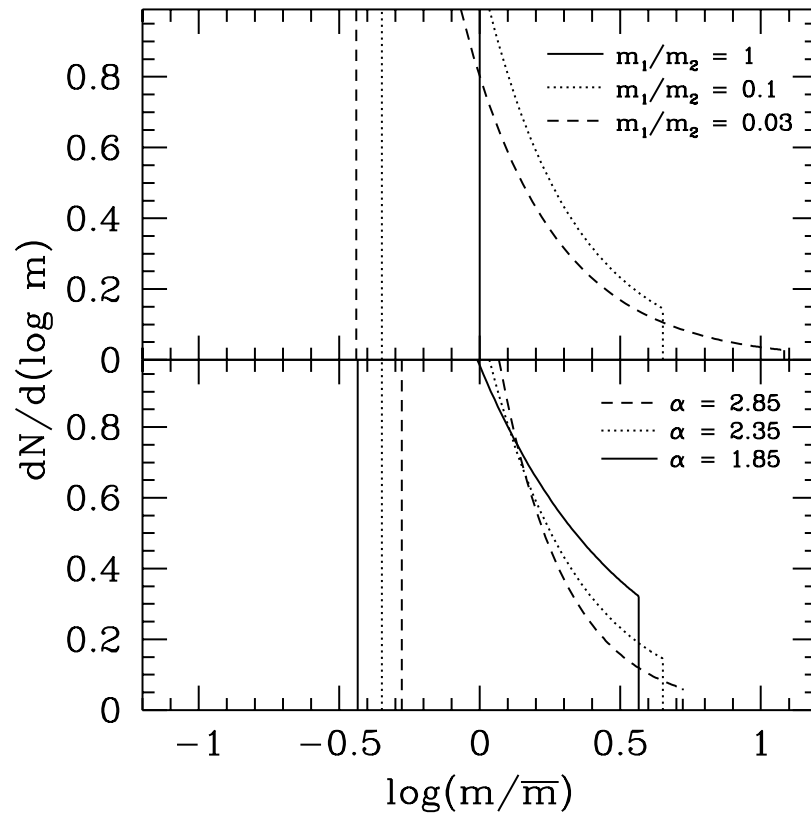


Figure 5.2 Mass functions with fixed means, \bar{m} , for various mass ranges, m_1/m_2 , and logarithmic slopes, α . The top panel shows mass functions with $\alpha = 2.35$. The solid, dotted and dashed curves have $m_1/m_2 = 1, 0.1$ and 0.03 , respectively. The bottom panel shows mass functions with $m_1/m_2 = 0.1$. The solid, dotted and dashed curves show $\alpha = 1.85, 2.35$ and 2.85 , respectively.

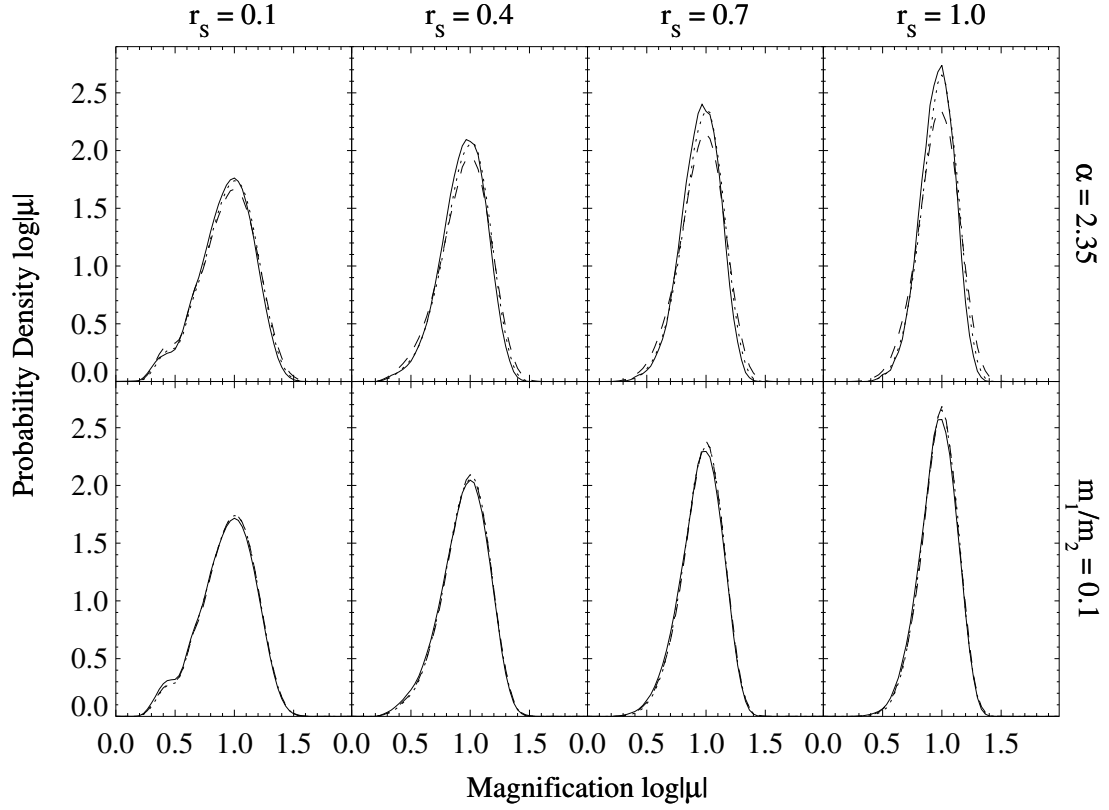


Figure 5.3 Magnification histograms for different source sizes and mass functions for a positive-parity image with $|\mu_0| = 10$. Columns show source sizes in mean-mass Einstein radii of $r_s = 0.1, 0.4, 0.7$ and 1.0 . The top row shows mass functions with logarithmic slopes of $\alpha = 2.35$. The solid, dotted and dashed curves have $m_1/m_2 = 1, 0.1$ and 0.03 , respectively (see Figure 5.2, top panel). The bottom row shows mass functions with $m_1/m_2 = 0.1$. The solid, dotted and dashed curves have $\alpha = 1.85, 2.35$ and 2.85 , respectively (see Figure 5.2, bottom panel).

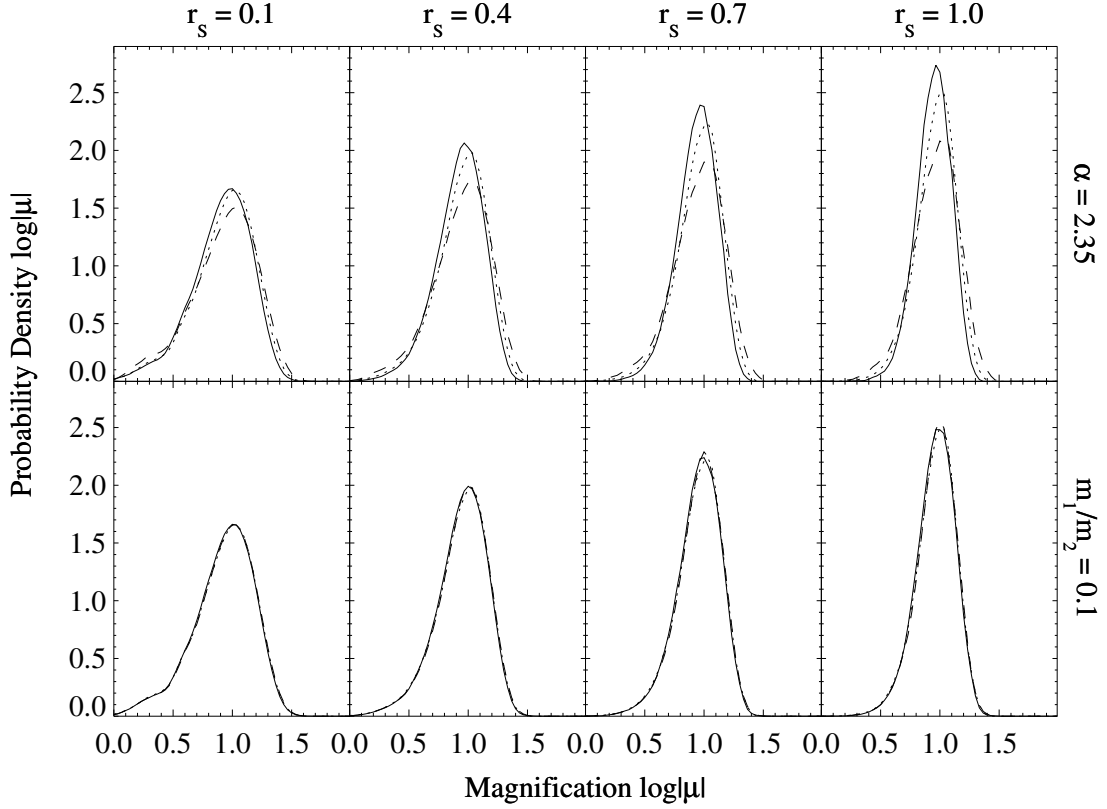


Figure 5.4 Same as Figure 5.3, but for a negative parity image with $|\mu_0| = 10$.

Figure 5.2 shows the mass functions we use. Figures 5.3 and 5.4 show magnification histograms for the different mass functions and different source sizes for positive and negative parity. First, we consider the effects of the mass range, shown in the top row of each figure. Increasing the mass range causes the magnification distribution to broaden, especially for larger sources. This is shown more directly in the top panel of Figure 5.5, which plots the magnification dispersion versus source size for the different mass ranges (for the positive-parity case). When the source is small, we recover the previous result that the mass range does not affect the magnification distribution (Wyithe & Turner 2001). However, as the source gets larger, there is a greater difference between the three mass functions.

To understand why the magnification dispersion *increases* as the mass range increases, we return to Figure 5.2. The top panel shows that increasing the mass range

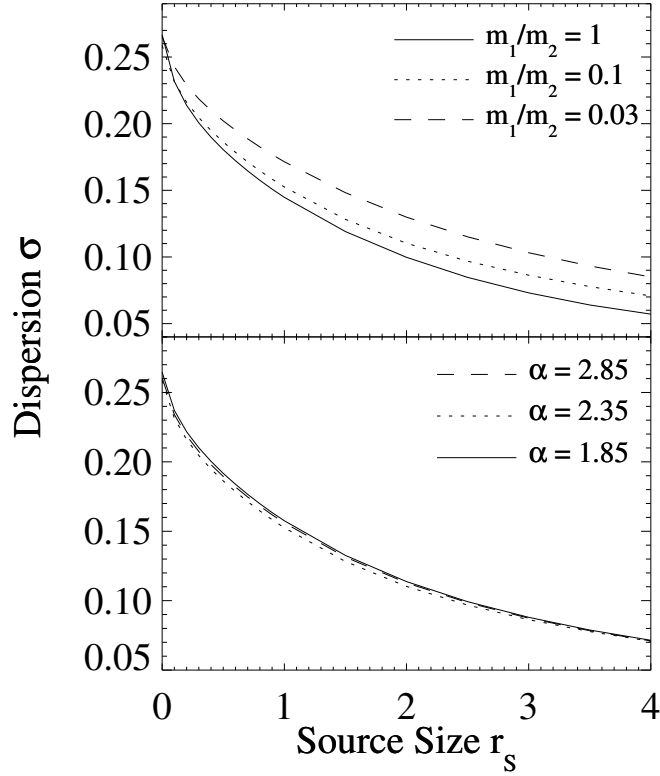


Figure 5.5 Dispersion in $\log |\mu|$ computed from histograms for source sizes in the range $0 \leq r_s \leq 4$ (see Fig. 5.3) versus source size for different mass functions for a positive-parity image with $|\mu_0| = 10$. The top panel shows mass functions with logarithmic slopes of $\alpha = 2.35$. The solid, dotted and dashed curves have $m_1/m_2 = 1, 0.1$ and 0.03 , respectively. The bottom panel shows mass functions with $m_1/m_2 = 0.1$. The solid, dotted and dashed curves have $\alpha = 1.85, 2.35$ and 2.85 , respectively.

causes the mass function to spread out: the lower limit decreases slightly, while the upper limit can increase substantially. A high upper limit allows massive stars to exist, although they will be fairly rare because the mass function is steep. Thus, some magnification maps will contain one or a few massive stars that significantly affect the microlensing, while many will not. We believe this explains why increasing the mass range increases the magnification dispersion. It also explains why the mass range becomes more important as the source size increases: large sources are most sensitive to massive stars.

Now consider the slope of the mass function. Figures 5.3–5.5 show that the slope hardly affects microlensing at all, regardless of the source size. The reason is that

changing the slope shifts the mass function left or right (see Fig. 5.2), but not dramatically.

We conclude that microlensing of an extended source may offer the possibility of determining the dynamic range (m_1/m_2) of the stellar mass function, but not for determining the mass function slope. In light of this result, we henceforth restrict our attention to a Salpeter mass function ($\alpha = 2.35$), and we focus attention on the case $m_1/m_2 = 0.1$.

5.3.2 Dark Matter Content

We now consider how the mass fraction in dark matter affects microlensing. Controversy remains as to whether cosmological simulations of dark matter agree with galaxy observations (e.g., Spekkens et al. 2005; Gerhard 2006, and references therein). Part of the problem is that most observations (e.g., galaxy dynamics and gravitational macrolensing) depend on the global mass distribution in a galaxy, rather than the local mass density. Schechter & Wambsganss (2002, 2004) argue that microlensing offers a new way to measure the density of dark matter at the positions of the lensed images. They consider a uniform mass function and a point source; we generalize the analysis to a mass function and an extended source.

Figure 5.6 shows magnification histograms for dark matter mass fractions of $f_c \equiv \kappa_c/\kappa = 0.2, 0.4, 0.6, 0.8$ and 0.99 . One might expect that as f_c increases, microlensing becomes less important, since fewer stars produce simpler caustic networks. For $f_c \rightarrow 1$, the magnification distribution indeed approaches a δ -function centered at μ_0 , as seen in the bottom row of Figure 5.6. For smaller values of f_c , however, the histograms show more structure. In particular, secondary peaks appear in several of the histograms (see also Rauch et al. 1992). The different peaks correspond to different numbers of microimages (see Granot et al. 2003, especially their Figure 4). If dark matter is the primary mass component, the probability that a source will have multiple microimages is low. In that case, the magnification distribution has a single peak near the expected magnification in the absence of microlensing (e.g., $f_c = 0.99$). For smaller values of f_c , the density of caustics increases, which in turn raises the probability that a source

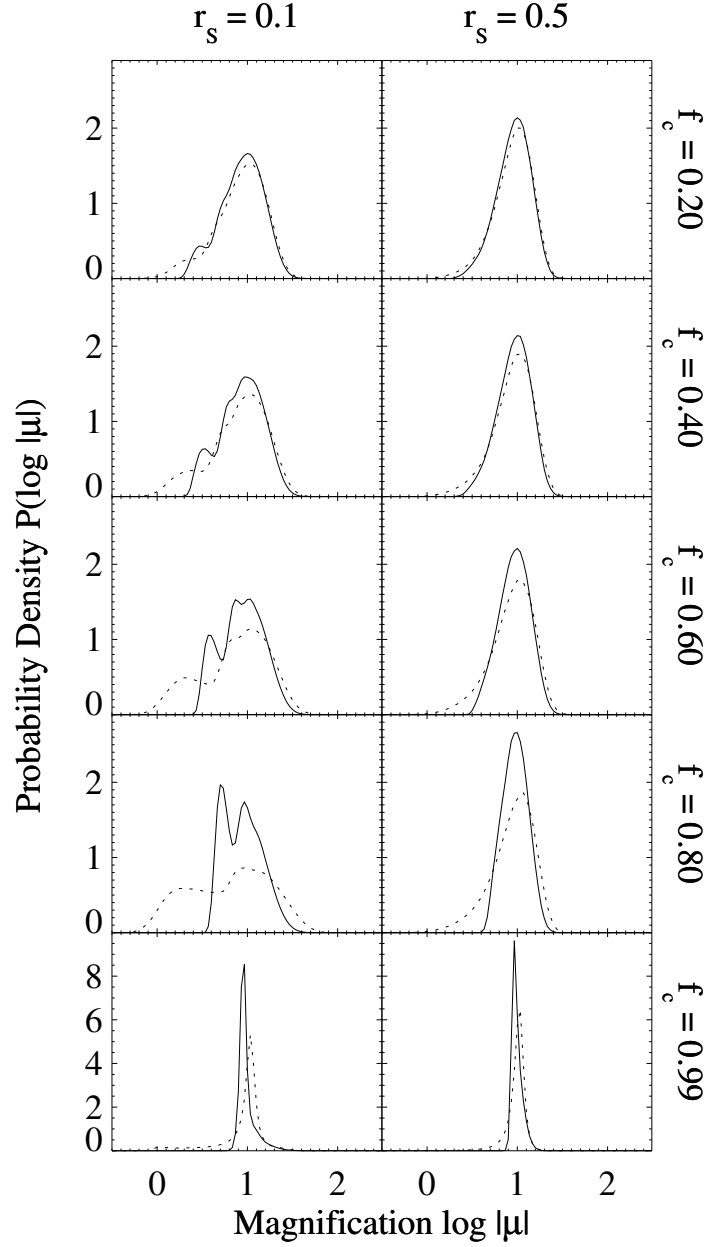


Figure 5.6 Magnification histograms for an image with $|\mu_0| = 10$ for different dark matter mass fractions. From top to bottom, panels show $f_c = 0.2, 0.4, 0.6, 0.8$ and 0.99 . The left and right columns have $r_s = 0.1$ and 0.5 , respectively. The solid and dotted curves have positive and negative parity, respectively. We use a Salpeter mass function ($\alpha = 2.35$) with $m_1/m_2 = 0.1$.

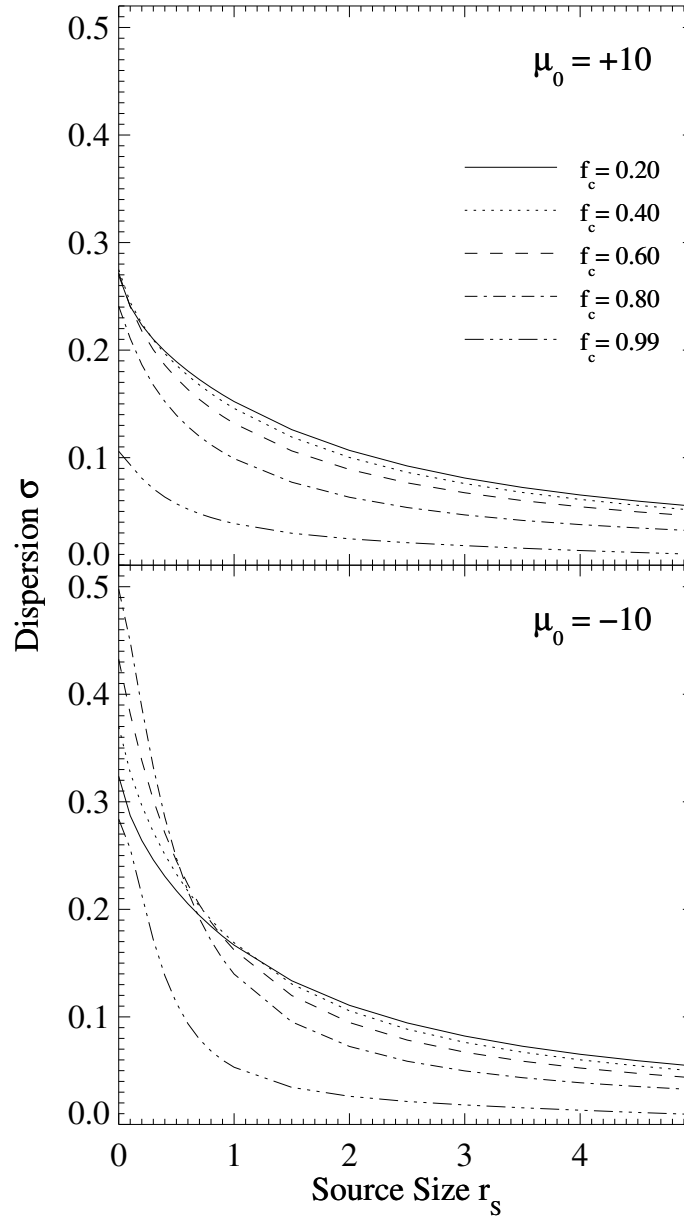


Figure 5.7 Dispersion in $\log |\mu|$ computed from histograms for source sizes in the range $0 \leq r_s \leq 5$ (see Fig. 5.6) versus source size for different dark matter fractions. The top (bottom) panel shows an image with positive (negative) parity. The solid, dotted, dashed, dot-dashed and dot-dot-dashed curves have $f_c = 0.2, 0.4, 0.6, 0.8$ and 0.99 , respectively.

will have extra microimage pairs. The magnification distribution therefore acquires a second peak associated with regions of the source plane for which an extra image pair is created (see left-hand column of Fig. 5.6). When f_c is low, regions with extra microimages become the norm, and the peaks corresponding to different numbers of microimages become less distinct. Also, an extended source often covers regions with different numbers of microimages, smearing out the effects of additional microimages (see right-hand column of Fig. 5.6).

Figure 5.6 also demonstrates the importance of parity. We find that negative-parity images lead to distributions with tails at low magnification. Schechter & Wambsganss (2002) find the same behavior for a point source. As the source size is increased, the tails become less apparent. When $r_S = 1.0$ (not shown), the two parities give nearly identical results. One surprise is that a difference between positive and negative parity can be observed in the skewness of the distributions even for $f_c = 0.99$. This means that even a small stellar mass fraction gives rise to noticeable parity-dependent effects.

Figure 5.7 uses the magnification dispersion to quantify the effects of parity and source size. In the positive-parity case (top panel), replacing stars with dark matter decreases the dispersion for all source sizes, which makes intuitive sense. However, in the negative-parity case (bottom panel), when the source is small, diluting the stars with dark matter *increases* the dispersion, at least in the range $f_c \leq 0.8$. Schechter & Wambsganss (2002) first found this result for a point source and a uniform stellar mass function. We now see that it holds for small extended sources as well. We discover though, that when the source is large, the trend reverses: increasing the dark matter fraction decreases the magnification dispersion. It seems notable that the curves of dispersion versus source size for different dark matter fractions all cross at roughly the same source size ($r_S \sim 0.8$), although we do not know whether this is significant.

It is worth pointing out that Dobler et al. (2007) examine the effects of dark matter and source size on the magnification for demagnified lensed images. They find that increasing the dark matter fraction always decreases the magnification dispersion for a demagnified negative-parity image. (Recall that our negative-parity image is magnified.) However, for a demagnified *central* image, diluting the stars with dark matter

increases the dispersion for a small source, but decreases the dispersion for a large source. Direct comparison between those results and ours is not possible due to the different macro parameters. Nevertheless, it seems clear that the effects of dark matter on microlensing depend in a complicated way on the parity, the macro-magnification and the source size.

Our findings imply that the continuum and broad-line regions may experience very different microlensing in negative-parity lensed images. The continuum emission region is small and should therefore have a magnification dispersion that increases with the dark matter fraction. By contrast, in many cases, the BLR may be large enough that the dispersion will decrease as the dark matter fraction increases (Richards et al. 2004; Keeton et al. 2006). For positive-parity images, the accretion disk and BLR will both have a dispersion that decreases with the dark matter fraction. This may turn out to be a very important physical effect allowing us to probe both the dark matter content of lens galaxies and the structure of lensed quasars.

5.3.3 Source Profile

In the remaining subsections, we return to models consisting purely of a stellar mass component and consider how microlensing depends on properties of the source. We first examine different surface brightness profiles, following Mortonson et al. (2005). Figure 5.8 shows the dispersion versus source size for Gaussian, uniform and linear profiles (defined in §5.2). We see that the dispersion decreases as the profile becomes steeper, although the effect is not strong. We therefore confirm that the dispersion depends weakly on the source profile.

5.3.4 Ellipticity and Position Angle

We now allow the source to be non-circular. This possibility has not been considered in previous microlensing analyses, although it is an important physical effect (see Kochanek et al. 2007). For a population of thin disks with random inclinations, a face-on source is rare; the average projected ellipticity is $\bar{e} = 0.5$. Therefore, models of microlensing need to allow a non-circular shape for the source. This is especially

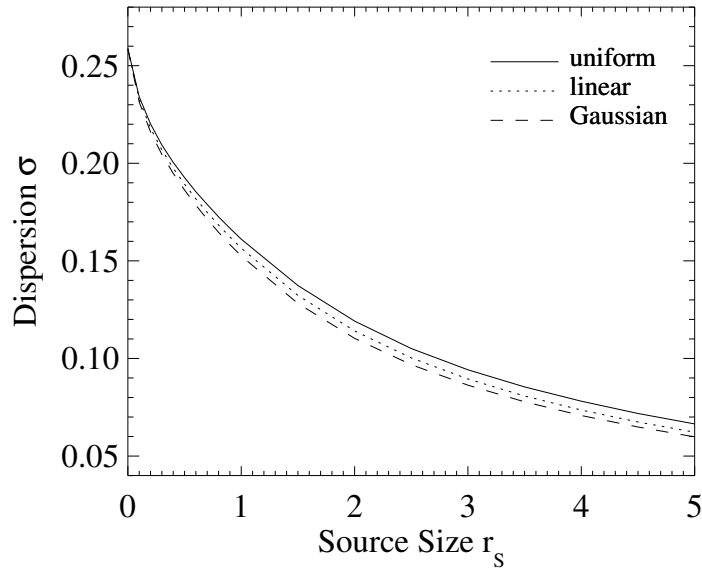


Figure 5.8 Dispersion in $\log |\mu|$ versus source size for a positive-parity image with different source profiles. Solid, dotted and dashed curves have uniform, linear and Gaussian source profiles, respectively. A Salpeter mass function with $m_1/m_2 = 0.1$ is used.

important for continuum microlensing, where the source is presumably a thin accretion disk. Non-circular source models may be relevant to broad-line microlensing as well, given evidence that BLRs may have some disk structure (e.g., Murray & Chiang 1998; Elvis 2000; Richards et al. 2004).

Figure 5.9 shows how the magnification dispersion depends on the ellipticity, $e \equiv 1 - q$, and position angle, PA, of the source. In each panel, we see that the dispersion increases monotonically with position angle, an effect which becomes more pronounced for large ellipticities. To understand this behavior, first note that $\text{PA}=0^\circ$ describes a source whose major axis is orthogonal to the direction of shear, which defines the long axis of the caustics. An extended source with $\text{PA}=0^\circ$ is likely to cover one or more caustics, regardless of where it is centered (see Fig. 5.10). Small changes in the source position do not produce dramatic changes in the magnification. By contrast, for a source with $\text{PA}=90^\circ$ (aligned with the caustics), small displacements of the source can change the number of caustics covered, with corresponding large deviations in the magnification. This explains why the magnification dispersion is higher for sources

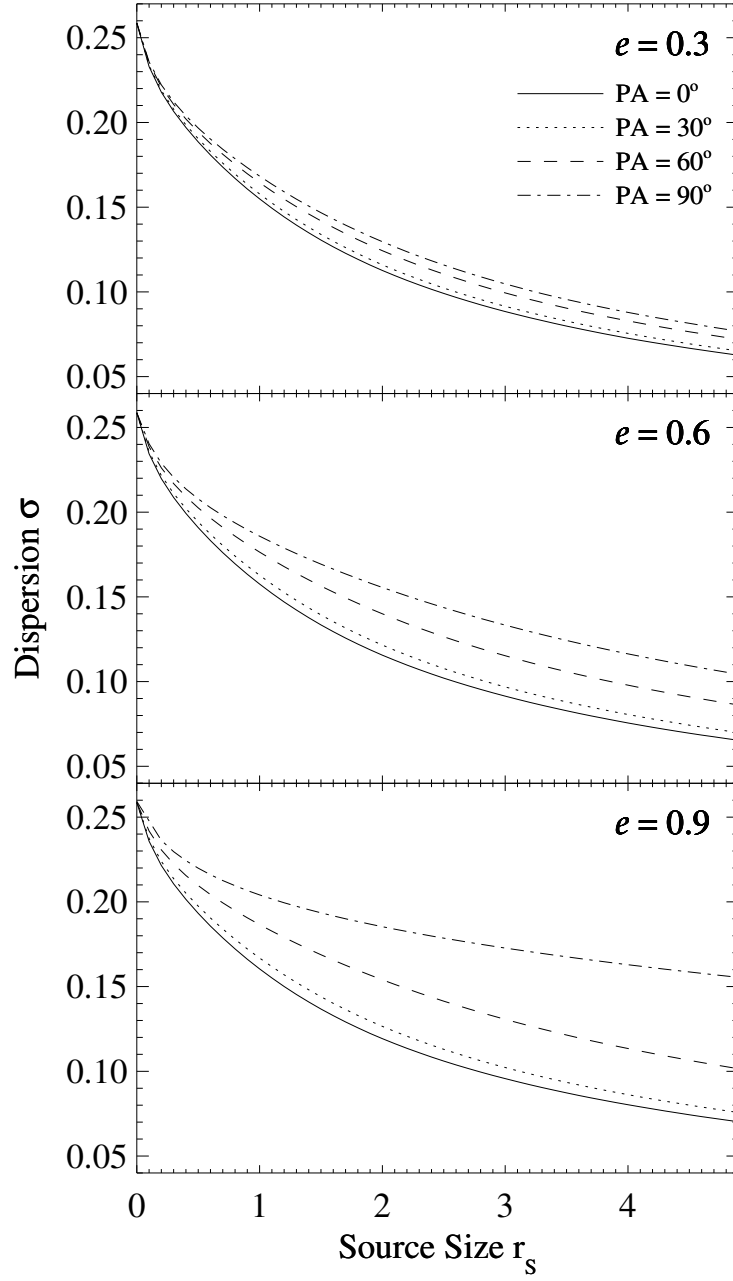


Figure 5.9 Dispersion in $\log |\mu|$ versus source size for a positive-parity image with different ellipticities and position angles. From top to bottom, panels show ellipticities of $e=0.3$, 0.6 and 0.9 . The solid, dotted, dashed and dot-dashed curves have position angles of $PA=0$, 30 , 60 and 90 degrees, respectively. The source is described by a Gaussian profile. The stellar distribution of the lens is modeled by a Salpeter mass function with $0.1 < m < 1$.

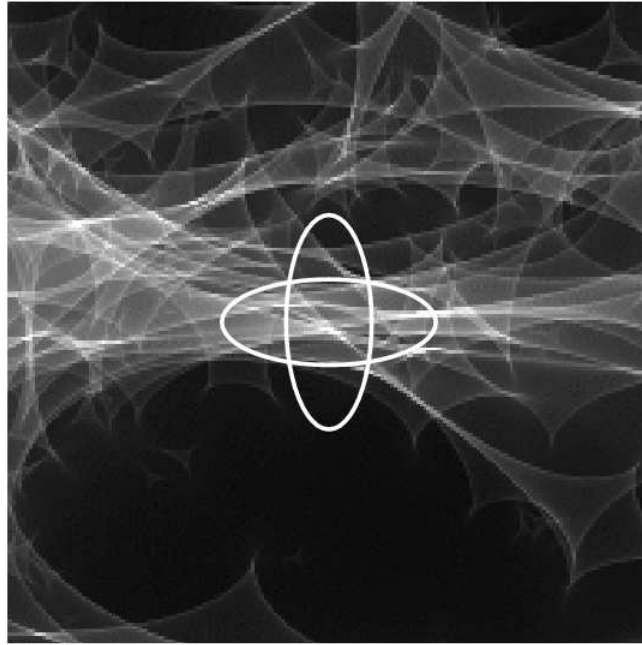


Figure 5.10 Illustration of why microlensing magnifications depend on the orientation of an elliptical source. Both ellipses have semimajor axes with lengths $a = R_E(\bar{m})$ and ellipticities $e = 0.6$.

aligned with the caustics (PA=90°) than for orthogonal sources (PA=0°). These effects become even more pronounced for more highly elongated sources.

In Figure 5.11, most of the effects discussed so far are considered simultaneously. As in Figure 5.5, the dispersion is larger for our fiducial model ($m_1/m_2 = 0.1$, dashed and dot-dashed curves) than for a uniform mass function (solid and dotted curves). As in Figure 5.8, the dispersion is smaller for the Gaussian profile (dotted and dot-dashed curves) than for the uniform source profile (solid and dashed curves). Perhaps the most interesting point is that as the source ellipticity increases, the difference between the four curves becomes smaller, i.e., the dispersion becomes even less sensitive to the mass function and source profile.

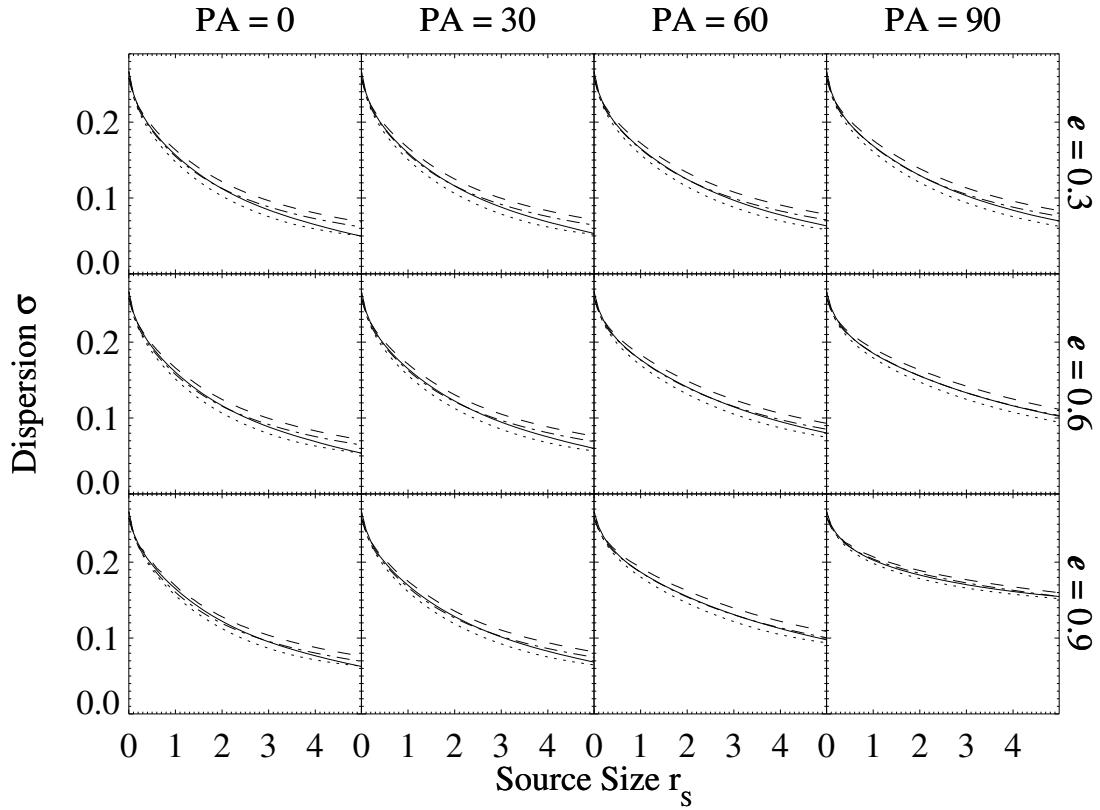


Figure 5.11 Dispersion in $\log |\mu|$ versus source size for a positive-parity image with various lens and source parameters. Rows show $e=0.3, 0.6$ and 0.9 , while columns show $PA=0, 30, 60$ and 90 degrees. Solid and dashed curves have a uniform source profile. The solid curve shows a uniform mass function ($m_1/m_2 = 1$) and the dashed curve shows a Salpeter mass function with $m_1/m_2 = 0.1$. Dotted and dot-dashed curves have a Gaussian profile. The dotted line shows a uniform mass function, while the dot-dashed line shows a Salpeter mass function.

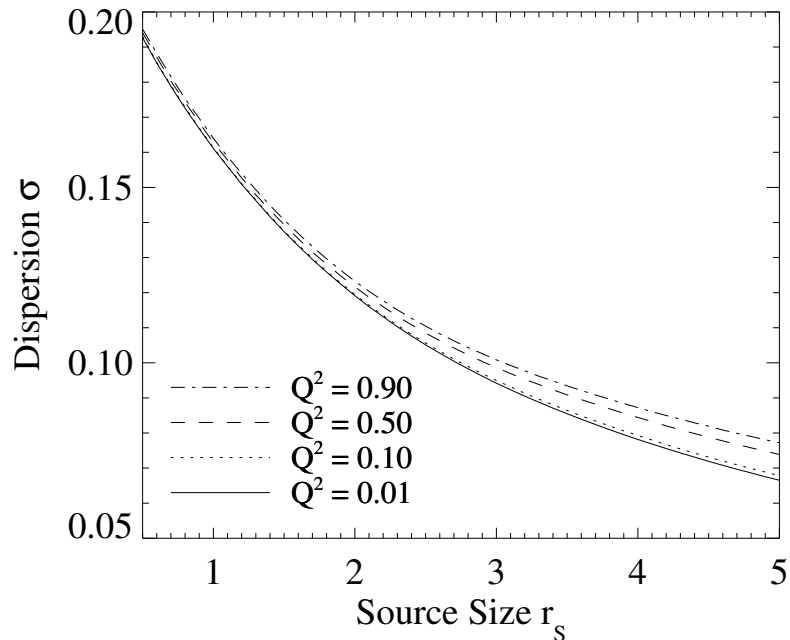


Figure 5.12 Dispersion in $\log |\mu|$ versus source size for a positive-parity image with different disk geometries. The source is modeled as an annulus with a given half-light radius. The solid, dotted, dashed and dot-dashed curves have hole-to-total area ratios of $Q^2 = 0.01, 0.1, 0.5$ and 0.9 , respectively.

5.3.5 Accretion Disk Geometry

Finally, we consider whether variations in accretion disk geometry result in observable differences for microlensing. We model the source as an annulus with a given half-light radius, r_s , and hole-to-total area ratio, Q^2 . This approach is useful in two ways. First, quasar accretion disks have inner radii defined by the innermost stable circular orbit of a particle in motion around the central black hole. Second, typical models (e.g., the Shakura-Sunyaev disk) emit over a wide range of wavelengths. Roughly distinct annular regions within the disk are revealed by observations in different bands (see, e.g., Mortonson et al. 2005). It is important to determine whether microlensing can be used to find the mass of the central black hole or the scale of the annulus within the disk emitting at some wavelength.

For simplicity, we focus on a uniform source. Figure 5.12 shows the dispersion versus source size for disks with $Q^2 = 0.01$ (solid curve), 0.1 (dotted), 0.5 (dashed) and 0.9

(dot-dashed). For small sources ($r_S \lesssim 1.5$), the dispersion is nearly identical for all values of Q^2 . For larger sources, the dispersion remains similar for $Q^2 = 0.01$ and for $Q^2 = 0.1$. However, the cases $Q^2 = 0.5$ and $Q^2 = 0.9$ have larger dispersions, suggesting that only large holes can significantly affect microlensing.

5.3.6 Light Curves

While our analysis has focused on magnification distributions, microlensing has a time domain as well, and we would like to understand whether variability timescales can provide more information about the lens and source. Although a complete study of microlensing light curves and light curve statistics is beyond the scope of this chapter, we can examine sample light curves and begin to identify useful results. We have found that source ellipticity and orientation have pronounced effects on the magnification distribution, so we now see how they affect light curves.

To obtain sample light curves, we move the source through the magnification map along some trajectory, as shown in Figure 5.13. The natural time scale is the Einstein crossing time, $t_E = R_E(\bar{m})/v_\perp$, where v_\perp is the relative transverse velocity between the lens and source. Figure 5.14 (left) shows the resulting light curves for a source with $r_S = 1$ and the same set of ellipticities and orientations used in Figure 5.9. Increasing either the ellipticity or the position angle increases the amount of variability, especially on short timescales. This is consistent with our previous interpretation: small changes to the source position have more effect when the source is aligned with the shear (PA=90°) than when the source is perpendicular (PA=0°). This can lead to a striking amount of rapid variability for highly flattened sources.

To quantify the amount of variability on different timescales, we follow Lewis & Irwin (1996) and use the structure function as a statistical measure of temporal variability. The structure function is defined to be the mean square change in the brightness after time Δt : $S(\Delta t) = \langle [M(t + \Delta t) - M(t)]^2 \rangle$, where M is the apparent magnitude, and the average is over t . To obtain statistically meaningful results, we average the structure function over 100 realizations of light curves for a given set of parameters.

The structure functions are shown in Figure 5.14 (right). They all have a roughly

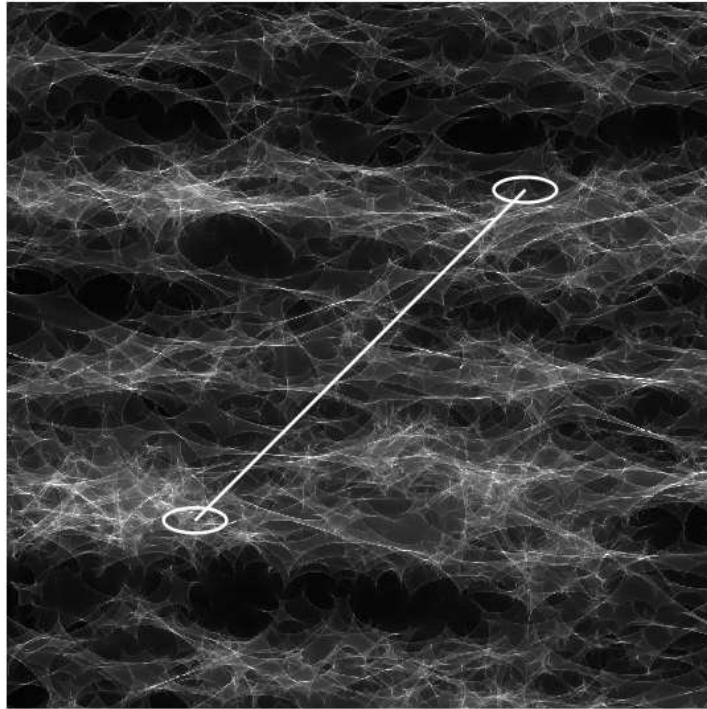


Figure 5.13 Construction of light curves. A source with ellipticity $e = 0.6$ and PA= 90° is moved along the trajectory from lower left to upper right. The resulting light curves are shown in the middle panel of the left column of Figure 5.14.

linear rise to a plateau beginning around $\Delta t/t_E \sim 5$. They confirm that there is more variability on shorter timescales when the source is elongated and/or aligned with the shear. It is customary to define a characteristic variability time scale as the interval at which the structure function reaches half its plateau value (see Lewis & Irwin 1996; Schechter et al. 2003). We see that this time scale can vary by a factor of ~ 2 depending on the ellipticity and orientation of the source.

The important implication is that elongated sources can lead to more rapid variability than circular sources that have identical half-light radii. This effect must be taken into account when interpreting observed variability timescales. It is not clear whether source shape can explain the rapid variability observed by Schechter et al. (2003) and Paraficz et al. (2006), but it should at least be considered as a possible alternative to relativistic motion.

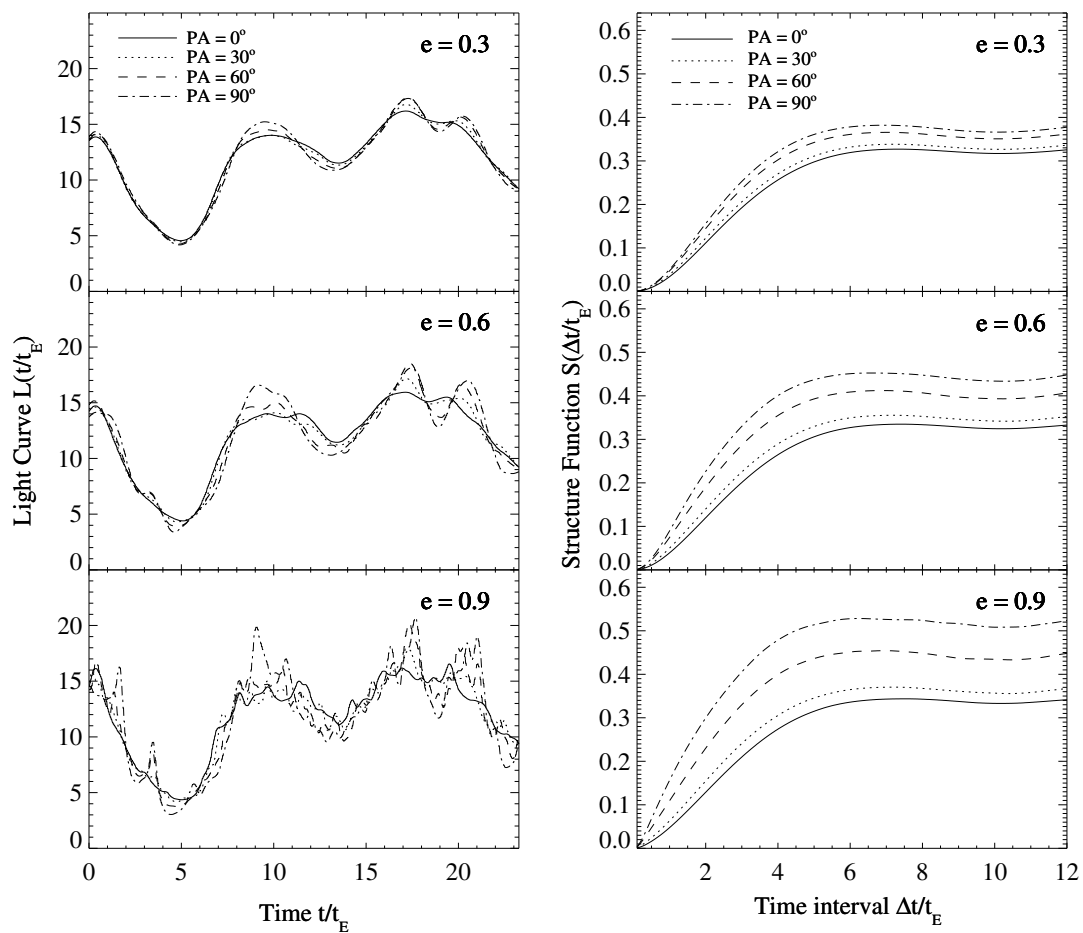


Figure 5.14 Light curves (left) and structure functions (right) for models with $e = 0.3$, 0.6 and 0.9 (top to bottom). Solid, dotted, dashed and dot-dashed curves have $PA = 0, 30, 60$ and 90 degrees, respectively.

5.4 Conclusions

We have presented a systematic study of microlensing of finite sources. We have extended earlier work by combining an finite source with a lens described by a stellar mass function. Following Mortonson et al. (2005), we have explored how the surface brightness profile and geometry of the source affect microlensing (§5.3.3 and §5.3.5). We find that both effects are of minimal importance, although subtle differences are apparent: making the source surface brightness profile steeper (Fig. 5.8) and introducing a large hole in the source (Fig. 5.12) both increase the magnification dispersion.

The mass function can play a more significant role. Although the slope of the mass function does not lead to noticeable changes in the magnification dispersion, the dynamic range can be important. The dispersion for an extended source becomes larger as the mass range increases. This result has been seen before for a broad, bimodal mass function (Schechter et al. 2004; Lewis & Gil-Merino 2006), but we have demonstrated it for a continuous and relatively narrow mass function, as would be appropriate for stars. This raises the possibility of using microlensing to determine the dynamic range of stellar mass functions in distant galaxies.

Our discussion of dark matter in Section 5.3.2 reveals many interesting results. We find that the monotonic increase in dispersion for a point source lensed by a mixture of stars and dark matter (Schechter & Wambsganss 2002) extends to the case of combining a small extended source with a power-law mass distribution. However, for moderately large sources, we find that microlensing becomes less pronounced as the dark matter mass fraction is increased. As in previous studies (e.g., Schechter & Wambsganss 2002), we find multiple peaks in the magnification histograms for moderate dark matter fractions. We also see that negative-parity images have tails to low magnifications (see Schechter & Wambsganss 2002), but only when the source is small.

Finally, we have for the first time considered non-circular sources with a range of position angles. We find that sources aligned with the shear have larger magnification dispersions than sources orthogonal to the shear.

Apart from source size, which is fundamentally important, we believe that two of

the effects we have identified have important physical implications. First, the continuum and BLR will be very different in their sensitivity to dark matter near a lensed image, particularly a negative-parity image. Thus, attempts to measure the dark matter content of galaxies with microlensing (see Schechter & Wambsganss 2004) would greatly benefit from *spectroscopic* observations (see Keeton et al. 2006). Second, elliptical sources, which are relevant for inclined disks, may experience much more rapid variability than circular sources. This effect will surely be important when interpreting microlensing variability time scales.

Acknowledgements

We are especially grateful to Joachim Wambsganss for allowing us to use his inverse ray-shooting software and for his helpful comments on the manuscript. We also thank Greg Dobler, Jerry Sellwood and Tad Pryor for useful discussions.

Bibliography

- Abajas C., Mediavilla E., Muñoz J. A., Popović L. Č., Oscoz A., 2002, *ApJ*, 576, 640
- Dalal N., Kochanek C. S., 2002, *ApJ*, 572, 25
- Dobler G., Keeton C. R., Wambsganss J., 2007, *MNRAS*, 377, 977
- Elvis M., 2000, *ApJ*, 545, 63
- Gerhard O., 2006, in *Planetary Nebulae Beyond the Milky Way*, Stanghellini L., Walsh J. R., Douglas N. G., eds., ESO Astrophys. Symp., Berlin: Springer, p. 299
- Granot J., Schechter P. L., Wambsganss J., 2003, *ApJ*, 583, 575
- Jaroszynski M., Wambsganss J., Paczyński B., 1992, *ApJ*, 396, L65
- Keeton C. R., Burles S., Schechter P. L., Wambsganss J., 2006, *ApJ*, 639, 1
- Kochanek C. S., 2004, *ApJ*, 605, 58

- Kochanek C. S., Dai X., Morgan C., Morgan N., Poindexter S. C. G., 2007, in ASP Conf. Ser., Vol. 371, *Statistical Challenges in Modern Astronomy IV*, Babu G. J., Feigelson E. D., eds., p. 43
- Lewis G. F., Gil-Merino R., 2006, ApJ, 645, 835
- Lewis G. F., Irwin M. J., 1996, MNRAS, 283, 225
- Metcalf R. B., Madau P., 2001, ApJ, 563, 9
- Mortonson M. J., Schechter P. L., Wambsganss J., 2005, ApJ, 628, 594
- Murray N., Chiang J., 1998, ApJ, 494, 125
- Paraficz D., Hjorth J., Burud I., Jakobsson P., Elíasdóttir Á., 2006, A&A, 455, L1
- Peterson B. M., Horne K., 2005, in *Planets to Cosmology: Essential Science in the Final Years of the Hubble Space Telescope*, Casertano S., Livio M., eds., STScI Symp. Ser., Cambridge: Cambridge University Press, p. 89
- Pooley D., Blackburne J. A., Rappaport S., Schechter P. L., 2007, ApJ, 661, 19
- Rauch K. P., Mao S., Wambsganss J., Paczyński B., 1992, ApJ, 386, 30
- Richards G. T., Keeton C. R., Pindor B., Hennawi J. F., Hall P. B., Turner E. L., Inada N., Oguri M., Ichikawa S.-I., Becker R. H., Gregg M. D., White R. L., Wyithe J. S. B., Schneider D. P., Johnston D. E., Frieman J. A., Brinkmann J., 2004, ApJ, 610, 679
- Rusin D., Kochanek C. S., 2005, ApJ, 623, 666
- Schechter P. L., Udalski A., Szymański M., Kubiak M., Pietrzyński G., Soszyński I., Woźniak P., Żebruń K., Szewczyk O., Wyrzykowski Ł., 2003, ApJ, 584, 657
- Schechter P. L., Wambsganss J., 2002, ApJ, 580, 685
- , 2004, in IAU Symp., Vol. 220, *Dark Matter in Galaxies*, Ryder S., Pisano D., Walker M., Freeman K., eds., p. 103

- Schechter P. L., Wambsganss J., Lewis G. F., 2004, *ApJ*, 613, 77
- Schneider P., Wambsganss J., 1990, *A&A*, 237, 42
- Spekkens K., Giovanelli R., Haynes M. P., 2005, *AJ*, 129, 2119
- Treu T., Koopmans L. V., Bolton A. S., Burles S., Moustakas L. A., 2006, *ApJ*, 640, 662
- Treu T., Koopmans L. V. E., 2004, *ApJ*, 611, 739
- Wambsganss J., 1992, *ApJ*, 386, 19
- , 1999, *J. Comp. Appl. Math.*, 109, 353
- Wambsganss J., Paczyński B., Schneider P., 1990, *ApJ*, 358, L33
- Woźniak P. R., Udalski A., Szymański M., Kubiak M., Pietrzyński G., Soszyński I., Żebruń K., 2000, *ApJ*, 540, L65
- Wyithe J. S. B., Agol E., Fluke C. J., 2002, *MNRAS*, 331, 1041
- Wyithe J. S. B., Turner E. L., 2001, *MNRAS*, 320, 21

Chapter 6

Prospects for Testing General Relativity with Lensing by Massive Black Holes

Abstract

Gravitational lensing by massive black holes may provide a way to test theories of gravity. While the theoretical foundation for such tests has been developed for many interesting cases, little has been done to determine whether the tests are observationally feasible. We consider prospects for observing strong lensing by the supermassive black hole at the Galactic center (Sgr A*). We compute the expected number of lensed stars in the central cusp, bulge and disk behind Sgr A*. We explicitly include density profiles and luminosity functions in our analysis, and we count only lenses where the two lensed images are resolved and bright enough to be detectable. For a K-band magnitude limit of 17, we find the total number of strong lenses to be 0.56, with the Galactic disk providing the dominant contribution. This number increases quickly with the limiting magnitude, reaching roughly 20 for a threshold of $K = 21.5$ mag. We examine various systematic uncertainties in our predictions, including extinction by dust. We also consider massive black holes in other stellar systems. If a globular cluster contains an intermediate-mass black hole, the probability that it lenses a star on the far side of the cluster is of order 10^{-6} . By contrast, the supermassive black hole in a typical massive elliptical galaxy should lens ~ 100 stars in its host galaxy, and this number could reach ~ 5800 for a giant elliptical galaxy such as M87. Using our results for Sgr A*, we consider how strong lensing could be used to constrain theories of gravity, finding that observations with a resolution of ~ 10 micro-arcsec would make this possible.

6.1 Introduction

Much theoretical work has been devoted in recent years to investigating how gravitational lensing can be used to probe the spacetime around black holes and constrain theories of gravity. However, a thorough analysis of how these ideas could be tested observationally has been lacking. The principal concept is that when a light source is lensed by a compact object, the positions, magnifications and time delays of the images will differ from their quasi-Newtonian, weak-field values due to higher-order gravity effects. If the higher-order terms can be measured, they can be used to test general relativity against alternate theories of gravity.

When a star is lensed by a black hole, there are various effects that may be used to probe gravity beyond the weak-field limit. A light ray that passes through the strong-field regime close to a black hole may execute a partial orbit, or even multiple orbits, on its way to the observer. For example, light from a foreground star can loop halfway around the black hole, although such “retrolensing” is unlikely to be observed (Holz & Wheeler 2002). The looping trajectories yield infinitely many images of a background star, and these “relativistic images” have drawn much theoretical interest (Darwin 1958; Atkinson 1965; Luminet 1979; Ohanian 1987; Virbhadra & Ellis 2000; Bozza et al. 2001; Eiroa et al. 2002; Bozza 2002, 2003; Bhadra 2003; Bozza & Mancini 2004; Bozza et al. 2005; Majumdar & Mukherjee 2005a,b; Eiroa 2005; Whisker 2005). Unfortunately, they are exceedingly faint and will be very difficult to observe (Virbhadra & Ellis 2000; Petters 2003). The primary and secondary lensed images, which reach the observer without looping around the black hole, are much more likely to be detectable; and while they do not pass through the strong-field regime, they may still carry the imprint of the spacetime beyond the weak-field limit. Keeton & Petters (2005, 2006) have developed a formalism for computing the higher-order effects on lensing observables for gravity theories in the post-post-Newtonian framework (which covers a wide range of generalizations of general relativity). Sereno & de Luca (2006) have recently extended the formalism to the case of a spinning (Kerr) black hole in general relativity.

Putting these theoretical ideas into practice requires that we identify appropriate

black holes and background stars, and assess whether detecting the lensed images is observationally feasible. The Galactic center (GC) provides a natural laboratory for this work. There is strong evidence that the GC harbors a supermassive black hole (SMBH) that coincides spatially with the radio source Sgr A*. This conclusion is based on observations of stars near the GC that execute Keplerian orbits about Sgr A*. Combining constraints from several stars yields an SMBH mass of $(3.6 - 3.7) \times 10^6 M_\odot$ (Ghez et al. 2005; Eisenhauer et al. 2005), and together with earlier work rules out alternatives to a single supermassive black hole, such as a dense cluster of stellar remnants (Maoz 1998) or a concentration of degenerate fermions (e.g., Tsiklauri & Viollier 1998; Munyaneza & Viollier 2002). The dark cluster hypothesis is difficult to maintain in light of the measured central density for the dark object at the GC of $\gtrsim 10^{13} M_\odot \text{pc}^{-3}$ (Eckart & Genzel 1997; Ghez et al. 1998, 2000; Eckart et al. 2002). For example, a central density of $2.4 \times 10^{14} M_\odot \text{pc}^{-3}$ would yield a cluster lifetime of only a few Myr (Maoz 1998; Eckart et al. 2002). On the other hand, if Sgr A* were a fermion ball, its total mass and radius would imply a particle mass of $\sim 74 \text{ keV } c^{-2}$ (Ghez et al. 2005), which is several orders of magnitude above upper limits on the neutrino mass from observations of the cosmic microwave background (Spergel et al. 2003). Thus, the compactness of Sgr A* is inconsistent with either a dark stellar cluster or a fermion ball. Although a massive boson star at the GC cannot rigorously be excluded as an SMBH alternative, accretion of surrounding material would likely cause such an object to collapse into an SMBH in a time less than the Galactic age (Schödel et al. 2002).

The stars observed to orbit Sgr A* are obvious candidates for lensing. The star S14, in particular, should produce a secondary image that will attain a peak brightness of 23.3 in the K-band (Bozza & Mancini 2005). However, this is still much fainter than the current detection threshold of ~ 17 mag. If a star with a somewhat larger orbit (out to ~ 1 pc) passes behind Sgr A*, we would observe a change in its brightness without resolving the individual images. Alexander & Sternberg (1999) investigated whether such “microlensing” might be able to explain flares at the GC observed at x-ray (Baganoff et al. 2001) and infrared (Genzel et al. 2003; Trippe et al. 2007) wavelengths with durations of minutes to hours. (While flares could arise from physical

processes in the accretion disk around the black hole, it was worthwhile to consider whether microlensing could provide an alternate explanation.) For a spherical black hole, the microlensing light curve would be symmetric in time. However, there may be perturbations from stars in the central stellar cusp (Bahcall & Wolf 1977), which extends ~ 10 – 100 pc from the GC, and from stellar remnants such as neutron stars and black holes that occupy the central parsec of the Galaxy (Miralda-Escudé & Gould 2000). For sources in the Galactic bulge (Chanamé et al. 2001) and disk (Alexander & Loeb 2001), the perturbations would increase the magnification and duration of a microlensing event. They would also increase the microlensing probability (cf. Alexander & Sternberg 1999), although the overall probability remains small ($\sim 1\%$ within 2 arcsec of the GC) (Alexander & Loeb 2001). In addition to amplifying the brightness of a background star, lensing by the Galactic SMBH would also perturb the star’s apparent position at the level of 0.1–2 milliarcsec (mas) (Nusser & Broadhurst 2004).

One aspect of lensing by Sgr A* that has not been fully explored is the case where the images of a background source can be spatially resolved. Such *strong* lensing is of particular relevance to stars in the bulge and disk, which move too slowly for microlensing variability to be observed. For example, a star with an orbital radius of 10 kpc would take 500 years to cross the Einstein radius. The first study of strong lensing by Sgr A* (Wardle & Yusef-Zadeh 1992) considered only the stellar cusp, and the results were limited by incomplete knowledge of the stellar density profile and luminosity function. One of our goals in this chapter is to carry out a thorough study of strong lensing by Sgr A*. We consider the full population of stars on the far side of the Galaxy ranging from ~ 1 pc to ~ 25 kpc from the black hole, and we incorporate new data on those populations. We seek to determine how many stars are expected to be lensed by Sgr A* such that detecting both the primary and secondary lensed images is observationally feasible.

We also consider lensing by massive black holes in other stellar systems. Although we lack the data to support a detailed treatment, we can obtain rough estimates for the expected number of strongly lensed stars in different systems. There is strong evidence that central black holes are present in galaxies other than the Milky Way (see Kormendy

& Richstone 1995, for a review). In fact, many galaxies may have black holes with masses $\gtrsim 10^8 M_\odot$ at their centers. There have also been claims of intermediate-mass black holes (IMBHs) in galactic (Gerssen et al. 2002) and extragalactic (Gebhardt et al. 2002; Maccarone et al. 2007) globular clusters. However, a conclusive measurement has not yet been made, and IMBH alternatives (Gerssen et al. 2003; Baumgardt et al. 2003a,b; Ho et al. 2003) such as a dense cluster of stellar remnants can explain the data equally well in some cases. It is conceivable that lensing could provide a way to resolve the controversy.

Our assessment of prospects for observing lensing by massive black holes goes into the most detail for Sgr A*, since it is the nearest SMBH and therefore the most accessible laboratory for testing general relativity. In Section 6.2 we compute the expected number of stars strongly lensed by Sgr A*, using realistic models of the population of stars behind the black hole, and taking care to consider only lenses for which both images are detectable. We carefully examine the systematic uncertainties in our lensing forecasts. In Section 6.3 we broaden our focus and consider lensing by black holes other than Sgr A*. We derive a rough estimate of the number of lensed stars in elliptical galaxies containing SMBHs, and in globular clusters containing IMBHs, in order to understand whether these systems are interesting from the lensing standpoint. In Section 6.4 we describe how lensing by SMBHs (particularly Sgr A*) may be used to constrain theories of gravity. We offer concluding remarks in Section 6.5.

6.2 Strong Lensing by the Galactic Supermassive Black Hole

We make detailed calculations for lensing by Sgr A* since it is the nearest supermassive black hole, and is surrounded by a stellar population whose parameters are reasonably well constrained. In Section 6.2.1 we identify the populations of stars that could be lensed, and specify their density profiles and luminosity function. In Section 6.2.2 we derive an expression for the number of stars that are strongly lensed by Sgr A*, accounting for the fact that we want both lensed images to be resolved and bright enough to detect. In Section 6.2.3 we present results for fiducial values of the model parameters, and we consider various systematic uncertainties in Sections 6.2.4–6.2.7.

We discuss the angular distribution of lensed images in Section 6.2.8.

6.2.1 Stellar Density Profiles and Luminosity Function

In order to compute the number of stars that should be strongly lensed by Sgr A* we must characterize the stellar population. For our purposes the Galaxy may be divided into three stellar components. The central SMBH gives rise to a stellar cusp that extends to $\sim 10\text{--}100$ pc. The stellar bulge extends out to a few kpc, while the disk dominates the density profile for radii $3 \text{ kpc} \lesssim r \lesssim 25 \text{ kpc}$. We assume spherical symmetry for the cusp and bulge. For the disk, note that the Solar System is ~ 30 pc out of the midplane of the disk, so a star lying 25 kpc behind Sgr A* along the line of sight to the GC is only ~ 90 pc from the midplane. This is small compared with the scale height of the disk (Carroll & Ostlie 1996), so we can equate the cylindrical radius with its spherical counterpart.

Kinematics of stars near the GC implies that the cusp is described by the density profile (Schödel et al. 2003)

$$\rho_{\text{cusp}}(r) = \rho_0 \left[1 + \left(\frac{r}{r_0} \right)^2 \right]^{-\alpha/2}, \quad (6.1)$$

with central density $\rho_0 = 3.6 \times 10^6 M_\odot \text{ pc}^{-3}$ and core radius $r_0 = 0.34$ pc. The power law index is $\alpha = 1.8$, similar to the theoretically expected value $\alpha = 1.75$ (Bahcall & Wolf 1977). The cusp is expected to be important only near the GC, so the density profile in Equation (6.1) should presumably be truncated at some radius, but the precise value of the truncation radius is unknown. Beyond ~ 1 kpc the bulge and disk are the important stellar components, with the profiles (Kent 1992)

$$\rho_{\text{bulge}}(r) = \rho_1 K_0(r/r_1) \quad \text{and} \quad \rho_{\text{disk}}(r) = \rho_2 e^{-r/r_2}, \quad (6.2)$$

where the scale densities of the bulge and disk are $\rho_1 = 3.53 M_\odot \text{ pc}^{-3}$ and $\rho_2 = 3 M_\odot \text{ pc}^{-3}$, respectively, while the scale radii are $r_1 = 667$ pc and $r_2 = 3001$ pc. The function $K_0(x)$ is the modified Bessel function of the second kind.¹ The density profiles of the three components are shown in Figure 6.1.

¹Here $K_0(x)$ indicates a Bessel function, but elsewhere in this chapter K refers to the $2.2 \mu\text{m}$ near-infrared band.

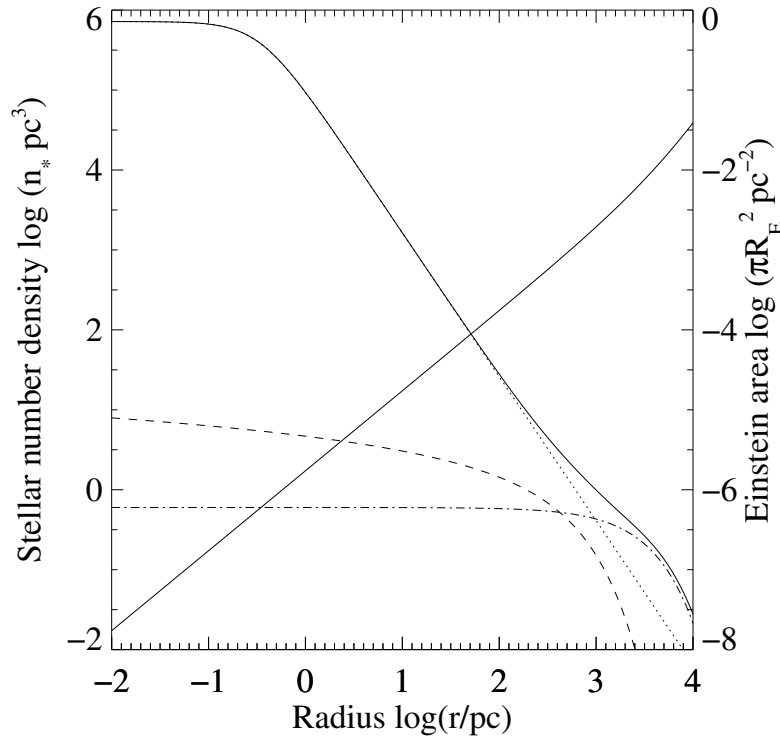


Figure 6.1 Stellar number density profiles (left vertical axis) of the Galactic cusp (dotted line), bulge (dashed line), disk (dot-dashed line) and the sum of all three components (decreasing solid line). The Einstein area (rising solid line) at a given lens-source distance provides a heuristic measure of the effective cross-section for lensing (right vertical axis).

The density profiles give the total mass density in stars, but we can observe only a subset of the stellar population. At optical wavelengths there is too much extinction by dust along the line of sight for observations of stars in or behind the GC to be practical. Infrared light is less affected by dust, so modern observations use the near-infrared K-band ($2.2 \mu\text{m}$) (e.g., Ghez et al. 2005; Eisenhauer et al. 2005). Therefore, we focus on stars that emit in the K-band. The number of stars we can actually see depends strongly on the luminosity function. We write the K-band luminosity function (KLF) as a power law (Alexander & Sternberg 1999),

$$\phi_K(L) \propto L^{-p} \quad \text{with} \quad p = 1.875. \quad (6.3)$$

The KLF is normalized to unity,

$$\int_{L_{\min}}^{\infty} \phi_K(L) dL \equiv 1, \quad (6.4)$$

where L_{\min} is the minimum luminosity. Although a realistic stellar population will not have stars with luminosities greater than some finite threshold L_{\max} , we can let $L_{\max} \rightarrow \infty$, since bright stars contribute little to the KLF. We assume that this luminosity function describes all three stellar components (Alexander & Sternberg 1999).

6.2.2 Strong Lensing of a Background Source Population by a Point Mass

For a source with angular position β relative to the lens, two images are produced with angular positions²

$$\theta_{\pm} = \frac{1}{2} \left(\beta \pm \sqrt{\beta^2 + 4\theta_E^2} \right), \quad (6.5)$$

where the Einstein angle for a lens with mass M_{\bullet} is

$$\theta_E \equiv \sqrt{\frac{4GM_{\bullet}}{c^2} \frac{D_{LS}}{D_L D_S}}. \quad (6.6)$$

Here D_L , D_S and D_{LS} are the distances from observer to lens, observer to source, and lens to source, respectively. The image at θ_+ is called the primary image, while that at θ_- is known as the secondary image. The image separation is

$$\Delta\theta \equiv \theta_+ - \theta_- = \sqrt{\beta^2 + 4\theta_E^2}. \quad (6.7)$$

We require that the two images be resolvable, i.e., $\Delta\theta \geq \theta_{\min}$ for some resolution limit θ_{\min} .

The magnifications of the two images are

$$\mu_{\pm} \equiv \mu(\theta_{\pm}) = \frac{\theta_{\pm}^4}{\theta_+^4 - \theta_-^4}. \quad (6.8)$$

The primary image is always magnified relative to the unlensed source, while the secondary image can be magnified or demagnified, depending on θ (or equivalently β).

²Here we consider lensing in the weak-field limit (see §6.4 for comments on corrections to weak-field lensing).

The number of stars with two detectable images has the form

$$N_{\text{lens}} = 2\pi \int_{D_S > D_L} n_*^{\text{eff}}(D_S, \beta; L_{\text{cut}}) D_S^2 \sin \beta \, d\beta \, dD_S, \quad (6.9)$$

where $n_*^{\text{eff}}(D_S, \beta; L_{\text{cut}})$ is the effective stellar number density, i.e., the number density of stars brighter than the cutoff luminosity, L_{cut} . It is related to the mass density of detectable sources, $\rho_*^{\text{eff}}(D_S, \beta; L_{\text{cut}})$, by (Alexander & Sternberg 1999)

$$n_*^{\text{eff}}(D_S, \beta; L_{\text{cut}}) = \frac{f_K}{\bar{m}} \rho_*^{\text{eff}}(D_S, \beta; L_{\text{cut}}). \quad (6.10)$$

Here f_K is the fraction of stars that emit in the K-band, while \bar{m} is the mean stellar mass. In the absence of lensing, the faintest observable source has luminosity $L_{\text{cut}} = L_0$ for some L_0 . To observe strong lensing, the fainter of the two images must be observable, so that the luminosity cutoff is given by $L_{\text{cut}} = L_0/|\mu_-|$. Note that for a *flux*-limited survey, the limiting luminosity L_0 depends on the distance to the source.

We can now write the effective number density as

$$\begin{aligned} n_*^{\text{eff}}(D_S, \beta; L_{\text{cut}}) &= \frac{f_K}{\bar{m}} \rho_*(D_S, \beta) \int_{L_{\text{cut}}}^{\infty} \phi_K(L) \, dL \\ &= \left[\frac{L_{\min} |\mu_-(D_S, \beta)|}{L_0(D_{LS})} \right]^{p-1} n_*(D_S, \beta), \end{aligned} \quad (6.11)$$

where $\rho_*(D_S, \beta)$ is the *total* mass density, and $n_* \equiv (f_K/\bar{m}) \rho_*$ is the number density of K-emitting stars. The number of strong lenses can then be written as

$$N_{\text{lens}} = 2\pi \int_{r_{\min}}^{\infty} r^2 \, dr \int_0^{\pi/2} \vartheta \, d\vartheta \, n_*(r) \left(|\mu_-| \frac{L_{\min}}{L_0} \right)^{p-1} \quad (6.12)$$

with galactocentric coordinates (r, ϑ) that are related to the geocentric coordinates (D_S, β) by

$$D_S \beta = D_{LS} \vartheta \approx r \vartheta \quad \text{and} \quad D_{LS} = r \cos \vartheta \approx r. \quad (6.13)$$

The advantage of galactocentric coordinates is that the density depends only on r , rather than D_S and β . The two coordinate systems are illustrated in Figure 6.2. The nonzero lower limit r_{\min} of the radial integral comes from the requirement that both lensed images be resolvable (see §6.2.3).

In addition to the total number of lenses, it is also of interest to compare the number of lensed images and the number of (unlensed) stars along a given line of sight. Consider

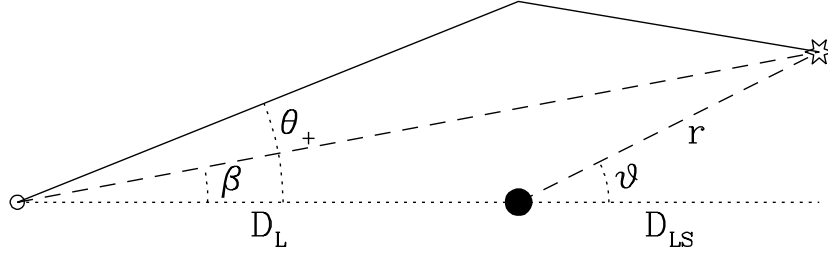


Figure 6.2 Lensing by a supermassive black hole (SMBH). Light from a background star (far right) is deflected by an SMBH (filled circle) on its way to the observer (open circle). As seen by the observer, the true source position is given by the angle β , while the image positions are θ_{\pm} . For clarity, only the primary image θ_+ is shown. The integral in Equation (6.12) is performed in terms of galactocentric coordinates (r, ϑ) ; see § 6.2.2 for details.

an annulus of radius θ and width $d\theta$ (recalling that θ is the angle on the sky measured by the observer). Let $dN_*/d\theta$ be the total number of stars per unit angle, while $dN_{\text{lens}}/d\theta$ is the number of lensed images. We first rewrite Equation (6.12) in terms of the source angle β ,

$$N_{\text{lens}} = 2\pi \int_{r_{\min}}^{\infty} D_s^2 dr \int \beta d\beta n_*(r) \left(|\mu_-| \frac{L_{\min}}{L_0} \right)^{p-1}. \quad (6.14)$$

To obtain $dN_{\text{lens}}/d\theta$, we must convert from source angle β to image angle θ . Since the lensing magnification is the Jacobian of the transformation between source and image planes, we have the relation $\beta d\beta = \theta d\theta / |\mu(\theta)|$. We also need to express μ_- in terms of θ rather than β . To do this, we note that $\mu(\theta) \equiv \mu_-$ if $\theta < \theta_E$, while $\mu(\theta) \equiv \mu_+ = 1 - \mu_-$ if $\theta > \theta_E$ (Keeton & Petters 2005). Thus, we can write

$$\mu_- = \mu(\theta) \Theta(\theta_E - \theta) + [1 - \mu(\theta)] \Theta(\theta - \theta_E), \quad (6.15)$$

where $\Theta(x)$ is the Heaviside step function. Recall that μ also depends on r through θ_E .

We can now obtain

$$\frac{dN_{\text{lens}}}{d\theta} = 2\pi\theta \int_{r_{\min}}^{\infty} D_s^2 n_*(r) \frac{1}{|\mu|} \left(|\mu_-| \frac{L_{\min}}{L_0} \right)^{p-1} dr. \quad (6.16)$$

A similar expression applies to the unlensed stars, with the simplification that the magnification is unity when there is no lensing, and hence

$$\frac{dN_*}{d\theta} = 2\pi\theta \int_{r_{\min}}^{\infty} D_s^2 n_*(r) \left(\frac{L_{\min}}{L_0} \right)^{p-1} dr. \quad (6.17)$$

We compute and discuss $dN_{\text{lens}}/d\theta$ and $dN_*/d\theta$ in Section 6.2.8.

6.2.3 Fiducial Model

The mass of Sgr A* determined from the Keplerian orbits of its nearby stars is usually taken to be $(3.6 - 3.7) \times 10^6 M_\odot$ (Ghez et al. 2005; Eisenhauer et al. 2005). However, the analysis of stellar kinematics that leads to the stellar cusp model Equation (6.1) yields a black hole mass of $2.87 \times 10^6 M_\odot$ (Schödel et al. 2003). We adopt the smaller mass in order to have a consistent model. The lensing cross section scales with the black hole mass, so it is conceivable that we are underestimating the number of lenses by $\sim 25\%$. We take the distance to the GC to be $D_L = 8$ kpc (Reid 1993). For these parameters, and assuming an angular resolution of $\theta_{\text{min}} = 0.05$ arcsec (Ghez et al. 1998), the condition that the two images be resolvable (see Eq. [6.7]) corresponds to the condition $D_{LS} \geq 1.71 \text{ pc} \equiv r_{\text{min}}$.³

We use a faint limit of the KLF that corresponds to the absolute magnitude $M_{\text{max}}^K = 3.5$ mag (Alexander & Sternberg 1999). The absolute magnitude of the faintest star that can be observed depends on the detection threshold K_0 and the amount of extinction along the line of sight, given by A_K :

$$M_0^K = K_0 - 5 \log \left(\frac{D_S}{1 \text{ kpc}} \right) - A_K - 10. \quad (6.18)$$

The luminosity ratio appearing in Equation (6.12) is then

$$\frac{L_{\text{min}}}{L_0} = 10^{-0.4(M_{\text{max}}^K - M_0^K)}. \quad (6.19)$$

We use the fiducial values $K_0 = 17$ mag (Alexander & Sternberg 1999) and $A_K = 2.6$ mag (Schödel et al. 2007), although we consider other possibilities below.

We numerically integrate Equation (6.12) for each stellar component (cusp, bulge, and disk). Even though the density profiles naturally decrease with radius (see Fig. 6.1), it is convenient to impose a finite truncation radius. We truncate the bulge and disk components at 3 kpc and 25 kpc, respectively, although the specific values are not very

³Strictly speaking, this limit on D_{LS} applies when $\beta = 0$. When $\beta > 0$ the source can be slightly closer to the lens and still yield resolvable images, but the difference is not important for our analysis.

important. The extent of the cusp component is less well defined. We adopt a fiducial truncation radius of 100 pc, but consider other possibilities in Section 6.2.7.

In contrast with previous work, we do not truncate the angular integral at the Einstein angle. A source can be located outside the Einstein angle and still be multiply-imaged, although as β increases, the secondary image gets fainter and falls below the detection threshold. In practice, we find that integrating ϑ out to 1° works well; this range is large enough to include all the weight in the integral, yet small enough for small-angle approximations to remain valid.

For our fiducial model we find $N_{\text{lens}}^c = 0.085$, $N_{\text{lens}}^b = 0.032$ and $N_{\text{lens}}^d = 0.440$, giving a total of $N_{\text{lens}}^{\text{tot}} = 0.557$. The superscripts denote the cusp, bulge and disk contributions, respectively. We see that the number of lensed disk stars is nearly an order of magnitude greater than in the cusp and bulge. While the cusp has a much higher density of stars, it is confined to small radii, where the lensing cross section is small (see Fig. 6.1). By contrast, the disk extends to much larger radii, where the lensing cross section is much larger. It was not obvious *a priori* whether the increased volume could compensate for the reduced density to allow the disk to contribute to the lensing signal; clearly it does, at least for our fiducial model.

6.2.4 Limiting Magnitude

Table 6.1 shows how the number of lenses changes as the limiting magnitude varies. For comparison, the magnitude of Sgr A* is $K = 16.1$ in quiescence (Genzel et al. 2003). The number of lenses increases by a factor of ~ 60 as the limiting luminosity decreases by a factor of 100. This comes directly from the luminosity function. The KLF decreases as $L^{-1.875}$, so the number of stars brighter than L_0 is proportional to $L_0^{-0.875}$. When we decrease L_0 by a factor of 100, i.e., from $K_0 = 16.5$ mag to $K_0 = 21.5$ mag, the change in the number of detectable stars is a factor of $100^{0.875} = 56.2$. (The maximum limit $K_0 = 21.5$ corresponds to a detection threshold equal to the minimum luminosity of the KLF.) We see that increasing the limiting magnitude greatly enhances the probability of observing strong lensing. This is promising because continued observations of the GC are making it possible to observe fainter and fainter stars.

Table 6.1 Number of strong lenses for limiting magnitudes, K_0 (Col. 1), spanning a factor of 100 in luminosity. Cols. 2–4 give the number of lenses for the cusp, bulge and disk, respectively, while Col. 5 gives the total number of lenses.

K_0	N_{lens}^c	N_{lens}^b	N_{lens}^d	$N_{\text{lens}}^{\text{tot}}$
16.5	0.06	0.02	0.29	0.37
17.5	0.13	0.06	0.66	0.85
18.5	0.28	0.11	1.47	1.86
19.5	0.63	0.25	3.30	4.18
20.5	1.42	0.53	7.39	9.34
21.5	3.18	1.20	16.55	20.93

6.2.5 Extinction by Dust

To this point we have assumed that all lines of sight near the GC are subject to 2.6 mag of extinction. There is some spatial variation—Baade’s window has only 0.4 mag of extinction—although only on scales larger than the Einstein radius even for a distant source. More problematic is our assumption that all background stars suffer the same amount of extinction no matter how far behind Sgr A* they are. If the distribution of dust on the far side of the GC is similar to that on the near side, we would expect a star in the disk 8 kpc behind Sgr A* to have a total $A_K = 5.2$ mag. If we assume this value for the entire disk, N_{lens}^d decreases by a factor of 8.13.

We explore the effect of extinction on N_{lens} by assuming a simple linear distance dependence for A_K , viz.:

$$A_K(D_{LS}) = 2.6 \left(1 + \frac{D_{LS}}{8 \text{ kpc}} \right). \quad (6.20)$$

This toy model provides a way to assess the importance of dust, while avoiding uncertainties related to the distribution of dust behind the GC. A complete treatment of extinction would require detailed knowledge of the dust distribution in the Galaxy, which is beyond the scope of this chapter. Instead, our main goal is to get a sense of how much extinction affects our results.

The linear extinction model yields $N_{\text{lens}} = 0.084, 0.025$ and 0.157 for the cusp, bulge and disk, respectively. We see that additional extinction is not very important for the

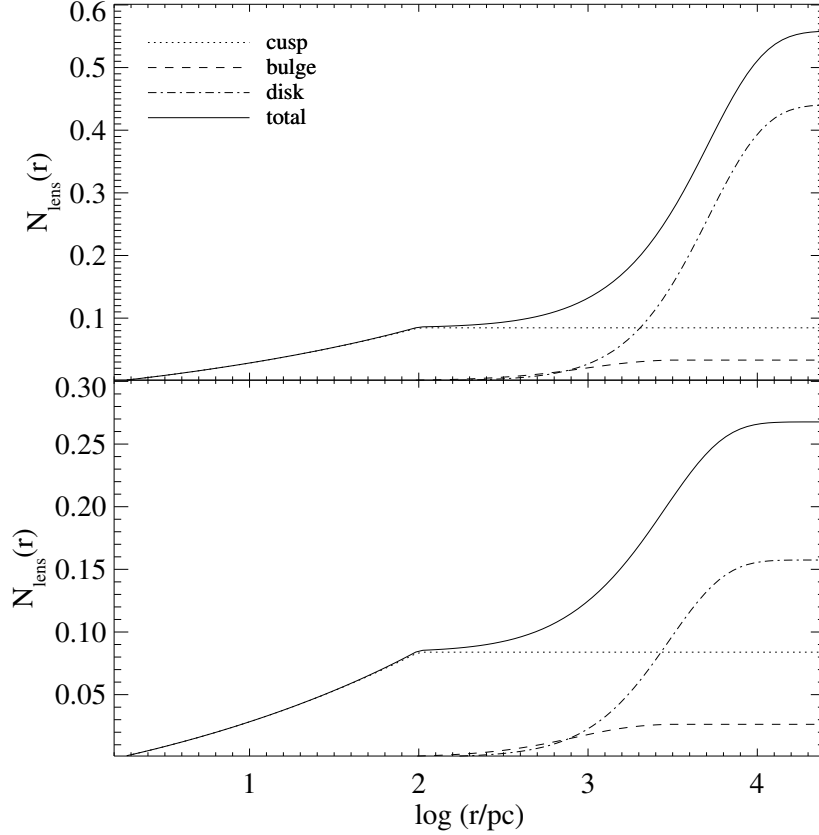


Figure 6.3 Cumulative number of strongly-lensed stars behind Sgr A* within galactocentric radius r . The top panel accounts only for extinction between the observer and Sgr A* ($A_K = 2.6$ mag) while the bottom panel includes additional extinction between Sgr A* and a background source ($A_K = 2.6[1 + r/8 \text{ kpc}]$ mag). The dotted, dashed and dot-dashed curves show the contributions of the cusp, bulge and disk, respectively. The solid line is the sum of all components.

cusp and bulge, but is significant for the disk (cf. §6.2.3). This makes sense intuitively since the cusp and bulge are confined to the inner ~ 100 – 1000 pc of the Galaxy, while the disk extends to 25 kpc from the GC. For comparison, in our linear extinction model the extinction is $A_K = 2.63$ mag at 100 pc, 3.58 mag at 3 kpc and 10.7 mag at 25 kpc.

To facilitate comparison between the two extinction models, we plot the cumulative number of strong lenses within radius r in Figure 6.3. We show the separate contributions from the cusp, bulge, and disk, as well as the total. The cusp and bulge contributions are virtually identical in the two extinction models. The differences are clearly in the disk contribution, which rises more slowly and saturates at a lower value

of $N_{\text{lens}}(r)$ in the linear extinction model.

When interpreting these results, it is important to remember that our model for A_K is overly simplistic. In particular, since dust is largely confined to the central regions of the Galaxy, our model probably overestimates the extinction for distances $\gtrsim 8$ kpc behind the GC. Again, for our purposes, the important thing is to have an estimate of how uncertainty in the amount of extinction affects the expected number of lenses.

6.2.6 Slope of the Luminosity Function

We now consider how N_{lens} depends on the assumed KLF. We focus on the power law index p , because the effects of varying L_{min} can be understood in terms of our earlier discussion of the limiting magnitude (§6.2.4). The power law index $p = 1.875$ was derived from observations of the bulge (Blum et al. 1996), and it agrees with stellar population-synthesis models (Alexander & Sternberg 1999). It seems reasonable to apply this value to the cusp as well. However, there may be a different stellar population and hence KLF in the disk.

In Figure 6.4 we see that N_{lens} decreases as p increases. As we vary p by ± 0.2 , N_{lens} varies by a factor of 5. We can understand the result qualitatively as follows. Increasing p means making the KLF steeper, which means that more of the stars are fainter, so the number of stars (and hence lenses) brighter than our magnitude limit is smaller. The quantitative scaling is more complicated, because the terms in Equation (6.12) that involve p vary with position. Thus, the p dependence cannot be isolated, and it ought to be different for stellar components with different spatial distributions. The cusp and disk curves in Figure 6.4 are in fact not quite parallel to each other. Nevertheless, it is interesting to see that the variation in N_{lens} with p is quite similar for the two very different source populations.

6.2.7 Truncation Radius of the Cusp

Taken at face value, the model for the stellar cusp given by Equation (6.1) implies that the cusp component dominates the density out to ~ 1 kpc, and always exceeds the bulge density (see Fig. 6.1). This is implausible, because the cusp owes its existence to the

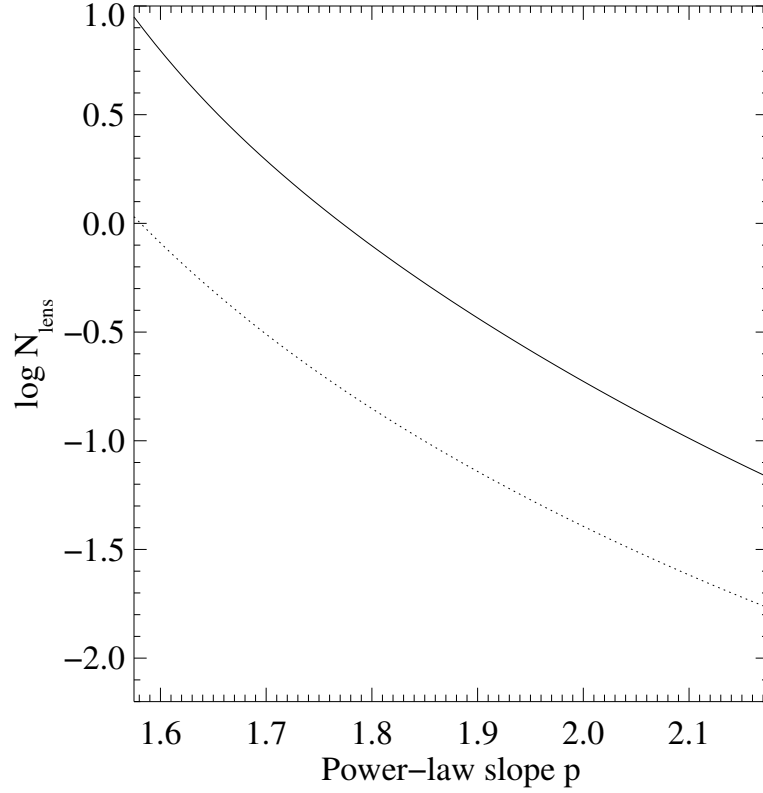


Figure 6.4 Number of strongly-lensed stars behind Sgr A* vs. the power-law slope, p , of the KLF. The solid and dotted curves denote the disk and cusp contributions to N_{lens} , respectively. The two curves are similar but not quite parallel.

SMBH, so it should not continue to dominate well beyond the black hole’s sphere of influence. Formally, the problem is that the profile in Equation (6.1) was determined from observations of stars in the central few parsecs, and should not be extrapolated to arbitrarily large radii. In our fiducial model we truncate the cusp component at 100 pc, which is consistent with earlier studies of lensing by Sgr A* (Alexander & Sternberg 1999). However, as the truncation is not well constrained by physical considerations, we wish to understand how changing the truncation radius affects the number of strong lenses.

For cusp truncation radii of 10 pc, 100 pc, 1 kpc, and 10 kpc, we find $N_{\text{lens}}^c = 0.03$, 0.08, 0.17, and 0.28, respectively. The truncation of the cusp produces a prominent

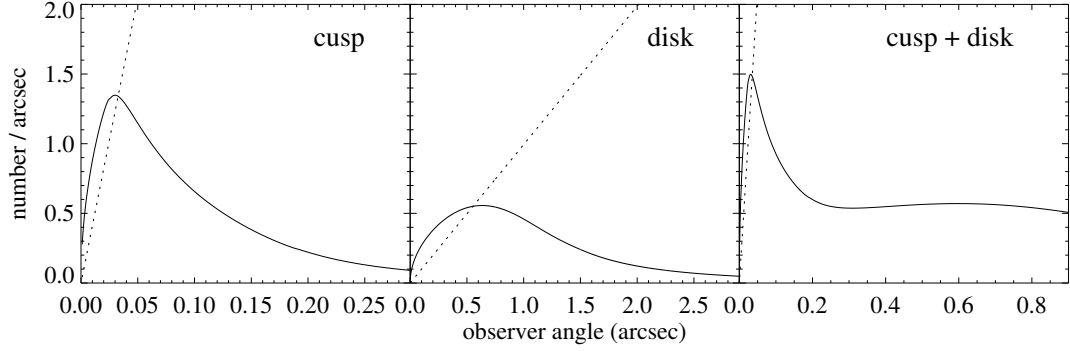


Figure 6.5 Angular distribution of lensed images. The solid lines give the number of lensed images per arcsecond ($dN_{\text{lens}}/d\theta$), while the dotted lines show the number of stars per arcsecond ($dN_*/d\theta$). The three panels show the contributions of the cusp (left), the disk (middle), and their sum (right). Note that the angular range differs from one panel to the next.

bump in the plot of the cumulative number of lenses within galactocentric radius r (see Fig. 6.3). The fact that this bump moves around, and N_{lens}^c changes, as we vary the truncation radius indicates that precise predictions for lensing will require more knowledge of how the cusp density decreases and blends into the bulge. (Understanding this would be of general interest for GC studies, beyond our specific focus on lensing.) Nevertheless, since a reasonable cusp provides a modest contribution to the total lensing signal, the details do not affect our general conclusions about lensing by Sgr A*.

6.2.8 Angular Distribution of Lensed Images

In order to observe strong lensing by Sgr A*, we will need to distinguish lensed images from unlensed stars, and from Sgr A* itself. Since lensed images tend to form in the vicinity of the Einstein radius, they will have a different distribution on the sky than unlensed stars. (The Einstein radius depends on the distance to the source, of course, but our formalism automatically accounts for this effect.) We use the functions $dN_{\text{lens}}/d\theta$ and $dN_*/d\theta$ from Equations (6.16) and (6.17) to identify the regions near Sgr A* where it is most favorable to look for lensed images.

Figure 6.5 shows $dN_{\text{lens}}/d\theta$ (solid lines) and $dN_*/d\theta$ (dotted lines) for the cusp, the disk, and the combination, using our fiducial model. (We omit the bulge component

here since our previous analysis has shown that it provides only a modest contribution to the number of lenses.) For both the cusp and disk, $dN_*/d\theta$ increases linearly with observing angle; this is simply a consequence of the increasing size of the annulus, and is evident from Equation (6.17). The slope of the line is determined by the integral of the number density of stars along the line of sight, and is much steeper for the cusp than for the disk, when looking within a few arcsec of the GC.

The dependence of $dN_{\text{lens}}/d\theta$ on observing angle is more complicated. For angles much larger than the Einstein radius, if we see a lensed image it will be the brighter image ($\theta = \theta_+$), and its counter-image at θ_- may be too faint to be detected. Specifically, at large θ we have $\mu \approx 1 + (\theta_E/\theta)^4$ and $\mu_- \approx -(\theta_E/\theta)^4$ from Equations (6.8) and (6.15). Then Equation (6.16) yields $dN_{\text{lens}}/d\theta \propto \theta^{5-4p}$, where p is the slope of the KLF. For our fiducial value $p = 1.875$, this yields $dN_{\text{lens}}/d\theta \propto \theta^{-2.5}$ at large angles.

For observing angles much smaller than θ_E , any lensed image present will be the fainter image ($\theta = \theta_-$), and the closer it is to the lens the fainter it will be. This is counteracted to some degree by the slope of the KLF. Specifically, $\mu_- \approx -(\theta/\theta_E)^4$ at small θ , so Equation (6.16) yields $dN_{\text{lens}}/d\theta \propto \theta^{4p-7}$. For our fiducial value $p = 1.875$, this yields $dN_{\text{lens}}/d\theta \propto \theta^{0.5}$ at small angles. Note that if we had $p < 1.75$ the function $dN_{\text{lens}}/d\theta$ would actually diverge at small θ .

The angular range in which $dN_{\text{lens}}/d\theta$ is appreciable depends on the Einstein radius and hence the distance to the source. Since cusp stars have small Einstein radii, to see lensing it would be ideal to observe within $\theta \lesssim 0.05$ arcsec, although this would be challenging given that the flux from Sgr A* itself fills the central resolution element. Even at $\theta = 0.3$ arcsec, though, the prospects of observing lensing are still reasonable: unlensed stars outnumber lensed images by about a factor of 120, which is actually smaller than the ratio of unlensed to lensed quasars.

For disk stars, the greater distance to the source causes the $dN_{\text{lens}}/d\theta$ curve to peak at a larger angle $\theta \approx 0.6$ arcsec. At this angle the number of lensed images is comparable to the number of lensed stars. Even for an angle as large as $\theta = 3$ arcsec, the factor by which stars outnumber lensed images is only about 60. In other words, the “background” of unlensed stars is not such a daunting problem, at least within a

few arcseconds of Sgr A*.

6.3 Lensing by Massive Black Holes in Other Systems

We now turn to black holes other than Sgr A* and make simple estimates (rather than detailed predictions) to understand whether it may be worthwhile to look for lensing in other stellar systems.

Stellar dynamical observations have recently provided good evidence for supermassive black holes (SMBHs) in nearby galaxies, and revealed correlations between the mass of the black hole and the properties of the host galaxy, including the velocity dispersion (Ferrarese & Merritt 2000; Gebhardt et al. 2000; Tremaine et al. 2002), mass (Magorrian et al. 1998), and luminosity (McLure & Dunlop 2002) of the bulge, and the rotational velocity of the disk (Ferrarese 2002; Baes et al. 2003). Outside of the nearby universe, SMBH masses have been probed only in Active Galactic Nuclei (AGN) through reverberation mapping (Kaspi et al. 2000; Peterson et al. 2004). Some previous work has considered whether lensed quasars can be used to constrain SMBH masses in distant lens galaxies (Bowman et al. 2004; Rusin et al. 2005), although the method relies on faint, “central” lensed images that are difficult to detect, and can probe only a narrow range of black hole masses. Rather than considering lensing of background quasars, we focus on lensing of stars *within* the galaxy hosting an SMBH.

There is evidence from velocity dispersion measurements (Gebhardt et al. 2002) and x-ray observations of an accretion flow (Maccarone et al. 2007) for intermediate mass black holes (IMBHs) in two extragalactic globular clusters, although a definitive discovery of an IMBH has yet to emerge (Gerssen et al. 2002, 2003; Baumgardt et al. 2003a,b; Ho et al. 2003). There are also theoretical reasons to believe globular clusters may host IMBHs. In these dense stellar systems, frequent interactions between stars would likely cause a black hole to form, which would then grow to the appropriate mass through accretion of nearby stars and stellar-mass black holes (Miller & Hamilton 2002). The velocity dispersions of globular clusters correspond to what we would expect for the host of an IMBH, if the correlation between black hole mass and host velocity

dispersion can be extrapolated downwards. The formalism we develop to consider lensing by SMBHs in galaxies may also be applied to lensing by IMBHs in globular clusters.

We seek an order-of-magnitude estimate of the number of lenses in a dynamical system containing a black hole of mass M_\bullet that is surrounded by stars with mass M_* (we assume the stars are identical for simplicity) and number density n_* . If $M_\bullet \gg M_*$ the black hole dominates the lensing signal (there is little star-star lensing). We estimate the number of lenses as the number of stars within the black hole's Einstein area, πR_E^2 :

$$N_{\text{lens}} \sim \int_{D_{LS} > 0} \pi R_E^2 n_* dD_{LS}. \quad (6.21)$$

This estimate omits many of the details that we included for Sgr A* (cf. Eq. [6.12]); in particular, it considers sources only out to the Einstein angle, and counts stars of all luminosities. Nevertheless, it is adequate for our purposes here.

To obtain n_* , we first use the virial theorem to estimate the total mass of a system with velocity dispersion σ and size L to be $M_{\text{tot}} \sim \sigma^2 L / G$. If the stars are uniformly distributed, the number density is

$$n_* \sim \frac{3\sigma^2}{4\pi G M_* L^2}. \quad (6.22)$$

Although the assumption of uniform density is not realistic, it is consistent with our goals in this section.

The Einstein radius, $R_E \equiv D_S \theta_E$, can be written as

$$R_E = \sqrt{\frac{4GM_\bullet D_S D_{LS}}{c^2 D_L}} \approx \sqrt{\frac{4GM_\bullet D_{LS}}{c^2}}. \quad (6.23)$$

In the second step we make the approximation $D_L \approx D_S$, which is reasonable for the systems of interest: globular clusters typically have $D_L \gtrsim 10$ kpc and $D_{LS} \leq L \sim 10$ pc; while galaxies are at distances $D_L \gtrsim 1$ Mpc and have sizes $L \sim 10$ kpc.

We can then evaluate the integral in Equation (6.21) to find

$$N_{\text{lens}} \sim \frac{3}{2} \frac{M_\bullet}{M_*} \left(\frac{\sigma}{c} \right)^2. \quad (6.24)$$

To proceed further, we estimate the black hole mass from the M_{\bullet} - σ relation (Tremaine et al. 2002),

$$M_{\bullet} = 1.35 \times 10^8 \left(\frac{\sigma}{200 \text{ km s}^{-1}} \right)^{4.02} M_{\odot}. \quad (6.25)$$

(We neglect the scatter in this relation since it has little impact on our estimates.) This relation is observed to hold for nearby galaxies; we assume that it can be extended down to the velocity dispersions of globular clusters, since the IMBH masses it predicts are consistent with theoretical models.

Using Equation (6.25) in Equation (6.24), and assuming the stars have mass $M_* \sim M_{\odot}$, we obtain an estimate for the number of lensed stars that depends only on the velocity dispersion of the system:

$$N_{\text{lens}} \sim 1.3 \times 10^{-6} \left(\frac{\sigma}{10 \text{ km s}^{-1}} \right)^{6.02} \quad (6.26)$$

$$\sim 90 \left(\frac{\sigma}{200 \text{ km s}^{-1}} \right)^{6.02}. \quad (6.27)$$

The reference units for σ in these relations are appropriate for globular clusters and galaxies, respectively. Recall that this is our estimate for the number of stars in a globular cluster or galaxy that are lensed by a massive black hole *within the same stellar system*.

We see that the lensing optical depth is very small for a globular cluster; we would need to observe on the order of a million clusters to have a good chance of finding an instance of lensing. It is worth saying that high stellar density in globular clusters could invalidate our assumption that the only object relevant for lensing is the central IMBH (cf. Chanamé et al. 2001; Alexander & Loeb 2001). Including the effects of other stars could enhance the optical depth. Nevertheless, the enhancement would have to be dramatic to make globular clusters viable candidates for lensing.

The situation is very different in galaxies. Our estimate indicates that for a typical massive elliptical galaxy with $\sigma \sim 200 \text{ km s}^{-1}$ there ought to be ~ 100 stars that are strongly lensed. For a particularly massive galaxy, such as the giant elliptical M87 with $\sigma \sim 400 \text{ km s}^{-1}$, the number of lensed stars could approach ~ 5800 . It is interesting to speculate about how we might look for evidence of this lensing. We could not

resolve individual lensed stars; rather, we would see an enhancement of the flux on an angular scale comparable to the Einstein radius, which for M87 is $\theta_E \sim 0.02$ arcsec. Roughly speaking, half the stars within this radius (those behind the black hole) would be magnified, and the average magnification for a point mass lens is $\langle \mu \rangle = \sqrt{5}$, so in total the flux within $\sim \theta_E$ would be enhanced by a factor of ~ 1.6 . A more careful analysis would account for the variation in both the Einstein radius and stellar density with radius in the galaxy. While that is beyond the scope of this chapter, it would be worthwhile to consider, since we conclude that every massive elliptical galaxy ought to contain many stars that are strongly lensed by the SMBH at the center of the galaxy.

6.4 Constraining Gravity with SMBH Lensing

Having found that it may be possible to observe lensing of stars by SMBHs, we now consider the prospects that such observations would allow us to probe the spacetime geometry around a black hole and thereby test general relativity and other theories of gravity. We return our focus to Sgr A*, because it is still the best place to look for black hole lensing, and because the formalism we developed in Section 6.2 permits us to forecast in some detail the ability of lensing observations to constrain gravity theories.

Keeton & Petters (2005, 2006) have presented a theoretical framework for lensing by a static, spherically symmetric compact object in the post-post-Newtonian (PPN) framework. Their formalism rests on three assumptions, all of which hold for our example: (i) The spacetime geometry far from the lens is flat. (ii) Both the observer and source lie in the asymptotically flat region of the spacetime; indeed, the smallest galactocentric distance we use is $D_{LS} \sim 1$ pc, whereas the gravitational radius of Sgr A* is $GM_\bullet/c^2 \sim 10^{-7}$ pc. (iii) The impact parameter of a light ray is much larger than the lens's gravitational radius; as we shall see, the ratio of light impact parameter to lens gravitational radius is $\gtrsim 10^4$ in our examples. With these assumptions, the properties of the lensed images can be written as Taylor series in the parameter

$$\varepsilon \equiv \frac{\theta_\bullet}{\theta_E} = \frac{R_E}{4D_{LS}}, \quad (6.28)$$

where

$$\theta_{\bullet} \equiv \tan^{-1} \left(\frac{GM_{\bullet}}{c^2 D_L} \right) \approx \frac{GM_{\bullet}}{c^2 D_L} \quad (6.29)$$

is the angle subtended by the gravitational radius of the black hole, and $R_E \equiv D_S \theta_E$ (cf. Eq. [62] in Keeton & Petters 2005). For example, one of the more interesting Taylor series involves the geometric mean of the image positions,

$$|\theta_+ \theta_-|^{1/2} = \frac{A_1}{4} \theta_E + \frac{A_2(A_1 + 2\hat{\beta}^2)}{4A_1(A_1 + \hat{\beta}^2)^{1/2}} \theta_E \varepsilon + \mathcal{O}(\varepsilon^2), \quad (6.30)$$

where $\hat{\beta} = \beta/\theta_E$ is the dimensionless source position. The constants A_1 and A_2 depend on the gravity theory. In general relativity $A_1 = 4$ and $A_2 = 15\pi/4$, while in the PPN framework these constants can be expressed in terms of the usual PPN parameters $(\alpha', \beta', \gamma', \delta')$ as

$$A_1 = 2(\alpha' + \gamma'), \quad (6.31)$$

$$A_2 = \frac{\pi}{4} [8\alpha'(\alpha' + \gamma') - 4\beta' + 3\delta']. \quad (6.32)$$

Measurements of light bending by the Sun constrain $A_1 = 3.99966 \pm 0.00090$ (Shapiro et al. 2004), but there are currently no good observational constraints on A_2 . It is interesting to consider whether we can use black hole lensing to measure A_2 .

Keeton & Petters (2005, 2006) discuss this issue in some detail; here we mainly want to use the expansion parameter ε to quantify the amplitude of higher-order effects. First consider some illustrative examples. We fix the mass and distance of Sgr A* as given in Section 6.2.3. Then a cusp star with $D_{LS} = 1$ pc has $\varepsilon = 1.9 \times 10^{-4}$. A bulge star with $D_{LS} = 1$ kpc has $\varepsilon = 6.2 \times 10^{-6}$. Finally, a disk star with $D_{LS} = 10$ kpc has $\varepsilon = 2.8 \times 10^{-6}$. To give more detail, we use our formalism⁴ from Section 6.2 to compute the cumulative number of lenses for which the correction terms are larger than ε , which is plotted in Figure 6.6. Note that $\varepsilon \ll 1$, which verifies assumption (iii) of the formalism, and also indicates that we have not made large errors by using weak-field lensing in Section 6.2.2.

⁴Specifically, for each value of ε , we solve for the corresponding value of D_{LS} and use this as the upper limit for the radial integral in Equation (6.12).

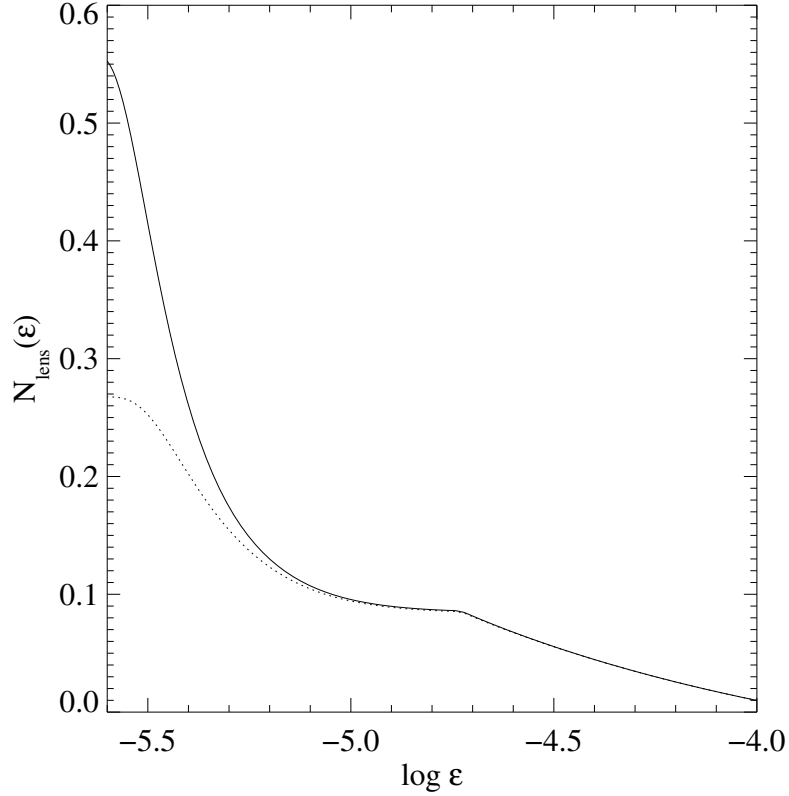


Figure 6.6 Cumulative number of strongly-lensed stars behind Sgr A* for which the PPN expansion parameter is larger than ε . The expansion parameter quantifies the strength of higher-order corrections to the usual weak-field approximation for lensing. The solid curve assumes our fiducial model (§ 6.2.3), including the limiting magnitude $K_0 = 17$. The dotted curve assumes our linear extinction model (§ 6.2.5). The bump at $\log \varepsilon \sim -4.75$ is caused by truncating the cusp at $r = 100$ pc (cf. Fig. 6.3).

We can think of ε as an order-of-magnitude estimate for the *fractional* corrections to the image positions, magnifications, and time delays. Measuring such small changes to the image brightnesses would be very challenging. Measuring such corrections to the time delay may be feasible if the source varies rapidly, as would be the case for a lensed pulsar. However, since pulsars comprise a small fraction of stars, it seems unlikely that we will be so fortunate as to observe a lensed pulsar.

For the image positions, it is more interesting to consider the *absolute* correction term, which is of order $\varepsilon \theta_E = \theta_\bullet$ (cf. Eq. [6.30]). Notice that the position correction is *independent of the distance from the lens to the source*. For Sgr A* the correction

is of order $\theta_{\bullet} = 3.5 \mu\text{as}$. While this level of astrometric precision is not currently feasible, it could be achieved with future instruments such as the Space Interferometry Mission (Unwin et al. 2008) and the Global Astrometry Interferometer for Astrophysics (Perryman et al. 2001) if these instruments include near-infrared capabilities.

If μas -level precision is achieved, how could we identify higher-order effects? From Equation (6.30), the geometric mean of the image positions is independent of the source position in the weak-field limit. Therefore, if we observe lensing of a source that moves and we find that $|\theta_+\theta_-|^{1/2}$ varies with time, we will know we have detected higher-order effects. A source moving with the typical Galactic velocity of 220 km s^{-1} will move $(0.1, 0.03, 0.01)$ Einstein radii per year if it lies $(10, 100, 1000)$ pc from Sgr A*. Therefore, in order to test theories of gravity with black hole lensing, our best hope is to observe lensing of a cusp star and then monitor the images as the source moves. Based on our results in Section 6.2.4, we are optimistic that this will be possible as observations of the GC continue.

6.5 Conclusions

We have considered prospects for testing theories of gravity with lensing by massive black holes, with particular emphasis on the Galactic SMBH Sgr A*. While previous authors have focused on theoretical aspects of black hole lensing, we have considered many practical issues that must be addressed before the theory can be implemented. In particular, we have sought to assess the likelihood that SMBH lensing can actually be observed.

We have complemented earlier work on lensing by massive black holes in several important ways. For the case of Sgr A*, we have focused on strong lensing, where the two images of a background star can be resolved. We have found that stars in the disk actually contribute more lenses than stars in the bulge or the central cusp; the lensing cross section for stars in the disk is high enough to compensate for the lower stellar density in the disk beyond the GC. Using the K-band luminosity function, we have explicitly computed the number of lenses for which *both* images are brighter than some

detection threshold. Using our fiducial parameters, we find the expected number of lenses to be in the range ~ 0.3 – 0.6 for the present magnitude limit $K = 17$ mag, where the range encompasses the choice of extinction model. Raising the magnitude limit to $K = 18.5$ mag increases the expected number of lenses by a factor of ~ 3 .

Our encouraging results for Sgr A* motivated us to consider black holes in other stellar systems. Even if globular clusters contain intermediate-mass black holes, the lensing probability is very low ($\sim 10^{-6}$), so lensing does not seem to provide a useful method for confirming or refuting the existence of IMBHs. Our results are more promising for supermassive black holes in other galaxies. A typical galaxy could contain ~ 100 lensed stars; the number of lenses could reach ~ 5800 for galaxies such as M87 that contain central black holes with masses in excess of $\sim 10^9 M_\odot$. This effect could be observable as an increase in the flux inside the Einstein radius, which is ~ 0.02 arcsec for M87.

Having established that there is a reasonable chance of observing SMBH lensing in either the Milky Way or an external galaxy, we considered whether such observations would allow us to probe gravity beyond the weak-field limit. For Sgr A*, measuring the image positions with microarcsecond-scale resolution would make it possible to detect higher-order gravity effects and test general relativity against alternate theories. Of course, the first step is to discover a strongly lensed star.

Acknowledgments

We thank Tal Alexander, Reinhard Genzel, Avi Loeb, M. Coleman Miller, and Tad Pryor for helpful discussions.

Bibliography

- Alexander T., Loeb A., 2001, ApJ, 551, 223
- Alexander T., Sternberg A., 1999, ApJ, 520, 137
- Atkinson R. d., 1965, AJ, 70, 517

- Baes M., Buyle P., Hau G. K. T., Dejonghe H., 2003, MNRAS, 341, L44
- Baganoff F. K., Bautz M. W., Brandt W. N., Chartas G., Feigelson E. D., Garmire G. P., Maeda Y., Morris M., Ricker G. R., Townsley L. K., Walter F., 2001, Nature, 413, 45
- Bahcall J. N., Wolf R. A., 1977, ApJ, 216, 883
- Baumgardt H., Hut P., Makino J., McMillan S., Portegies Zwart S., 2003a, ApJ, 582, L21
- Baumgardt H., Makino J., Hut P., McMillan S., Portegies Zwart S., 2003b, ApJ, 589, L25
- Bhadra A., 2003, Phys. Rev. D, 67, 103009
- Blum R. D., Sellgren K., Depoy D. L., 1996, ApJ, 470, 864
- Bowman J. D., Hewitt J. N., Kiger J. R., 2004, ApJ, 617, 81
- Bozza V., 2002, Phys. Rev. D, 66, 103001
- , 2003, Phys. Rev. D, 67, 103006
- Bozza V., Capozziello S., Iovane G., Scarpetta G., 2001, General Relativity and Gravitation, 33, 1535
- Bozza V., de Luca F., Scarpetta G., Sereno M., 2005, Phys. Rev. D, 72, 083003
- Bozza V., Mancini L., 2004, General Relativity and Gravitation, 36, 435
- , 2005, ApJ, 627, 790
- Carroll B. W., Ostlie D. A., 1996, *Modern Astrophysics*. Reading, MA: Addison-Wesley
- Chanamé J., Gould A., Miralda-Escudé J., 2001, ApJ, 563, 793
- Darwin C., 1958, Proc. R. Soc. London, A249, 180
- Eckart A., Genzel R., 1997, MNRAS, 284, 576

- Eckart A., Genzel R., Ott T., Schödel R., 2002, MNRAS, 331, 917
- Eiroa E. F., 2005, Phys. Rev. D, 71, 083010
- Eiroa E. F., Romera G. E., Torres D. F., 2002, Phys. Rev. D, 66, 024010
- Eisenhauer F., Genzel R., Alexander T., Abuter R., Paumard T., Ott T., Gilbert A., Gillessen S., Horrobin M., Trippe S., Bonnet H., Dumas C., Hubin N., Kaufer A., Kissler-Patig M., Monnet G., Ströbele S., Szeifert T., Eckart A., Schödel R., Zucker S., 2005, ApJ, 628, 246
- Ferrarese L., 2002, ApJ, 578, 90
- Ferrarese L., Merritt D., 2000, ApJ, 539, L9
- Gebhardt K., Bender R., Bower G., Dressler A., Faber S. M., Filippenko A. V., Green R., Grillmair C., Ho L. C., Kormendy J., Lauer T. R., Magorrian J., Pinkney J., Richstone D., Tremaine S., 2000, ApJ, 539, L13
- Gebhardt K., Rich R. M., Ho L. C., 2002, ApJ, 578, L41
- Genzel R., Schödel R., Ott T., Eckart A., Alexander T., Lacombe F., Rouan D., Aschenbach B., 2003, Nature, 425, 934
- Gerssen J., van der Marel R. P., Gebhardt K., Guhathakurta P., Peterson R. C., Pryor C., 2002, AJ, 124, 3270
- , 2003, AJ, 125, 376
- Ghez A. M., Klein B. L., Morris M., Becklin E. E., 1998, ApJ, 509, 678
- Ghez A. M., Morris M., Becklin E. E., Tanner A., Kremenek T., 2000, Nature, 407, 349
- Ghez A. M., Salim S., Hornstein S. D., Tanner A., Lu J. R., Morris M., Becklin E. E., Duchêne G., 2005, ApJ, 620, 744
- Ho L. C., Terashima Y., Okajima T., 2003, ApJ, 587, L35
- Holz D. E., Wheeler J. A., 2002, ApJ, 578, 330

- Kaspi S., Smith P. S., Netzer H., Maoz D., Jannuzi B. T., Giveon U., 2000, *ApJ*, 533, 631
- Keeton C. R., Petters A. O., 2005, *Phys. Rev. D*, 72, 104006
- , 2006, *Phys. Rev. D*, 73, 044024
- Kent S. M., 1992, *ApJ*, 387, 181
- Kormendy J., Richstone D., 1995, *ARA&A*, 33, 581
- Luminet J.-P., 1979, *A&A*, 75, 228
- Maccarone T. J., Kundu A., Zepf S. E., Rhode K. L., 2007, *Nature*, 445, 183
- Magorrian J., Tremaine S., Richstone D., Bender R., Bower G., Dressler A., Faber S. M., Gebhardt K., Green R., Grillmair C., Kormendy J., Lauer T., 1998, *AJ*, 115, 2285
- Majumdar A. S., Mukherjee N., 2005a, *International Journal of Modern Physics D*, 14, 1095
- , 2005b, *Modern Physics Letters A*, 20, 2487
- Maoz E., 1998, *ApJ*, 494, L181
- McLure R. J., Dunlop J. S., 2002, *MNRAS*, 331, 795
- Miller M. C., Hamilton D. P., 2002, *MNRAS*, 330, 232
- Miralda-Escudé J., Gould A., 2000, *ApJ*, 545, 847
- Munyanenza F., Viollier R. D., 2002, *ApJ*, 564, 274
- Nusser A., Broadhurst T., 2004, *MNRAS*, 355, L6
- Ohanian H. C., 1987, *American Journal of Physics*, 55, 428
- Perryman M. A. C., de Boer K. S., Gilmore G., Høg E., Lattanzi M. G., Lindegren L., Luri X., Mignard F., Pace O., de Zeeuw P. T., 2001, *A&A*, 369, 339

- Peterson B. M., Ferrarese L., Gilbert K. M., Kaspi S., Malkan M. A., Maoz D., Merritt D., Netzer H., Onken C. A., Pogge R. W., Vestergaard M., Wandel A., 2004, *ApJ*, 613, 682
- Petters A. O., 2003, *MNRAS*, 338, 457
- Reid M. J., 1993, *ARA&A*, 31, 345
- Rusin D., Keeton C. R., Winn J. N., 2005, *ApJ*, 627, L93
- Schödel R., Eckart A., Alexander T., Merritt D., Genzel R., Sternberg A., Meyer L., Kul F., Moulata J., Ott T., Straubmeier C., 2007, *A&A*, 469, 125
- Schödel R., Ott T., Genzel R., Eckart A., Mouawad N., Alexander T., 2003, *ApJ*, 596, 1015
- Schödel R., Ott T., Genzel R., Hofmann R., Lehnert M., Eckart A., Mouawad N., Alexander T., Reid M. J., Lenzen R., Hartung M., Lacombe F., Rouan D., Gendron E., Rousset G., Lagrange A.-M., Brandner W., Ageorges N., Lidman C., Moorwood A. F. M., Spyromilio J., Hubin N., Menten K. M., 2002, *Nature*, 419, 694
- Sereno M., de Luca F., 2006, *Phys. Rev. D*, 74, 123009
- Shapiro S. S., Davis J. L., Lebach D. E., Gregory J. S., 2004, *Physical Review Letters*, 92, 121101
- Spergel D. N., Verde L., Peiris H. V., Komatsu E., Nolte M. R., Bennett C. L., Halpern M., Hinshaw G., Jarosik N., Kogut A., Limon M., Meyer S. S., Page L., Tucker G. S., Weiland J. L., Wollack E., Wright E. L., 2003, *ApJS*, 148, 175
- Tremaine S., Gebhardt K., Bender R., Bower G., Dressler A., Faber S. M., Filippenko A. V., Green R., Grillmair C., Ho L. C., Kormendy J., Lauer T. R., Magorrian J., Pinkney J., Richstone D., 2002, *ApJ*, 574, 740
- Trippe S., Paumard T., Ott T., Gillessen S., Eisenhauer F., Martins F., Genzel R., 2007, *MNRAS*, 375, 764

Tsiklauri D., Viollier R. D., 1998, *ApJ*, 500, 591

Unwin S. C., Shao M., Tanner A. M., Allen R. J., Beichman C. A., Boboltz D., Catanzarite J. H., Chaboyer B. C., Ciardi D. R., Edberg S. J., Fey A. L., Fischer D. A., Gelino C. R., Gould A. P., Grillmair C., Henry T. J., Johnston K. V., Johnston K. J., Jones D. L., Kulkarni S. R., Law N. M., Majewski S. R., Makarov V. V., Marcy G. W., Meier D. L., Olling R. P., Pan X., Patterson R. J., Pitesky J. E., Quirrenbach A., Shaklan S. B., Shaya E. J., Strigari L. E., Tomsick J. A., Wehrle A. E., Worthey G., 2008, *PASP*, 120, 38

Virbhadra K. S., Ellis G. F. R., 2000, *Phys. Rev. D*, 62, 084003

Wardle M., Yusef-Zadeh F., 1992, *ApJ*, 387, L65

Whisker R., 2005, *Phys. Rev. D*, 71, 064004

Vita

ARTHUR BENJAMIN CONGDON

EDUCATION:

- | | |
|-----------|---|
| 2002–2008 | Rutgers University, New Brunswick, NJ
Ph.D. in Physics and Astronomy |
| 1997–2001 | Temple University, Philadelphia, PA
B.S. in Physics, Summa Cum Laude |

PROFESSIONAL EXPERIENCE:

- | | |
|------|--|
| 2001 | AAAS Entry Point Internship, Goddard Space Flight Center |
|------|--|

PUBLICATIONS:

1. **Congdon A. B.**, Keeton C. R., Nordgen C. E., “Using Differential Time Delays to Identify Gravitational Lenses with Small-Scale Structure,” in preparation
2. **Congdon A. B.**, Keeton C. R., Nordgen C. E., “Analytic Relations for Fold and Cusp Lenses: Implications for Galactic Structure,” in preparation
3. **Congdon A. B.**, Keeton C. R., Nordgen C. E., “Prospects for Testing General Relativity with Lensing by Massive Black Holes,” 2007, *Physical Review D*, submitted
4. **Congdon A. B.**, Keeton C. R., Osmer S. J., “Microlensing of an Extended Source by a Power-law Mass Distribution,” 2007, *Monthly Notices of the Royal Astronomical Society*, 376, 263
5. **Congdon A. B.**, Keeton C. R., “Multipole Models of Four-image Gravitational Lens with Anomalous Flux Ratios,” 2005, *Monthly Notices of the Royal Astronomical Society*, 364, 1459